Modeling of Nonlinear Unsteady Aerodynamics, Dynamics and Fluid Structure Interactions

Zhimiao Yan

Dissertation submitted to the Faculty of
Virginia Polytechnic Institute and State University
in partial fulfillment of the requirements for the degree of

Doctor of Philosophy
in
Engineering Mechanics

Muhammad R. Hajj, Chair
Saad A. Ragab
Shane D. Ross
Mark R. Paul
Mayuresh J. Patil

Dec 2, 2014
Blacksburg, Virginia

Keywords: Nonlinear Dynamics, Unsteady Aerodynamics, Vibration, Energy Harvesting, Galloping, Autoparametric Vibration Absorber, Method of Multiple Scale, Bifurcation, Saturation, Quenching, Chaos

Modeling of Nonlinear Unsteady Aerodynamics, Dynamics and Fluid Structure Interactions

Zhimiao Yan

ABSTRACT

We model different nonlinear systems, analyze their nonlinear aspects and discuss their applications.

First, we present a semi-analytical, geometrically-exact, unsteady potential flow model is developed for airfoils undergoing large amplitude maneuvers. Towards this objective, the classical unsteady theory of Theodorsen is revisited by relaxing some of the major assumptions such as (1) flat wake, (2) small angle of attack, (3) small disturbances to the mean flow components, and (4) time-invariant free-stream. The kinematics of the wake vortices is simulated numerically while the wake and bound circulation distribution and, consequently, the associated pressure distribution are determined analytically. The steady and unsteady behaviors of the developed model are validated against experimental and computational results. The model is then used to determine the lift frequency response at different mean angles of attack.

Second, we investigate the nonlinear characteristics of an autoparametric vibration system. This system consists of a base structure and a cantilever beam with a tip mass. The dynamic equations for the system are derived using the extended Hamilton's principle. The method of multiple scales is then used to analytically determine the stability and bifurcation of the system. The effects of the amplitude and frequency of the external force, the damping coefficient and frequency of the attached cantilever beam and the tip mass on the nonlinear responses of the system are determined. As an application, the concept of energy harvesting based on the autoparametric vibration system consisting of a base structure subjected to the external force and a cantilever beam with a tip mass is evaluated. Piezoelectric sheets are attached to the cantilever beam to convert the vibrations of the base structure into electrical energy. The coupled nonlinear distributed-parameter model is developed and analyzed. The effects of the electrical load resistance on the global frequency and damping ratio of the cantilever beam are analyzed by linearizion of the governing equations and perturbation method. Nonlinear analysis is performed to investigate the impacts of external force and load resistance on the response of the harvester.

Finally, the concept of harvesting energy from ambient and galloping vibrations of a bluff body is investigated. A piezoelectric transducer is attached to the transverse degree of freedom of the body in order to convert the vibration energy to electrical power. A coupled nonlinear distributed-parameter model is developed that takes into consideration the galloping force and moment nonlinearities and the base excitation effects. The aerodynamic loads are modeled using the quasi-steady approximation. Linear analysis is performed to

determine the effects of the electrical load resistance and wind speed on the global damping and frequency of the harvester as well as on the onset of instability. Then, nonlinear analysis is performed to investigate the impact of the base acceleration, wind speed, and electrical load resistance on the performance of the harvester and the associated nonlinear phenomena. Short- and open-circuit configurations for different wind speeds and base accelerations are assessed.

Dedication

To my parents, Ziyou Yan and Suying Chen, who always supported me and showed the benefits of higher education though they both did not finish primary school.

To all my teachers from the primary school to the university, especially, my two master advisors, Professors Zhengliang Li and Zhitao Yan. Without their guide and help, I could not come to Virginia Tech to earn this degree.

To my girlfriend, Ting Tan, who helped me in making the decision to come to Virginia Tech and pursue my studies. Also, I could not have finished my Ph. D degree in three years without her support.

Acknowledgments

First and foremost, I would like to express my sincere appreciation and gratitude to my supervisor Prof. Muhammad Hajj, for his guidance and mentorship during my graduate studies. He is a very nice person and always encourages me to work with other persons in our group. Also, I would like to thank Prof. Ali Nayfeh for recommending me to Prof. Hajj and his rich technical support and guidance.

Next, I want to thank all of my committee members, Profs. Saad Ragab, Shane Ross, Mark Paul and Mayuresh Patil, for their support and useful feedback about my research. Also, their courses were very helpful to me.

Moreover, I should thank my colleagues in Dr Hajj's research group. I want to thank Dr. Abdessattar Abdelkefi for his help when I started my research. I also want to thank Dr. Haithem Taha. He was very helpful in the modeling of the unsteady aerodynamics. I should also thank Drs. Arshad Mehmood, Samah Ben Ayed, Abdulmohsen Alothman, Mohammad Haik and Mohamed Zakaria.

Finally, I want to thank all of my Chinese friends at Virginia Tech.

Contents

List of Figures

List of Tables

1 Introduction

1.1 Motivation

Nonlinear dynamics and phenomena are encountered in many disciplines, design and applications. These include fluid flows where nonlinear aspects such as flow separation and shock formation cause significant variations in flow quantities. In structures, large deformations, concentrated masses and material properties are significant sources of nonlinearities. Fluid-structure interaction is another field where nonlinearities can be inherent to the system and where nonlinear responses are of significant interest. This thesis is concerned with modeling nonlinear phenomena associated with unsteady aerodynamics, internal resonance and the galloping of structures. Applications related to theses areas are discussed and the effects of nonlinearities are related.

The objective of this thesis is to consider a series of applications where nonlinearities cannot be neglected, could be exploited or should be avoided. The first of these applications is to establish the nonlinear unsteady flow model to extend Theodorsen's work. The linearizion of unsteady flow model becomes inaccurate in natural flows and engineering applications such as rapidly maneuvering aircraft, flow over wind turbines, flapping-wing flight and swimming fish. The second is to exploit the nonlinear aspects of autoparametric vibration systems to control undesired motions and/or to create useful vibrations for engineering applications. The third is to exploit energy harvesting from hybrid vibrations.

1.2 Nonlinear Unsteady Aerodynamics

In complicated engineering applications, such as rapidly maneuvering aircraft, flow over wind turbines and flapping-wing flight, there is no effective analytical unsteady nonlinear

flow model. Until now, the analytical unsteady aerodynamic models [1, 2, 3, 4, 5] are all based on the assumptions of (1) small angle of attack, (2) flat wake, (3) small disturbances to the mean flow components and (4) time-invariant free-stream. However, the angle of attack is around 25^0 to 45^0 when insects flap their wings [6]. In this and other cases, a simplified unsteady flow model with assumptions of small angle of attack, flat wake, small disturbance to the mean flow components and time-invariant free-stream will not be valid.

Table 1.1: Taxonomy of the unsteady flow regimes

$K < 0.1$	$K > 0.1$, $\alpha < 20^o$	$K > 0.1$, $\alpha > 20^o$
Quasi-steady aerodynamics	Two-Dimensional: • Wagner [7] • Theodorsen [8] • Peters [10] Three-Dimensional: • Reissner [11] • Unsteady vortex lattice [12]	Challenges: • Unsteadiness • Nonlinearity and new phenomena • Efficiency (computational burden)

Table 1 shows a taxonomy of the unsteady flow regimes. For a low reduced frequency ($k < 0.1$), the quasi-steady assumption may be applicable. For a relatively high reduced frequency, the unsteady flow characteristics cannot be neglected. If small-amplitude maneuvers are to be investigated, then the attached flow assumption and, hence, linearization of the flow dynamics may be justifiable. There are many unsteady, linear aerodynamic theories that can be applied successfully and efficiently in this regime for both two- and three-dimensional applications. Wagner [7] determined the time-response of the lift due to a step input (indicial response problem). Theodorsen [8] determined the frequency response of the lift (i.e., lift response due to harmonically oscillating input) and applied it to the flutter problem of fixed-wing aircraft. However, if large-amplitude maneuvers are of interest, the nonlinearity of the flow can no longer be neglected and non-conventional phenomena and/or lift mechanisms emerge (e.g., leading edge vortex in flapping flight). In this regime, the challenge is to capture both of the prominent unsteadiness and flow nonlinearity with a feasible computational burden so as to perform optimization, sensitivity analysis, dynamics, and control synthesis.

There have been few trials aiming at covering the gap discussed above. Ansari et al. [13, 14] extended the work of Von Karman and Sears [9] to include the leading edge vortex effect on flapping wings by shedding vortices from both leading and trailing edges. They derived two nonlinear integral equations for the shed wake and leading edge vortices. The incompact representation of Ansari's model dictates a quite complicated numerical implementation. This was the main reason for very high frequency components of the flow quantities when used for a coupled aeroelastic flight dynamic simulation of flapping wings by Weihua and Cesnik [15]. Weihua and Cesnik reported that their coupled aeroelastic-flight dynamic simulation could not complete one cycle because of this issue. Brunton and Rowley [16] presented

an empirical formula for the unsteady lift in a low Reynolds number (100) regime that is based on Theodorsen's model [8]. Ramesh et al. [17] developed an inviscid theoretical approach to account for non-planar wakes. However, the developed model still considers the induced velocities as small perturbations to the airfoil velocity; an assumption that considerably influences the aerodynamic forces at high angles of attack with the low Reynolds number.

In an earlier work [4, 18], Taha et al. extended the application of Duhamel's superposition principle, usually applied in linear unsteady aerodynamics, to account for non-conventional lift mechanisms. The main objective was to capture the leading edge vortex effect on flapping wings in an unsteady fashion. The developed model comprises two internal aerodynamic states for two-dimensional applications and four internal aerodynamic states for three-dimensional applications using strip theory. The strength of the model of Taha et al. is that its asymptotic steady behavior can match any arbitrarily given steady lift variation with the angle of attack. However, its underpinning flow dynamics is the Wagner's response. That is, it assumes that the linearity of the flow dynamics still hold. Therefore, there is still a need to develop similar efficient models while capturing the nonlinearity of the lift evolution.

1.3 Autoparametric Vibration System

Autoparameteric vibration systems are characterized by a nonlinear internal coupling that involves at least two modes. This coupling results in energy transfer from one mode of the system to another. The secondary mode, which is unforced, draws the energy from a primary mode and undergoes sustained oscillations. The primary mode is, as such, suppressed. For engineering applications, an autoparameteric vibration system can be used to suppress the oscillatory motion of the primary mode and/or create multi-directional actuations through excitation of the second mode.

For control purposes, an autoparameteric vibration system can be designed to suppress vibrations resulting from resonance or near resonance excitations or oscillations due to a Hopf bifurcation. Examples of such systems include civil structures (e.g., buildings, offshore rigs, towers and bridges). Such structures could undergo large-amplitude oscillations when the main frequency of seismic, wave or wind forces is close to the natural frequency of civil structure. Dynamic motions due to Hopf bifurcation include flutter of wings and bridges and galloping of iced-transmission lines and towers. In such applications, a secondary system can be added to draw energy from the structure's motion and reduce its vibrations. Haxton and Barr [19] devised an autoparametric vibration absorber by attaching a cantilever beam with a tip mass to a base structure that is subjected to external forcing. Their experimental validation showed that such an absorber is very effective when it comes to

reducing the vibrations of the base structure. Cartmell et al. [20] revised the system by attaching a bar with a spring instead of the cantilever beam. In Cartmell's system, the relative placement of the mass along the bar could be modified to adapt the optimum natural frequency of the secondary mode to control the motion of the base structure. Other designs of autoparametric vibration systems are based on attaching pendulums to the base structure, such as spring-mass-damper system [21], beam-tip mass-pendulum system [22], driven-Froude-pendulum system [23], multiple-pendulums systems [24, 25] and pendulum-magnetorheological-damper-nonlinear-spring system [26]. Dai and Singh [23] analyzed the dynamic behavior of the driven-Froude-pendulum system and found the system to undergo periodic and quasiperiodic oscillations, and even chaotic motions. Vyas et al. [24, 25] noted a large-amplitude resonant response of structures over a wide band of excitation frequencies by attaching multiple pendulums of different natural frequencies to a single-degree-of-freedom linear system. Kecik and Borowiec [26] found that the nonlinear spring can effectively suppress the autoparametric system and shrink the domains of unstable and chaotic responses. Moreover, Taguchi et al. [27] used pendulum absorbers to suppress vibration of helicopter rotor blades. Extensive work about autoparametric vibration systems has been done to show their potential to effectively control a base structure that is subjected to resonant or near resonant excitation. However, assessment of their nonlinear aspects, such as, saturation, jumps, hysteresis and chaos, which are important when considering other potential applications for such systems, have not been investigated.

To date, most of the research on autoparametric vibration systems has aimed at controlling the motion of the main structure. Yet, this motion can be employed to create multi-directional actuations. Alternatively, the energy from the oscillatory motion of the secondary mode can be harvested and accumulated to operate self-powered devices including micro-electromechanical systems (MEMS) or actuators [28, 29, 30], health monitoring and wireless sensors [31, 32], or replacing small batteries that have a finite life span or would require hard and expensive maintenance [33, 34, 35]. In return, harvesting the energy would reduce the oscillation's amplitude of the secondary system.

1.4 Vibration-based Energy Harvesting

Vibration-based energy harvesters have been proposed to operate self-powered devices including microelectromechanical systems (MEMS) or actuators [28, 29, 30], health monitoring and wireless sensors [31, 32], or replacing small batteries that have a finite life span or would require hard and expensive maintenance [33, 34, 35]. Harvesting mechanical energy through converting vibrations to electrical energy can be achieved using either electromagnetic [36, 37], electrostatic [37, 38], or piezoelectric [38, 39, 40, 41, 42, 43]. Of these mechanisms, the piezoelectric transduction is most suitable for MEMS devices [28] and wireless

sensors[31, 32], mostly because it can be effectively placed in small volumes and used to harvest energy over a wide range of frequencies. Considerable researches have shown that base excitations [32, 41, 42, 44, 45, 46] and aeroelastic vibrations [47, 48, 49, 50, 51, 52, 53, 54, 55, 56, 57, 58, 59, 60] can be effectively transformed into electric power sufficient for most of commercially available wireless sensors.

Energy harvesting from cantilever beams subjected to a base excitation has been extensively studied. Roundy et al. [32] showed the ability to generate a power output of 375 $\mu W cm^{-3}$ from the base vibration of 2.5 ms^{-2} at 120 Hz. Erturk et al. [41, 42] proposed one theoretical mode of the cantilever beam bounded with the piezoelectric material with experimental validation. Moreover, Abdelkefi et al. [44, 45] established one nonlinear coupling mode and discussed nonlinear effects of the parametrically excited vibration on piezoelectric energy harvesters. Recently, Stanton et al. [46] investigated the concept of a bistable piezoelectric inertial generator and found some interesting nonlinear phenomena: bifurcation and chaos. However, the energy harvesting only from the base excitation cannot be used widely because they can only harvest energy in the small range of environmentally vibrational frequencies that are near the natural frequency of the structure.

Other researchers have focused on energy harvesting from wind. Energy harvesters from the vortex-induced vibration [47, 48, 49] have been proposed. Few other studies [50, 51, 53, 54, 55, 56] have focused on generation of electric energy from aeroelastic vibration of airfoil sections. However, they can only harvest the energy at relatively high wind speed and the harvesting power is relatively low. Recently, energy harvesting from galloping motion has proven to be much more effective. Sirohi et al. [52] proposed harvesting energy from transverse galloping of a structure that has an equilateral triangle section and generates more than 50 mW at a wind speed of 11.6 mph. Abdelkefi et al. [58] derived a nonlinear distributed-parameter model for galloping-based piezoaeroelastic energy harvesters in which their numerical results were validated by the experimental measurements of [52]. They also reported that maximum levels of harvested power are accompanied by minimum transverse displacement amplitudes for a band of load resistances. Abdelkefi et al. [57] investigated the concept of exploiting galloping of square cylinders to harvest energy. Their focus was on the effect of the Reynolds number on the aerodynamic force, the onset of galloping, and the level of the harvested power. Their results showed that the electrical load resistance and the Reynolds number play an important role in determining the level of the harvested power and the onset of galloping. They also showed that the maximum levels of harvested power are accompanied with minimum transverse displacements for both low- and high-Reynolds number configurations. Moreover, Abdelkefi et al. [60] investigated the effects of different cross sections on the energy harvester from galloping vibration and found that different sections are better for harvesting energy over different regions of the flow speed. Furthermore, because of the great effect of temperature on the property of piezoelectric materials, Abdelkefi et al. [59] found that the same energy harvester will have different

onset galloping wind speeds and levels of harvested power in different environments.

1.5 Outline of the Thesis

This thesis is organized as follows:

In Chapter 2, a semi-analytical, geometrically-exact, unsteady potential flow model is developed for airfoils undergoing large amplitude maneuvers. To realize this objective, the classical unsteady theory of Theodorsen is revisited relaxing some of the major assumptions such as (1) flat wake, (2) small angle of attack, (3) small disturbances to the mean flow components, and (4) time-invariant free-stream. The kinematics of the wake vortices is simulated numerically while the wake and bound circulation distribution and, consequently, the associated pressure distribution are determined analytically. The steady and unsteady behaviors of the developed model are validated against experimental and computational results. The model is then used to determine the frequency response of the lift force at different mean angles of attack. Both qualitative and quantitative discrepancies are found between the obtained frequency response and that of Theodorsen at high angles of attack.

In Chapter 3, the nonlinear characteristics of an autoparametric vibration system are investigated. This system consists of a base structure and a cantilever beam with a tip mass. The dynamic equations for the system are derived using the extended Hamilton's principle. The method of multiple scales is used to analytically determine the stability and bifurcation of the system. The effects of the amplitude and frequency of the external force, the damping coefficient and frequency of the attached cantilever beam and the tip mass on the nonlinear responses of the system are determined. The results show that this system exhibits many interesting nonlinear phenomena including saturation, jumps, hysteresis and different kinds of bifurcations, such as saddle-node, supercritical pitchfork, subcritical pitchfork, reversed saddle-node and reversed saddle-saddle bifurcations. Power spectra, phase portraits and Poincare maps are employed to analyze the unstable behavior and the associated Hopf bifurcation and chaos. Depending on the application for such systems, the resulting responses could be exploited or should be avoided.

In Chapter 4, the concept of harvesting energy from ambient and galloping vibrations of a bluff body with a triangular cross-section geometry is investigated. A piezoelectric transducer is attached to the transverse degree of freedom of the body in order to convert these vibrations to electrical energy. A coupled nonlinear distributed-parameter model is developed that takes into consideration the galloping force and moment nonlinearities and the base excitation effects. The aerodynamic loads are modeled using the quasi-steady approximation. Linear analysis is performed to determine the effects of the electrical load resistance and wind speed on the global damping and frequency of the harvester as well as on the onset of instability.

Then, nonlinear analysis is performed to investigate the impact of the base acceleration, wind speed, and electrical load resistance on the performance of the harvester and the associated nonlinear phenomena that take place. Short- and open-circuit configurations for different wind speeds and base accelerations are assessed.

In Chapter 5, the concept of energy harvesting through autoparametric resonance is investigated. A system that consists of a base structure subjected to external forcing and a cantilever beam with a tip mass is considered. The energy is harvested by attaching piezoelectric sheets to the cantilever beam. A coupled nonlinear distributed-parameter model is developed by extended Hamiton's principle and the exact mode shapes of cantilevered beam are established by Galerkin Method. The effects of the electrical load resistance on the global frequency and damping ratio of the cantilever beam are analyzed by linearizion of the governing equations and perturbation method. Nonlinear analysis is performed to investigate the impacts of external force and load resistance on the response of the harvester. Moreover, the method of multiple scales is used to determine the stability and bifurcations of the system as a function of the external force and load resistance.

Conclusions and future work are presented in Chapter 6.

2

Geometrical-Exact Unsteady Model for foils Undergoing Large Amplitude Maneuvers

The objective is to develop a hybrid analytical-numerical approach to determine the lift associated with unsteady aerodynamics that involve high angles of attack. For this purpose, we revisit the classical model of Theodorsen [8] and relax the small angle of attack and the flat wake assumptions to obtain a geometrically-exact unsteady aerodynamic theory for two-dimensional applications. Due to the challenges encountered when relaxing these assumptions, full analyticity of the model is not expected (e.g., the lift deficiency due to wake cannot be analytically represented via some explicit expression such as Theodorsen's function). In contrast, the developed model is semi-analytic; that is, the vortex kinematics is simulated numerically. But the wake and bound circulation distribution and, consequently, the associated pressure distribution are computed analytically. Hence, there will be no need to solve an algebraic system of equations to determine the bound circulation as usually done in the implementation of discrete vortex models such as the unsteady vortex lattice method. The developed model is applied to some canonical pitch motions such as the ones introduced by Eldredge et al. [61]. The obtained results are validated against the numerical and experimental results of Ramesh et al. [17].

2.1 Problem Formulation

We consider a two-dimensional flat plate undergoing horizontal, vertical, and rotational motions, as shown in Fig. 2.1. The horizontal velocity U, the vertical velocity $\dot{h}$, and the angular velocity $\dot{\alpha}$ of the flat plate are taken positive to the left, downward, and clockwise directions, respectively. Two axis-systems are considered; the inertial frame **X**-**Z** and the plate-fixed frame x-z. While the origins of the two systems (O and O') are located at the mid-chord point, the plate is rotating about the hinge point which lies at a distance ab along

the x-axis ahead of the mid-chord point. Here, b denotes the half chord length.

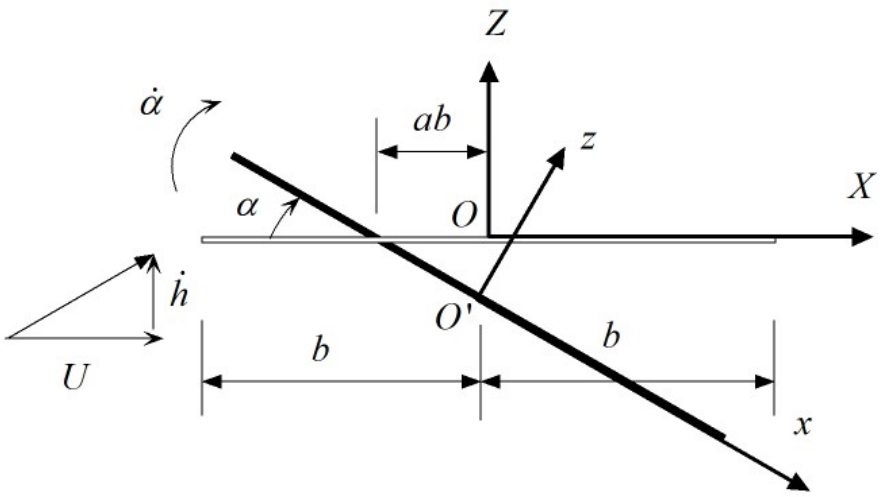

Figure 2.1: A schematic diagram showing the flat plate motion and axis-systems. Note that the translational motion of the plate is considered in the wind speed

In local coordinates (x-z system), the relative wind speed is expressed as:

$$\mathbf{q} = (U\cos\alpha - \dot{h}\sin\alpha + u')\mathbf{i} + (U\sin\alpha + \dot{h}\cos\alpha + w')\mathbf{k} \tag{2.1}$$

where α is the angle of attack and u' and w' represent the components of the induced velocity (disturbance/perturbation velocity) in the x and z directions, respectively. As such, the velocity potential is written as:

$$\phi = (U\cos\alpha - \dot{h}\sin\alpha)x + (U\sin\alpha + \dot{h}\cos\alpha)z + \phi' \tag{2.2}$$

where ϕ' is the disturbance velocity potential that satisfies the following expression: $\frac{\partial\phi'}{\partial x} = u'$ and $\frac{\partial\phi'}{\partial z} = w'$.

Based on the fact that the plat plate will not change shape during the movement,the non-penetration boundary condition (i.e., the total flow velocity perpendicular to the plate is zero) is expressed as [62]:

$$\frac{DF}{Dt} = \frac{\partial F}{\partial t} + (Ucos\alpha - \dot{h}\sin\alpha + u'(x,0))\frac{\partial F}{\partial x} + (U\sin\alpha + \dot{h}\cos\alpha + w'(x,0))\frac{\partial F}{\partial z} = 0 \tag{2.3}$$

where $F(x,z,t) = 0$ is the equation of the surface of a body moving in a time-dependent fashion which is given by $F(x,z,t) = z - z_{suf}(x,t)$. Inspecting figure 2.1, we find the geometrical relationships as $\frac{\partial F}{\partial x} = 0$, $\frac{\partial F}{\partial z} = 1$ and $\frac{\partial F}{\partial t} = (x + ab)\dot{\alpha}$. To this end, the boundary

condition Eq. (2.3) is simplified as:

$$w'(x,0,t) = -U\sin\alpha - \dot{h}\cos\alpha - (x+ab)\dot{\alpha} \tag{2.4}$$

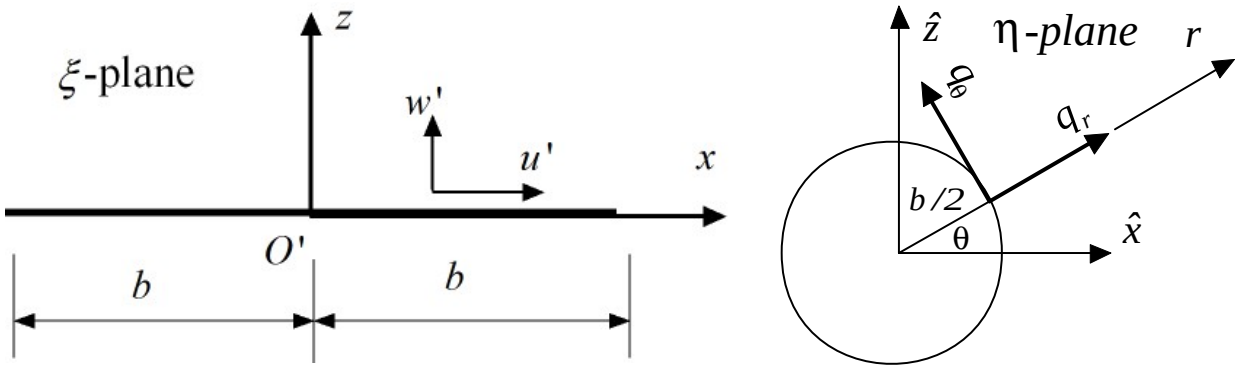

(a) (b)

Figure 2.2: Joukowski conformal mapping between (a) the plate (ξ-plane) and (b) the cylinder (η-plane).

Fig. 2.2 shows the conventional Joukowsking conformal mapping between the plate (ξ-plane) and the cylinder (η-plane), see [62, 63] for example. The mapping is written as

$$\xi = \eta + \frac{b^2}{4\eta} \tag{2.5}$$

where, $\xi = x + iz$ and $\eta = \hat{x} + i\hat{z} = re^{i\theta}$. As such, the surface of flat plate in the ξ-plane is transformed into the surface of the circle in the η-plane. The relationship is expressed as $x = b\cos\theta$ and $z = 0$. Moreover, the velocity vectors in the two planes are related via the transformation relation

$$u' - iw' = \frac{q'_{\hat{x}} - iq'_{\hat{z}}}{d\xi/d\eta} \tag{2.6}$$

In this expression, the component $d\xi/d\eta_{r=b/2}$ is calculated from Eq. (2.5) as $2i\sin\theta e^{-i\theta}$. Inspecting Fig. 2.2, we also note the following relationship $q'_{\hat{x}} - iq'_{\hat{z}} = e^{-i\theta}(q_r - iq_\theta)$. To this end, the velocities $u'(x,0,t)$ and $w'(x,0,t)$ in the ξ-plane are expressed by the velocities $q'_r(b/2,\theta,t)$ and $q'_\theta(b/2,\theta,t)$ in the η-plan as

$$\begin{aligned} q'_\theta(b/2,\theta,t) &= -2u'(x,0,t)\sin\theta \\ q'_r(b/2,\theta,t) &= 2w'(x,0,t)\sin\theta \end{aligned} \tag{2.7}$$

Also, taking the datum of the disturbance velocity potential at the leading edge (i.e.,

$\phi'(b/2, \pi, t) = 0$), then the distribution of ϕ' on the cylinder surface is written as

$$\phi'(\theta, t) = -\frac{b}{2}\int_{\theta}^{\pi} q_\theta(b/2, \beta, t)d\beta \tag{2.8}$$

The aerodynamic loads are calculated by integrating the pressure distribution over the surface, which can be determined using the following unsteady Bernoulli's equation [62, 64]

$$\frac{\partial\phi}{\partial t} + \frac{|\mathbf{q}|^2}{2} + \frac{p}{\rho} = C(t) \tag{2.9}$$

where p and ρ are respectively the pressure and density of the air, and $C(t)$ is a spatially-constant quantity, which can be calculated from the far field conditions as
$C(t) = \frac{\partial((U\cos\alpha - \dot{h}\sin\alpha)x + (U\sin\alpha + \dot{h}\cos\alpha)z)}{\partial t} + \frac{(U\cos\alpha - \dot{h}\sin\alpha)^2 + (U\sin\alpha + \dot{h}\cos\alpha)^2}{2} + \frac{p_\infty}{\rho}$.
Considering the expression of $C(t)$ in the far field condition, velocity potential equation (2.2) and the unsteady Bernoulli's equation (2.9), we express the pressure distribution related to the disturbance velocities and velocity potential via

$$p = p_\infty - \rho\left[\frac{\partial\phi'}{\partial t} + (U\cos\alpha - \dot{h}\sin\alpha)u' + (U\sin\alpha + \dot{h}\cos\alpha)w' + \frac{1}{2}(u'^2 + w'^2)\right] \tag{2.10}$$

where p_∞ is the free-stream pressure.

Integrating the pressure distribution to calculate the resultant aerodynamic loads may be deficient because it does not account for the leading edge suction force. We use Blasius theorem [12] to remedy this deficiency. According to Blasius theorem, the components (F_x and F_z) of the aerodynamic loads acting on an immersed body are given by

$$F_x - iF_z = \frac{i\rho}{2}\oint (u - iw)^2\, d\xi \tag{2.11}$$

where u and w are the components of the fluid velocity vector in the body axes. Since the perturbations u' and w' near the leading edge outweigh by far the other contributions, one can write the components of the leading edge suction force as

$$F_x - iF_z = \frac{i\rho}{2}\int_{LE} (u' - iw')^2\, d\xi = -\frac{i\rho}{2}\int_{\pi^-}^{\pi^+} \left(\frac{-iq'_\theta(b/2, \pi, t)e^{-i\theta}}{d\xi/d\eta}\right)^2 b\sin\theta d\theta \tag{2.12}$$

Noting that $\frac{d\xi}{d\eta}|_{r=b/2} = 2i\sin\theta e^{-i\theta}$ and $i\int_{\pi^-}^{\pi^+} \frac{1}{\sin\theta}d\theta = \pi$, we determine the components of the leading edge suction force as

$$F_x - iF_z = -F_s = -\frac{\pi\rho b}{8} q_\theta(b/2, \pi, t)^2 \tag{2.13}$$

where F_s is the suction force.

Next, we follow Theodorsen's work [8] relaxing some of the simplifying assumptions such as (1) flat wake, (2) small angle of attack, (3) small disturbances to the mean flow components, and (4) time-invariant free-stream. Some of the applicable Theodorsen's results will be stated here without proof and emphasis will be given to the extended parts. Following Theodorsen's approach, we divide the problem into non-circulatory and circulatory contributions.

2.2 Non-circulatory Contributions

The non-circulatory contributions are included by considering a time-varying continuous distribution of two-dimensional sources with strength $H^+(x,0,t)$ and strength $H^-(x,0,t)$ per unit x-distance respectively on the upper and bottom sides of the plate [62]. The strength $H^+(x,0,t)$ and $H^-(x,0,t)$ are given by [62]:

$$H^+(x,0,t) = -H^-(x,0,t) = 2w'(x,0,t) \tag{2.14}$$

Similarly, the local sources on the upper circle and bottom circle are derived from Eq. (2.7) as [62]

$$H^+(b/2,\theta,t) = -H^-(b/2,\theta,t) = 4w'(x,0,t)sin\theta \tag{2.15}$$

where $H^+(b/2,\theta,t)$ and $H^-(b/2,\theta,t)$ are the strengths of the source per unit length on the upper circle and bottom circle, respectively. As such, velocity in the θ direction and the disturbance velocity potential on the circle are calculated as [62]

$$\begin{array}{l} q'_{\theta N}(b/2,\theta,t) = \frac{2}{\pi}\int_0^\pi \frac{w'(x,0,t)sin^2\beta d\beta}{(cos\beta - \cos\theta)} \\ \phi_N^{\prime(u)}(b/2,\theta,t) = -\phi_N^{\prime(l)}(b/2,\theta,t) = -\frac{b}{\pi}\int_\theta^\pi \int_0^\pi \frac{w'(x,0,t)sin^2\beta d\beta d\theta}{(cos\beta - \cos\theta)} \end{array} \tag{2.16}$$

where $q'_{\theta N}$ is the non-circulation angular velocity and $\phi_N^{\prime(u)}$ and $\phi_N^{\prime(l)}$ are the disturbance velocity potentials respectively on the upper and bottom circle in the non-circulation condition. Substitute Eq. (2.4) into Eq. (2.16), we obtain the expression of the non-circulation velocity potential of the upper circle as

$$\begin{array}{l} \phi_N^{\prime(u)}(b/2,\theta,t) = -\frac{b}{\pi}\int_\theta^\pi \int_0^\pi \frac{(-U\sin\alpha - \dot{h}\cos\alpha - (x+ab)\dot{\alpha})sin^2\beta d\beta d\theta}{(cos\beta - \cos\theta)} \\ = b(U\sin\alpha + \dot{h}\cos\alpha)sin\theta + (a + \frac{1}{2}cos\theta)b^2\dot{\alpha}\sin\theta \end{array} \tag{2.17}$$

Using the pressure distribution expression (Eq. (2.10)), we determine the expression of the non-circulation pressure difference as:

$$\begin{aligned} p^{(u)} - p^{(l)} = -\rho[&\tfrac{\partial \phi_N'^{(u)}}{\partial t} - \tfrac{\partial \phi_N'^{(l)}}{\partial t} + (U cos\alpha - \dot{h}\sin\alpha)(u'^{(u)} - u'^{(l)}) \\ &+(U\sin\alpha + \dot{h}cos\alpha)(w'^{(u)} - w'^{(l)}) + \tfrac{1}{2}({u'^{(u)}}^2 + {w'^{(u)}}^2 - {u'^{(l)}}^2 - {w'^{(l)}}^2)] \end{aligned} \tag{2.18}$$

In this expression, the superscripts (u) and (l) denote the upper and lower surfaces of the plate, respectively. Considering the expressions $w'^{(u)} = w'^{(l)} = w'(x,0,t)$, $u'^{(u)} = \frac{\partial \phi_N'^{(u)}}{\partial x} = \frac{\partial(-\phi_N'^{(l)})}{\partial x} = -u'^{(l)}$ and $\frac{\partial \phi_N'^{(u)}}{\partial t} = -\frac{\partial \phi_N'^{(l)}}{\partial t}$, we simplify the non-circulatory distribution of the pressure difference across the plate plate as

$$\Delta p_N = p^{(u)} - p^{(l)} = -2\rho\left[\frac{\partial \phi_N'^{(u)}}{\partial t} + (U\cos\alpha - \dot{h}\sin\alpha)\frac{\partial \phi_N'^{(u)}}{\partial x}\right] \tag{2.19}$$

Considering the wind speed in x direction as $\frac{\partial x}{\partial t} = U\cos\alpha - \dot{h}\sin\alpha$, we derive the non-circulation normal force from Eq. (2.19) as following:

$$\begin{aligned} &N_N = -\int_{-b}^{b}\Delta p_N dx = 2\rho\int_{-b}^{b}\tfrac{\partial \phi_N'^{(u)}}{\partial t} + (U\cos\alpha - \dot{h}\sin\alpha)\tfrac{\partial \phi_N'^{(u)}}{\partial x}dx = 2\rho\tfrac{\partial}{\partial t}(\int_{-b}^{b}\phi_N'^{(u)}dx) \\ &= 2\rho\tfrac{\partial}{\partial t}(\int_0^{\pi}[b(U\sin\alpha + \dot{h}\cos\alpha)sin\theta + (a+\tfrac{1}{2}cos\theta)b^2\dot{\alpha}\sin\theta]b\sin\theta d\theta) \\ &= \pi\rho b^2\tfrac{\partial}{\partial t}(U\sin\alpha + \dot{h}\cos\alpha + ab\dot{\alpha}) \\ &= \pi\rho b^2(\dot{U}\sin\alpha + \ddot{h}\cos\alpha + (U\cos\alpha - \dot{h}\sin\alpha)\dot{\alpha} + ab\ddot{\alpha}) \end{aligned} \tag{2.20}$$

Similarly, the non-circulation moment relative to the rotational point, as shown in Fig. 2.1, is derived as

$$\begin{aligned} &M_{hN} = \textstyle\int_{-b}^{b}(p^{(u)} - p^{(l)})(x+ab)dx \\ &= -2\rho(U\cos\alpha - \dot{h}\sin\alpha)\textstyle\int_{-b}^{b}\tfrac{\partial \phi_N'^{(u)}}{\partial x}xdx - 2\rho\int_{-b}^{b}\tfrac{\partial \phi_N'^{(u)}}{\partial t}xdx - abN_{NC} \\ &= -2\rho(U\cos\alpha - \dot{h}\sin\alpha)\{\left[\phi_N'^{(u)}x\right]_{x=-b}^{x=b} - \textstyle\int_{-b}^{b}\phi_N'^{(u)}dx\} - 2\rho\tfrac{\partial}{\partial t}(\int_{-b}^{b}\phi_N'^{(u)}xdx) - abN_{NC} \\ &= -2\rho(U\cos\alpha - \dot{h}\sin\alpha)\{0 - \tfrac{\pi}{2}[b(U\sin\alpha + \dot{h}\cos\alpha) + ab^2\dot{\alpha}]\} - \tfrac{\pi}{8}\rho b^4\ddot{\alpha} \\ &-ab[\pi\rho b^2(\dot{U}\sin\alpha + \ddot{h}\cos\alpha + (U\cos\alpha - \dot{h}\sin\alpha)\dot{\alpha} + ab\ddot{\alpha})] \\ &= \pi\rho b^2[\tfrac{1}{2}(U^2 - \dot{h}^2)sin(2\alpha) + U\dot{h}\cos(2\alpha) - ab(\dot{U}\sin\alpha + \ddot{h}\cos\alpha) - (\tfrac{1}{8} + a^2)b^2\ddot{\alpha}] \end{aligned} \tag{2.21}$$

In this derivation, we use the fact that $\phi_N'^{(u)}$ vanishes both on the leading and trailing edge, which can be found based on equation (2.17). In addition to allowing for a time-varying free stream, equations (2.20) and (2.21) represent a geometrically-exact extension of Theodorsen's result [8]:

$$\begin{aligned} N_N &= \pi\rho b^2\left[\ddot{h} + U\dot{\alpha} + ab\ddot{\alpha}\right] \\ M_{hN} &= \pi\rho b^2\left[U^2\alpha + U\dot{h} - ab\ddot{h} - (\tfrac{1}{8} + a^2)b^2\ddot{\alpha}\right] \end{aligned} \tag{2.22}$$

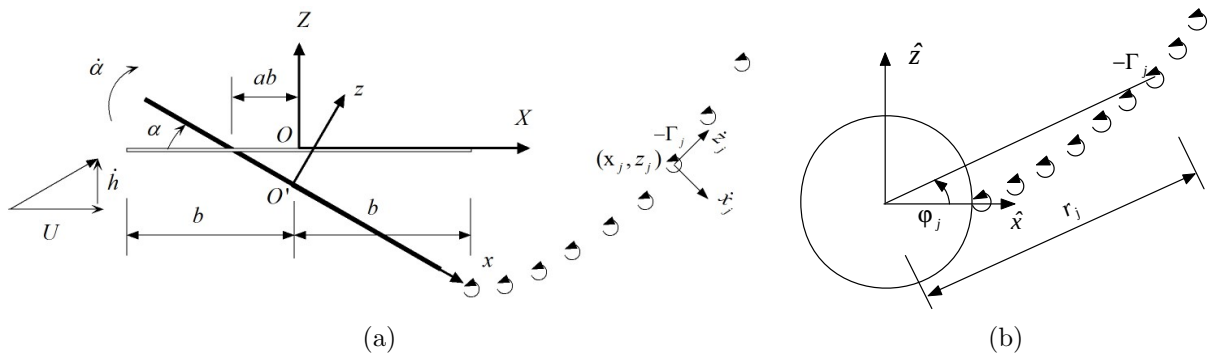

Figure 2.3: Comparison between the proposed formula, Polhamus, potential flow, and benchmark results for C_L due to a stabilized LEV: (a) Plate's wake and (b) Cylinder's wake.

Equations (2.20) and (2.21) are consistent with the fact that the non-circulatory force is the force required to accelerate a mass of air cylinder of radius b with the acceleration of the mid-chord point. However, it should be noted that the acceleration term between the brackets is not the inertial acceleration of the mid-chord point (i.e., not the acceleration with respect to the still fluid), but rather the time rate of change of the velocity of the mid-chord point with respect to the body axes. Also, it is noteworthy to mention that the non-circulatory lift and drag forces are given by $L_N = N_N \cos\alpha$ and $D_N = N_N \sin\alpha$, respectively.

2.3 Circulatory force

The Kutta condition dictates finite velocity at the trailing edge ($\theta = 0$). To satisfy this condition, equation (2.7) yields $q_\theta(b/2, 0, t) = 0$. However, Eq. (2.16) indicates the inability to achieve this requirement for arbitrary motion of the plate which is represented by w' via the no-penetration boundary condition. Hence, an additional contribution (circulatory one) to the tangential velocity is invoked such that both contributions could satisfy the Kutta condition together; that is

$$q_{\theta N}(b/2, 0, t) + q_{\theta C}(b/2, 0, t) = 0$$

Thus, a circulation distribution is added to represent the wake of the flow past the flat plate (circular cylinder), as shown in Fig. 2.3.

One circulation $-\Gamma_j$ is chosen to analyze the circulation force of the plate. It is assumed that the displacement and velocity of circulation $-\Gamma_j$ in local coordinate are respectively $x_j\mathbf{i} + z_j\mathbf{k}$ and $\dot{x}_j\mathbf{i} + \dot{z}_j\mathbf{k}$, as shown in Fig. 2.3(a). According to the displacement relationship between

the η plane and the ξ plane (Eq. (2.5)), the displacements x_j and z_j are given by:

$$\begin{aligned} x_j &= r_j \cos\varphi_j + \tfrac{b^2}{4r_j}\cos\varphi_j \\ z_j &= r_j \sin\varphi_j - \tfrac{b^2}{4r_j}\sin\varphi_j \end{aligned} \tag{2.23}$$

where r_j and φ_j are respectively the radius and angular displacements of circulation $-\Gamma_j$ in polar coordinate, as shown in Fig. 2.4. For each vortex $-\Gamma_j$ in the cylinder's wake, there has to exist an image circulation Γ_j to maintain zero total circulation. Since one of the main objectives of this work is to account for wake deformation, the position of the wake vortex $-\Gamma_j$ is considered arbitrarily free. In order to keep the no-penetration boundary condition satisfied, the radial components of the velocities induced by Γ_j and $-\Gamma_j$ must cancel each other. Thus, if the wake vortex is arbitrarily located at $\eta_j = r_j e^{i\varphi_j}$, then its image has to lie inside the cylinder at $\frac{b^2}{4r_j}e^{i\varphi_j}$, as shown in Fig. 2.4.

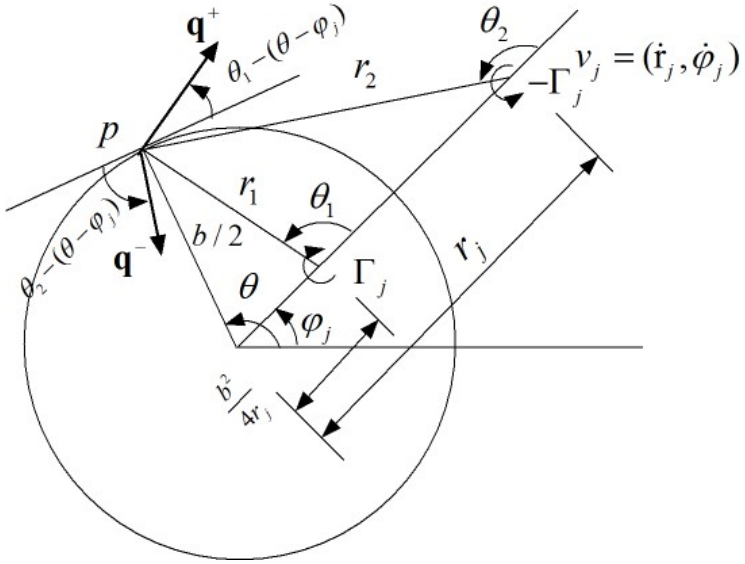

Figure 2.4: A schematic diagram showing a circulation Γ_i in the cylinder's wake and its image inside the cylinder along with their induced velocities on the cylinder.

Also, as shown in Fig. 2.4, the j^{th} wake vortex $-\Gamma_j$ and its image Γ_j induce velocity vectors $\mathbf{q}^-$ and $\mathbf{q}^+$, respectively, at an arbitrary point p on the cylinder. The tangential component of the total velocity vector $\mathbf{q}^+ + \mathbf{q}^-$ on the upper surfaces is given by

$$\begin{aligned} q_{\theta j}^{(u)} &= -\left|\mathbf{q}^+\right|\cos\left[\theta_1-(\theta-\varphi_j)\right] + \left|\mathbf{q}^-\right|\cos\left[\theta_2-(\theta-\varphi_j)\right] \\ &= -\tfrac{\Gamma_j}{2\pi}\left\{\tfrac{r_1\cos[\theta_1-(\theta-\varphi_j)]}{{r_1}^2} - \tfrac{r_2\cos[\theta_2-(\theta-\varphi_j)]}{{r_2}^2}\right\} \end{aligned} \tag{2.24}$$

where θ is changed from 0 on the trailing edge to π on the leading edge. According to the cosine-law of two triangles and geometrical relationship in Fig. 2.4, the terms

$r_1\cos[\theta_1-(\theta-\varphi_j)]$, $r_2\cos[\theta_2-(\theta-\varphi_j)]$, ${r_1}^2$ and ${r_2}^2$ in equation (2.24) are given by

$$\begin{array}{l} r_1\cos[\theta_1-(\theta-\varphi_j)]=\frac{b}{2}-\frac{b^2}{4r_j}\cos(\theta-\varphi_j) \\ r_2\cos[\theta_2-(\theta-\varphi_j)]=\frac{b}{2}-r_j\cos(\theta-\varphi_j) \\ r_1^2=(\frac{b^2}{4r_j})^2+(\frac{b}{2})^2-\frac{b^2}{4r_j}b\cos(\theta-\varphi_j) \\ r_2^2=r_j^2+(\frac{b}{2})^2-r_jb\cos(\theta-\varphi_j) \end{array} \tag{2.25}$$

Substitute Eq. (2.25) into Eq. (2.24), we simplify the expression of $q_{\theta j}^{(u)}$ as

$$q_{\theta j}^{(u)}=-\frac{\Gamma_j}{2\pi}\left\{\frac{\frac{b}{2}-\frac{b^2}{4r_j}\cos(\theta-\varphi_j)}{(\frac{b^2}{4r_j})^2+(\frac{b}{2})^2-\frac{b^2}{4r_j}b\cos(\theta-\varphi_j)}-\frac{\frac{b}{2}-r_j\cos(\theta-\varphi_j)}{r_j^2+(\frac{b}{2})^2-r_jb\cos(\theta-\varphi_j)}\right\}=-\frac{\Gamma j}{\pi b}\left[\frac{r_j^2-(\frac{b}{2})^2}{(\frac{b}{2})^2+r_j^2-r_jb\cos(\theta-\varphi_j)}\right] \tag{2.26}$$

Similarly, the tangential velocity at the lower surface $q_{\theta j}^{(l)}$ is calculated as

$$q_{\theta j}^{(l)}=-\frac{\Gamma_j}{\pi b}\left[\frac{r_j^2-(\frac{b}{2})^2}{(\frac{b}{2})^2+r_j^2-r_jb\cos(\theta+\varphi_j)}\right] \tag{2.27}$$

where θ is changed from 0 on the trailing edge to π on the leading edge. Recalling the non-circulatory contribution of q_θ from Eq. (2.16) and discretizing the wake sheet of vorticity into a finite number of point vortices, we write the Kutta condition as

$$\frac{2}{\pi}\int_0^\pi\frac{w'(b/2,\beta,t)\sin^2\beta d\beta}{(\cos\beta-1)}+\sum_j^N\frac{\Gamma_j}{\pi b}\left[\frac{r_j^2-(\frac{b}{2})^2}{r_j^2-r_jb\cos\varphi_j+(\frac{b}{2})^2}\right]=0 \tag{2.28}$$

where N is the total number of discrete wake vortices. Substituting by w' from the no-penetration boundary condition, Eq. (2.4), and carrying out the integration in the left hand side, we write

$$\sum_j^N\frac{\Gamma_j}{2\pi b}\left[\frac{r_j^2-(\frac{b}{2})^2}{r_j^2-r_jb\cos\varphi_j+(\frac{b}{2})^2}\right]=-U\sin\alpha-\dot{h}\cos\alpha-(\frac{1}{2}+a)b\dot{\alpha}=w_{3/4} \tag{2.29}$$

where $w_{3/4}$ is the component of the plate velocity relative to the air normal to the plate surface at the three-quarter chord point. Equation (2.29) will be used to determine the strength $-\Gamma_j$ of the newly shed wake vortex at each time step in the numerical implementation, as will be shown later.

After solving for the wake vortex distribution at each time step, the circulatory loads are determined by using the unsteady Bernoulli's equation. Using Eq. (2.8), we determine the disturbance velocity potential on the cylinder due to the j^{th} vortex $-\Gamma_j$ and its image Γ_j as

follows:

$$\begin{aligned}
\phi_{Cj}^{\prime(u)}(\theta,t) &= -\frac{\Gamma_j}{\pi}\begin{cases} \tan^{-1}\left(\frac{r_j-b/2}{r_j+b/2}\tan\frac{\varphi_j}{2}\right)-\tan^{-1}\left(\frac{r_j-b/2}{r_j+b/2}\cot\frac{\theta-\varphi_j}{2}\right)-\pi, & \theta<\varphi_j,\varphi_j>0 \\ \tan^{-1}\left(\frac{r_j-b/2}{r_j+b/2}\tan\frac{\varphi_j}{2}\right)-\tan^{-1}\left(\frac{r_j-b/2}{r_j+b/2}\cot\frac{\theta-\varphi_j}{2}\right), & \text{otherwise}\end{cases} \\
\phi_{Cj}^{\prime(l)}(\theta,t) &= -\frac{\Gamma_j}{\pi}\begin{cases} \tan^{-1}\left(\frac{r_j-b/2}{r_j+b/2}\tan\frac{\varphi_j}{2}\right)+\tan^{-1}\left(\frac{r_j-b/2}{r_j+b/2}\cot\frac{\theta+\varphi_j}{2}\right)-\pi, & \theta<\varphi_j,\varphi_j>0 \\ \tan^{-1}\left(\frac{r_j-b/2}{r_j+b/2}\tan\frac{\varphi_j}{2}\right)+\tan^{-1}\left(\frac{r_j-b/2}{r_j+b/2}\cot\frac{\theta+\varphi_j}{2}\right), & \text{otherwise}\end{cases}
\end{aligned} \tag{2.30}$$

where $\phi_{Cj}^{\prime(u)}(\theta,t)$ and $\phi_{Cj}^{\prime(l)}(\theta,t)$ are disturbance velocity potential on the upper and lower circle due to the jth circulation $-\Gamma_j$ and its image Γ_j, respectively.

Then, the circulation pressure difference due to the jth circulation $-\Gamma_j$ and its image Γ_j can be derived from the pressure distribution expression (Eq. (2.10)) as

$$\begin{aligned}
&\Delta p_j = p_j^{(u)} - p_j^{(l)} = -\rho[\frac{\partial(\phi_j^{\prime(u)}-\phi_j^{\prime(u)})}{\partial t} + (U\cos\alpha - \dot{h}\sin\alpha)(u_j^{\prime(u)} - u_j^{\prime(l)}) \\
&+(U\sin\alpha + \dot{h}\cos\alpha)(w_j^{\prime(u)} - w_j^{\prime(l)}) + \tfrac{1}{2}({u_j^{\prime(u)}}^2 + {w_j^{\prime(u)}}^2 - {u_j^{\prime(l)}}^2 - {w_j^{\prime(l)}}^2)]
\end{aligned} \tag{2.31}$$

where $w_j^{\prime(u)} = w_j^{\prime(l)} = 0$ which are caused by the symmetric of $-\Gamma_j$ and Γ_j. As such, Eq. (2.31) is simplified as

$$\Delta p_j = -\rho[\frac{\partial(\phi_j^{\prime(u)} - \phi_j^{\prime(u)})}{\partial t} + (U\cos\alpha - \dot{h}\sin\alpha)(u_j^{\prime(u)} - u_j^{\prime(l)}) + \frac{1}{2}({u_j^{\prime(u)}}^2 - {u_j^{\prime(l)}}^2] \tag{2.32}$$

where the horizontal velocity $u_j^{\prime(u)}$ and $u_j^{\prime(l)}$ is determined from the disturbance velocity potential equation (2.30) as

$$\begin{aligned}
&u_j^{\prime(u)} = \frac{\partial\phi_j^{\prime(u)}}{\partial x} = -\frac{1}{b\sin\theta}\frac{\partial\phi_j^{\prime(u)}}{\partial\theta} = -\frac{1}{b\sin\theta}\frac{\partial}{\partial\theta}(\frac{\Gamma_j}{\pi}arctan(\frac{r_j-1/2b}{r_j-1/2b})cot(\frac{\theta-\varphi_j}{2})) \\
&= \frac{1}{2\sin\theta}\frac{\Gamma_j}{\pi b}\frac{{r_j}^2-(1/2b)^2}{{r_j}^2+(1/2b)^2-r_j b\cos(\theta-\varphi_j)} \\
&u_j^{\prime(l)} = \frac{\partial\phi_j^{\prime(l)}}{\partial x} = -\frac{1}{b\sin\theta}\frac{\partial\phi_j^{\prime(l)}}{\partial\theta} = -\frac{1}{b\sin\theta}\frac{\partial}{\partial\theta}(-\frac{\Gamma_j}{\pi}arctan(\frac{r_j-1/2b}{r_j+1/2b}cot(\frac{\theta+\varphi_j}{2})) \\
&= -\frac{1}{2\sin\theta}\frac{\Gamma_j}{\pi b}\frac{{r_j}^2-(1/2b)^2}{{r_j}^2+(1/2b)^2-r_j b\cos(\theta+\varphi_j)}
\end{aligned} \tag{2.33}$$

In this expression, we use the fact that $x = b\cos\theta$ on the surface of the flat plate which has been discussed in Section 2.1.

Using Eq. (2.32), the circulational normal force due to the circulation $-\Gamma_j$ and its image Γ_j is given by

$$\begin{aligned}
&N_{Cj} = -\int_{-b}^{b}\Delta p_j dx = \rho\int_{-b}^{b}\frac{\partial(\phi_j^{\prime(u)}-\phi_j^{\prime(l)})}{\partial t}dx \\
&+\rho(U\cos\alpha - \dot{h}\sin\alpha)\int_{-b}^{b}(u_j^{\prime(u)} - u_j^{\prime(l)})dx + \tfrac{\rho}{2}\int_{-b}^{b}{u_j^{\prime(u)}}^2 - {u_j^{\prime(l)}}^2 dx
\end{aligned} \tag{2.34}$$

where the term $\int_{-b}^{b}(u_j'^{(u)} - u_j'^{(l)})dx$ is determined from Eq. (2.33) as

$$\begin{aligned}&\int_{-b}^{b}(u_j'^{(u)} - u_j'^{(l)})dx\\&= \frac{\Gamma_j}{\pi}\int_0^{\pi}\frac{[{r_j}^2-(1/2b)^2]}{2\sin\theta}\left(\frac{1}{{r_j}^2+(1/2b)^2-r_j b\cos(\theta-\varphi_j)}+\frac{1}{{r_j}^2+(1/2b)^2-r_j b\cos(\theta+\varphi_j)}\right)b\sin\theta d\theta\\&= \Gamma_j\end{aligned} \tag{2.35}$$

and the term $\int_{-b}^{b}{u_j^{(u)}}^2 - {u_j'^{(l)}}^2 dx$ is given by

$$\begin{aligned}&\int_{-b}^{b}{u_j^{(u)}}^2 - {u_j'^{(l)}}^2 dx\\&= \frac{\Gamma_j^2}{\pi^2}\int_0^{\pi}\frac{[{r_j}^2-(1/2b)^2]^2}{4(\sin\theta)^2}\left(\frac{1}{[{r_j}^2+(1/2b)^2-r_j b\cos(\theta-\varphi_j)]^2}-\frac{1}{[{r_j}^2+(1/2b)^2-r_j b\cos(\theta+\varphi_j)]^2}\right)b\sin\theta d\theta\\&= \frac{\Gamma_j^2 b{r_j}^2\mathrm{sign}(\sin\varphi)}{2\sqrt{2}\pi}\frac{p_4p_2\mathrm{Im}(p)-p_1(p_2^2+2p_3-2p_1^2)\mathrm{Re}(p)}{(p_1^2-p_2^2)[{r_j}^2-(1/2b)^2]|p|^2}\end{aligned} \tag{2.36}$$

where p_1, p_2, p_3 and p_4 are coefficients and given by $p_1 = {r_j}^2 + (1/2b)^2$, $p_2 = -r_j b\cos(\varphi_j)$, $p_3 = {r_j}^2 b^2/2$, $p_4 = ({r_j}^2 - (1/2b)^2) r_j b\,|\sin(\varphi_j)|$ and $p = \sqrt{p_2^2 p_3 + p_1^2(p_3 - p_2^2) + \mathbf{i}p_1p_2p_4}$. In this expression, Im and Re are the respective image and real parts of complex number, $sign(x)$ denotes the sign of x and $\mathbf{i}$ indicates $\sqrt{-1}$. Moreover, we derive the term $\frac{\partial(\phi_j'^{(u)}-\partial\phi_j^{(l)})}{\partial t}$ form equation (2.30) as

$$\begin{aligned}&\frac{\partial(\phi_j'^{(u)}-\partial\phi_j^{(l)})}{\partial t} = \frac{\Gamma_j}{\pi}\frac{\partial}{\partial t}(arctan(\frac{r_j-1/2b}{r_j-1/2b}cot(\frac{\theta-\varphi_j}{2})) + arctan(\frac{r_j-1/2b}{r_j-1/2b}cot(\frac{\theta+\varphi_j}{2})))\\&= \frac{\Gamma_j}{\pi}\frac{\partial}{\partial t}(arctan(\sqrt{\frac{x_j-b\cos\varphi_j}{x_j-b\cos\varphi_j}}cot(\frac{\theta-\varphi_j}{2})) + arctan(\sqrt{\frac{x_j-b\cos\varphi_j}{x_j-b\cos\varphi_j}}cot(\frac{\theta+\varphi_j}{2})))\\&= \frac{\Gamma_j}{\pi}(\frac{M+N\sin(\theta-\varphi_j)}{m+n\cos(\theta-\varphi_j)} + \frac{-M+N\sin(\theta+\varphi_j)}{m+n\cos(\theta+\varphi_j)})\end{aligned} \tag{2.37}$$

where the coefficients M, N, m and n are given by $M = [x_j - (bcos\varphi_j)^2]\dot{\varphi}_j$, $N = bx_j\dot{\varphi}_j\sin\varphi_j + b\dot{x}_j\cos\varphi_j$, $m = 2x_j\sqrt{x_j^2 - (bcos\varphi_j)^2}$ and $n = -2bcos\varphi_j\sqrt{x_j^2 - (bcos\varphi_j)^2}$. In these expressions, the dot is the derivative with perspective to time t. As such, the expression $\int_{-b}^{b}\frac{\partial(\phi_j'^{(u)}-\phi_j'^{(l)})}{\partial t}dx$ is simplified as

$$\begin{aligned}&\int_{-b}^{b}\frac{\partial(\phi_j'^{(u)}-\phi_j'^{(l)})}{\partial t}dx = \frac{\Gamma_j}{\pi}\int_0^{\pi}(\frac{M+N\sin(\theta-\varphi_j)}{m+n\cos(\theta-\varphi_j)} + \frac{-M+N\sin(\theta+\varphi_j)}{m+n\cos(\theta+\varphi_j)})b\sin\theta d\theta\\&= \Gamma_j\frac{x_j\dot{x}_j+b^2\dot{\varphi}_j\sin\varphi_j\cos\varphi_j}{\sqrt{x_j^2-(bcos\varphi_j)^2}} - \Gamma_j\dot{x}_j\end{aligned} \tag{2.38}$$

Substitute equations (2.35), (2.36) and (2.38) into equation (2.34), the circulational normal force due to the circulation $-\Gamma_j$ and its image Γ_j is turned out:

$$\begin{aligned}&N_{Cj} = \rho\Gamma_j(\frac{x_j\dot{x}_j+b^2\dot{\varphi}\sin\varphi_j\cos\varphi_j}{\sqrt{x_j^2-(bcos\varphi_j)^2}} - \dot{x}_j + U\cos\alpha - \dot{h}\sin\alpha)\\&+\frac{\rho\Gamma_j^2 b{r_j}^2\mathrm{sign}(\sin\varphi_j)}{4\sqrt{2}\pi}\frac{p_4p_2\mathrm{Im}(p)-p_1(p_2^2+2p_3-2p_1^2)\mathrm{Re}(p)}{(p_1^2-p_2^2)[{r_j}^2-(1/2b)^2]|p|^2}\end{aligned} \tag{2.39}$$

Similarly, the circulational moment caused by the circulation $-\Gamma_j$ and its image Γ_j is given by:

$$\begin{aligned}
M_{hCj} &= -\rho(U\cos\alpha-\dot{h}\sin\alpha)\int_{-b}^{b}\frac{\partial(\phi_j'^{(u)}-\phi_j^{(l)})}{\partial x}xdx-\rho\int_{-b}^{b}\frac{\partial(\phi_j^{(u)}-\phi_j^{(l)})}{\partial t}xdx+\\
&\quad -\tfrac{\rho}{2}\int_{-b}^{b}(u_j'^{(u)^2}-u_j'^{(l)^2})xdx-abN_{Cj}\\
&= -\rho(U\cos\alpha-\dot{h}\sin\alpha)\left\{\left[(\phi_j'^{(u)}-\phi_j'^{(l)})x\right]_{x=-b}^{x=b}-\int_{-b}^{b}(\phi_j'^{(u)}-\phi_j'^{(l)})dx\right\}+\\
&\quad -\rho\left(\int_{-b}^{b}\frac{\partial(\phi_j'^{(u)}-\phi_j'^{(l)})}{\partial t}xdx\right)-\tfrac{\rho}{2}\int_{-b}^{b}\left(u_j'^{(u)^2}-u_j'^{(l)^2}\right)xdx-abN_{Cj}\\
&= -\rho(U\cos\alpha-\dot{h}\sin\alpha)\Gamma_j\left(x_j-\sqrt{x_j^2-b^2}\right)\cos\varphi_j+\\
&- \rho\Gamma_j\left(\frac{4x_j^2+b^2-2b^2\cos^2\varphi_j-2x_j^2\sec^2\varphi_j}{2\sqrt{x_j^2-b^2\cos^2\varphi_j}}-(2-\sec^2\varphi_j)x_j\right)\dot{x}_j+\\
&- \rho\Gamma_j\left(x_j\sec\varphi_j\frac{b^2(\cos 2\varphi_j+2)-2x_j^2\sec^2\varphi_j}{2\sqrt{x_j^2-b^2\cos^2\varphi_j}}+x_j^2\sec^3\varphi_j-b^2\cos\varphi_j\right)\dot{\varphi}_j\sin\varphi_j+\\
&- \rho\Gamma_j^2\frac{sgn(\sin\varphi_j)}{4\sqrt{2}\pi}\frac{\left(-p_1^4p_2+p_1^2p_2(p_2^2-2p_3)+4p_2p_3^2\right)Re(\overline{p})-\left(p_1^3p_4-p_1p_4(p_2^2+2p_3)\right)Im(\overline{p})}{(p_1^2-p_2^2)|\overline{p}|^2\sqrt{p_1^2-2p_3}}-abN_{Cj}
\end{aligned}\tag{2.40}$$

where the coefficients p_1, p_2, p_3 and p_4 are the same as equation (2.36), N_{Cj} is the circulational normal force of circulation $-\Gamma_j$ and its image Γ_j, $sign(x)$ denotes the sign of x, $\mathbf{i}$ indicates $\sqrt{-1}$ and Re and Im are respectively the real and image parts of complex number. Moreover, according to the displacement relationship between η and ξ coordinates (Eq. (2.23)), the radius displacement r_j and the angular velocity $\dot{\varphi}_j$ of circulation $-\Gamma_j$ in η plane is given by

$$\begin{aligned}
r_j &= \frac{x_j}{2\cos\varphi_j}+\frac{z_j}{2\sin\varphi_j}\\
\dot{\varphi}_j &= \frac{z_j\dot{z}_j sin\varphi_j(\cos\varphi_j)^3-x_j\dot{x}_j(\sin\varphi_j)^3\cos\varphi_j}{x_j^2(\sin\varphi_j)^4+z_i^2(\cos\varphi_j)^4}
\end{aligned}\tag{2.41}$$

where x_j and z_j are respectively the horizontal and vertical displacements of circulation $-\Gamma_j$ in the ξ plane , $\dot{x}_j$ and $\dot{z}_j$ are respectively the horizontal and vertical velocities of the circulation $-\Gamma_j$ in the ξ plane and φ_j is the angular displacement of the circulation $-\Gamma_j$ in the η plane. Also, $\sin\varphi_j$ and $\cos\varphi_j$ are given by:

$$\begin{aligned}
sin\varphi_j &= \text{sign}(z_j)\sqrt{\frac{b^2-x_j^2-z_j^2+\sqrt{(x_j^2+z_i^2-b^2)+4b^2z_j^2}}{2b^2}}\\
\cos\varphi_j &= \text{sign}(x_j)\sqrt{\frac{x_j^2+z_j^2+b^2-\sqrt{(x_j^2+z_j^2+b^2)^2-4b^2x_j^2}}{2b^2}}
\end{aligned}\tag{2.42}$$

where $\text{sign}(x)$ is the sign of variable x.

The terms (that is proportional to Γ_j^2) of Eqs. (2.39, 2.40) stem from the nonlinear term u'^2 in Bernoulli's equation (2.10), which has been usually neglected in the previous studies.

If we neglect this term, considered a small angle of attack, constant free stream, and a flat wake ($\varphi_j = 0$), then the shedding velocity will be given by $\dot{x}_j = U$ and, hence, Theodorsen's result [8] is recovered

$$\begin{aligned} N_C &= \rho U \Gamma \tfrac{x}{\sqrt{x^2-b^2}} \\ M_{hC} &= -\tfrac{\rho U \Gamma b^2}{2\sqrt{x^2-b^2}} - abN_C \end{aligned} \tag{2.43}$$

Equations (2.39, 2.40) are more than a geometrically exact extension of Theodorsen's result, Eq. (2.43). In addition to accounting for the geometric nonlinearities, Eqs. (2.39, 2.40) allow for a time-varying (non-uniform) free stream, non-flat wake deformation, shedding by the local velocity $\dot{x}_j$ rather the free stream one, and finally accounts for the higher order perturbation u'^2-effect.

As for the total suction force on the flat plate, we substitute the non-circulatory and circulatory contributions of q'_θ into Eq. (2.13) to obtain

$$F_s = \frac{\pi\rho b}{8}\left[\sum_j -\frac{\Gamma_j}{\pi b}\left(\frac{r_j^2 - \left(\frac{b}{2}\right)^2}{r_j^2 + r_j b\cos(\varphi_j) + \left(\frac{b}{2}\right)^2}\right) - 2\left(U\sin\alpha + \dot{h}\cos\alpha + (a-1/2)b\dot{\alpha}\right)\right]^2 \tag{2.44}$$

2.4 Numerical Implementation

In this section, we show the implementation of the unsteady model developed in the previous sections. The developed model is semi-analytical in the sense that closed form algebraic equations are written for the aerodynamic loads, though the wake convection needs to be performed numerically. As stated before, we discretize the wake sheet of vorticity into a finite number of point vortices. As shown in Eqs. (2.39,2.40), the coordinates of the discrete wake vortices and their velocities with respect to O' are required to determine the unsteady aerodynamic loads. The velocity of each wake vortex $-\Gamma_j$ comprises three components: (1) a component due to the undisturbed flow, (2) a circulatory component due to the other separated vortices and their images, and (3) a non-circulatory component due to the source/sink distribution over the cylinder/plate. All the components are transformed to the inertial axes (X-Z system) where they are added together and marched forward to predict the location of each point vortex in the next time step.

The first contribution to the components of the convection velocity of a wake vortex $-\Gamma_j$ that is due to the undisturbed flow, as shown in Fig. 2.1, is written as

$$\dot{X}_j^{(1)}(t) = U(t) \;\;,\;\; \dot{Z}_j^{(1)}(t) = \dot{h}(t) \tag{2.45}$$

Figure 2.5 (a) shows the induced velocity on a wake vortex $-\Gamma_j$ due to another wake vortex

$-\Gamma_k$ and its image. Then, the components of the total induced velocity on a wake vortex $-\Gamma_j$ due to the other wake vortices and their images are given by

$$\begin{aligned}
q_{rj}^{(2)} &= \sum_{k=1,k\neq j}^{N} \left[\mathbf{q_{jk}^{+}} \sin\delta_{\mathbf{1jk}} - \mathbf{q_{jk}^{-}} \sin\delta_{\mathbf{2jk}}\right] \\
&= \sum_{k=1,k\neq j}^{N} \left\{ -\frac{\Gamma_k \sin(\varphi_j-\varphi_k)}{2\pi} \left[\frac{r_j}{r_j^2-2r_j r_k \cos(\varphi_j-\varphi_k)+{r_k}^2} - \frac{\frac{b^2}{4r_k}}{r_j^2-2r_j \frac{b^2}{4r_k}\cos(\varphi_j-\varphi_k)+\left(\frac{b^2}{4r_k}\right)^2} \right] \right\} \\
q_{\theta j}^{(2)} &= \sum_{k=1,k\neq j}^{N} \left[\mathbf{q_{jk}^{-}} \cos\delta_{\mathbf{2jk}} - \mathbf{q_{jk}^{+}} \cos\delta_{\mathbf{1jk}}\right] \\
&= \sum_{k=1,k\neq j}^{N} \left\{ -\frac{\Gamma_k}{4\pi r_j} \left[\frac{r_j^2-\left(\frac{b^2}{4r_k}\right)^2}{r_j^2-2r_j \frac{b^2}{4r_k}\cos(\varphi_j-\varphi_k)+\left(\frac{b^2}{4r_k}\right)^2} - \frac{r_j^2-{r_k}^2}{r_j^2-2r_j r_k \cos(\varphi_j-\varphi_k)+{r_k}^2} \right] \right\}
\end{aligned} \tag{2.46}$$

Similarly, Fig. 2.5 (b) shows the induced velocity on a wake vortex $-\Gamma_j$ due to an element of the source/sink distribution. Hence, the non-circulatory components of the total induced velocity on a wake vortex $-\Gamma_j$ are given by

$$\begin{aligned}
q_{rj}^{(3)} &= \int_0^{\pi} d\mathbf{q_{Hj}^{+}} \cos\delta_{\mathbf{3j}} - \mathbf{dq_{Hj}^{-}} \cos\delta_{\mathbf{4j}} \\
&= -\frac{b^2}{2{r_j}^2}\left(U\sin\alpha + \dot{h}\cos\alpha + ab\dot{\alpha}\right)\sin\varphi_j - \frac{b^4\dot{\alpha}}{8{r_j}^3}\sin(2\varphi_j) \\
q_{\theta j}^{(3)} &= -\int_0^{\pi} d\mathbf{q_{Hj}^{+}} \sin\delta_{\mathbf{3j}} + \mathbf{dq_{Hj}^{-}} \sin\delta_{\mathbf{4j}} \\
&= \frac{b^2}{2{r_j}^2}\left(U\sin\alpha + \dot{h}\cos\alpha + ab\dot{\alpha}\right)\cos\varphi_j + \frac{b^4\dot{\alpha}}{8{r_j}^3}\cos(2\varphi_j)
\end{aligned} \tag{2.47}$$

According to the transformation between the plate domain (ξ-plane) and the cylinder domain (η-plane), as presented in Eq. (2.6), the components of the above induced velocity vectors $\mathbf{q^{(2)}}$ and $\mathbf{q^{(3)}}$ in the ξ-plane are written as

$$\begin{aligned}
\dot{x}_j^{(p)} &= \frac{q_{rj}^{(p)}\left(1-\frac{b^2}{4{r_j}^2}\right)\cos\varphi_j - q_{\theta j}^{(p)}\left(1+\frac{b^2}{4{r_j}^2}\right)\sin\varphi_j}{1-\frac{b^2}{2{r_j}^2}\cos(2\varphi_j)+\left(\frac{b^2}{4{r_j}^2}\right)^2} \\
\dot{z}_j^{(p)} &= \frac{q_{rj}^{(p)}\left(1+\frac{b^2}{4{r_j}^2}\right)\sin\varphi_j + q_{\theta j}^{(p)}\left(1-\frac{b^2}{4{r_j}^2}\right)\cos\varphi_j}{1-\frac{b^2}{2{r_j}^2}\cos(2\varphi_j)+\left(\frac{b^2}{4{r_j}^2}\right)^2}
\end{aligned} \tag{2.48}$$

where $p = 2, 3$. These velocity components are then transformed to the inertial axes $(X-Z)$ as

$$\begin{aligned}
\dot{X}_j^{(p)} &= \dot{x}_j^{(p)}\cos\alpha + \dot{z}_j^{(p)}\sin\alpha \\
\dot{Z}_j^{(p)} &= -\dot{x}_j^{(p)}\sin\alpha + \dot{z}_j^{(p)}\cos\alpha
\end{aligned} \tag{2.49}$$

Thus, the total velocity components of the wake vortex $-\Gamma_j$ with respect to the plate's center

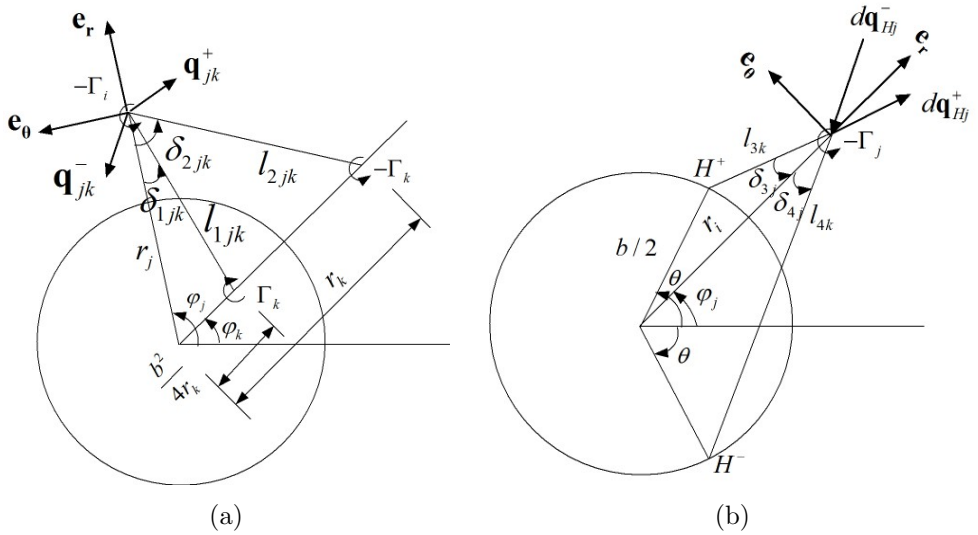

Figure 2.5: A schematic for circulation Γ_i effected by (a) other circulation Γ_k and its image circulation and (b) sources on the η-plane

O' in the inertial frame are determined as

$$\begin{aligned}\dot{X}_{j-O'}(t) &= \dot{X}^{(1)}_j(t) + \dot{X}^{(2)}_j(t) + \dot{X}^{(3)}_j(t) + ab\dot{\alpha}(t)\sin\alpha(t)\\ \dot{Z}_{j-O'}(t) &= \dot{Z}^{(1)}_j(t) + \dot{Z}^{(2)}_j(t) + \dot{Z}^{(3)}_j(t) + ab\dot{\alpha}(t)\cos\alpha(t)\end{aligned} \tag{2.50}$$

We use a simple first-order Euler scheme to predict the new position of the wake vortex as

$$\begin{aligned}X_j(t+\Delta t) &= X_j(t) + \dot{X}_j(t)\Delta t\\ Z_j(t+\Delta t) &= Z_j(t) + \dot{Z}_j(t)\Delta t\end{aligned} \tag{2.51}$$

Finally, the velocities ($\dot{x}$ and $\dot{z}$) and positions (x and z) in the body frame, as required in Eqs. (2.39,2.40), can be calculated from their inertial counterparts according to the inverse of Eq.(2.49).

As for the aerodynamic loads, the non-circulatory contributions are given directly in equations (2.20) and (2.21). After determining the positions and the velocities of the wake vortices, the circulatory loads induced by each wake vortex can be determined from Eqs. (2.39, 2.40). Finally, the total suction force is determined from Eq. (2.44). Thus, the horizontal

and vertical components of the resultant force are given by

$$\begin{aligned} F_X &= \left(N_N + \sum_j^N N_{Cj} \right) \sin\alpha - F_S \cos\alpha \\ F_Z &= \left(N_N + \sum_j^N N_{Cj} \right) \cos\alpha + F_S \sin\alpha \end{aligned} \tag{2.52}$$

2.5 Validation and Analysis

Although the model is mainly developed for unsteady applications, it is of interest to validate its asymptotic steady behavior first in the following subsection, while the unsteady behavior will be validated in the next subsection.

2.5.a Steady Behavior

The asymptotic steady behavior of the developed model is validated against the wind tunnel experimental results of Brandon [65] on the F-18 wing experiencing high angles of attack ($5^\circ - 75^\circ$). We divide the wing into 100 segments, apply the developed aerodynamic model on each segment, and integrate over the span to obtain the total lift force L. Then, we use

$$C_L = \frac{\mathit{AR}}{2\left(1+\sqrt{\left(\frac{\mathit{AR}}{2}\right)^2+1}\right)} \frac{L}{\frac{1}{2}\rho U^2 S} \tag{2.53}$$

to account for the induced downwash due to the three dimensional effects in a simple way through the *Extended Lifting Line Theory* (see [66]). In this equation, AR denotes the aspect ratio of the wing. Figure 2.6 shows a comparison between the lift coefficient using Eq. (2.53), with the lift L determined from the proposed model, and the experimental data given in Ref. [65]. Two model predictions are presented in Fig. 2.6; with and without considering the leading edge (LE) suction force. Figure 2.6 also shows the static lift coefficient using the conventional extended lifting line theory; that is

$$C_L = \frac{\pi \mathit{AR}}{1+\sqrt{\left(\frac{\pi \mathit{AR}}{a_0}\right)^2+1}} \sin\alpha$$

The plots show that the variation of the static lift coefficient with the angle of attack (C_L-α curve) using the proposed model accounting for the LE suction force exactly matches that of the classical wing theory. This matching indicates that both have the same nonlinearity

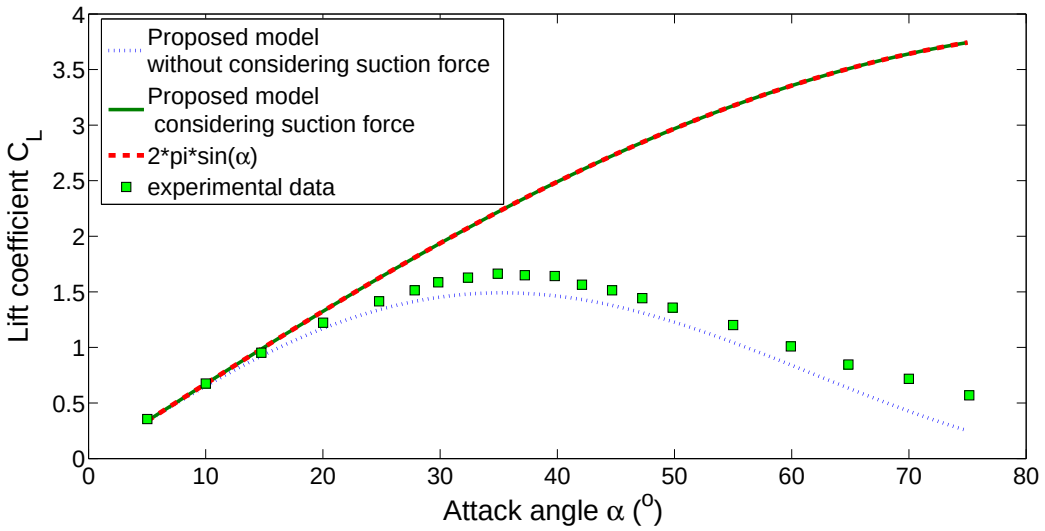

Figure 2.6: Comparison between the static lift coefficient using the proposed model (with and without suction force), the static wing theory and the experimental data [65]

($\sin\alpha$), that is induced by the no-penetration boundary condition. Moreover, since both of these curves closely match the experimental data up to $\alpha = 20°$, we can conclude that the nonlinearity induced by the no-penetration boundary condition is the dominant one in this range of the angle of attack (as well as the flow remains attached). At large angles of attack, the separation effects are more pronounced. Consequently, the contribution of the LE suction force is expected to diminish as shown by Dickinson and Gotz [67] and Usherwood and Ellington [68]. Therefore, within the framework of potential flow, we account for the flow separation by neglecting the LE suction force. The fact that the predicted C_L-α curve, ignoring the LE suction force, closely matches the experimental data shows that the effects of the geometric nonlinearities may dominate other separation effects. Although the F-18 wing section (NACA 65A005) is a typical cambered, thick airfoil with a rounded LE, it is envisaged that the high sweep angle of the wing helps stabilizing a LE vortex, consequently, eliminates abrupt stall from taking place and leads to a smooth lift-curve. This may explain the good matching between the F-18 wing experimental data and the potential flow results when ignoring the LE suction (clearly, the LE suction force and the LE vortex cannot coexist [69]).

Since the developed model is two-dimensional, it is still of interest to validate its steady behavior versus two dimensional experimental results. We choose the experimental results of Dickinson and Gotz [67] for validation. Their experimental setup consisted of a two dimensional flat plate undergoing an impulsive start from rest to some specific forward speed through almost a constant acceleration at a constant angle of attack. They covered a wide range of positive angles of attack at low Reynolds numbers (between 79-236). Dickinson and

Gotz found that for large angles of attack, a strong leading edge vortex (LEV) forms with a large diameter (of the order of a chord length). After about four chord lengths ($4c$), the vortex becomes extended rearwards and eventually shed. As this vortex is shed, a vortex of opposite sign is formed at the trailing edge. This alternating pattern continues, forming Von Karman street, which is similar to the numerical results of Wang [70]. Dickinson and Gotz provided two polar plots for the measured lift and drag coefficients at $2c$ and $7c$ referring to them as "early" and "late" measurements, respectively. The "late" data correspond to the inception of the Von Karman street and the load oscillations while the "early" ones correspond to the steady loads reached after the transient response.

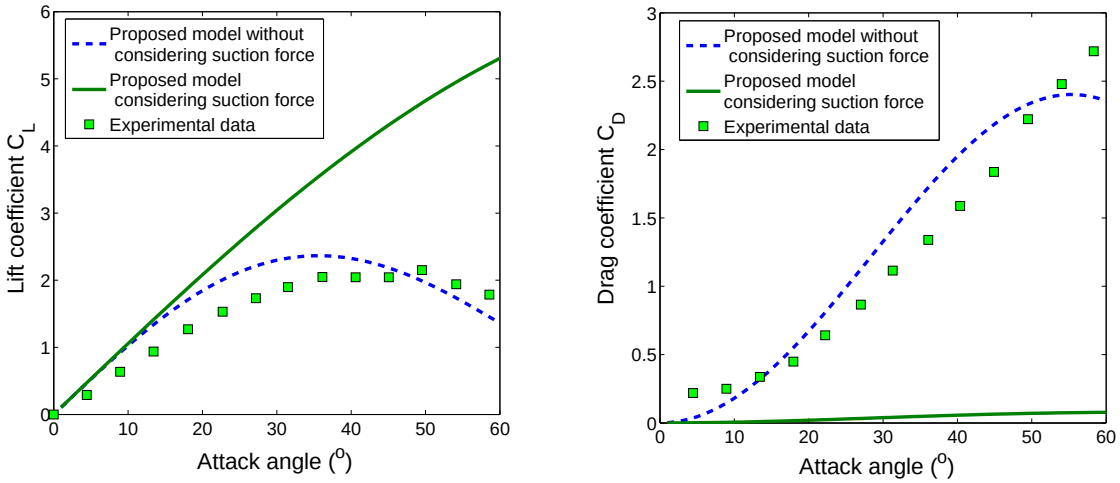

(a) (b)

Figure 2.7: Comparison between the two-dimensional static lift and drag coefficient using the proposed model (with and without suction force) and the experimental results of Dickinson and Gotz [67].

Fig. 2.7 shows a comparison between the lift and drag coefficients as determined by the proposed model and the "early" results of Dickinon and Gotz [67]. The results show that the developed model ignoring the LE suction gives a satisfactory trend for the lift and drag variation in comparison to the experimental data of Dickinson and Gotz. It is important to note that, in contrast to the previous validation case, the experiment of Dickinson and Gotz is performed at low Reynolds numbers. This explains the deviation of the experimental data for the lift coefficient from the current results even at small angles of attack. As expected, considering the LE suction force in a potential flow framework predicts no drag, as shown in Fig. 2.7 (b). The difference between the potential flow results for drag and the experimental data at zero angle of attack is attributed to the skin friction drag that is not captured within the potential flow framework.

2.5.b Unsteady Behavior

The unsteady predictions of the proposed model are validated against the computational and experimental results of Ramesh et al. [17]. They solved the two-dimensional Navier-Stokes equations on a flat plate undergoing large amplitude canonical pitch maneuvers that are presented in Ref. [61] and shown here in Fig. 2.8. The plate is pitching around the mid point uniformly from 0° up to a specific angle of attack (25° and 45°), retains this angle for a while, and then returns back uniformly to 0° with a total maneuver non-dimensional time of six.

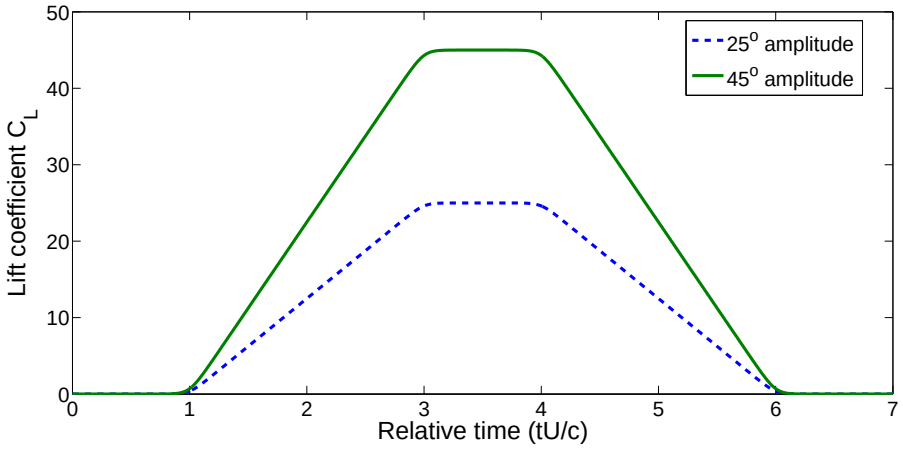

Figure 2.8: Canonical pitch maneuvers [61].

Figures 2.9 and 2.10 show comparisons of the time variations of the resulted lift coefficients among the proposed model (with and without considering the LE suction force), the computational results and experimental data of Ramesh at el. [17], and the classical unsteady model of Leishman and Nguyen [71] for the 25° and 45° maneuvers, respectively. Noting that the Reynolds number of the experiment and simulation of Ramesh et al. [17] is 10,000 where delayed stall is evidenced [67], considerable flow separation is not expected to occur during the relatively small angle of attack maneuver (25°). Hence, it is expected that the role of the LE suction force would be significant in this maneuver. This explains the agreement between the experimental data and the lift curve predicted by the proposed model (accounting for the LE suction) as well as that of the classical unsteady theory, as shown in Figure 2.9 for the 25° maneuver. However, when the maneuver amplitude becomes larger, separation effects become more pronounced. Hence, the LE suction is not expected to play a role. As shown in Fig. 2.10, the lift curves predicted by the proposed model (accounting for the LE suction) as well as the classical unsteady theory deviate considerably from the experimental data, particularly at the times where the large angles of attack are encountered ($\frac{Ut}{c} = 3-4$). On the other hand, the lift curve of the proposed model, neglecting the LE suction, closely matches the experimental data.

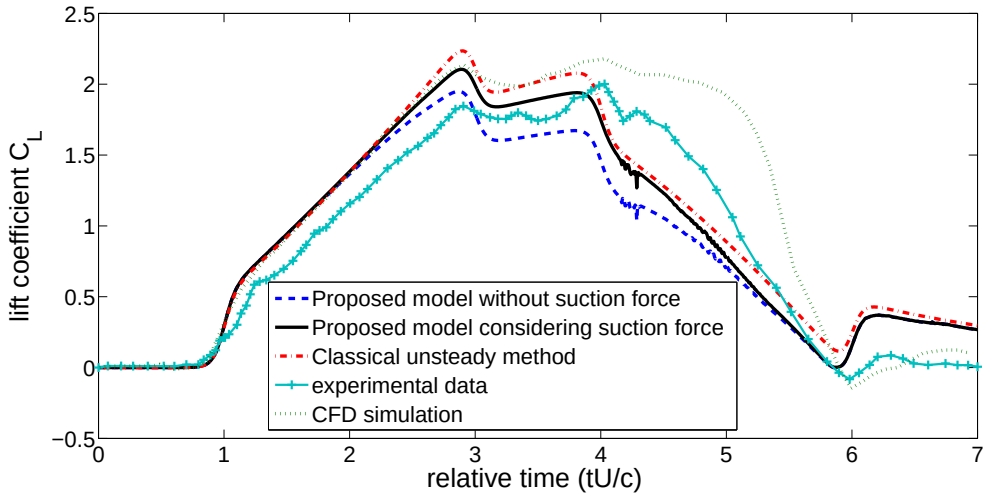

Figure 2.9: A comparison for the unsteady lift evolution among the proposed models (with and without considering the leading edge suction force), the computational results and experimental data of Ramesh et al. [17], and the classical unsteady model of Leishman and Nguyen [71], for the 25^o-maneuver.

Table 2.1: Error metrics quantifying the deviations from the experimental results of Ramesh et al. [17] of the results of the proposed model with and without including the LE suction force, the computational results of Ramesh et al. [17], and the results of the classical unsteady model of Leishman and Nguyen [71].

$\alpha_{\max}$	Simulation Method	$e_{\text{rms}} = \frac{\sqrt{\overline{(C_L - C_{\text{exp}})^2}}}{\max(C_{\text{exp}})} \times 100$	$\bar{e} = \frac{\overline{\lvert C_L - C_{\text{exp}} \rvert}}{\max(C_{exp})} \times 100$
25^o	Proposed model without LE suction	14.50	11.47
	Proposed model with LE suction	12.06	10.11
	Computational results [17]	16.28	12.26
	Classical unsteady model [71]	12.50	10.78
45^o	Proposed model without LE suction	13.16	10.91
	Proposed model with LE suction	23.05	19.72
	Computational results [17]	16.52	14.16
	Classical unsteady model [71]	30.63	25.99

For each of the two considered maneuvers, we provide a quantitative comparison among the models discussed above. We consider the experimental data of Ramesh at el. [17] as a benchmark and calculate the deviation of each of the other results with respect to it, as shown in Table 2.1. Two error metrics are calculated. These are the root mean squared error in the lift coefficient in percent of the maximum lift coefficient $e_{\text{rms}} = \frac{\sqrt{\overline{(C_L - C_{\text{exp}})^2}}}{\max(C_{\text{exp}})} \times 100$, and the mean value of the deviation in the lift coefficient in percent of the maximum lift coefficient $\bar{e} = \frac{\overline{\lvert C_L - C_{\text{exp}} \rvert}}{\max(C_{exp})}$. We use the over bar to denote an average quantity. Because low Reynolds number (10,000) is encountered, the associated delayed stall indicates that the flow will

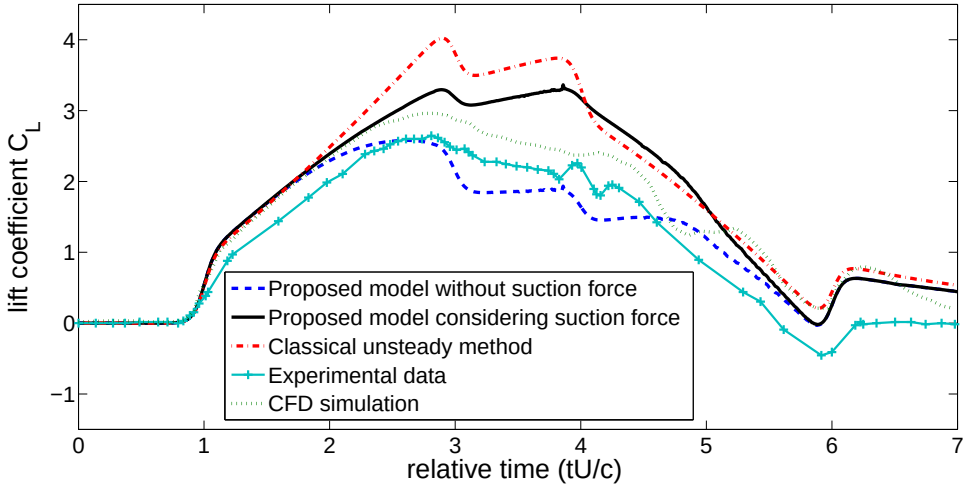

Figure 2.10: A comparison for the unsteady lift evolution among the proposed models (with and without considering the leading edge suction force), the computational results and experimental data of Ramesh et al. [17], and the classical unsteady model of Leishman and Nguyen [71], for the 45^o-maneuver.

remain attached during the relatively small angle of attack maneuver ($25°$). Thus, in such a maneuver, the two error metrics of the proposed model (considering the LE suction) and the classical unsteady theory are comparable to that of the computational results. But when considerable separation effects are encountered in the large amplitude maneuver, the two error metrics of the proposed model (considering the LE suction) and the classical unsteady theory are too large in comparison to the that of the proposed model, without considering the LE suction, and that of the computational results. It is noteworthy to mention that in addition to the efficiency of the proposed model (in terms of computational cost and number of degrees of freedom), it resulted in the minimum error metrics in comparison to all of the other models for the high angle of attack case. That is, the proposed unsteady aerodynamic model is efficient enough to be used in multi-disciplinary analyses (e.g., dynamics, control, and optimization) and also rich enough to cover the gaps that the classical unsteady theory cannot cover.

The capability of the developed model to capture the effects of unsteady free stream is validated against the predictions of Isaac's theory [72], Greenberg's theory [73], and Peters finite state theory [74] for the case of a sinusoidal variation of the free stream. The unsteady free stream is written as

$$U(t) = U_0[1 + \mu \sin(\omega t)] = U_0[1 + \mu \sin \Psi]$$

where α is kept constant. Figure 2.11 shows a comparison of the normalized lift $\frac{L}{2\pi\rho b U_0^2 \alpha}$

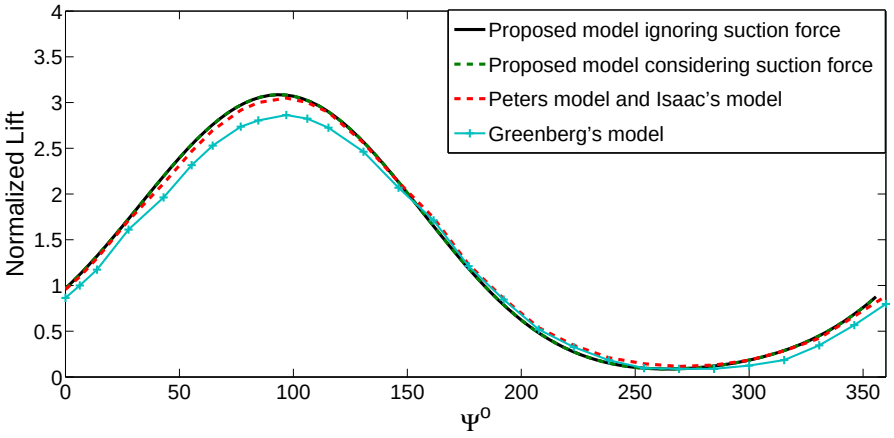

Figure 2.11: A comparison for the normalized lift (unsteady to quasi-steady ratio) among the proposed models (with and without considering the leading edge suction force), Isaac's theory [72], Greenberg's theory [73], and Peters finite state theory [74] for a sinusoidally varying free stream.

(unsteady to quasi-steady ratio), for the case $\mu = 0.8$ and $k = 0.2$, as obtained by the proposed model and the results of the models discussed above. The simulation is performed at $\alpha = 5°$ (in the linear range) in order to have a meaningful comparison with the linear theories. The plots show that whether the LE suction effects are included or not, the unsteady lift can be satisfactorily predicted by the proposed model for the case of a small angle of attack where the linear theory is applicable (mainly because of the absence of separation).

2.5.c Oscillation motions of different methods

In this section, Classical Theodorsen's method [62] and Taha's unsteady aerodynamic model [4] are chosen to compare with the proposed model. Here, the only pitch motion is considered and the dynamic attack model is chosen as $\alpha = A1 + A1\cos\omega t$. $A1$ is the amplitude of the attack angle and four different values is chosen: 5^o, 10^o, 15^o and 20^o. In Taha's unsteady aerodynamic model, when the suction force is considered, the quasi-steady lift coefficient is chosen as $C_{L,s}(\alpha) = 2\pi sin\alpha$, which is shown in Fig. 2.6. Moreover, the wind speed U, the chord length c and frequency of attack angle ω are chosen as $10m/s$, $1m$ and $10rad/s$, respectively. Therefore, the time history of lift coefficients for the four different cases are shown in Fig. 2.12.

Inspecting Fig. 2.12, we note that the time history of the lift coefficient of proposed model is almost same as that of Classical Theodorsen's and Taha's methods when the angle of attack is $\alpha = 5+5\cos\omega t$. This is expected that Classical Theodorsen's and Taha's methods are derived

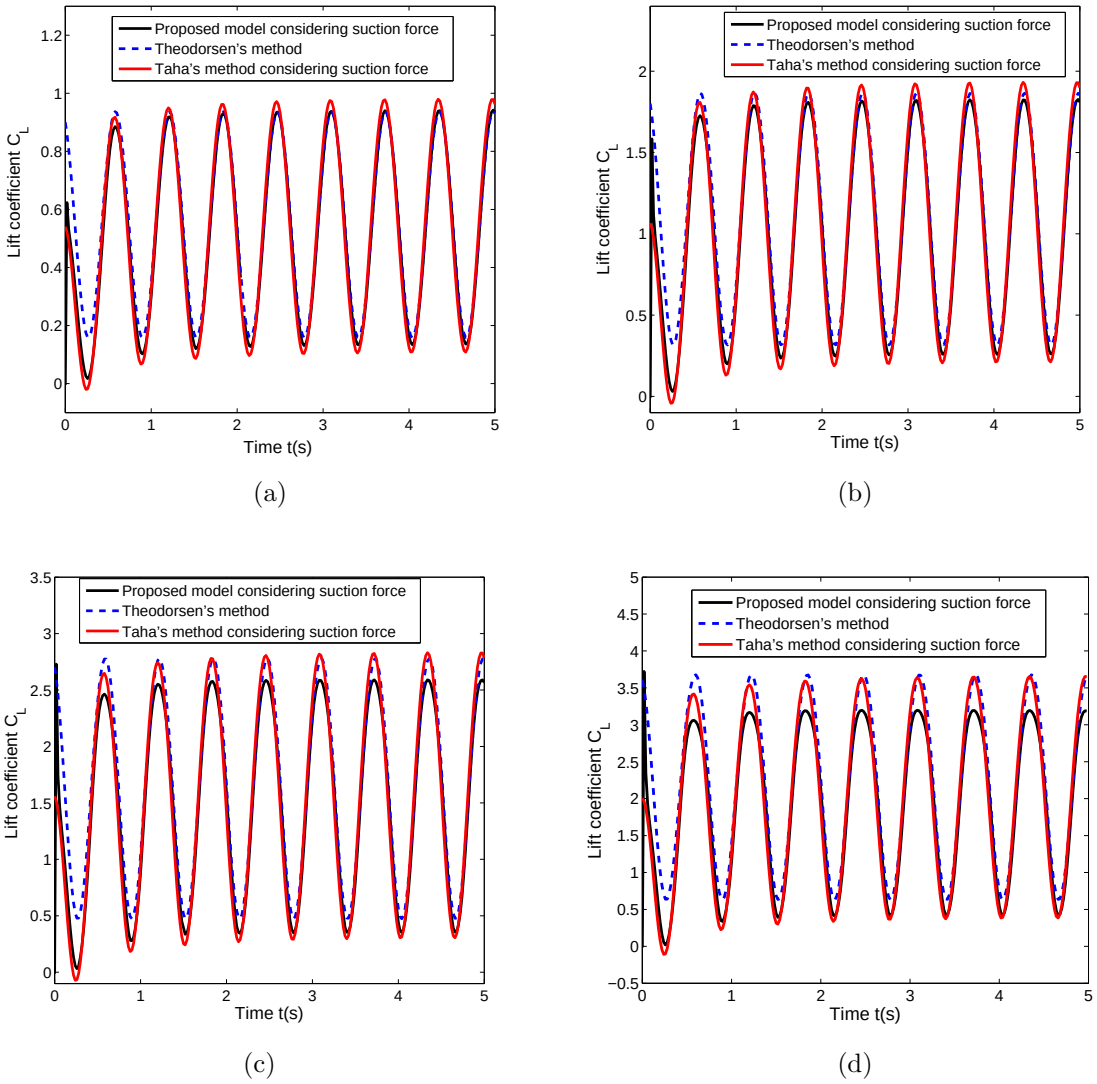

Figure 2.12: The lift coefficient varied by time history with there different methods (proposed model considering suction force, Taha's model considering suction force [4] and Theodorsen's method [62]) in different amplitude of attack angle: (a) $\alpha = 5{+}5\cos\omega t$, (b) $\alpha = 10{+}10\cos\omega t$, (c) $\alpha = 15 + 15\cos\omega t$ and (d) $\alpha = 20 + 20\cos\omega t$

from the assumption of small angle of attack. Classical Theodorsen's and Taha's methods become inaccurate as the amplitude of angle of attack is increased to $\alpha = 20 + 20\cos\omega t$ and the amplitude of lift force becomes 20% larger than the proposed model. Therefore, it is necessary to adopt our proposed geometrically-exact model to consider the unsteady flow especially when the angle of attack is relatively large.

2.5.d Pressure distribution

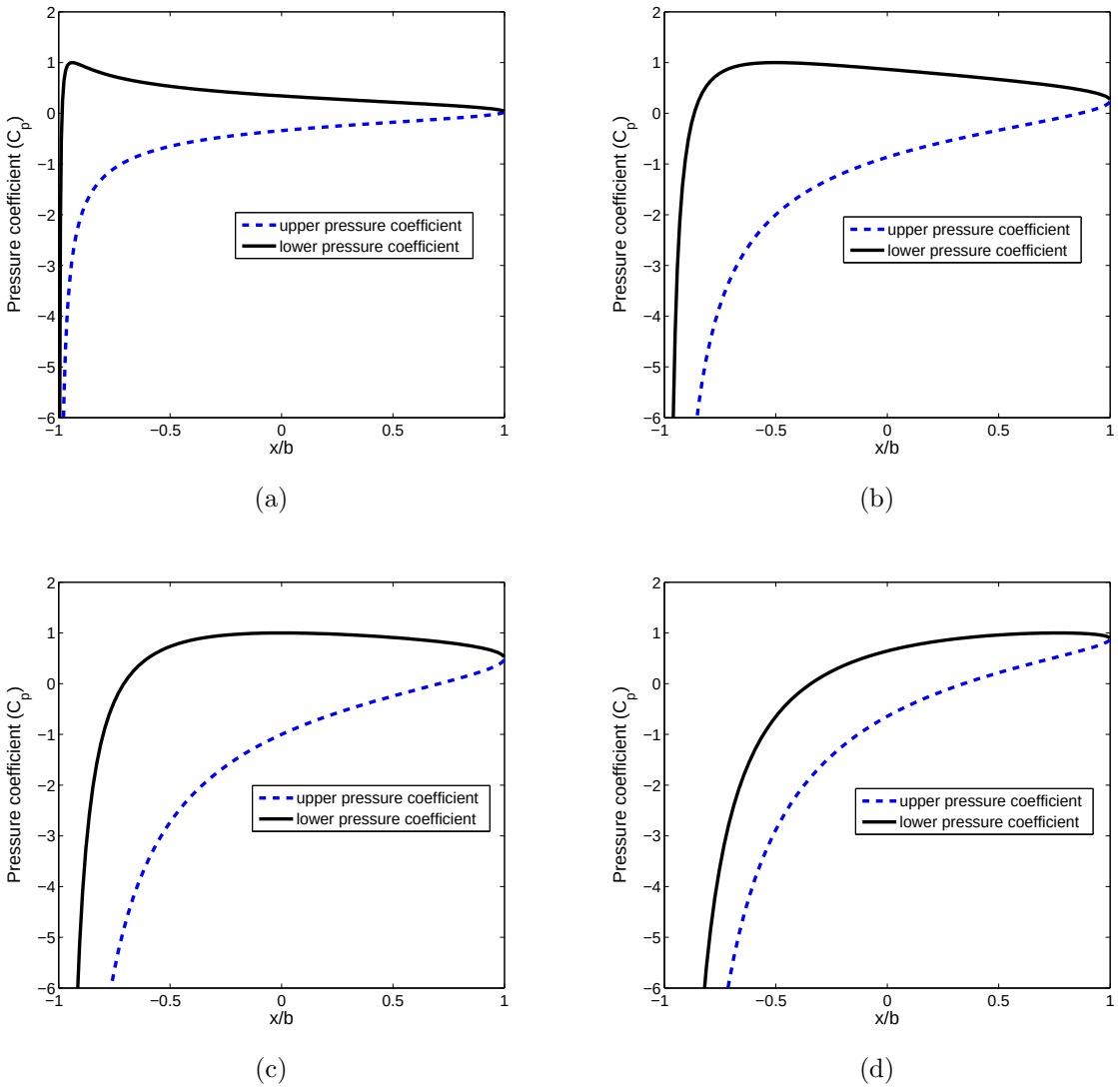

Figure 2.13: Upper and low pressure distributions along the flat plane with different attack angles: (a)$\alpha = 10^o$, (b) $\alpha = 30^o$, (c) $\alpha = 45^o$ and (d) $\alpha = 70^o$

In this section, we will do some further discussion about the upper and lower pressures along the chord line with different attack angles. First, based on Eq. (2.10), the pressure distribution can be expressed as:

$$\begin{aligned} C_p &= \frac{p-p_\infty}{1/2\rho U^2} \\ &= \frac{\frac{\partial \phi'}{\partial t} + (U\cos\alpha - \dot{h}\sin\alpha)u' + (U\sin\alpha + \dot{h}\cos\alpha)w' + \frac{1}{2}(u'^2 + w'^2)}{1/2\rho U^2} \end{aligned} \tag{2.54}$$

where the disturbance velocity potential ϕ' is the sum of the noncirculational and circulational effects shown in Eq. (2.17) and Eq. (2.30), the disturbance vertical velocity w' is caculated by Eq. (2.4) and the disturbance horizontal velocity u' is the sum of the noncirculational effects and circulational effects which is calculated from Eq. (2.16), Eq. (2.26), Eq. (2.27) and Eq. (2.48).

Based on the above derivation, the upper and low pressure distributions along the chord line with the different angles of attack are plotted in Fig. 2.13. Inspecting Fig. 2.13(a), we note that the pressure on the lower surface is almost positive and the pressure on the upper surface is negative along the chords of the plat plane when the attack angle is small ($\alpha = 10^o$). However, as the attack angle is increased, the pressure of the lower surface in the leading part becomes negative and the pressure of the upper surface in the trailing part becomes positive. When the attack angle is 70^o, pressure of the lower surface in the first quarter of the chord is negative and the upper surface in last quarter of chord becomes positive, as shown in Fig. 2.13(d). To this end, it can be concluded that the attack angle have strong effect on the pressure distribution along the chord.

2.5.e Frequency Response at Different Angles of Attack

Having validated the proposed model for a high angle of attack maneuver, it is interesting to investigate how the frequency response (Theodorsen's main result) changes as the angle of attack increases. Theodorsen's model is based on a linear approximation for the flow dynamics, which results in a frequency response that is independent on the operating condition and/or the amplitude of the aerodynamic input (airfoil motion). The developed model accounts for the geometric and nonplanar-wake nonlinearities. As such, it will not result in a single frequency response. Rather, a different frequency response (i.e., linearized flow dynamics) will be obtained at different operating conditions (angles of attack). In this section, we determine the frequency response of the circulatory normal force at different angles of attack, namely 5°, 20°, and 40°. At each value of these angles of attack, the following plunging maneuver is simulated:

$$h(t) = \bar{H} b \sin \omega t$$

where $\bar{H}$ is the amplitude of oscillation normalized by the half-chord length (b) and ω is the frequency of oscillation. That is, the effective angle of attack is given by

$$\alpha_{eff} \approx \alpha_0 + \frac{\dot{h}}{U} = \alpha_0 + k\bar{H} \cos \omega t$$

where α_0 is the mean/steady angle of attack (5^o, 20^o and 40^o) and k is the reduced frequency. For each value of α_0, we simulate the above plunging maneuver at various frequencies to determine the frequency response at this value of α_0. For each frequency, the value of $\bar{H}$

is adjusted such that the amplitude of the oscillating angle of attack ($k\bar{H}$) is 5°; that is, we simulate small angle maneuvers around different mean values of α_{eff} to determine the frequency response of the linearized aerodynamic system around the considered α_0.

For each combination of α_0 and k, the above plunging maneuver is simulated and the steady state time history of the non-circulatory normal force is obtained. We then simulate the same maneuver (i.e., same α_{eff}) at almost steady conditions (at very small value of k). Thus, the magnitude of the frequency response at this combination of α_0 and k is simply the ratio of the unsteady amplitude to the almost steady one and its argument (phase) is the phase shift between the two signals far out in time.

Figure 2.14 shows the magnitude, phase, and polar lots of the calculated frequency response at the considered three values of α_0 along with that of Theodorsen. For $\alpha_0 = 5°$, the obtained frequency response closely matches that of the Theodorsen function. If α_0 is increased to 20°, good matching is still being seen with a bit of discrepancy at large reduced frequencies. A noteworthy observation is the large deviation at $\alpha_0 = 40°$, not only quantitatively but also qualitatively. The magnitude of Theodorsen's frequency response does not go below $\frac{1}{2}$. In fact, it asymptotically reaches such a value as k goes to infinity. However, Fig. 2.14 (a) shows that the magnitude of the frequency response decreases for large values of α_0 and approaches 0.35 as k goes to infinity. Moreover, unlike the phase of the Theodorsen function, which asymptotically reaches zero (in phase) as k goes to infinity, the phase angle of the frequency response decreases considerably at large angles of attack so that it asymptotically reaches $-180°$ (out of phase) as k goes to infinity. This observation is worth discussing. Note that because the phase of the Theodorsen function approaches zero at high reduced frequencies (i.e., the input and output signals are exactly in phase), it invokes modeling the high-frequency, oscillatory flows with quasi-steady means with some magnitude drop [18]. However, the obtained frequency response (which accounts for the nonlinear wake deformation) refutes this concept because the phase shift approaches $-180°$ rather (i.e., the input and output signals are completely out of phase).

2.5.f Model Validity, Limitations and Extensions

Although the developed model provides an efficient, satisfactory means of predicting the unsteady aerodynamic loads due to large amplitude maneuvers, it is still lying within the framework of potential flow and, hence, cannot capture specific physical aspects. These include viscous friction, LE separation, and dynamic stall. One important extension is to study the appropriate conditions for switching between including and ignoring the LE suction. Recently, there have been relevant efforts in Refs. [75, 76]. Ramesh et al. [75] introduced a new criterion for LE separation based on LE suction. Note that according to

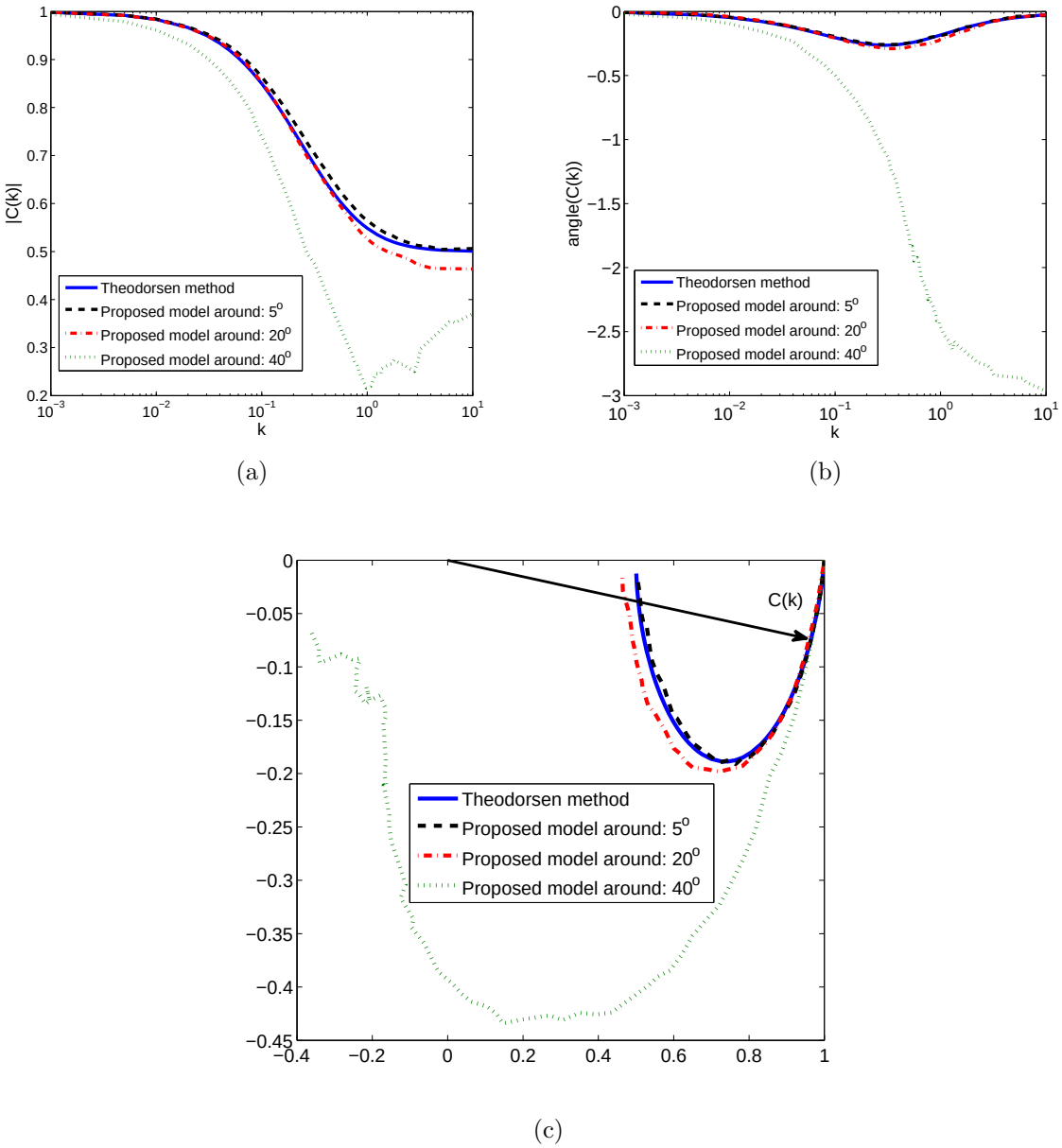

Figure 2.14: Magnitude and phase plots along with the polar plot for the obtained frequency response at different angles of attack along with that of Theodorsen: (a) magnitude of the frequency response, (b) phase angle of the frequency response and (c) polar plot of the frequency response

Garrick [77], the flow velocity at the LE, V_{LE}, can be written as

$$V_{LE} = \lim_{x \to LE} \frac{S}{\sqrt{x}}$$

where $S = \lim_{x \to LE} \frac{1}{2}\gamma(x,t)\sqrt{x}$ is a measure of the LE suction force and γ is the bound vorticity distribution that is written in Fourier series as

$$\gamma(\theta,t) = 2U\left[A_0(t)\frac{1+\cos\theta}{\sin\theta} + \sum_{n=1}^{\infty} A_n(t)\sin(n\theta)\right]$$

where $x = \frac{c}{2}(1-\cos\theta)$. All the Fourier series terms vanish at the LE except the A_0-term, which is infinite at the LE (having $\frac{1}{\sqrt{x}}$ singularity). Thus, S is finite and equal to $S = \sqrt{c}UA_0(t)$, where c is the chord length and U is the free stream velocity. As such, the A_0 parameter is a measure of the flow velocity at the LE and the LE suction force. Since the LE separation is related to the flow conditions at the LE, Ramesh et al. [75] proposed the A_0 parameter to be a measure for LE separation and called it "Leading Edge Suction Parameter(LESP)". If A_0 exceeds a certain limit ($LESP_{cr}$) (that depends on the airfoil type and the Reynolds number), a LE vortex is shed. They determine the strength of the newly shed LE vortex such that $A_0 = LESP_{cr}$.

Morris and Rusak [76] also studied the onset of steady LE stall on thin airfoils using the method of matched asymptotic expansion. In their formulation, the problem outer region is the flow around most of the airfoil chord and is modeled using thin airfoil theory. The inner region is the flow in the vicinity of the LE and is determined by solving the incompressible viscous Navier Stokes equation on a semi-infinite parabola. The two solutions are then made to asymptotically match each other. They showed the existence of a critical angle of attack (that depends on Reynolds number) that is responsible for the inception of LE stall. It should be noted that $A_0 = \frac{1}{2}\sin\alpha$ for steady conditions. Thus, the LESP criterion of Ramesh et al. [75] is equivalent to the angle of attack criterion of Morris and Rusak [76]. However, for unsteady cases, the LESP criterion is more representative than the angle of attack criterion because it accounts for the effective angle of attack over the whole airfoil surface.

For the high Reynolds number of Brandon's experiment on the F-18 wing [65], the critical steady angle of attack $\alpha_{cr} \sim 15°$ according to Morris and Rusak [76]. This is consistent with our results of the F-18 wing (shown in Fig. 2.6); including the suction force closely matches the experimental results up to $\alpha_{cr} \sim 15°$ at which separation occurs. Above 15°, since separation occurs, ignoring the LE suction closely matches the experimental results. On the other hand, considering the unsteady validation cases (shown in Figs. 2.9 and 2.10), $LESP_{cr} \sim 0.18$ [75], which corresponds to an angle of attack of $\alpha_{cr} \sim 21.1°$. This is also consistent with our results since including the LE suction gives satisfactory results for the 25°-maneuver which most of the time lies below the critical condition. On the other hand, during the 45°-maneuver, considerable separation occurs (and consequently LE suction is diminished). As such, ignoring the LE suction yields very comparable results to the computational and experimental data.

Another straightforward extension to the developed model is to allow for the emanation of

a vortex sheet from the LE. The strength of the LE vorticity can be determined to satisfy the Kutta condition at the LE in the same way it is satisfied here at the TE. That is, the following two equations will be solved simultaneously to determine the strengths of the shed vorticity at both edges:

$$q'_{\theta N}(r = b/2, \theta = 0, t) + q'_{\theta TE}(r = b/2, \theta = 0, t) + q'_{\theta LE}(r = b/2, \theta = 0, t) = 0$$
$$q'_{\theta N}(r = b/2, \theta = \pi, t) + q'_{\theta TE}(r = b/2, \theta = \pi, t) + q'_{\theta LE}(r = b/2, \theta = \pi, t) = 0$$

where the subscripts N, TE, and LE refers to the non-circulatory, trailing edge wake, and leading edge wake contributions, respectively. This extension will be more suitable to capture the LE separation effects in comparison to the mere manipulation of the LE suction force inclusion.

2.6 Conclusions

We developed a hybrid analytical-numerical approach to determine the lift coefficient associated with unsteady aerodynamics that involve high angles of attack. For this purpose, we revisited the classical Theodorsen's frequency response model and relaxed the major simplifying assumptions that led to limited region of applicability of Theodorsen's model such as (1) flat wake, (2) small angle of attack, (3) small disturbances to the mean flow components, and (4) time-invariant free-stream. By relaxing these assumptions, we managed to develop a geometrically-exact potential flow model. In the developed model, the vortex kinematics were determined numerically. However, unlike the discrete vortex models, the circulation distribution and the associated aerodynamic loads were determined analytically after solving for the vortex kinematics.

The asymptotic steady behavior of the developed model was validated against two-dimensional experimental data and on the F-18 wing showing a good matching up to 75° angle of attack. The unsteady behavior of the developed model was validated against some experimental and computational results of canonical large-amplitude pitch maneuvers. The model also showed a good agreement with the experimental results in comparison to the classical unsteady theory without requiring high computational burden. The developed model was then used to determine the lift frequency response at various angles of attack. For small angles of attack, the obtained frequency response closely matches that of Theodorsen function. However, for high angles of attack (40°), both qualitative and quantitative discrepancies are observed between the obtained frequency response and that of Theodorsen. The obtained frequency response at the high angle of attack approaches 0.2 magnitude and $-180°$ phase at large values for the reduced frequency, which is in contrast to the $\frac{1}{2}$ magnitude and 0° phase approached by Theodorsen frequency response. The developed model is efficient enough to be used in multi-disciplinary applications (e.g., dynamics and control) and also rich enough

to cover some gaps that the classical theory of Theodorsen cannot cover.

3 Autoparametric Vibration Systems

Autoparameteric vibration systems have been proposed to control structures' vibrations by exploiting an internal resonance with an introduced second degree of freedom. We revisit the model proposed by Haxton and Barr [19] of a base structure and a cantilever beam with a tip mass. Assessment of other nonlinear aspects of this system, such as, saturation, jumps, hysteresis and chaos, is important when considering other potential applications for such systems, such as multi-directional actuation or energy harvesting. To this end, we perform a detailed analysis of an autoparametric system to show the effects of different parameters, such as the amplitude and frequency of the excitation force, the damping coefficient and frequency of the attached cantilever beam and tip mass, on the nonlinear response of the system.

3.1 Modeling of autoparametric vibration system

The autoparametric absorber system considered here is similar to the one considered by Haxton and Barr [19] and consists of a base structure and a beam with a tip mass. The base structure of this system is subjected to an external force $F(t)$, as shown in figure 3.1. This structure undergoes a vertical displacement x_d and has a stiffness k_2 and damping coefficient c_2. One local coordinate $x - y$ is chosen to be fixed on the top of the base structure. The horizontal motion of the cantilever beam is denoted by $y(s)$, where s represents coordinate along the cantilevered beam.

To establish the governing equation, we use the extended Hamilton's principle [78] which is written as

$$\int_{t_1}^{t_2} (\delta T - \delta V + \delta W_{nc}) dt = 0 \tag{3.1}$$

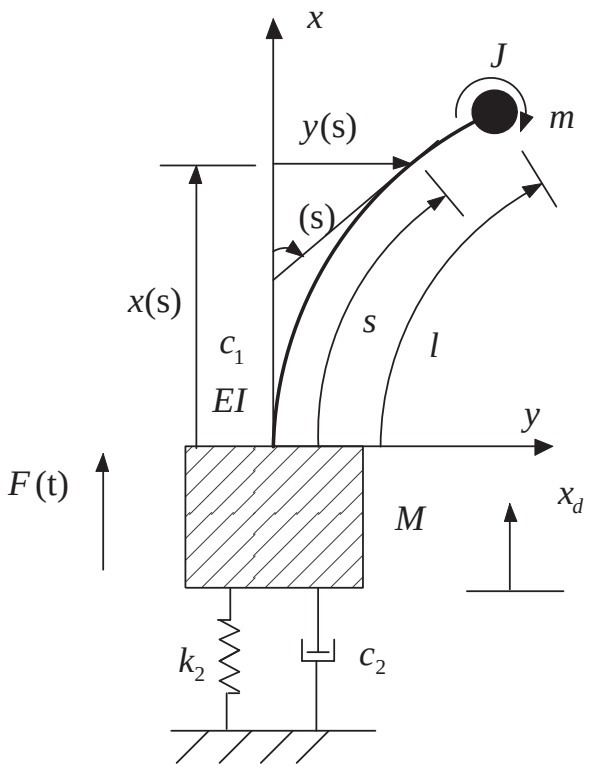

Figure 3.1: Schematic diagram of autoparametric absorber system

where, T, V and W_{nc} are respectively the kinetic energy, potential energy and virtual work due to the nonconservative forces. Inspecting figure 3.1, the kinetic energy T and potential energy V are respectively expressed as

$$T = \tfrac{1}{2}M\dot{x}_d^2 + \tfrac{1}{2}m[\dot{x}_d + \tfrac{d}{dt}(-l + x(l))]^2 + \tfrac{1}{2}\int_0^l \rho[\dot{x}_d + \tfrac{d}{dt}(-s + x(s))]^2 ds$$
$$+\tfrac{1}{2}m\dot{y}(l)^2 + \tfrac{1}{2}J\dot{y}'(l)^2 + \tfrac{1}{2}\int_0^l \rho\dot{y}(s)^2 ds$$
and
$$V = \int_0^l \tfrac{1}{2}EI(\theta'(s))^2 ds + \int_0^l \rho g(x_d + x(s) - s)ds + mg(x_d + x(l) - l) + Mgx_d + \tfrac{1}{2}k_2 x_d^2 \tag{3.2}$$

where, m and M are the tip mass and mass of the base structure, respectively, l is the length of the cantilever beam, J is the rotational inertia of the tip mass relative to tip of the cantilever beam, ρ is the mass of the beam per unit length, EI is the stiffness of the cantilever beam, $x(s)$ and $y(s)$ are the vertical and horizontal displacements of the cantilever beam in the local coordinate $x - y$, $\theta(s)$ is the rotational angle of the cantilever beam and $\dot{x}$ and x' are the derivatives of the variable x with time t and distance s, respectively. Inspecting figure 3.1, we note the following geometrical relationship between $y(s)$, $x(s)$ and $\theta(s)$: $y(s) = \int_0^s \sin(\theta(\eta))d\eta$ and $x(s) = \int_0^s \cos(\theta(\eta))d\eta$. Therefore, the component of $\theta'(s)$

and $x(s)$ are written as

$$\begin{aligned}
&\theta'(s) = \frac{y''(s)}{\sqrt{1-y'(s)^2}} \approx y''(s)(1+\tfrac{1}{2}y'(s)^2) \\
&\text{and} \\
&x(s) = \int_0^s \sqrt{1-y'(\eta)^2}d\eta \approx \int_0^s (1-\tfrac{y'(\eta)^2}{2})d\eta
\end{aligned} \tag{3.3}$$

Assuming that the value $y'(s)$ is much smaller than one, substituting Eq. (3.3) into Eq. (3.2), and keeping up to fourth-order terms, we simplify the kinetic energy T and potential energy V to

$$\begin{aligned}
&T = \tfrac{1}{2}M\dot{x}_d^2 + \tfrac{1}{2}m[\dot{x}_d - \tfrac{d}{dt}(\int_0^l \tfrac{y'(\eta)^2}{2}d\eta)]^2 + \tfrac{1}{2}\int_0^l \ \rho[\dot{x}_d - \tfrac{d}{dt}(\int_0^s \tfrac{y'(\eta)^2}{2}d\eta)]^2 ds \\
&+\tfrac{1}{2}m\dot{y}(l)^2 + \tfrac{1}{2}J\dot{y}'(l)^2 + \tfrac{1}{2}\int_0^l \rho\dot{y}(s)^2 ds \\
&\text{and} \\
&V = \int_0^l \tfrac{1}{2}EI(y''(s)^2 + y''(s)^2y'(s)^2)ds + \int_0^l \rho g(x_d - (l-s)\tfrac{y'(s)^2}{2})ds \\
&+mg(x_d - \int_0^l \tfrac{y'(s)^2}{2}ds) + Mgx_d + \tfrac{1}{2}k_2x_d^2
\end{aligned} \tag{3.4}$$

Moreover, inspecting figure 3.1, the virtual work due to nonconservative forces is given by

$$\delta W_{nc} = \int_0^l F_{d1}\delta y(s)ds + F_{d2}\delta x_d(s) + F(t)\delta x_d(s) \tag{3.5}$$

where, $F(t)$ is the external force acting on the base structure, as shown in figure 3.1, and assumed to be $F(t) = Fcos\Omega t$, F_{d1} is the damping force of the cantilever beam whose expression is $F_{d1} = -c_1\dot{y}(s)$ and F_{d2} is the damping force of base structure and written as $F_{d2} = -c_2\dot{x}_d$.

Substituting the expressions of the kinetic energy T, potential energy V and virtual work W_{nc} due to nonconservative forces into equation (3.1), we obtain the dynamic equation of autoparametric vibration system as

$$\begin{aligned}
&\rho\ddot{y} + c_1\dot{y} + EI(y^{IV} + y'^2y^{IV} + 4y'y''y''' + y''^3) + Ny'' \\
&+[-\rho g - \rho\ddot{x}_d + \rho\int_0^s \tfrac{d^2}{dt^2}(\tfrac{y'^2}{2})d\eta - m\ddot{x}_d\delta(s-l) + m\int_0^l \tfrac{d^2}{dt^2}(\tfrac{y'^2}{2})d\eta\delta(s-l)]y' = 0 \\
&\text{and} \\
&(M+m+\overline{m})\ddot{x}_d + c_2\dot{x}_d + k_2x_d - m\int_0^l \tfrac{d^2}{dt^2}(\tfrac{y'^2}{2})ds - \int_0^l \rho\int_0^s \tfrac{d^2}{dt^2}(\tfrac{y'^2}{2})d\eta ds \\
&+(M+m+\overline{m})g = F\cos(\Omega t)
\end{aligned} \tag{3.6}$$

where, $\overline{m}$ is the total mass of the cantilever beam and calculated as $\overline{m} = \int_0^l \rho ds$ and $\delta(x)$ is the Dirac delta function. The expression of N is $N = \rho g(l-s) + mg + m\ddot{x}_d + \rho\ddot{x}_d(l-s) - m\int_0^l \tfrac{d^2}{dt^2}(\tfrac{y'^2}{2})d\eta - \int_s^l \rho\int_0^\xi \tfrac{d^2}{dt^2}(\tfrac{y'^2}{2})d\eta d\xi$. Moreover, inspecting figure 3.1, we note that: $y(0,t) = 0$, $y'(0,t) = 0$, $y(l,t) \neq 0$ and $y'(l,t) \neq 0$. Similarly, upon substituting the kinetic energy T, potential energy V and virtual work W_{nc} due to nonconservative forces into the

extended Hamilton's equation (3.1), the boundary conditions of the systems are written as

$$\begin{aligned} &y(0,t)=0, \quad y'(0,t)=0, \\ &EI(y''(l,t)+y'(l,t)^2y''(l,t))+J\ddot{y}'(l,t)=0, \\ &EI(y'''(l,t)+y'(l,t)y''(l,t)^2+y'(l,t)^2y'''(l,t))+mgy'(l,t)-m\ddot{y}(l,t)=0 \end{aligned} \tag{3.7}$$

3.2 Representative reduced-order model

To characterize the nonlinear performance of the autoparametric vibration system, we solve the vibration problem for the distributed-parameter system. To this end, we discretize the motion of the cantilever beam using the Galerkin approach and determine its exact mode shapes. We consider first the free vibration of the cantilever beam, which leads naturally to the eigenvalue problem. Therefore, we drop the damping and nonlinear coupling terms in the first equation of (3.6) to obtain

$$\rho\ddot{y}+EIy^{IV}+mgy''+\rho g(l-s)y''-\rho gy'=0 \tag{3.8}$$

Next, we separate the horizontal displacement $y(x,t)$ into spatial and time variables as

$$y(x,t)=\sum_{i=1}^{\infty}\phi_i(x)q_{di}(t) \tag{3.9}$$

where, $q_{di}(t)$ and $\phi_i(x)$ are the modal coordinates and shapes of the cantilever beam with the tip mass, respectively. The modal shape is expressed as [79]

$$\phi_i(x)=A_i\sin\beta_ix+B_i\cos\beta_ix+C_i\sinh\beta_ix+D_i\cosh\beta_ix \tag{3.10}$$

where A_i, B_i, C_i and D_i are the coefficients and are determined by the boundary equation (3.7). To determine the orthogonality conditions of the modal shapes, we use the linearized boundary conditions. These conditions are:

$$\begin{aligned} &\phi_i(0)=0, \quad \phi_i'(0)=0, \\ &EI\phi_i''(l)-\omega_i^2J\phi_i'(l)=0, \\ &EI\phi_i'''(l)+mg\phi_i'(l)+\omega_i^2m\phi_i(l)=0 \end{aligned} \tag{3.11}$$

Using the linearized dynamic equation and linearized boundary conditions, the eigenfunctions are normalized by the following expression:

$$\begin{aligned} &\int_0^l\rho\phi_b(s)\phi_r(s)ds+m\phi_b(l)\phi_r(l)+J\phi_b{}'(l)\phi_r{}'(l)=\delta_{br} \\ &\int_0^l EI\phi_b{}''(s)\phi_r{}''(s)ds-\int_0^l mg\phi_b{}'(s)\phi_r{}'(s)ds-\int_0^l\rho g(l-s)\phi_b{}'(s)\phi_r{}'(s)ds=\delta_{br}\omega_r^2 \end{aligned} \tag{3.12}$$

where b and r are used to represent the vibration modes, ω_r is the rth natural frequency of the cantilever beam, and δ_{br} is the Kronecker delta, defined as unity when b is equal to r and zero otherwise.

Considering Eq. (3.9), Eq. (3.12) and the first mode shape of the cantilever beam, we rewrite the governing equations (3.6) of the autoparametric vibration system as

$$\begin{aligned} &\ddot{q}_d + \eta_1\dot{q}_d + \omega_1^2 q_d + \eta_2 q_d^3 + \eta_3 q_d(\dot{q}_d^2 + q_d\ddot{q}_d) - \eta_4\ddot{x}_d q_d = 0 \\ &\text{and} \\ &(M+m+\overline{m})\ddot{x}_d + c_2\dot{x}_d + k_2 x_d - \eta_4(\dot{q}_d^2 + q_d\ddot{q}_d) + (M+m+\overline{m})g = F\cos(\Omega t) \end{aligned} \tag{3.13}$$

where, $q_d(t)$ is the first modal coordinate and $\phi(s)$ is the first modal shape. The coefficients η_1, η_2, η_3 and η_4 are expressed as $\eta_1 = \int_0^l c_1\phi^2 ds$, $\eta_2 = \int_0^l EI(\phi\phi'^2\phi^{IV} + 4\phi\phi'\phi''\phi''' + \phi\phi''^3)ds$, $\eta_3 = m\Big(\int_0^l \phi'^2 ds\Big)^2 + \int_0^l \rho(\int_0^s \phi'(\eta)^2 d\eta)^2 ds$ and $\eta_4 = m\int_0^l \phi'^2 ds + \int_0^l \rho\int_0^s \phi'(\eta)^2 d\eta ds$. In the considered system, the mass of the beam is very small compared to the tip mass m [19]. Thus, we neglect the terms considering the effect of the mass of beam ρ in the expressions of η_i. The coefficients η_3 and η_4 can then be simplified to $\eta_3 = m\Big(\int_0^l \phi'^2 ds\Big)^2$ and $\eta_4 = m\int_0^l \phi'^2 ds$. Furthermore, to nondimensionalize the governing equation, we choose the static displacement of the system $X_0 = \frac{(M+m+\overline{m})g}{k_2}$ as the basic variable. The governing equation (3.13) is then simplified to:

$$\begin{aligned} &\ddot{q} + 2\varepsilon\mu_1\dot{q} + \omega_1^2 q + \delta_1\varepsilon^2 q^3 + R\varepsilon^2 q(\dot{q}^2 + q\ddot{q}) - \varepsilon\ddot{x}q = 0 \\ &\text{and} \\ &\ddot{x} + 2\varepsilon\mu_2\dot{x} + \omega_2^2 x - \varepsilon(\dot{q}^2 + q\ddot{q}) = F_0\cos(\Omega t) \end{aligned} \tag{3.14}$$

where the new nondimensional displacements q and x are given by $q = \frac{q_d}{\sqrt{m+M+\overline{m}}X_0}$ and $x = \frac{x_d+X_0}{X_0}$, ω_2 is the natural frequency of base structure and is given by $\omega_2 = \sqrt{\frac{k_2}{m+M+\overline{m}}}$, μ_1 and μ_2 are respective damping coefficients of attached beam and base structure and the expressions of these two values are: $\mu_1 = \frac{\eta_1}{2\varepsilon}$ and $\mu_2 = \frac{c_2}{2\varepsilon(m+M+\overline{m})}$, the ratio of the mass R is $\frac{M+m+\overline{m}}{m}$, small nondimensional coefficient ε is $X_0\eta_4$, the coefficient δ_1 is $\frac{(M+m+\overline{m})\eta_2}{\eta_4^2}$ and the nondinemensional amplitude of force F_0 is $\frac{F}{(M+m+\overline{m})X_0}$.

3.3 Approximate solution

We use the method of mutiple sacles [80, 81] to determine an approximate solution of the governing equations and assess the system's stability and bifurcation points. So, we define new time variables as:

$$T_n = \varepsilon^n t, \quad n = 0, 1, 2 \tag{3.15}$$

where T_0 is a fast-time scale, and T_1 and T_2 are slow-time scales. Because the original independent time scale t has been replaced by the new independent time scales T_0, T_1 and T_2, the derivatives with respect to t are changed to:

$$\begin{array}{l} \frac{d}{dt} = D_0 + \varepsilon D_1 + \varepsilon^2 D_1 + \vartheta(\varepsilon^3) \\ \frac{d^2}{dt^2} = D_0^2 + 2\varepsilon D_0 D_1 + \varepsilon^2(D_1 + 2D_0 D_2) + \vartheta(\varepsilon^3) \end{array} \tag{3.16}$$

where $D_i = \partial/\partial T_i$ and $\vartheta(\varepsilon^3)$ indicates order 3 of ε or higher. Then, we write $q = u_1$ and $x = u_2$, follow Nayfeh [80] and write the solutions as

$$u_j(t;\varepsilon) = u_{j0}(T_0, T_1, T_2) + \varepsilon u_{j1}(T_0, T_1, T_2) + \varepsilon^2 u_{j2}(T_0, T_1, T_2) + \vartheta(\varepsilon^3) \tag{3.17}$$

where u_{jk} are functions that depend on T_n and do not depend explicitly on ε, and $j = 1, 2$. To analyze the autoparametric vibration system, we assume the amplitude of the external force to be $F_0 = \varepsilon f$. Then, we substitute equations (3.15), (3.16) and (3.17) into nondimensional governing equation (3.14) and equate the terms with coefficients of equal ε powers to obtain the following set of equations

ε^0 order

$$\begin{array}{l} D_0^2 u_{10} + \omega_1^2 u_{10} = 0 \\ D_0^2 u_{20} + \omega_2^2 u_{20} = 0 \end{array} \tag{3.18}$$

ε^1 order

$$\begin{array}{l} D_0^2 u_{11} + \omega_1^2 u_{11} = -2D_0 D_1 u_{10} - 2\mu_1 D_0 u_{10} + u_{10} D_0^2 u_{20} \\ D_0^2 u_{21} + \omega_2^2 u_{21} = -2D_0 D_1 u_{20} - 2\mu_2 D_0 u_{20} + u_{10} D_0^2 u_{10} + (D_0 u_{10})^2 \\ + \frac{1}{2} f e^{iT_0\Omega} + \frac{1}{2} f e^{-iT_0\Omega} \end{array} \tag{3.19}$$

ε^2 order

$$\begin{array}{l} D_0^2 u_{12} + \omega_1^2 u_{12} = -2D_0 D_1 u_{11} - 2\mu_1 D_0 u_{11} - D_1^2 u_{10} - 2D_0 D_2 u_{10} - 2\mu_1 D_1 u_{10} \\ -R u_{10}(D_0 u_{10})^2 + u_{10} D_0^2 u_{21} + 2u_{10} D_0 D_1 u_{20} - R u_{10}^2 D_0^2 u_{10} - \delta_1 u_{10}^3 + u_{11} D_0^2 u_{20} \\ D_0^2 u_{22} + \omega_2^2 u_{22} = -2D_0 D_1 u_{21} - 2\mu_2 D_0 u_{21} - D_1^2 u_{20} - 2D_0 D_2 u_{20} - 2\mu_2 D_1 u_{20} \\ +2D_0 u_{10} D_0 u_{11} + 2D_0 u_{10} D_1 u_{10} + 2u_{10} D_0 D_1 u_{10} + u_{11} D_0^2 u_{10} + u_{10} D_0^2 u_{11} \end{array} \tag{3.20}$$

The solution of equation (3.18) is of the form as:

$$u_{j0} = A_j(T_1, T_2) e^{\mathbf{i}\omega_j T_0} + cc \tag{3.21}$$

where $\mathbf{i} = \sqrt{-1}$, A_1 and A_2 are complex amplitudes of the displacements of cantilever beam and base structure depending on the slow time scales, respectively, cc stands for the complex conjugate, and $j = 1, 2$. Moreover, to determine the values of A_1 and A_2, we express the nearness of Ω to ω_2 and of ω_1 to $\frac{1}{2}\omega_2$ by using the detuning parameters σ_1 and σ_2 as

follows:

$$\begin{aligned}\Omega &= \omega_2 + \varepsilon\sigma_1 \\ \omega_1 &= \tfrac{1}{2}\omega_2 + \varepsilon\sigma_2\end{aligned} \tag{3.22}$$

Based on the above frequency relationship of ω_1, ω_2 and Ω and substituting equation (3.21) into the ε^1 order equation (3.19), we obtain D_1A_1 and D_1A_2 from the secular terms as

$$\begin{aligned}D_1A_1 &= -\mu_1A_1 + \tfrac{\mathrm{i}\omega_2^2}{2\omega_1}A_2\overline{A_1}e^{-2\mathrm{i}\sigma_2T_1} \\ D_1A_2 &= -\mu_2A_2 + \tfrac{\mathrm{i}\omega_1^2}{\omega_2}A_1^2e^{2\mathrm{i}\sigma_2T_1} - \tfrac{\mathrm{i}f}{4\omega_2}e^{\mathrm{i}\sigma_1T_1}\end{aligned} \tag{3.23}$$

Moreover, u_{11} and u_{21} are determined by eliminating the secular terms, which yields:

$$\begin{aligned}u_{11} &= \tfrac{\omega_2}{2\omega_1+\omega_2}A_1A_2e^{\mathrm{i}(\omega_1+\omega_2)T_0} + B_1(T_1,T_2)e^{\mathrm{i}\omega_1T_0} + cc \\ u_{21} &= B_2(T_1,T_2)e^{\mathrm{i}\omega_2T_0} + cc\end{aligned} \tag{3.24}$$

where B_1 and B_2 are complex amplitudes of the displacements of the cantilever beam, u_{11}, and base structure, u_{21}, depending on the slow time scales, respectively. Then, substituting equations (3.21) and (3.24) into ε^2 order equation (3.20), we obtain the following expressions for D_2A_1 and D_2A_2

$$\begin{aligned}&D_2A_1 = -D_1B_1 - \mu_1B_1 + \tfrac{\mathrm{i}}{2\omega_1}D_1^2A_1 + \tfrac{\mathrm{i}\mu_1}{\omega_1}D_1A_1 + \tfrac{\mathrm{i}(3\delta_1-2R\omega_1^2)}{2\omega_1}A_1^2\overline{A_1} + \tfrac{\omega_2}{\omega_1}\overline{A_1}D_1A_2e^{-2\mathrm{i}\sigma_2T_1} \\ &+\tfrac{\mathrm{i}\omega_2^2}{2\omega_1}\overline{A_1}B_2e^{-2\mathrm{i}\sigma_2T_1} + \tfrac{\mathrm{i}\omega_2^3}{2\omega_1(2\omega_1+\omega_2)}A_1A_2\overline{A_2} + \tfrac{\mathrm{i}\omega_2^2}{2\omega_1}A_2\overline{B_1}e^{-2\mathrm{i}\sigma_2T_1} \\ &D_2A_2 = -D_1B_2 - \mu_2B_2 + \tfrac{2\omega_1}{\omega_2}A_1D_1A_1e^{2\mathrm{i}\sigma_2T_1} + \tfrac{\mathrm{i}}{2\omega_2}D_1^2A_2 + \tfrac{\mathrm{i}\mu_2}{\omega_2}D_1A_2 + \tfrac{2\mathrm{i}\omega_1^2}{\omega_2}A_1B_1e^{2\mathrm{i}\sigma_2T_1} \\ &+\tfrac{\mathrm{i}\omega_2^2}{2(2\omega_1+\omega_2)}A_1A_2\overline{A_1}\end{aligned} \tag{3.25}$$

To determine the time variations of the complex amplitudes A_1 and A_2, we write the above equations in the form of complex-valued modulation equations that are given by

$$\begin{aligned}2\mathrm{i}\omega_1\dot{A}_1 &= 2\mathrm{i}\omega_1(\varepsilon D_1A_1 + \varepsilon^2D_2A_1) \\ 2\mathrm{i}\omega_2\dot{A}_2 &= 2\mathrm{i}\omega_2(\varepsilon D_1A_2 + \varepsilon^2D_2A_2)\end{aligned} \tag{3.26}$$

where the dot indicates the derivative with respect to time t. To derive equations (3.26) from a Lagrangian, we write B_1 and B_2 in equation (3.25) as

$$\begin{aligned}B_1 &= (\lambda_1 + \mathbf{i}\lambda_2)D_1A_1 \\ B_2 &= (\lambda_3 + \mathbf{i}\lambda_4)D_1A_2\end{aligned} \tag{3.27}$$

where, λ_j are real values and $\mathbf{i} = \sqrt{-1}$. Substituting equations (3.23), (3.25) and (3.27) into equation (3.26) and letting $\mu_1 = \mu_2 = f = 0$ (non-conservative force), we simplify the

complex-valued modulation equation (3.26) to

$$\begin{aligned} 2\mathrm{i}\omega_1\dot{A}_1 &= b_1A_1^2\overline{A_1} + b_2e^{-2\mathrm{i}\sigma_2T_1}A_2\overline{A_1} + b_3A_1A_2\overline{A_2} \\ 2\mathrm{i}\omega_2\dot{A}_2 &= b_4e^{2\mathrm{i}\sigma_2T_1}A_1^2 + b_5A_1A_2\overline{A_1} \end{aligned} \tag{3.28}$$

To satisfy the Lagrangian condition, the coefficients p_i should have the following relationships: $b_2 = 2b_4$ and $b_3 = b_5$. Based on the above two expressions, the coefficients λ_i are determined as $\lambda_1 = 0$, $\lambda_2 = \frac{1}{2\omega_1+\omega_2}$, $\lambda_3 = 0$ and $\lambda_4 = \frac{8\omega_1^4-4\omega_1^3\omega_2-8\omega_1^2\omega_2^2-2\omega_1\omega_2^3+\omega_2^4}{16\omega_1^4\omega_2+8\omega_1^3\omega_2^2}$. Substituting equations (3.23), (3.25) and (3.27) and the expressions of coefficients λ_i into equation (3.26), we obtain complex-valued modulation equations

$$\begin{aligned} &\dot{A}_1 = (m_{11}+\mathbf{i}m_{12})A_1 + (m_{21}+\mathbf{i}m_{22})A_2\overline{A_1}e^{-2\mathbf{i}\varepsilon\sigma_2t} + (m_{31}+\mathbf{i}m_{32})A_1^2\overline{A_1} \\ &+(m_{41}+\mathbf{i}m_{42})A_1A_2\overline{A_2} + (m_{51}+\mathbf{i}m_{52})f\overline{A_1}e^{\mathbf{i}\varepsilon(\sigma_1-2\sigma_2)t} \\ &\text{and} \\ &\dot{A}_2 = (n_{11}+\mathbf{i}n_{12})A_2 + (n_{21}+\mathbf{i}n_{22})fe^{\mathbf{i}\varepsilon\sigma_1t} + (n_{31}+\mathbf{i}n_{32})A_1^2e^{2\mathbf{i}\varepsilon\sigma_2t} \\ &+(n_{41}+\mathbf{i}n_{42})A_1A_2\overline{A_1} \end{aligned} \tag{3.29}$$

where the coefficients m_{jk} and n_{jk} are given by
$m_{11} = -\varepsilon\mu_1$, $m_{12} = -\frac{\varepsilon^2\mu_1^2}{2\omega_1}$, $m_{21} = -\frac{\varepsilon^2\omega_2\left(16\mu_1\omega_1^3\omega_2+\mu_2\left(24\omega_1^4+20\omega_1^3\omega_2+4\omega_1^2\omega_2^2+2\omega_1\omega_2^3-\omega_2^4\right)\right)}{16\omega_1^4(2\omega_1+\omega_2)}$, $m_{22} = \frac{\varepsilon\omega_2^2\left(4\omega_1^2+4\omega_1\omega_2-\omega_2^2\right)}{4\omega_1^2(2\omega_1+\omega_2)}$, $m_{31} = 0$, $m_{32} = \frac{\varepsilon^2\left(-8(-3+4R)\omega_1^4-4(-5+4R)\omega_1^3\omega_2+4\omega_1^2\omega_2^2+2\omega_1\omega_2^3-\omega_2^4+24\delta_1\omega_1(2\omega_1+\omega_2)\right)}{16\omega_1^2(2\omega_1+\omega_2)}$,
$m_{41} = 0$, $m_{42} = \frac{\varepsilon^2\omega_2^3\left(4\omega_1^2-2\omega_1\omega_2+\omega_2^2\right)}{8\omega_1^3(2\omega_1+\omega_2)}$, $m_{51} = 0$, $m_{52} = -\frac{\varepsilon^2\left(24\omega_1^4+20\omega_1^3\omega_2+4\omega_1^2\omega_2^2+2\omega_1\omega_2^3-\omega_2^4\right)}{64\omega_1^4(2\omega_1+\omega_2)}$, $n_{11} = -\varepsilon\mu_2$, $n_{12} = -\frac{\varepsilon^2\mu_2^2}{2\omega_2}$, $n_{21} = \frac{\varepsilon^2\mu_2}{8{\omega_2}^2}$, $n_{22} = \frac{\varepsilon\left(-16\omega_1^4+8\omega_1^3(\Omega-2\omega_2)+8\omega_1^2(\Omega-\omega_2)\omega_2+2\omega_1(\Omega-\omega_2)\omega_2^2+\omega_2^3(-\Omega+\omega_2)\right)}{32\omega_1^3\omega_2(2\omega_1+\omega_2)}$,
$n_{31} = -\frac{\varepsilon^2\left(\mu_1\omega_2^3(-2\omega_1+\omega_2)+2\mu_2\omega_1^3(2\omega_1+\omega_2)\right)}{4\omega_1\omega_2^2(2\omega_1+\omega_2)}$, $n_{32} = \frac{\varepsilon\omega_2\left(4\omega_1^2+4\omega_1\omega_2-\omega_2^2\right)}{8\omega_1(2\omega_1+\omega_2)}$, $n_{41} = 0$ and $n_{42} = \frac{\varepsilon^2\omega_2^2\left(4\omega_1^2-2\omega_1\omega_2+\omega_2^2\right)}{8\omega_1^2(2\omega_1+\omega_2)}$.
When we assume $\mu_1 = \mu_2 = f = 0$ (non-conservative force), the complex-valued modulation equations without the effect of non-conservative force are given by

$$\begin{aligned} &2\mathbf{i}\omega_1\dot{A}_1 = -2\omega_1m_{32}A_1^2\overline{A_1} - 2\omega_1m_{22}e^{-2\mathbf{i}\sigma_2T_1}A_2\overline{A_1} - 2\omega_1m_{42}A_1A_2\overline{A_2} \\ &\text{and} \\ &2\mathbf{i}\omega_2\dot{A}_2 = -2\omega_2n_{32}e^{2\mathbf{i}\sigma_2T_1}A_1^2 - 2\omega_2n_{42}A_1A_2\overline{A_1} \end{aligned} \tag{3.30}$$

These equations are derivable from the Lagrangian

$$\begin{aligned} &L = 2\mathbf{i}\omega_1(A_1\overline{A}_1 - \overline{A}_1\dot{A}_1) + 2\mathbf{i}\omega_2(A_2\overline{A}_2 - \overline{A}_2\dot{A}_2) + \frac{\varepsilon\omega_2^2\left(-4\omega_1^2-4\omega_1\omega_2+\omega_2^2\right)}{4\omega_1(2\omega_1+\omega_2)}(A_2\overline{A}_1^2e^{-2\mathbf{i}\sigma_2T_1} + A_1^2\overline{A}_2e^{2\mathbf{i}\sigma_2T_1}) \\ &-\frac{\varepsilon^2\omega_2^3\left(4\omega_1^2-2\omega_1\omega_2+\omega_2^2\right)}{4\omega_1^2(2\omega_1+\omega_2)}A_1A_2\overline{A}_1\overline{A}_2 + \frac{\varepsilon^2\left(8(-3+4R)\omega_1^4+4(-5+4R)\omega_1^3\omega_2-4\omega_1^2\omega_2^2-2\omega_1\omega_2^3+\omega_2^4-24\delta_1\omega_1(2\omega_1+\omega_2)\right)}{16\omega_1(2\omega_1+\omega_2)}A_1^2\overline{A}_1^2 \end{aligned} \tag{3.31}$$

From the above two equation, we can find that $n_{32} = \frac{\omega_1}{2\omega_2}m_{22}$ and $n_{42} = \frac{\omega_1}{\omega_2}m_{42}$.

A_1 and A_2 are complex-valued quantities. So, we choose the polar form to express these two

variables as:

$$A_j = \tfrac{1}{2} a_j(t) e^{\mathbf{i}\alpha_j(t)} \quad for \quad j = 1, 2 \tag{3.32}$$

In this expression, a_j and α_j are the amplitudes and phases of A_j. In fact, a_1 and a_2 are also the amplitudes of q and x shown in nondimenional governing equation (3.14), respectively. Substituting equation (3.32) into the complex-valued modulation equations (3.29) and separating the real and imaginary parts, we obtain the following averaged equation:

$$\begin{aligned}
&\dot{a}_1 = m_{11}a_1 + \tfrac{1}{2}m_{21}a_1a_2\cos\gamma_1 + \tfrac{1}{2}m_{22}a_1a_2\sin\gamma_1 + \tfrac{1}{4}m_{31}a_1^3 + \tfrac{1}{4}m_{41}a_1a_2^2 \\
&+m_{51}fa_1\cos(\gamma_1-\gamma_2) + m_{52}fa_1\sin(\gamma_1-\gamma_2) \\
&a_1\dot{\alpha}_1 = m_{12}a_1 - \tfrac{1}{2}m_{21}a_1a_2\sin\gamma_1 + \tfrac{1}{2}m_{22}a_1a_2\cos\gamma_1 + \tfrac{1}{4}m_{32}a_1^3 + \tfrac{1}{4}m_{42}a_1a_2^2 \\
&-m_{51}fa_1\sin(\gamma_1-\gamma_2) + m_{52}fa_1\cos(\gamma_1-\gamma_2) \\
&\text{and} \\
&\dot{a}_2 = n_{11}a_2 + 2n_{21}f\cos\gamma_2 - 2n_{22}f\sin\gamma_2 + \tfrac{1}{2}n_{31}a_1^2\cos\gamma_1 \\
&-\tfrac{1}{2}n_{32}a_1^2\sin\gamma_1 + \tfrac{1}{4}n_{41}a_1^2a_2 \\
&a_2\dot{\alpha}_2 = n_{12}a_2 + 2n_{21}f\sin\gamma_2 + 2n_{22}f\cos\gamma_2 + \tfrac{1}{2}n_{31}a_1^2\sin\gamma_1 \\
&+\tfrac{1}{2}n_{32}a_1^2\cos\gamma_1 + \tfrac{1}{4}n_{42}a_1^2a_2
\end{aligned} \tag{3.33}$$

where $\gamma_1 = 2\alpha_1 - \alpha_2 + 2\varepsilon\sigma_2 t$ and $\gamma_2 = \varepsilon\sigma_1 t - \alpha_2$. The equilibrium solutions of equation (3.33) are obtained by setting $\dot{a}_1 = \dot{a}_2 = 0$ and $\dot{\gamma}_1 = \dot{\gamma}_2 = 0$. Based on the relationship between γ_i and α_i discussed above, $\dot{\alpha}_1$ and $\dot{\alpha}_2$ can be calculated as: $\dot{\alpha}_1 = \varepsilon(\frac{\sigma_1}{2} - \sigma_2)$ and $\dot{\alpha}_2 = \varepsilon\sigma_1$. The fixed point of the autoparametric vibration system can be determined:

$$\begin{aligned}
&0 = m_{11}a_1 + \tfrac{1}{2}m_{21}a_1a_2\cos\gamma_1 + \tfrac{1}{2}m_{22}a_1a_2\sin\gamma_1 + \tfrac{1}{4}m_{31}a_1^3 + \tfrac{1}{4}m_{41}a_1a_2^2 \\
&+m_{51}fa_1\cos(\gamma_1-\gamma_2) + m_{52}fa_1\sin(\gamma_1-\gamma_2) \\
&\varepsilon(\tfrac{\sigma_1}{2} - \sigma_2)a_1 = m_{12}a_1 - \tfrac{1}{2}m_{21}a_1a_2\sin\gamma_1 + \tfrac{1}{2}m_{22}a_1a_2\cos\gamma_1 + \tfrac{1}{4}m_{32}a_1^3 + \tfrac{1}{4}m_{42}a_1a_2^2 \\
&-m_{51}fa_1\sin(\gamma_1-\gamma_2) + m_{52}fa_1\cos(\gamma_1-\gamma_2) \\
&\text{and} \\
&0 = n_{11}a_2 + 2n_{21}f\cos\gamma_2 - 2n_{22}f\sin\gamma_2 + \tfrac{1}{2}n_{31}a_1^2\cos\gamma_1 \\
&-\tfrac{1}{2}n_{32}a_1^2\sin\gamma_1 + \tfrac{1}{4}n_{41}a_1^2a_2 \\
&\varepsilon\sigma_1 a_2 = n_{12}a_2 + 2n_{21}f\sin\gamma_2 + 2n_{22}f\cos\gamma_2 + \tfrac{1}{2}n_{31}a_1^2\sin\gamma_1 \\
&+\tfrac{1}{2}n_{32}a_1^2\cos\gamma_1 + \tfrac{1}{4}n_{42}a_1^2a_2
\end{aligned} \tag{3.34}$$

3.4 Stability and bifurcation

Inspecting the first two equations in (3.34), we note that all terms contain the variable a_1. As such, $a_1 = 0$ yield the fixed-point equations that are identities [82, 83]. Subsequently, the polar form cannot be used to analyze the system's stability. To analyze the stability of the equilibrium points, we use the Cartesian form:

$$A_j = \tfrac{1}{2}(p_j(t) - \mathbf{i}q_j(t))e^{\mathbf{i}\theta_j(t)} \quad for \quad j = 1, 2 \tag{3.35}$$

In this expression, the variables p_j and q_j are functions of a_1, a_2, γ_1 and γ_2 which are determined from equations (3.22), (3.32), (3.35) and the definitions of γ_1 and γ_2 as [83]

$$\begin{aligned} p_1 &= a_1 \cos\tfrac{\gamma_2-\gamma_1}{2} \\ q_1 &= a_1 \sin\tfrac{\gamma_2-\gamma_1}{2} \\ p_2 &= a_2 \cos\gamma_2 \\ q_2 &= a_2 \sin\gamma_2 \end{aligned} \tag{3.36}$$

Substituting equation (3.35) into the complex-valued modulation equation (3.29) and separating the real and imaginary parts, we obtain the Cartesian form of the modulation equations as

$$\begin{aligned} &\dot{p}_1 = \tfrac{1}{2}\epsilon(2\sigma_2-\sigma_1)q_1 + m_{11}p_1 + m_{12}q_1 + \tfrac{1}{2}m_{21}(p_1p_2+q_1q_2) + \tfrac{1}{2}m_{22}(p_1q_2-p_2q_1) + \tfrac{1}{4}m_{31}(p_1^3+p_1q_1^2) \\ &+\tfrac{1}{4}m_{32}(p_1^2q_1+q_1^3) + \tfrac{1}{4}m_{41}(p_1p_2^2+p_1q_2^2) + \tfrac{1}{4}m_{42}(p_2^2q_1+q_1q_2^2) + m_{51}fp_1 - m_{52}fq_1 \\ &\dot{q}_1 = -\tfrac{1}{2}\epsilon(2\sigma_2-\sigma_1)q_1 + m_{11}q_1 - m_{12}p_1 + \tfrac{1}{2}m_{21}(p_1q_2-p_2q_1) - \tfrac{1}{2}m_{22}(p_1p_2+q_1q_2) + \tfrac{1}{4}m_{31}(p_1^2q_1+q_1^3) \\ &-\tfrac{1}{4}m_{32}(p_1^3+p_1q_1^2) + \tfrac{1}{4}m_{41}(p_2^2q_1+q_1q_2^2) - \tfrac{1}{4}m_{42}(p_1p_2^2+p_1q_2^2) - m_{51}fq_1 - m_{52}fp_1 \\ &\text{and} \\ &\dot{p}_2 = -\epsilon\sigma_1q_2 + n_{11}p_2 + n_{12}q_2 + 2n_{21}f + \tfrac{1}{2}n_{31}(p_1^2-q_1^2) + n_{32}p_1q_1 + \tfrac{1}{4}n_{41}(p_1^2p_2+p_2q_1^2) \\ &+\tfrac{1}{4}n_{42}(p_1^2q_2+q_1^2q_2) \\ &\dot{q}_2 = \epsilon\sigma_1p_2 + n_{11}q_2 - n_{12}p_2 - 2n_{22}f + n_{31}p_1q_1 - \tfrac{1}{2}n_{32}(p_1^2-q_1^2) + \tfrac{1}{4}n_{41}(p_1^2q_2+q_1^2q_2) \\ &-\tfrac{1}{4}n_{42}(p_1^2p_2+p_2q_1^2) \end{aligned} \tag{3.37}$$

In this equation, we have made use of $2\theta_1-\theta_2+2\varepsilon\sigma_2 t = 2n\pi$, $\varepsilon\sigma_1 t-\theta_2 = 2m\pi$, $\dot{\theta}_1 = \varepsilon\frac{\sigma_1-2\sigma_2}{2}$ and $\dot{\theta}_2 = \varepsilon\sigma_1$ [83], where, m and n are integers.

Inspecting equation (3.34), we identify two types of solutions: (1) $a_1 = 0$ and $a_2 \neq 0$ and (2) $a_1 \neq 0$ and $a_2 \neq 0$. The stability of these fixed points can be analyzed by the Jacobian matrix of the Cartesian form of the modulation equations (3.37). If the four eigenvalues λ_i have negative real parts, then the fixed point is stable. Otherwise, the equilibrium point will form a saddle point. Note that the Cartesian form of the equilibrium point (p_1, p_2, p_3, p_4) is needed to determine the Jacobian matrix of Cartesian form of the modulation equations (3.37), which can be obtained using Eq. (3.36). Four types of motions are identified. The first type is $a_1 = 0$ and $a_2 \neq 0$. This solution corresponds to the case where the attached cantilever beam moves with the base structure (the base structure and the cantilever beam basically form a rigid body). The second type is obtained when $a_1 \neq 0$ and $a_2 \neq 0$. In this case, the cantilever beam undergoes a horizontal motion in addition to that induced by the base structure. Because part of the energy has been transfered to the horizontal motion of the beam, the amplitude of vertical motion of the base structure is reduced. This solution is desired to control the vertical motion of the base structure. It can also be used to obtain actuation in the horizontal direction from a vertical excitation. In a third type of motion, both fixed points are stable. Both masses could undergo different motions depending on the

initial conditions. The system exhibits interesting nonlinear phenomena, such as jumps and hysteresis. In the fourth type, none of the fixed points is stable and the system may undergo Hopf bifurcations and could become chaotic.

3.5 Results and discussion

Next, we perform numerical integration to determine the response of the system under different excitation conditions. We also use the above solution to unravel the physics associated with the determined solutions. Particularly, we are interested in evaluating the effects of different parameters on the motions of the base structure and the attached beam. Analyzing the different responses is important for enabling the use of such systems in different applications. For example, some parameters, such as the amplitude F and frequency Ω of the external force, are determined by the environmental vibration source. Other parameters (e.g. tip mass) can be adjusted to control the motion of the base structure. Moreover, if energy is to be harvested from the vibration by attaching piezoelectric sheets to the cantilever beam, the coupled mechanical damping coefficient μ_1 and natural frequency ω_1 of the cantilever beam will be strongly affected by the external load resistance [79, 84].

3.5.a Effect of amplitude of the external force

In figure 3.2, we show amplitudes of the displacements of the base structure and the cantilever beam as a function of the non-dimensional external force f for different values of σ_2 when the other non-dimensional parameters are fixed as follows: $\varepsilon = 0.005$, $\omega_2 = 45.35 rad/s$, $R = 6.2$, $\delta_1 = -R\omega_1^2$, $\varepsilon\mu_1 = 0.0035\omega_1$, $\varepsilon\mu_2 = 0.0035\omega_2$ and $\varepsilon\sigma_1 = 0.25$. The solid lines correspond to sinks (stable solutions) and the dashed lines indicate saddles (unstable solutions). The plots in figure 3.2(a,b) show the system's response for the case of $\varepsilon\sigma_2 = 0.125$. These plots show that, when f is small, the system's response is similar to that of a linear vibrational system. In this case, the base structure and attached beam form a rigid body and the vertical displacement of the system a_2 increases linearly as f is increased. However, when f exceeds a certain threshold, the nonlinear response becomes prevalent and the horizontal motion of the tip mass is initiated. As f is increased further, a_2 remains almost constant and a_1 increases monotonically. This phenomenon, known as modal saturation [85], shows that the increased energy due to the external forcing of the base structure is absorbed by the attached beam which is very useful to control the vibration of base structures. Furthermore, beyond a critical value of f, a supercritical pitchfork bifurcation appears as shown in figure 3.2(a). Through validation with the numerical integration of the non-dimensional governing equations (3.14), we determine that the first-order perturbation solution is not accurate because it does not account for the effects of the cubic terms of the governing equations

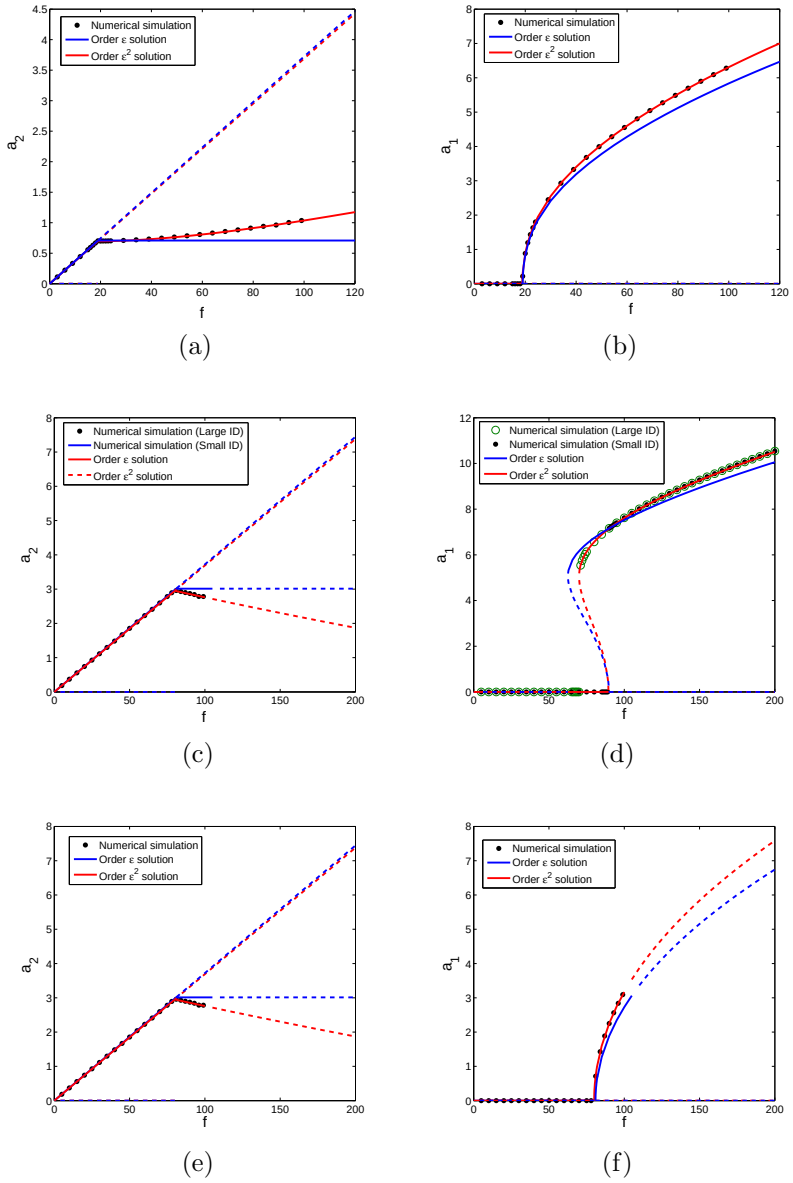

Figure 3.2: Force-response curves ((a, c, e) amplitude of displacement of base structure and (b, d, f) amplitude of horizontal displacement of the tip mass attached cantilever beam) for different $\varepsilon = 0.005$, $\omega_2 = 45.35 rad/s$, $R = 6.2$, $\delta_1 = -R\omega_1^2$, $\varepsilon\mu_1 = 0.0035\omega_1$, $\varepsilon\mu_2 = 0.0035\omega_2$ and $\varepsilon\sigma_1 = 0.25$: (a, b), $\varepsilon\sigma_2 = 0.125$, (b,c) $\varepsilon\sigma_2 = -0.25$ and (c,d) $\varepsilon\sigma_2 = 0.45$. ID denotes initial displacements. The dashed lines are used to denote unstable solutions and the solid line are used to denote stable solution. Different types of motions are identified depending on the forcing amplitude and detuning between the frequencies of the base structure and beam-tip mass system.

(3.14). The second order solution gives results that agree well with the numerical results but shows a deviation from a perfect saturation phenomenon.

When $\varepsilon\sigma_2 = -0.25$, the response of the system is similar to that of the case $\varepsilon\sigma_2 = 0.125$ except that there exists multiple stable solutions in the range between $f = 70.1$ and $f = 89.5$. The system's response exhibits some special nonlinear phenomena, including jumps and hysteresis, as shown in figure 3.2(c,d). The plot in figure 3.2(c) shows that, as f increases, a_2 first increases linearly until $f = 89.5$. At that level, it undergoes a jump and increases slightly as the forcing amplitude f is increased. However, as f is reduced, a_2 remains constant until $f = 70.1$. At that point, the amplitude of a_2 drops to the level obtained when f was increased and decreases further as f is decreased. This phenomenon is also demonstrated by the numerical integration of Eq. (3.14) with different initial displacements. Similar nonlinear phenomena, jumps and hysteresis, are noted in figure 3.2(d). Moreover, saddle-node and subcritical pitchfork bifurcations appear at the critical points near $f = 70.1$ and $f = 89.5$, respectively, as shown in figure 3.2(c).

As the detuning is increased to $\varepsilon\sigma_2 = 0.45$, the nonlinear response is initiated at higher f values than the case of $\varepsilon\sigma_2 = 0.125$. Only a_2 is nonzero and increases linearly as f is increased up to $f = 80$, as shown in figure 3.2(e, f). As f is increased further, a_1 increases while a_2 decreases slightly due to the effect of the cubic nonlinearity. However, as f reaches the value of 100, there are no more stable equilibrium points for both a_1 and a_2. In this situation, the system's response undergoes a Hopf bifurcation and becomes chaotic, which will be discussed in section 3.5.f. In summary, the system's response is highly dependent on the forcing amplitude and detuning parameters which is discussed further in the next section.

3.5.b Effect of frequency of the external force

Next, we analyze the effects of the excitation frequency on the nonlinear response of the autoparametric vibration system by varying the detuning parameter σ_1. We do so by considering different cases of detuning between the primary and secondary systems, namely, $\varepsilon\sigma_2$: 0, 0.5, -0.5, 1 and -1. The results are presented in figures 3.3, 3.4 and 3.5. In these cases, the other parameters are fixed to $\varepsilon = 0.005$, $f = 400$, $\omega_2 = 45.35 rad/s$, $R = 6.2$, $\delta_1 = -R\omega_1^2$, $\varepsilon\mu_1 = 0.0035\omega_1$ and $\varepsilon\mu_2 = 0.0035\omega_2$.

Figure 3.3 shows the frequency response of the system for the case of $\varepsilon\sigma_2 = 0$. Compared with numerical simulation, the first-order perturbation solution does not give an accurate representation of the nonlinear responses because the nonlinear cubic effects are neglected. Including these effects, the second-order perturbation method leads to more accurate responses that are validated with the numerical integration. Three kinds of motions are discerned from the plots. These are (1) the linear motion of rigid body ($a_1 = 0$) when

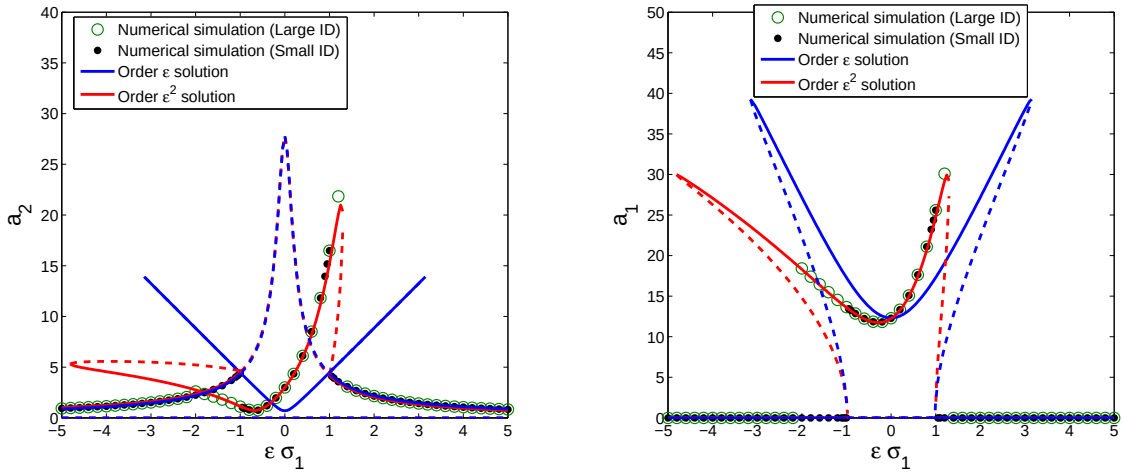

(a) (b)

Figure 3.3: Frequency-response curves for $\varepsilon = 0.005$, $f = 400$, $\omega_2 = 45.35 rad/s$, $R = 6.2$, $\delta_1 = -R\omega_1^2$, $\varepsilon\mu_1 = 0.0035\omega_1$, $\varepsilon\mu_2 = 0.0035\omega_2$ and $\varepsilon\sigma_2 = 0$ (no detuning between base structure and beam-tip mass system): (a) Vertical displacement of base structure and (b) Horizontal displacement of the tip mass attached cantilever beam. ID denotes initial displacements. The dashed lines are used to denote unstable solutions and the solid line are used to denote stable solution. Depending on the values of $\varepsilon\sigma_1$ which represents the detuning between the frequencies of the excitations and base structure, the system exhibits different responses that include rigid-body like motions and energy transfer to the secondary mode. This transfer is highly dependent on the initial displacements. The method of multiple scales shows a small basin of attraction away from resonance when the system is activated with a large initial condition.

$\varepsilon\sigma_1 < -4.8$ and $\varepsilon\sigma_1 > 1.3$, (2) a regime where both motions are different than zero for $-0.98 < \varepsilon\sigma_1 < 1.005$, and (3) a regime where the motions depend on the initial conditions when $-4.8 < \varepsilon\sigma_1 < -0.98$ and $1.005 < \varepsilon\sigma_1 < 1.3$. Inspecting figure 3.3(a), as $\varepsilon\sigma_1$ is increased, the response of a_2 increases ('rigid-body' motion) until $\varepsilon\sigma_1 = -0.98$. At that point, there is a jump up in the amplitude of a_1 (as noted from the green dots), indicating energy transfer from the base to the beam. As $\varepsilon\sigma_1$ is increased further, a_2 decreases to a minimum value when $\varepsilon\sigma_1 = -0.65$, then increases as $\varepsilon\sigma_1$ is increased to 1.3. At that level, it jumps back down indicating a recovery of the 'rigid-body' motion. Approaching from the high frequency range, as $\varepsilon\sigma_1$ is decreased, a_2 increases ('rigid-body' motion) until $\varepsilon\sigma_1 = 1.005$ (as noted from the green points), then it jumps up. It then decreases and increases again until $\varepsilon\sigma_1 = -4.8$ with a minimum near $\varepsilon\sigma_1 = -0.65$. As $\varepsilon\sigma_1$ is decreased to values less than -4.8, the 'rigid-body' motion is recovered. We note that the response of a_1 has the same jumps and hysteresis in figure 3.3(b). It is important to note here that, as we consider the numerical integration of the governing equation (3.14), the numerical results using small ini-

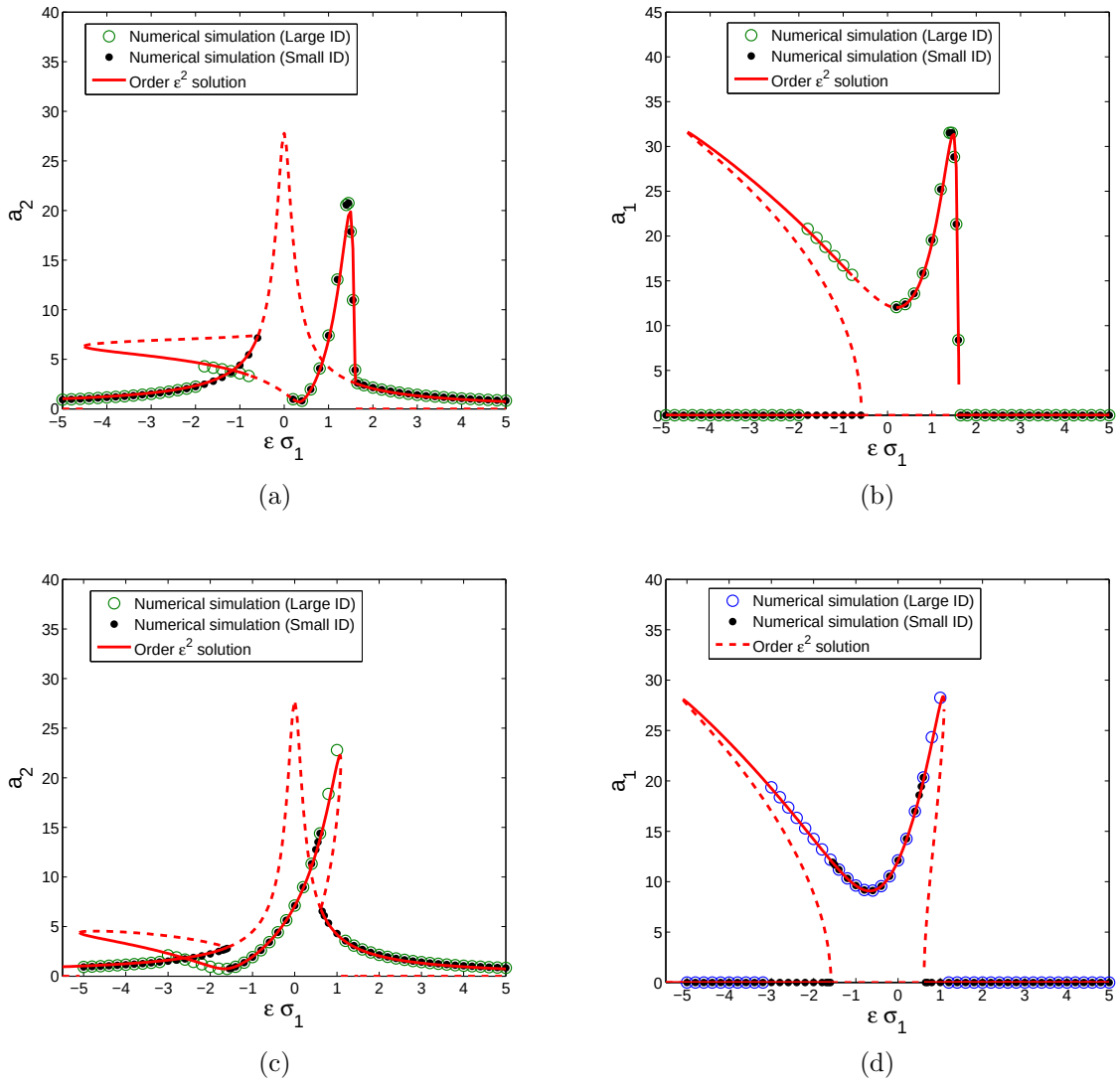

Figure 3.4: Frequency-response curves for different values of σ_2 for $\varepsilon = 0.005$, $f = 400$, $\omega_2 = 45.35 rad/s$, $R = 6.2$, $\delta_1 = -R\omega_1^2$, $\varepsilon\mu_1 = 0.0035\omega_1$ and $\varepsilon\mu_2 = 0.0035\omega_2$ ((a ,b) $\varepsilon\sigma_2 = 0.5$ and (c, d) $\varepsilon\sigma_2 = -0.5$): amplitude of (a, c) vertical displacements of the base structure and (b, d) horizontal displacements of the tip mass attached the cantilever beam. ID denotes initial displacements. The dashed lines are used to denote unstable solutions and the solid line are used to denote stable solution. The plots show qualitatively similar responses for the cases $\varepsilon\sigma_2 = 0$ and $\varepsilon\sigma_2 = -0.5$. However, the case $\varepsilon\sigma_2 = 0.5$ shows an additional unstable regime.

tial displacements exactly match those obtained with the method of multiple scales. On the other hand, numerical simulations using large initial displacements fail to show the interac-

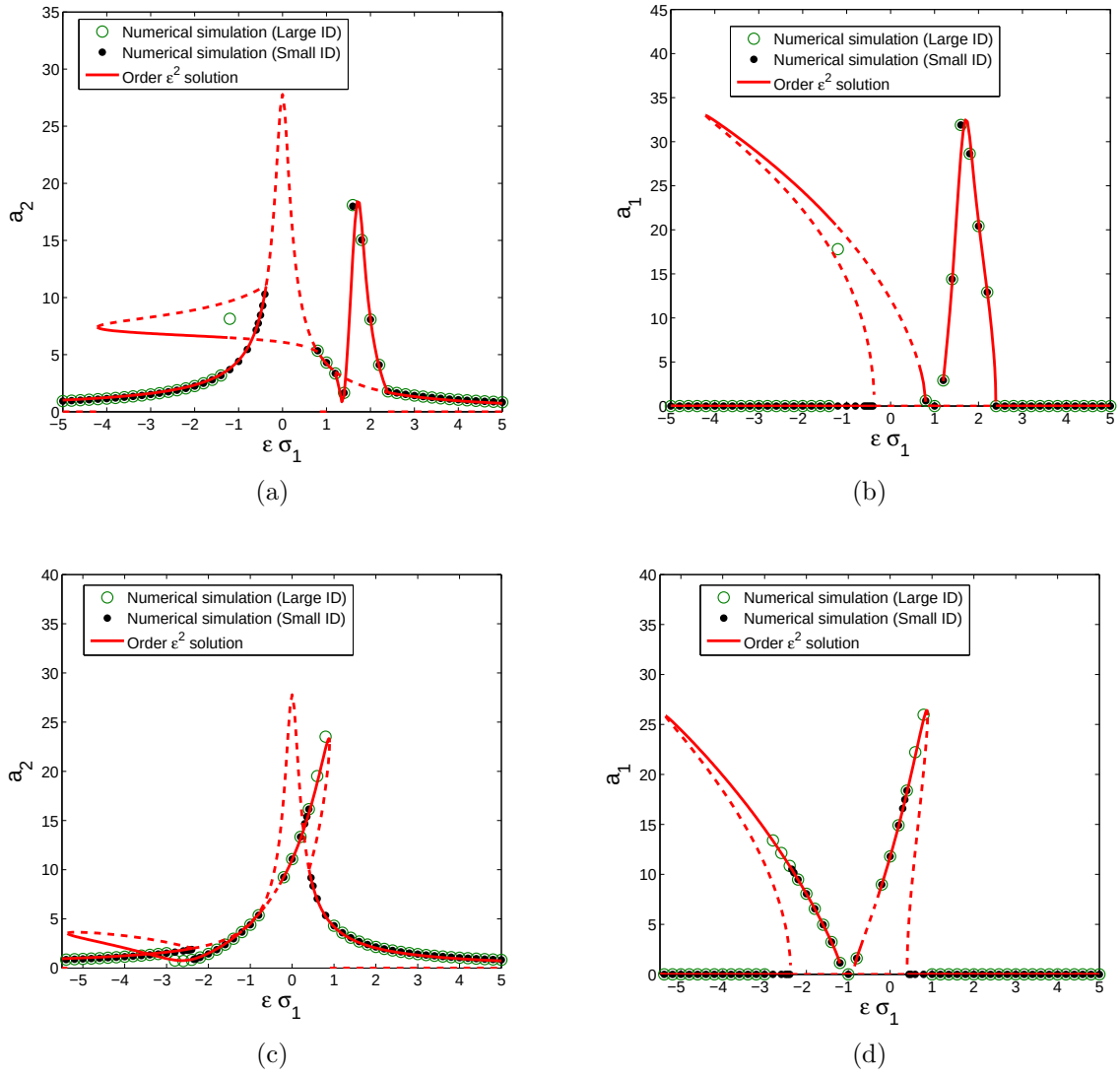

Figure 3.5: Frequency-response curves at different values of σ_2 for $\varepsilon = 0.005$, $f = 400$, $\omega_2 = 45.35 rad/s$, $R = 6.2$, $\delta_1 = -R\omega_1^2$, $\varepsilon\mu_1 = 0.0035\omega_1$ and $\varepsilon\mu_2 = 0.0035\omega_2$ ((a ,b) $\varepsilon\sigma_2 = 1$ and (c, d) $\varepsilon\sigma_2 = -1$): amplitude of (a, c) vertical displacements of the tip mass attached the base structure and (b, d) horizontal displacements of the cantilever beam. ID denotes initial displacements. The dashed lines are used to denote unstable solutions and the solid line are used to denote stable solution. The plots show similar qualitative responses to the cases considered in figure 3.4.

tion between the base structure and the cantilever beam when $|\sigma_1|$ is relatively large because the basin of attraction of the fixed point $a_1 \neq 0$ is narrow. The system exhibits asymmetric responses for the jump and hysteresis as discussed above (i.e. $-4.8 < \varepsilon\sigma_1 < -0.98$ and

$1.005 < \varepsilon\sigma_1 < 1.3$). This asymmetric response is mainly due to the effect of cubic terms for the different responses between first-order (symmetric) and second-order perturbations (asymmetric). In addition to the jumps and hysteresis in the range of $-4.8 < \varepsilon\sigma_1 < -0.98$ and $1.005 < \varepsilon\sigma_1 < 1.3$, there are some interesting characteristics for engineering applications, such as, energy harvesting from the vibration system. If the system is activated with large initial displacements, the amplitude of the horizontal displacement of the tip mass increases even if the external frequency is away from the natural frequency of the base structure (away from the resonance), as shown in figure 3.3(b). This phenomenon shows the possibility for energy harvesting even if the resonance requirement is not met. However, this needs to be investigated from a global perspective because adding the harvester and electric load affects the global system's parameters. For validation of control purposes, this system exhibits a minimum displacement of the base structure when $\varepsilon\sigma_1 = -0.65$ (i.e., the external frequency is very close to the natural frequency). Moreover, The amplitudes of a_2 are much smaller than the ones obtained from linear analysis when $-1.8 < \varepsilon\sigma_1 < 0.55$. Therefore, if the natural frequency of the attached beam is tuned to be close to 1/2 of the natural frequency of the base structure ($\sigma_2 \approx 0$), this autoparametric vibration system will be very effective in suppressing the oscillatory motion of the base structure. Besides good control of base structure near resonance, a relatively large displacement of the cantilevered beam is obtained which can be employed to other engineering applications. In the rest of this Chapter, we will present results from the second order solution only. The reason is that it has been shown above that the first-order solution is deficient.

In figures 3.4 and 3.5, we present the frequency response curves as $\varepsilon\sigma_1$ is varied for the cases of $\varepsilon\sigma_2 = 0.5$, -0.5 and 1 -1, respectively. We note that there exists the same jumps and hysteresis when $\sigma_2 < 0$ with different amplitudes and regimes as the case $\sigma_2 = 0$ discussed above. However, the jumps and hysteresis for the positive value of σ_1 disappear for the positive values of $\varepsilon\sigma_2$; i.e. $\varepsilon\sigma_2 = 0.5$ and $\varepsilon\sigma_2 = 1$. Particularly, we note the fourth type of response is in the case $\varepsilon\sigma_2 = 0.5$. That is, there are no stable fixed points in the range $-0.79 < \varepsilon\sigma_1 < 0.175$. The details of this response will be discussed in section 3.5.f. Besides this difference, we also find that the values of $\varepsilon\sigma_1$ corresponding to the minimum a_2 are changed to 0.35 when $\varepsilon\sigma_2 = 0.5$ and -1.65 when $\varepsilon\sigma_2 = -0.5$. It is concluded that the minimum value of a_2 occurs when $\varepsilon\sigma_1 = 2\varepsilon\sigma_2 - 0.65$. As the natural frequency of the secondary system moves away from 1/2 of frequency of base structure, we find the similar relation $\varepsilon\sigma_1 = 2\varepsilon\sigma_2 - 0.65$ at which the minimum value of a_2 occurs, that is, $\varepsilon\sigma_1 = 1.35$ when $\varepsilon\sigma_2 = 1$ and $\varepsilon\sigma_1 = -2.65$ and $\sigma_2 = -1$. It is also noted that the range of $\varepsilon\sigma_1$ for which both kinds of fixed points are unstable increases as $|\varepsilon\sigma_2|$ is increased. Moreover, for $0.8 < \varepsilon\sigma_1 < 1.1$ when $\varepsilon\sigma_2 = 1$ and $-1.15 < \varepsilon\sigma_1 < -0.9$ when $\varepsilon\sigma_2 = -1$, the fixed point of nonlinear interaction between the base structure and attached cantilever beam disappears and the unstable linear rigid-body motion is stabilized. This phenomenon is also demonstrated by numerical integration of the governing equations (3.14), as shown in figure 3.5.

3.5.c Effect of frequency of cantilever beam

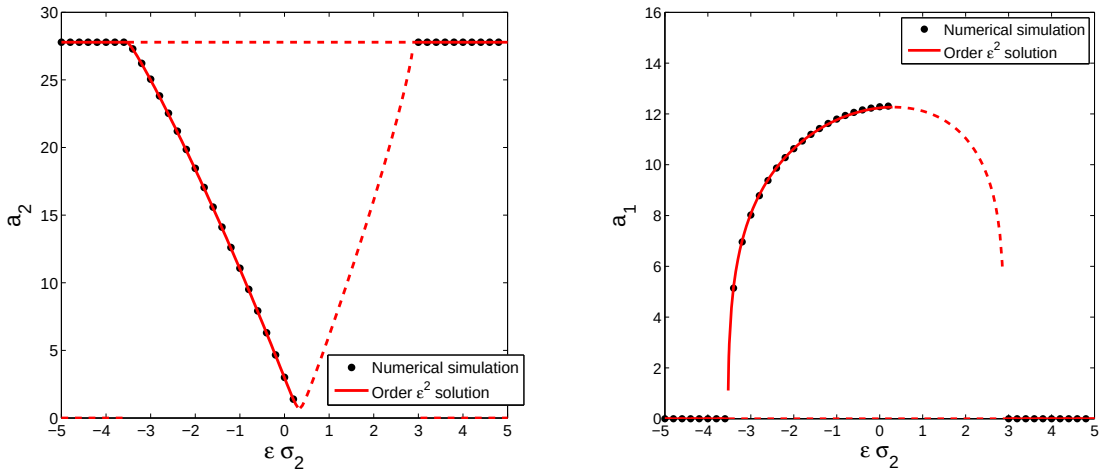

(a) (b)

Figure 3.6: Frequency-response curves when σ_2 is varied when $\varepsilon = 0.005$, $f = 400$, $\omega_2 = 45.35 rad/s$, $R = 6.2$, $\delta_1 = -R\omega_1^2$, $\varepsilon\mu_1 = 0.0035\omega_1$, $\varepsilon\mu_2 = 0.0035\omega_2$ and $\varepsilon\sigma_1 = 0$: (a) Vertical displacement of base structure and (b) Horizontal displacement of the tip mass attached cantilever beam. The dashed lines are used to denote unstable solutions and the solid line are used to denote stable solution. The plots show rigid body-like motion for large absolute values of $\varepsilon\sigma_2$ and effective control over the range where $\varepsilon\sigma_2$ is negative and unstable motions for positive values of $\varepsilon\sigma_2$.

To better understand how to tune the parameters of the autoparametric vibration system, it is necessary to study the effects of varying the frequency of the cantilever beam on the nonlinear response of the system. According to equation (3.22), the variation of the frequency of the cantilever beam can be expressed by the parameter $\varepsilon\sigma_2$. Therefore, we analyze the effects of the parameter $\varepsilon\sigma_2$ on the nonlinear characteristics of system for different values at $\varepsilon\sigma_1$, namely, 0, 0.5, -0.5, 1 and -1, as shown in figures 3.6, 3.7 and 3.8. In these cases, the other parameters are fixed to: $\varepsilon = 0.005$, $f = 400$, $\omega_2 = 45.35 rad/s$, $R = 6.2$, $\delta_1 = -R\omega_1^2$, $\varepsilon\mu_1 = 0.0035\omega_1$ and $\varepsilon\mu_2 = 0.0035\omega_2$.

The variation of the displacement amplitudes for the base structure and tip mass with $\varepsilon\sigma_2$, for the cases of $\varepsilon\sigma_1 = 0$, are plotted in figure 3.6. We note that the system behaves as a linear oscillator with the base structure and attached beam forming a rigid body and moving vertically ($a_1 = 0$) over the ranges $\varepsilon\sigma_2 < -3.55$ and $\varepsilon\sigma_2 > 2.95$. Increasing $\varepsilon\sigma_2$ from -3.55 to 0.25, the resonant amplitude of base structure a_2 decreases from 27.79 to 0.778 and the displacement of the tip mass a_1 increases from 0 to 12.27. Under these conditions, an autoparametric vibration system is useful to control of the base structure or obtain multiple

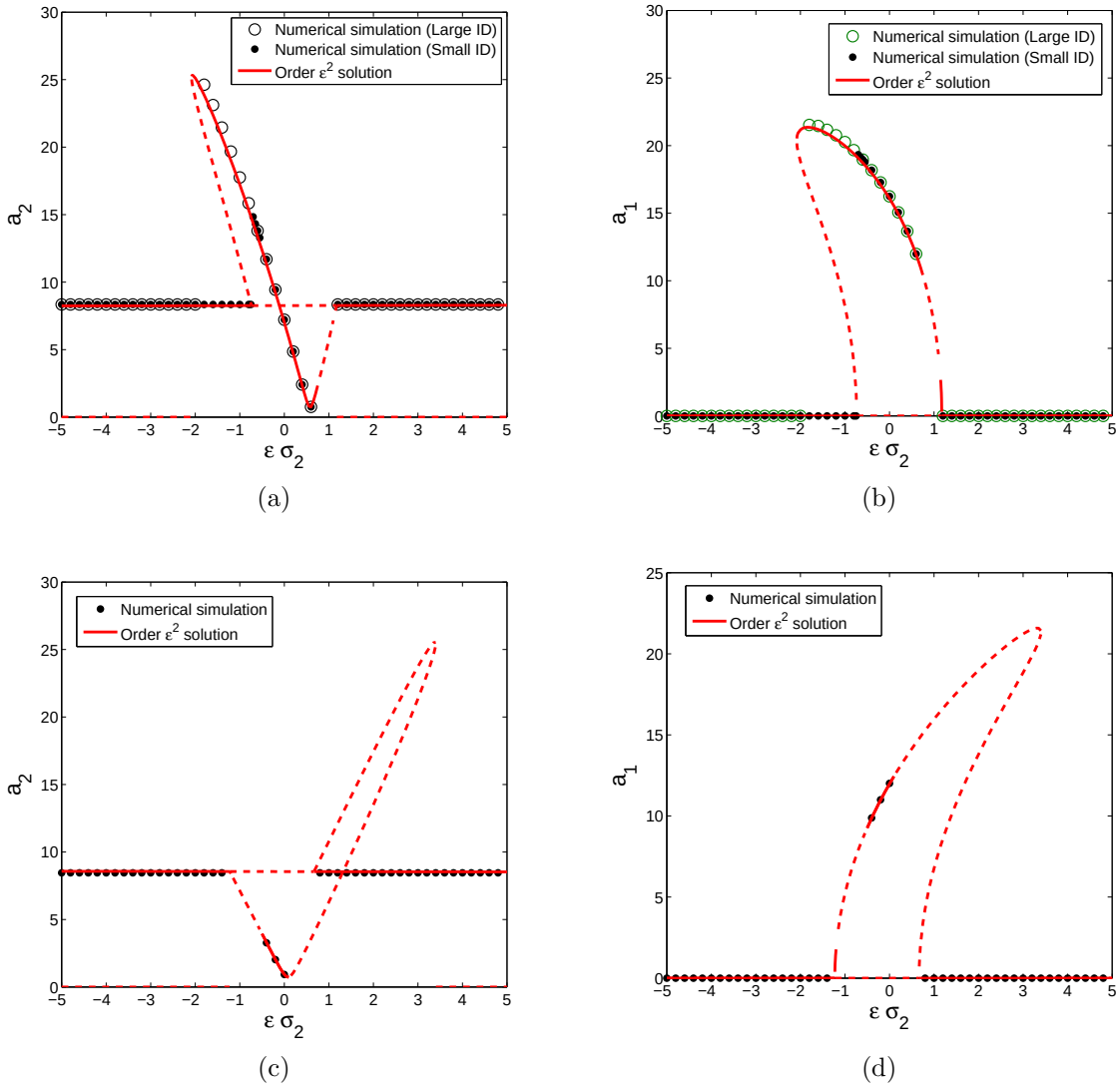

Figure 3.7: Frequency-response curves when σ_2 is varied for two different values of σ_1 when other parameters are $\varepsilon = 0.005$, $f = 400$, $\omega_2 = 45.35 rad/s$, $R = 6.2$, $\delta_1 = -R\omega_1^2$, $\varepsilon\mu_1 = 0.0035\omega_1$ and $\varepsilon\mu_2 = 0.0035\omega_2$ ((a ,b) $\varepsilon\sigma_1 = 0.5$ and (c, d) $\varepsilon\sigma_1 = -0.5$): amplitude of (a, c) vertical displacement of base structure and (b, d) horizontal displacement of the cantilever beam. ID denotes initial displacements. The dashed lines are used to denote unstable solutions and the solid line are used to denote stable solution. The plots show stable and unstable solutions with hysteresis.

actuation. Of interest is the notion that as σ_2 is increased further, both fixed points become unstable up to the point where the system recovers its rigid-body-like motion.

Figure 3.7 shows that the responses of the system as a function of the non-dimensional fre-

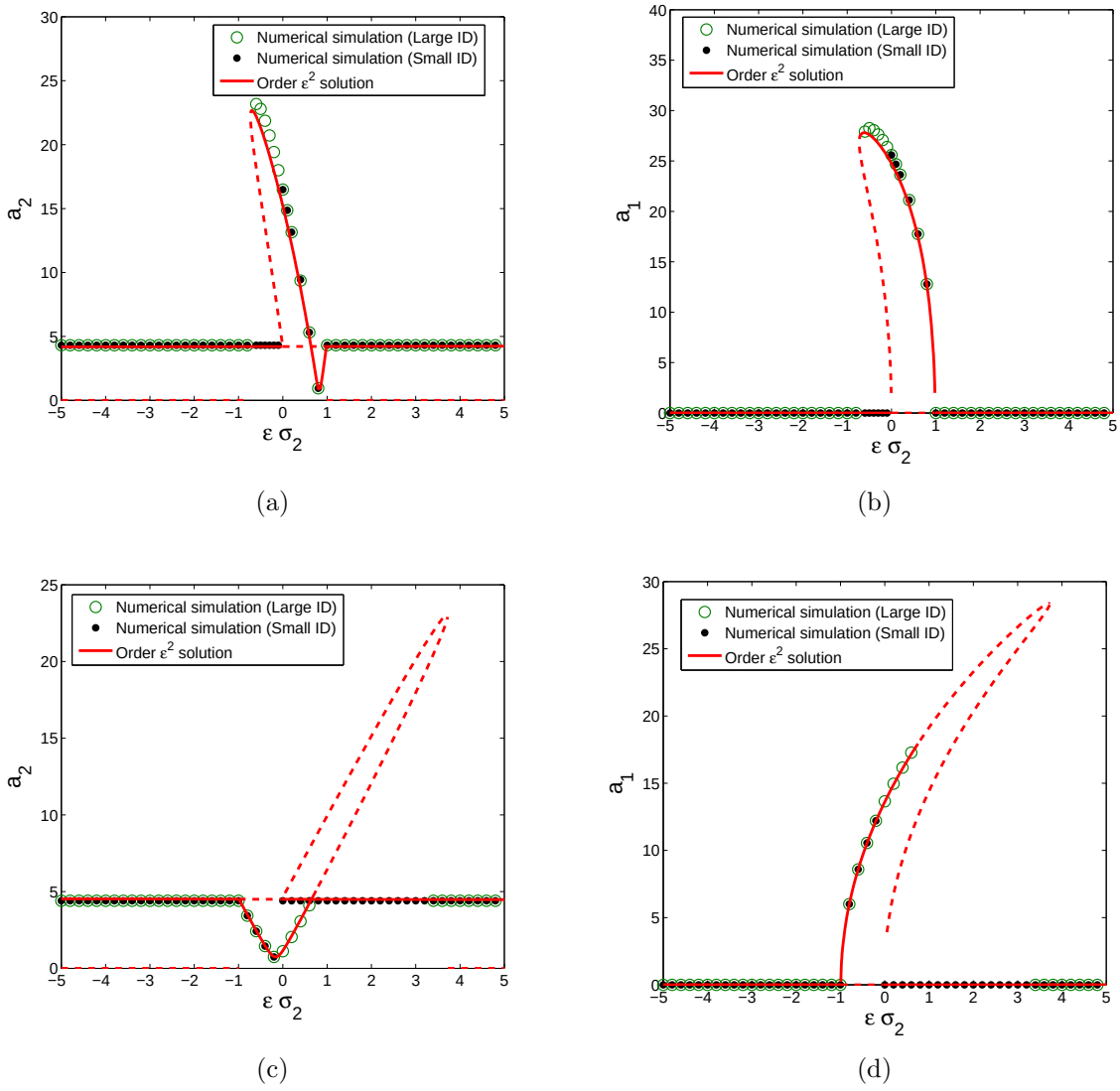

Figure 3.8: Frequency-response curves when σ_2 is varied for two different values of σ_1 when other parameters are $\varepsilon = 0.005$, $f = 400$, $\omega_2 = 45.35 rad/s$, $R = 6.2$, $\delta_1 = -R\omega_1^2$, $\varepsilon\mu_1 = 0.0035\omega_1$ and $\varepsilon\mu_2 = 0.0035\omega_2$ ((a ,b) $\varepsilon\sigma_1 = 1$ and (c, d) $\varepsilon\sigma_1 = -1$): amplitude of (a, c) vertical displacement of base structure and (b, d) horizontal displacement of the cantilevered beam. ID denotes initial displacements. The dashed lines are used to denote unstable solutions and the solid line are used to denote stable solution.

quency of cantilever beam $\varepsilon\sigma_2$ for $\varepsilon\sigma_1 = 0.5$ and -0.5. The plots show that a saddle-node bifurcation occurs at $\varepsilon\sigma_2 = -2.07$ for $\varepsilon\sigma_1 = 0.5$. Moreover, both equilibrium solutions are stable and jumps and hysteresis appear between $\varepsilon\sigma_2 = -2.07$ and -0.74. This is also demonstrated from the numerical simulation with large and small initial displacements presented in

figure 3.7(a,b). Similarly to the case of $\varepsilon\sigma_1 = 0$, the two fixed points become unstable when $0.75 < \varepsilon\sigma_2 < 1.155$. However, this unstable range is much smaller than that for $\varepsilon\sigma_1 = 0$. In the case of $\varepsilon\sigma_1 = -0.5$, the frequency response curve exhibits a reversed response to the one sustained for the case $\varepsilon\sigma_1 = 0.5$. However, except for two unstable equilibrium solutions on left side of the minimum value of a_2, both equilibrium points become unstable on the right side of the minimum value of a_2 similar to the case of $\varepsilon\sigma_1 = 0$. Figure 3.8 shows the frequency response of the autoparametric vibration system for larger values of $\varepsilon\sigma_1$ (1 and -1). The nonlinear phenomenon of the two coexisting unstable fixed points disappears when $\varepsilon\sigma_1 = 1$. For the case of $\varepsilon\sigma_1 = -1$, the range of two coexisting unstable fixed points disappears on the left side of the minimum value of a_2 and decreases on the right side of the minimum value of a_2 compared with case of $\varepsilon\sigma_1 = -0.5$. As expected, the minimum value of a_2 occurs when $\varepsilon\sigma_1 = 2\varepsilon\sigma_2 - 0.65$ for all cases. The corresponding a_2 values are about same for all cases. On the other hand, the maximum a_1 values are higher as $|\varepsilon\sigma_1|$ is increased and is highly dependent on the initial conditions.

3.5.d Effect of damping of the cantilever beam

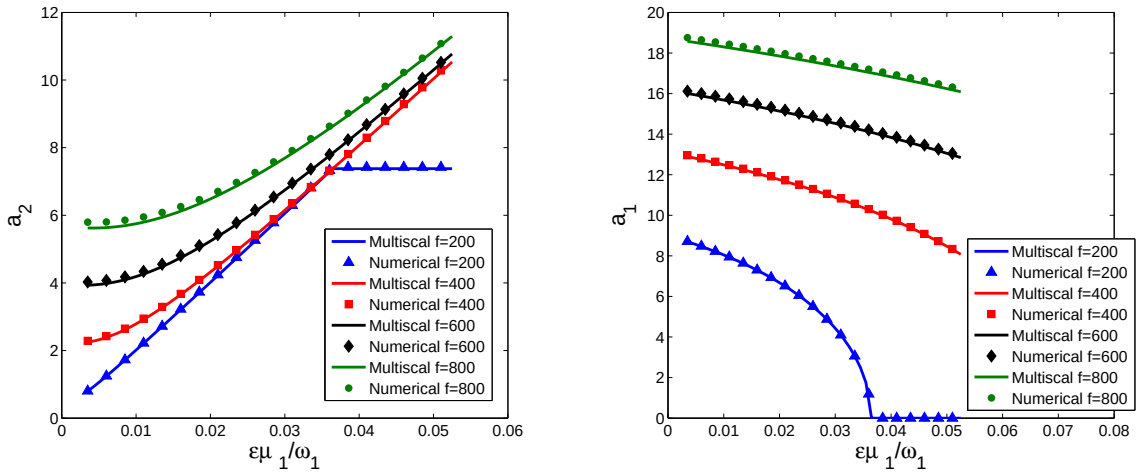

(a) (b)

Figure 3.9: Response variations as a function of the damping ratio of cantilevered beam for different amplitudes of the external force ($f = 200$, 400, 600 and 800) when $\varepsilon = 0.005$, $\omega_2 = 45.35 rad/s$, $R = 6.2$, $\delta_1 = -R\omega_1^2$, $\varepsilon\mu_1 = 0.0035\omega_1$, $\varepsilon\mu_2 = 0.0035\omega_2$ and $\varepsilon\sigma_1 = \varepsilon\sigma_2 = 0.25$: (a) vertical displacement of base structure and (b) horizontal displacement of the cantilever beam.

Next, we investigate the effects of the damping ratio of the cantilever beam on the nonlinear responses of the autoparametric vibration system for four different amplitudes of the external

force (f = 200, 400, 600, and 800). The other parameters are fixed as follows: $\varepsilon = 0.005$, $\omega_2 = 45.35 rad/s$, $R = 6.2$, $\delta_1 = -R\omega_1^2$, $\varepsilon\mu_1 = 0.0035\omega_1$, $\varepsilon\mu_2 = 0.0035\omega_2$ and $\varepsilon\sigma_1 = \varepsilon\sigma_2 = 0.25$. Figure 3.9 shows the response variations of the steady state amplitudes as a function of the damping ratio of the cantilever beam, $\varepsilon\mu_1/\omega_1$, for the different values of f. The plots show that a_2 increases as the external force is increased when the damping ratio $\varepsilon\mu_1/\omega_1$ is relatively small. However, This increase becomes become smaller as the damping ratio $\varepsilon\mu_1/\omega_1$ is increased. It is also noted that a_2 increases and a_1 decreases as the damping ratio of the cantilever beam is increased when f = 400, 600 and 800. For large damping ratios ($\varepsilon\mu_1/\omega_1 > 0.036$) and small external force ($f = 200$), a_2 remains constant and a_1 is equal to 0 as $\varepsilon\mu_1/\omega_1$ varies. Clearly, the damping ratio could be optimized depending on the amplitude of the excitation force and allowed response amplitude.

3.5.e Effects of tip mass m

The ratio of the tip mass to the mass of the base structure is an important design parameter for the autoparametric vibration system. For example, in many cases, a minimum tip mass would be favorable. As such, we analyze the effects of varying the tip mass m on the nonlinear characteristics of the system with different external forces and damping ratios of the cantilever beam, as shown in figure 3.10. The other parameters are chosen as following: $\varepsilon = 0.005$, $k = 2500$, $M = 1$, $\overline{m} = 0.1m$, $\delta_1 = -R\omega_1^2$, $\varepsilon\mu_2 = 0.0035\omega_2$ and $\varepsilon\sigma_1 = \varepsilon\sigma_2 = 0.25$.

Inspecting figure 3.10(a), we note that for all the values of f, the amplitude of the displacement of the base structure decreases as m is increased. The extent of this dependence decreases as m is increased. Figure 3.10(b) shows that the amplitude of the tip mass a_1 is almost independent on the tip mass m for m between 0.1 and 0.35. As the damping ratio $\varepsilon\mu_1/\omega_1$ is increased to 0.0335, we note a similar effect for the tip mass m on the displacements of the base structure a_2. The effective range of the tip mass variation decreases to $m = 0.15$, as shown in figures 3.10(c). Moreover, inspecting 3.10(c) for $f = 200$, the effects of nonlinear interaction between the cantilever beam and base structure increases as the tip mass is increased. For a large damping ratio μ_1 ($\varepsilon\mu_1/\omega_1 = 0.0435$), the effective range for the tip mass variation on the response of the system becomes smaller, as shown in figures 3.10(e). It is of interest to note that for $f = 200$, the displacement of the base structure increases linearly as the tip mass is increased for the cases of $\varepsilon\mu_1/\omega_1 = 0.0335$. This indicates that better control can be obtained with a smaller mass when f is small and $\varepsilon\mu_1/\omega_1$ is above a specific value. From the above discussion, it is noted that the larger the external force is and the smaller the damping ratio of the cantilever beam is, the stronger is the effect of the tip mass m on the nonlinear response.

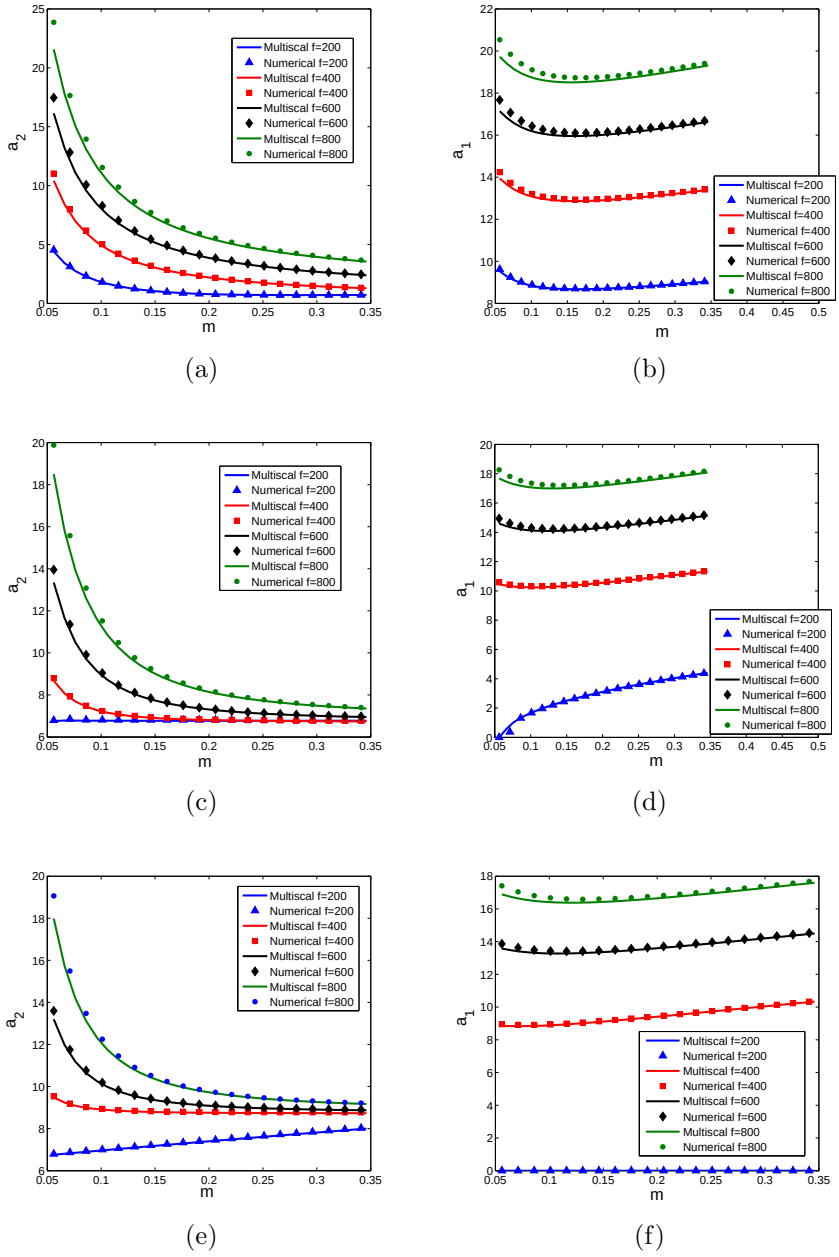

Figure 3.10: Response amplitudes of the base structure (a, c, e) and of of the cantilever beam (b, d, f) as a function of the tip mass m for different values of the external force and damping ratio of the cantilever beam when $\varepsilon = 0.005$, $k = 2500$, $M = 1$, $m = 0.196M$, $\overline{m} = 0.1m$, $\delta_1 = -R\omega_1^2$, $\varepsilon\mu_2 = 0.0035\omega_2$ and $\varepsilon\sigma_1 = \varepsilon\sigma_2 = 0.25$: (a, b) $\varepsilon\mu_1 = 0.0035\omega_1$, (c, d) $\varepsilon\mu_1 = 0.0335\omega_1$ and $\varepsilon\mu_1 = 0.0435\omega_1$.

3.5.f Hopf-bifurcation and chaos

To characterize the unstable responses of the system, we focus on the response variations with $\varepsilon\sigma_1$ when the other parameters are set to $\varepsilon = 0.005$, $f = 400$, $\omega_2 = 45.35 rad/s$, $R = 6.2$, $\delta_1 = -R\omega_1^2$, $\varepsilon\mu_1 = 0.0035\omega_1$, $\varepsilon\mu_2 = 0.0035\omega_2$ and $\varepsilon\sigma_2 = 0.5$. Inspecting figure 3.4, it is noted that both fixed points are unstable when $-0.79 < \varepsilon\sigma_1 < 0.175$. Power spectra, phase portraits and Poincare sections are used to characterize these responses.

Figures 3.11(a, b, c) show the time history, power spectra, phase portrait and Poincare section of displacement of the base structure for $\varepsilon\sigma_1 = -0.8$. All of the results indicate that the displacement of the base structure is periodic. That is, the motion of the base structure is period-1 response. As $\varepsilon\sigma_1$ is increased to -0.785, figure 3.11 (d) shows that time series has three dominant frequencies as they appear in power spectrum, indicating quasi-periodic responses. Figure 3.11 (f) shows that the Poincare map become one elliptical circle and the system become two-torus motion. Comparing figure 3.11 (f) with figure 3.11 (c), we note that a supercritical hopf-bifurcation takes place between $\varepsilon\sigma_1 = -0.8$ and -0.785 because the fixed point of a_2 is changed from stable to unstable in this range of $\varepsilon\sigma_1$. As $\varepsilon\sigma_1$ is increased further to -0.5, the maximum amplitude is much larger than those of $\varepsilon\sigma_1 = -0.8$ and -0.785 as deduced from the time history and portrait map, which are shown in figures 3.11 (g, h). Inspecting the power spectra (figure 3.11 (g)), we find more frequencies than those in cases of $\varepsilon\sigma_1 = -0.8$ and -0.785. Moreover, the attractor is increased to two circles in the Poincare section, as shown in figure 3.11 (i). This indicates that the system has undergone a second Hopf bifurcation.

As $\varepsilon\sigma_1$ is increased to -0.4325, the Poincare section shows four circles and the number of frequencies in the corresponding power spectrum is more than in the case of $\varepsilon\sigma_1 = -0.5$, as shown in figures 3.12(a,b,c). Moreover, the ellipse of attractor gets distorted and the two sides of attractor bench to the left, as shown in figure 3.12(c). This can be considered as a sign for a transition to a chaotic response, as observed by Nayfeh [86]. As $\varepsilon\sigma_1$ is increased slightly to -0.432, the torus in Poincare map is destroyed, as illustrated in figure 3.12 (f). The time history and power spectra in figure 3.12 (d) show that the displacement time variation becomes random and subharmonics of the modulation frequency in the power spectrum are noted. This can be considered as an indication of a period-multiplying bifurcation [86]. Therefore, chaos has emerged as a result of the destruction of the torus when $\varepsilon\sigma_1 = -0.432$. As $\varepsilon\sigma_1$ is increased to -0.3975, the time history exhibits varying amplitudes as shown in figure 3.12(g) with almost no dominant frequency in the corresponding power spectrum (figure 3.12 (g)). Figure 3.12 (i) shows that the points in Poincare section become more random which indicates that the displacement of the base structure has become more chaotic.

As $\varepsilon\sigma_1$ is increased to -0.3905, dominant frequencies reappear in the power spectrum. The time history is much more regular than the one in the case of $\varepsilon\sigma_1 = -0.3975$, as shown in

figure 3.13 (a). Inspecting figure 3.13 (c), one circle appears in Poincare section. As $\varepsilon\sigma_1$ is increased slightly to -0.39, the time history is changed back to a periodic motion and subharmonics of the modulation frequencies disappear. Moreover, the attractor shown in Poincare map forms a one-circle shape, as shown in figure 3.12 (f). Therefore, the motion of the system changes from being chaotic to a periodic motion with multiple frequencies. As $\varepsilon\sigma_1$ is increased further to 0.15, the maximum displacement is reduced to 2.5, as shown in time history and phase portrait in figures 3.13(g,h). It is also noted that the number of dominant frequencies becomes three in the power spectrum and the shape of the attractor becomes elliptic. If we increase $\varepsilon\sigma_1$ further, the motion of the interaction between the base structure and the cantilevered beam will become stable again.

3.6 Conclusion

Nonlinear characterizations of the autoparametric vibration system were analyzed. The governing equations were derived using the extended Hamilton's principle and non-dimensionalized. Then, the method of multiple scales was used to solve for the equilibrium points. The Cartesian form of the modulation equations was then used to determine the stability and bifurcation of these equilibrium points. We identified four types of motion that include (1) only $a_1 = 0$ and $a_2 \neq 0$ is stable where the attached cantilevered beam move with the same motion as the base structure and the system behaves as a rigid body; (2) only $a_1 \neq 0$ and $a_2 \neq 0$ is stable where the strong nonlinear interaction between the base structure and the attached beam occurs; (3) both fixed points are stable where the system undergoes different motions depending on the initial conditions and the system may have some interesting nonlinear phenomena, such as, jumps and hysteresis; and (4) none of fixed point is stable where the system may undergo Hopf bifurcations and even become chaotic. Furthermore, the effects of different parameters, such as the amplitude and frequency of external force, the damping coefficient and frequency of the attached cantilever beam and the tip mass, on the nonlinear responses of the system are analyzed.

We find that the saturation phenomenon occurs as the external force is increased above a certain threshold and is very helpful to control the vibration of the base structure, particularly when the base structure undergoes resonance or near resonance and the frequency of the cantilevered beam is close to 1/2 of the natural frequency of the base structure. Moreover, there exists jumps and hysteresis for a specific range of parameters. Some interesting bifurcations, such as saddle-node, supercritical pitchfork, subcritical pitchfork, reversed saddle-node and reversed saddle-saddle bifurcations, are also observed. we also find that the tip mass has a considerable effect on the nonlinear response of the system, particularly when the damping ratio of the cantilever beam is small and the external force is large. Finally, time history, power spectra, phase portrait and Poincare section were used to analyze the sys-

tem's responses. The results show that responses characterized by Hopf bifurcations and chaos.

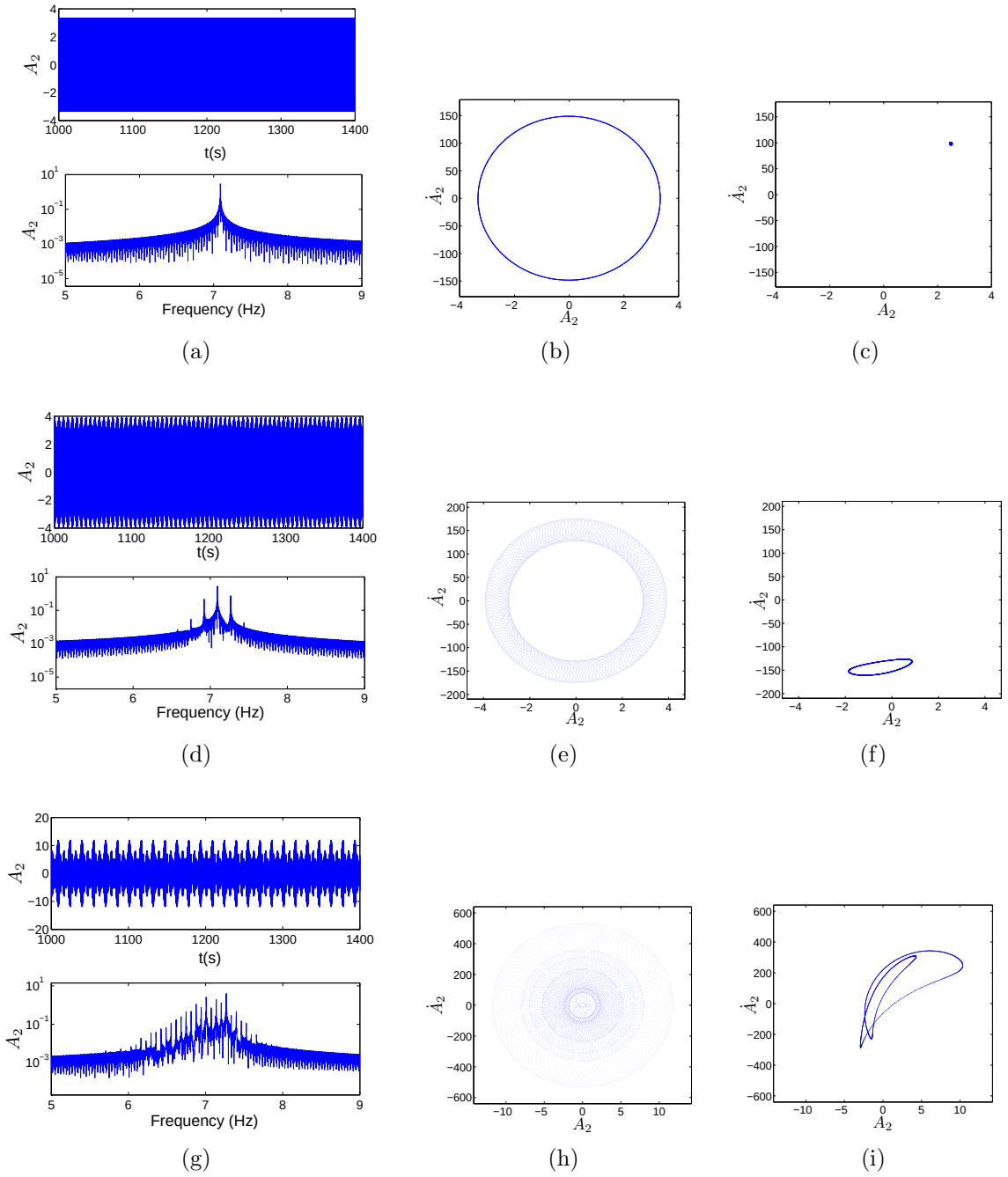

Figure 3.11: (a,d,g) Time histories and power spectra, (b,e,h) phase portraits, and (c,f,i) Poincare sections of the vertical displacement of base structure for different $\varepsilon\sigma_1$ when other parameters are $\varepsilon = 0.005$, $\omega_2 = 45.35 rad/s$, $R = 6.2$, $\delta_1 = -R\omega_1^2$, $\varepsilon\mu_1 = 0.0035\omega_1$, $\varepsilon\mu_2 = 0.0035\omega_2$ and $\varepsilon\sigma_2 = 0.5$: (a, b, c) $\varepsilon\sigma_1 = -0.8$, (b, e, f) $\varepsilon\sigma_1 = -0.785$ and (g, h, i) $\varepsilon\sigma_1 = -0.5$.

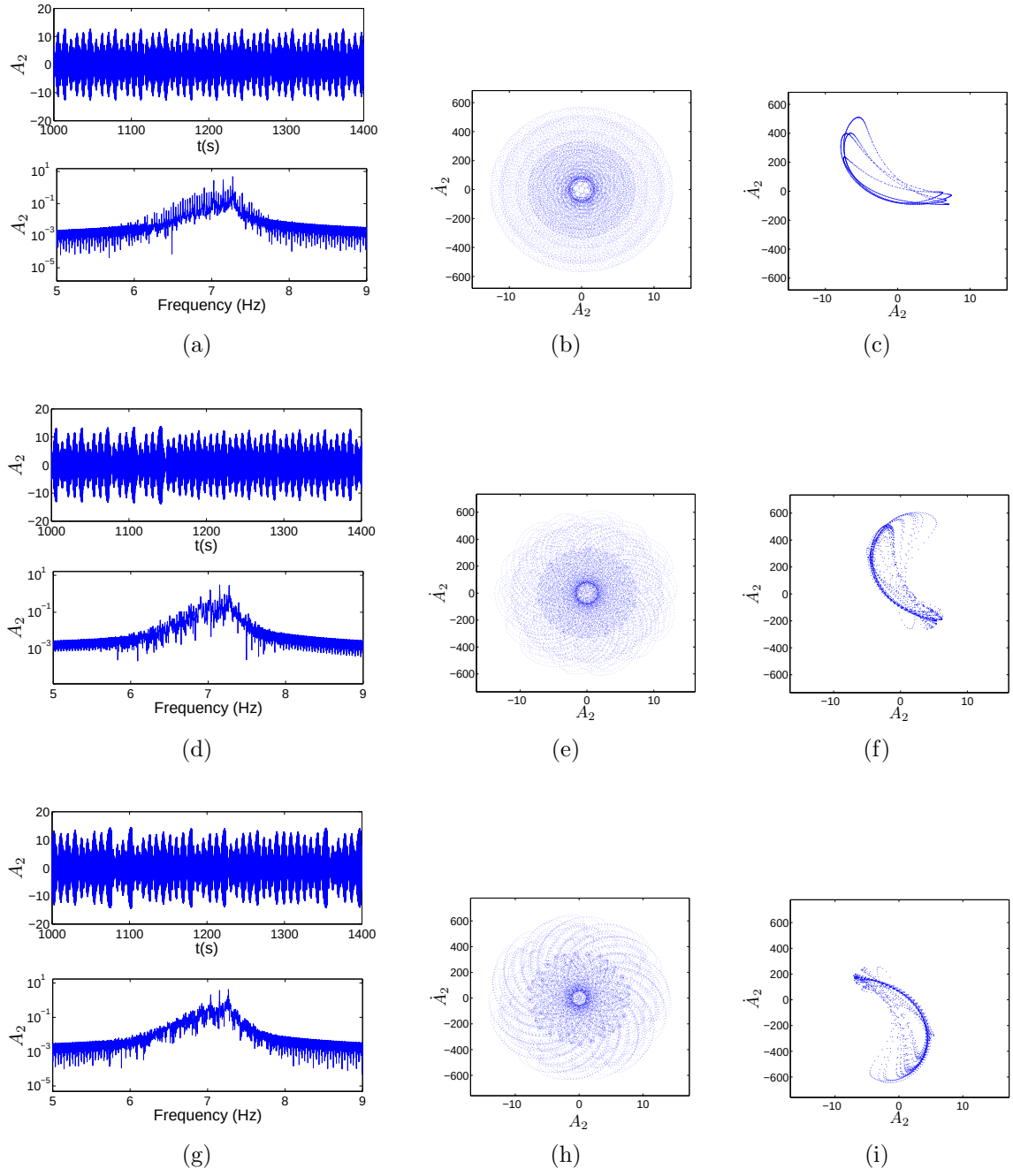

Figure 3.12: (a,d,g) Time histories and power spectra, (b,e,h) phase portraits, and (c,f,i) Poincare sections of the vertical displacement of base structure for different $\varepsilon\sigma_1$ when other parameters are $\varepsilon = 0.005$, $\omega_2 = 45.35 rad/s$, $R = 6.2$, $\delta_1 = -R\omega_1^2$, $\varepsilon\mu_1 = 0.0035\omega_1$, $\varepsilon\mu_2 = 0.0035\omega_2$ and $\varepsilon\sigma_2 = 0.5$: (a, b, c) $\varepsilon\sigma_1 = -0.4325$, (b, e, f) $\varepsilon\sigma_1 = -0.432$ and (g, h, i) $\varepsilon\sigma_1 = -0.3975$.

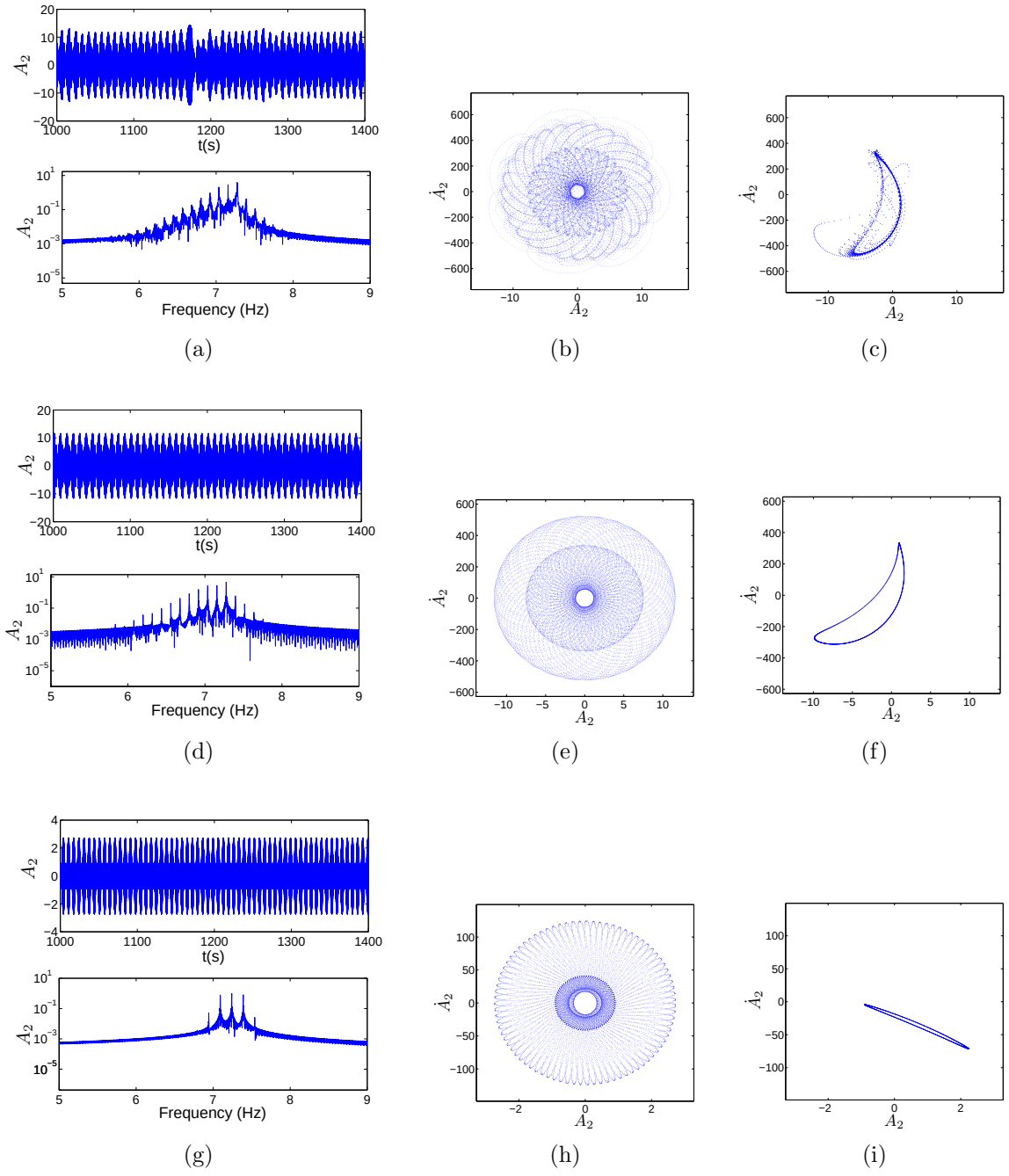

Figure 3.13: (a,d,g) Time histories and power spectra, (b,e,h) phase portraits, and (c,f,i) Poincare sections of the vertical displacement of base structure for different $\varepsilon\sigma_1$ when other parameters are $\varepsilon = 0.005$, $\omega_2 = 45.35 rad/s$, $R = 6.2$, $\delta_1 = -R\omega_1^2$, $\varepsilon\mu_1 = 0.0035\omega_1$, $\varepsilon\mu_2 = 0.0035\omega_2$ and $\varepsilon\sigma_2 = 0.5$:(a, b, c) $\varepsilon\sigma_1 = -0.3905$, (b, e, f) $\varepsilon\sigma_1 = -0.39$ and (g, h, i) $\varepsilon\sigma_1 = 0.15$.

4 Piezoelectric energy harvesting from hybrid vibrations

Galloping-based piezoaeroelastic systems have been studied recently by Abdelkefi et al [58, 59, 60, 87]. The system consists of galloping structure that is mounted on the tip of a vibration beam. As such, it is plausible to design a harvester that can generate energy from both ambient and galloping vibrations. Yet, the system's response to both types of vibrations under different conditions may not be a simple superposition of individual responses to both type of vibrations. We investigate the concept of harvesting energy from hybrid (ambient and galloping) vibrations and determine the effects of the load resistance, wind speed, and base acceleration on the performance of the harvester. The harvester consists of a cantilever beam with a triangular cross-section geometry tip mass attached to its end.

4.1 Representation of the hybrid energy harvester

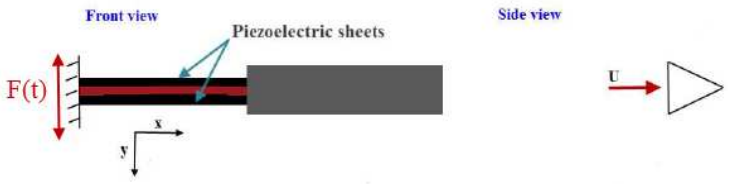

Figure 4.1: A schematic of the piezoaeroelastic energy harvester

The energy harvester under investigation consists of a triangular cross-section tip mass attached to a multi-layered cantilever beam. This energy harvester is subjected to two types of excitations, namely, base and galloping, as shown in figure 4.1. The cantilever beam is composed of one aluminum and two piezoelectric layers. The two piezoelectric sheets are bonded on both sides of the aluminum layer and connected in parallel with opposite polarity

Table 4.1: Physical and geometric properties of the cantilever beam and the tip body

E_s	Aluminum Young's Modulus (GN/m^2)	70
E_p	Piezoelectric material Young's Modulus (GN/m^2)	62
ρ_s	Aluminum density (kg/m^3)	2700
ρ_p	Piezoelectric material density (kg/m^3)	7800
L	Length of the beam (mm)	90
b_1	Width of the aluminum layer (mm)	38
b_2	Width of the piezoelectric layer (mm)	36.2
h_s	Aluminum layer thickness (mm)	0.635
h_p	Piezoelectric layer thickness (mm)	0.267
M_t	Tip mass (g)	65
L_{struc}	Length of the tip body (mm)	235
b_{struc}	Width of the tip body (mm)	30
d_{31}	Strain coefficient of piezoelectric layer (pC/N)	-320
ϵ_{33}^s	Permittivity component at constant strain (nF/m)	27.3

to an electrical load resistance. The geometric and material properties of the system are presented in table 4.1.

To establish the governing equation of the piezoelectric energy harvesting from hybrid vibrations, it is assumed that the multi-layered cantilever beam is Euler-Bernoulli beam. Also, the extended Hamilton's principle [78] is introduced as following:

$$\int_{t_1}^{t_2} (\delta T - \delta V + \delta W_{nc}) dt = 0 \tag{4.1}$$

Where, T, V and W_{nc} are respectively the kinetic energy, potential energy and virtual work due to the nonconservative forces and δx is the derivation of the x. Inspecting Figure 4.1, we express kinetic energy T as:

$$T = \frac{1}{2}\int_0^L m\left(\frac{\partial v(x,t)}{\partial t}\right)^2 dx + \frac{1}{2}M_t\left(\frac{\partial v(L,t)}{\partial t} + L_c\frac{\partial^2 v(L,t)}{\partial x \partial t}\right)^2 + \frac{1}{2}I_c(\frac{\partial^2 v(L,t)}{\partial x \partial t})^2 \tag{4.2}$$

In this expression, M_t, L_c and I_c are respectively the tip mass, distance from the center of the tip mass to the tip of the cantilever beam and rotational inertia of the tip mass relative to the center of the tip mass, L is the length of the cantilever beam, m is the mass of the beam per unit length and is given by $m{=}b_1\rho_s h_s + 2b_2\rho_p h_p$. In the expression of m, ρ_s and ρ_p are the respective densities of the aluminum and piezoelectric layers and h_s and h_p are the respective thicknesses of these layers. As such, the term of kinetic energy $\int_{t_1}^{t_2} \delta T dt$ in

Hamilton's equation 4.1 is calculated as

$$\begin{aligned}
&\int_{t_1}^{t_2} \delta T dt = \int_0^L \int_{t_1}^{t_2} m\frac{\partial v(x,t)}{\partial t}\frac{\partial \delta v(x,t)}{\partial t} dt dx + \int_{t_1}^{t_2} I_c \frac{\partial^2 v(L,t)}{\partial x \partial t}\frac{\partial^2 \delta v(L,t)}{\partial x \partial t} dt dx \\
&+ \int_{t_1}^{t_2} M_t \left(\frac{\partial v(L,t)}{\partial t} + L_c \frac{\partial^2 v(L,t)}{\partial x \partial t}\right)\left(\frac{\partial \delta v(L,t)}{\partial t} + L_c \frac{\partial^2 \delta v(L,t)}{\partial x \partial t}\right) dt \\
&= -\int_0^L \int_{t_1}^{t_2} m\frac{\partial^2 v(x,t)}{\partial t^2}\delta v(x,t) dt dx - \int_{t_1}^{t_2} M_t \left(\frac{\partial^2 v(L,t)}{\partial t^2} + L_c \frac{\partial^3 v(L,t)}{\partial x \partial t^2}\right)\delta v(L,t) dt dx \\
&- \int_{t_1}^{t_2} \left(M_t L_c \frac{\partial^2 v(L,t)}{\partial t^2} + I_t \frac{\partial^3 v(L,t)}{\partial x \partial t^2}\right)\frac{\partial \delta v(L,t)}{\partial x} dt
\end{aligned} \tag{4.3}$$

where I_t is the rotational inertia of the tip mass relative to the tip of the cantilever beam and is given by $I_t = M_t L_c^2 + I_c$. In the derivation, we use the properties of the virtual kinetic energy: $\delta v(x,t) = 0$ and $\frac{\partial \delta v(L,t)}{\partial x} = 0$ at $t = t_1, t_2$. The potential energy V is give by:

$$V = \frac{1}{2}\int_0^L EI\left(\frac{\partial^2 v(x,t)}{\partial x^2}\right)^2 dx \tag{4.4}$$

where EI is the stiffness of the cantilever beam and is given by
$EI = \frac{1}{12} b_1 E_s {h_s}^3 + \frac{2}{3} b_2 E_p[(h_p + \frac{h_s}{2})^3 - \frac{{h_s}^3}{8}]$. In this formulation, E_s and E_p are the respective Young's Modulus of the aluminum and piezoelectric layers and b_1 and b_2 are the beam widths of repetitive multiple layers. To this end, the term of potential energy $\int_{t_1}^{t_2} \delta V dt$ in Hamilton's equation 4.1 is calculated as

$$\begin{aligned}
&\int_{t_1}^{t_2} \delta V dt = \int_{t_1}^{t_2}\int_0^L EI\frac{\partial^2 v(x,t)}{\partial x^2}\frac{\partial^2}{\partial x^2}(\delta v(x,t)) dx dt \\
&= \int_{t_1}^{t_2} EI\left(\frac{\partial^2 v(L,t)}{\partial x^2}\right)\frac{\partial}{\partial x}(\delta v(L,t)) dt - \int_{t_1}^{t_2} EI\left(\frac{\partial^2 v(0,t)}{\partial x^2}\right)\frac{\partial}{\partial x}(\delta v(0,t)) dt \\
&- \int_{t_1}^{t_2} EI\left(\frac{\partial^3 v(L,t)}{\partial x^3}\right)\delta v(L,t) dt + \int_{t_1}^{t_2} EI\left(\frac{\partial^3 v(0,t)}{\partial x^3}\right)\delta v(0,t) dt + \int_{t_1}^{t_2}\int_0^L EI\frac{\partial^4 v(x,t)}{\partial x^4}\delta v(x,t) dx dt
\end{aligned} \tag{4.5}$$

In the system of energy harvesting, nonconservative forces are separated into following three parts: damping force, electronic force and galloping force. As such, the virtual work due to the nonconservative forces is given by:

$$W_{nc} = W_{ele} + W_{damp} + W_{gallop} \tag{4.6}$$

where W_{ele}, W_{damp} and W_{gallop} are the virtual works due to the respective electric, damping and galloping forces. According to Ref. [42], the virtual works due to electric force W_{ele} is given by:

$$W_{ele} = \int_0^L -M_{ele}\frac{\partial^2 v(x,t)}{\partial x^2} dx \tag{4.7}$$

where M_{ele} is the moment due to the electric effect and is expressed as following when the

upper and lower layer are parallelly connected [42]:

$$\begin{aligned} &M_{ele} = b_2[\int_{-h_p-h_s/2}^{-h_s/2} -e_{31}(-\tfrac{V(t)}{h_p})ydy + \int_{h_s/2}^{h_p+h_s/2} -e_{31}(\tfrac{V(t)}{h_p})ydy](H(x) - H(x-L)) \\ &= \vartheta_p V(t)(H(x) - H(x-L)) \end{aligned} \tag{4.8}$$

where $V(t)$ is the voltage of the piezoelectric layer, $H(x)$ is the step function, $e_{31} = E_p d_{31}$ is the piezoelectric stress coefficient and ϑ_p is the piezoelectric coupling term which is given by $\vartheta_p = -b_2 e_{31}(h_p + h_s)$. Incepting figure 4.1, the virtual work due to the damping force W_{damp} and due to the galloping force W_{gallop} are given by:

$$\begin{aligned} &W_{damp} = \int_0^L \oint F_d dv dx \\ &W_{gallop} = F_{tip} v(L,t) + M_{tip}\tfrac{\partial v(L,t)}{\partial x} \end{aligned} \tag{4.9}$$

where F_{tip} and M_{tip} are the respective galloping force and moment relative to the tip of the cantilever beam, F_d is the damping force whose expression is $F_d = -c_s I \frac{\partial^5 v_{rel}(x,t)}{\partial^4 x \partial t} - c_a \frac{\partial v_{rel}(x,t)}{\partial t}$ [42]. In the expression of F_d, c_s and c_a are the respective viscous strain and air damping coefficients, $v_{rel}(x,t)$ is the relative displacement to the base of the cantilever beam. Based on equations (4.6), (4.7) and (4.9), the virtual work due to nonconservative forces is calculated as

$$\begin{aligned} &\int_{t_1}^{t_2} \delta W_{nc} dt = \int_{t_1}^{t_2} \int_0^L -\vartheta_p V(t)(\tfrac{\partial \delta(x)}{\partial x} - \tfrac{\partial \delta(x-L)}{\partial x})\delta v(x,t) dx dt + \int_{t_1}^{t_2} F_{tip}\delta v(x,t) dt \\ &+ \int_{t_1}^{t_2} M_{tip}\tfrac{\partial \delta v(x,t)}{\partial x} dt + \int_{t_1}^{t_2} \int_0^L (-c_s I \tfrac{\partial^5 v_{rel}(x,t)}{\partial^4 x \partial t} - c_a \tfrac{\partial v_{rel}(x,t)}{\partial t})\delta v(x,t) dx dt \end{aligned} \tag{4.10}$$

Substitute equations (4.3), (4.5) and (4.10) into equation (4.1) and using the fact that $v(x,t) = v_{rel}(x,t) + v_b(t)$ ($v_b(t)$ is the base displacement), Hamilton's equation is translated into:

$$\begin{aligned} &\int_{t_1}^{t_2} \delta T - \delta V + \delta W_{nc} dt \\ &= -\int_{t_1}^{t_2} \int_0^L [EI\tfrac{\partial^4 v_{rel}(x,t)}{\partial x^4} + c_s I \tfrac{\partial^5 v_{rel}(x,t)}{\partial^4 x \partial t} + c_a \tfrac{\partial v_{rel}(x,t)}{\partial t} + m\tfrac{\partial^2 v_{rel}(x,t)}{\partial t^2} + m\tfrac{\partial^2 v_b(t)}{\partial t^2} \\ &+\vartheta_p V(t)(\tfrac{\partial \delta(x)}{\partial x} - \tfrac{\partial \delta(x-L)}{\partial x}) + (M_t \tfrac{\partial^2 v_b(t)}{\partial t^2} - F_{tip})\delta(x-L) - (M_t L_c \tfrac{\partial^2 v_b(t)}{\partial^2 t} - M_{tip})\tfrac{\partial \delta(x-L)}{\partial x}]\delta v(x,t) dx dt \\ &- \int_{t_1}^{t_2} EI\left(\tfrac{\partial^3 v_{rel}(0,t)}{\partial x^3}\right)\delta v(0,t) dt + \int_{t_1}^{t_2} EI\left(\tfrac{\partial^2 v_{rel}(0,t)}{\partial x^2}\right)\tfrac{\partial}{\partial x}(\delta v(0,t)) dt \\ &- \int_{t_1}^{t_2} (M_t(\left(\tfrac{\partial^2 v_{rel}(L,t)}{\partial t^2} + L_c \tfrac{\partial^3 v_{rel}(L,t)}{\partial x \partial t^2}\right)) - EI\left(\tfrac{\partial^3 v_{rel}(L,t)}{\partial x^3}\right))\delta v(L,t) dt \\ &- \int_{t_1}^{t_2} (M_t L_c \tfrac{\partial^2 v_{rel}(L,t)}{\partial t^2} + I_t \tfrac{\partial^3 v_{rel}(L,t)}{\partial x \partial t^2} + EI\left(\tfrac{\partial^2 v(L,t)}{\partial x^2}\right))\tfrac{\partial}{\partial x}(\delta v(L,t)) dt = 0 \end{aligned} \tag{4.11}$$

Based on the extended Hamilton's equation (4.11), the governing equation of the electromechanical systems is written as

$$\begin{aligned} &EI\tfrac{\partial^4 v_{rel}(x,t)}{\partial x^4} + c_s I \tfrac{\partial^5 v_{rel}(x,t)}{\partial x^4 \partial t} + c_a \tfrac{\partial v_{rel}(x,t)}{\partial t} + m\tfrac{\partial^2 v_{rel}(x,t)}{\partial t^2} + (\tfrac{d\delta(x)}{dx} - \tfrac{d\delta(x-L)}{dx})\vartheta_p V(t) \\ &= F_{tip}\delta(x-L) - M_{tip}\tfrac{d\delta(x-L)}{dx} - M_t\delta(x-L)\tfrac{\partial^2 v_b(t)}{\partial t^2} + M_t L_c \tfrac{\partial^2 v_b(t)}{\partial t^2}\tfrac{d\delta(x-L)}{dx} - m\tfrac{\partial^2 v_b(t)}{\partial t^2} \end{aligned} \tag{4.12}$$

Inspecting Figure 4.1 we find the boundary geometry of the cantilever beam as $v(0,t) = 0$, $\frac{\partial}{\partial x}(v(0,t)) = 0$, $v(L,t) \neq 0$ and $\frac{\partial}{\partial x}(v(L,t)) \neq 0$. Similarly, based on the extended Hamilton's equation (4.11), the boundary conditions of the electromechanical systems is given by:

$$\begin{aligned} &v(0,t) = 0; \frac{\partial}{\partial x}(v(0,t)) = 0; \\ &M_t \left(\frac{\partial^2 v_{rel}(L,t)}{\partial t^2} + L_c \frac{\partial^3 v_{rel}(L,t)}{\partial x \partial t^2}\right) - EI \left(\frac{\partial^3 v_{rel}(L,t)}{\partial x^3}\right) = 0 \\ &M_t L_c \frac{\partial^2 v_{rel}(L,t)}{\partial t^2} + I_t \frac{\partial^3 v_{rel}(L,t)}{\partial x \partial t^2} + EI \left(\frac{\partial^2 v(L,t)}{\partial x^2}\right) = 0 \end{aligned} \tag{4.13}$$

To relate the mechanical and electrical variables, the Gauss law [88] is used as following:

$$\frac{d}{dt} \int_A \mathbf{D}.\mathbf{n}\, dA = \frac{d}{dt} \int_A D_2\, dA = \frac{V}{R} \tag{4.14}$$

where $\mathbf{D}$ is the electric displacement vector and $\mathbf{n}$ is the normal vector to the plane of the beam. The electric displacement component D_2 is given by the following relation [42]:

$$D_2(x,t) = e_{31}\varepsilon_{11}(x,t) + \epsilon_{33}^s E_2 \tag{4.15}$$

where ε_{11} is the axial strain component in the aluminum and piezoelectric layers and is given by $\varepsilon_{11}(x,y,t) = -y\frac{\partial^2 v_{rel}(x,t)}{\partial x^2}$, and ϵ_{33}^s is the permitting component at constant strain. Substituting equation (5.9) into equation (5.8), we obtain the equation governing the strain-voltage relation:

$$-e_{31}(h_p + h_s)b_2 \int_0^L \frac{\partial^3 v_{rel}(x,t)}{\partial t \partial x^2} dx - \frac{2\epsilon_{33}^s b_2 L}{h_p} \frac{dV(t)}{dt} = \frac{V(t)}{R} \tag{4.16}$$

4.2 Galerkin discretization

Characterization of the different physical aspects of the harvester is best obtained by performing linear stability and nonlinear analyses. We discretized the motion of the system by using the Galerkin procedure, which requires the exact mode shapes of the structure. As such, the relative transverse displacement, $v_{rel}(x,t)$, is expressed in the following form:

$$v_{rel}(x,t) = \phi_i(x) q_i(t) \tag{4.17}$$

where $q_i(t)$ are the modal coordinates and $\phi_i(x)$ are the mode shapes of a cantilever beam-mass system. These mode shapes are determined by dropping the damping, forcing, and polarization from equation (4.12) as [58]:

$$\phi(x) = A\sin\beta x + B\cos\beta x + C\sinh\beta x + D\cosh\beta x \tag{4.18}$$

where the relation between β and ω is given by $\omega = \beta^2\sqrt{\frac{EI}{m}}$.

To obtain the relation between the different coefficients in (4.18), we use the associated boundary conditions of the system, see in equation (4.13), and then normalize the eigenfunctions (orthogonality conditions). These conditions are, respectively, given by:

$$\begin{aligned} &\phi_i(0) = 0; \phi_i'(0) = 0; \\ &EI\phi_i''(L) - \omega^2 M_t L_c \phi_i(L) - \omega^2 I_t \phi_i'(L) = 0; \\ &EI\phi_i'''(L) + \omega^2 M_t L_c \phi_i'(L) + \omega^2 M_t \phi_i(L) = 0 \end{aligned} \tag{4.19}$$

and

$$\begin{aligned} &\int_0^L \phi_s(x) m \phi_r(x) dx + \phi_s(L) M_t \phi_r(L) + \phi_s{}'(L) I_t \phi_r{}'(L) \\ &+\phi_s(L) M_t L_c \phi_r{}'(L) + \phi_r(L) M_t L_c \phi_s{}'(L) = \delta_{rs} \\ &\int_0^L \phi_s{}''(x) EI \phi_r{}''(x) dx = \delta_{rs}\omega_r^2 \end{aligned} \tag{4.20}$$

Where, s and r are used to represent the vibration modes and δ_{rs} is the Kronecker delta, defined as unity when s is equal to r and zero otherwise.

Substituting equation (4.17) into equations (4.12) and (4.16) and considering the first mode, we obtain the following coupled equations:

$$\ddot{q}(t) + 2\xi\omega\dot{q}(t) + \omega^2 q(t) + \theta_p V(t) = f(t) \tag{4.21}$$

$$\frac{V(t)}{R} + C_p\dot{V}(t) - \theta_p\dot{q}(t) = 0 \tag{4.22}$$

where ξ is the mechanical damping coefficient, $f(t)$ is the first mode of the external force due to galloping and base excitation which is given by: $f(t) = \phi(L)F_{tip} + \phi'(L)M_{tip} - M_t\phi(L)\frac{\partial^2 v_b(t)}{\partial t^2} - \phi'(L)M_t L_c\frac{\partial^2 v_b(t)}{\partial t^2} - \frac{\partial^2 v_b(t)}{\partial t^2}\int_0^L \phi(x)mdx$, ω is the fundamental natural frequency of the structure, and the coefficients θ_p and C_p are the respective piezoelectric coupling term and capacitance of the harvester which are given by $\theta_p = \phi'(L)\vartheta_p$ and $C_p = \frac{2\varepsilon_{33}^s b_2 L}{h_p}$.

4.3 Determination of the aerodynamic galloping force

The use of the quasi-steady hypothesis to evaluate the aerodynamic loads has been justified by the fact that the characteristic time scale of the oscillations is much larger than the characteristic time scale of the flow motion [89, 90]. As such, the lift force F_L and the drag force F_D per unit length are written as

$$\begin{aligned} F_L &= \tfrac{1}{2}\rho_{air}U^2 b_{struc} C_L \\ F_D &= \tfrac{1}{2}\rho_{air}U^2 b_{struc} C_D \end{aligned} \tag{4.23}$$

where ρ_{air} is the density of air, U is the incoming wind speed, b_{struc} is the width of the bluff body at the tip, and C_L and C_D are, respectively, the lift and drag coefficients. The tip force and moment are determined by integrating the aerodynamic loads over the whole length of the galloping structure as

$$\begin{aligned} F_{tip} &= -\int_0^{L_{struc}} (F_L \cos\alpha + F_D \sin\alpha) ds \\ M_{tip} &= -\int_0^{L_{struc}} s(F_L \cos\alpha + F_D \sin\alpha) ds \end{aligned} \tag{4.24}$$

where L_{struc} is the length of the prismatic structure and s is the length coordinate along the tip body. These coefficients depend on the angle of attack, α, as well as the Reynolds number. The angle of attack is expressed as: $\alpha = \tan^{-1}(\frac{\dot{v}_{rel}(L,t)+s\dot{v}'_{rel}(L,t)+\dot{v}_b(t)}{U})$.

The total aerodynamic force per unit length, F_y, applied to the prismatic structure in the direction normal to the incoming flow is directly related to the lift and drag forces and is given by:

$$F_y = \frac{1}{2}\rho_{air} U^2 b_{struc} C_y = -\frac{1}{2}\rho_{air} U^2 b_{struc} [C_L \cos(\alpha) + C_D \sin(\alpha)] \tag{4.25}$$

where C_y is the total aerodynamic force coefficient in the direction normal to the incoming flow. Barrero-Gil et al [90] showed that, for applications where the Reynolds number is relatively high, the total aerodynamic force coefficient can be expressed by a polynomial function of $tan(\alpha)$ in the form:

$$C_y = a_1 \tan\alpha + a_3 (\tan\alpha)^3 \tag{4.26}$$

where a_1 and a_3 are empirical coefficients obtained by polynomial fitting of C_y vs $tan(\alpha)$. A positive value for a_1 indicates that the structure is susceptible to galloping [91]. As for the nonlinear coefficient a_3, it is always negative because C_y always has a maximum value, which decreases as a function of the angle of attack. Both of the linear and nonlinear coefficients depend on the geometry of the cross-section. Here, we consider isosceles triangles with $\delta = 30^o$. The empirical values of a_1 and a_3, as determined by Barrero-Gil et al [90], are 2.9 and -6.2, resepctively. Using the above equations, the aerodynamic force and moment at the tip are expressed as:

$$\begin{aligned} F_{tip} &= \tfrac{1}{2}\rho_{air} U^2 b_{struc} \int_0^{L_{struc}} a_1(\tfrac{\dot{v}_{rel}(L,t)+s\dot{v}'_{rel}(L,t)+\dot{v}_b(L,t)}{U}) + a_3(\tfrac{\dot{v}_{rel}(L,t)+s\dot{v}'_{rel}(L,t)+\dot{v}_b(L,t)}{U})^3 ds \\ M_{tip} &= \tfrac{1}{2}\rho_{air} U^2 b_{struc} \int_0^{L_{struc}} s(a_1(\tfrac{\dot{v}_{rel}(L,t)+s\dot{v}'_{rel}(L,t)+\dot{v}_b(L,t)}{U}) + a_3(\tfrac{\dot{v}_{rel}(L,t)+s\dot{v}'_{rel}(L,t)+\dot{v}_b(L,t)}{U})^3) ds \end{aligned} \tag{4.27}$$

4.4 Linear analysis

Substituting the discretized form into equation (4.27), the external force due to galloping and base citation is given as following:

$$\begin{aligned} f(t) &= \phi(L)F_{tip} + \phi'(L)M_{tip} - \frac{\partial^2 v_b(t)}{\partial t^2}(M_t\phi(L) + \phi'(L)M_tL_c + \int_0^L \phi(x)m\mathrm{d}x) \\ &= \tfrac{1}{2}\rho_{air}U^2 b_{struc}\left[k_1\frac{\dot{q}}{U} + k_2\frac{\dot{v}_b}{U} + k_3(\frac{\dot{q}}{U})^3 + k_4\frac{\dot{v}_b}{U}(\frac{\dot{q}}{U})^2 + k_5(\frac{\dot{v}_b}{U})^2(\frac{\dot{q}}{U}) + k_6(\frac{\dot{v}_b}{U})^3\right] + k_7\ddot{v}_b \end{aligned} \tag{4.28}$$

where k_1, k_2, k_3, k_4, k_5, k_6 and k_7 are given by:

$$\begin{aligned} k_1 &= a_1(\phi^2(L)L_{struc} + \phi(L)\phi'(L)L_{struc}^2 + \tfrac{1}{3}\phi'^2(L)L_{struc}^3) \\ k_2 &= a_1(\phi(L)L_{struc} + \tfrac{1}{2}\phi'(L)L_{struc}^2) \\ k_3 &= a_3(\phi(L)\int_0^{L_{struc}}(\phi(L) + s\phi'(L))^3 ds + \phi'(L)\int_0^{L_{struc}} s(\phi(L) + s\phi'(L))^3 ds) \\ k_4 &= 3a_3(\phi(L)\int_0^{L_{struc}}(\phi(L) + s\phi'(L))^2 ds + \phi'(L)\int_0^{L_{struc}} s(\phi(L) + s\phi'(L))^2 ds) \\ k_5 &= 3a_3(\phi^2(L)L_{struc} + \phi(L)\phi'(L)L_{struc}^2 + \tfrac{1}{3}\phi'^2(L)L_{struc}^3) \\ k_6 &= a_3(\phi(L)L_{struc} + \tfrac{1}{2}\phi'(L)L_{struc}^2) \\ k_7 &= -(M_t\phi(L) + \phi'(L)M_tL_c + \textstyle\int_0^L \phi(x)m dx) \end{aligned} \tag{4.29}$$

Introduce the following state variables:

$$\mathbf{X} = \begin{bmatrix} X_1 \\ X_2 \\ X_3 \end{bmatrix} = \begin{bmatrix} q \\ \dot{q} \\ V \end{bmatrix} \tag{4.30}$$

The equations of motion are rewritten as

$$\dot{X}_1 = X_2 \tag{4.31}$$

$$\begin{aligned} \dot{X}_2 &= -(2\xi\omega - \tfrac{\rho_{air}Ub_{struc}k_1}{2})X_2 - \omega^2 X_1 - \chi X_3 + \tfrac{\rho_{air}Ub_{struc}k_2}{2}\dot{v}_b \\ &+ \tfrac{\rho_{air}b_{struc}}{2U}(k_3X_2^3 + k_4\dot{v}_bX_2^2 + k_5\dot{v}_b^2X_2 + k_6\dot{v}_b^3) + k_7\ddot{v}_b \end{aligned} \tag{4.32}$$

$$\dot{X}_3 = -\frac{1}{RC_p}X_3 + \frac{\chi}{C_p}X_2 \tag{4.33}$$

Clearly, these equations have the form

$$\dot{\mathbf{X}} = \mathbf{B}(U)\mathbf{X} + \mathbf{G}(U, \dot{v}_b) + \mathbf{N}(X, X, X) + \mathbf{C}(X, \dot{v}_b) + \mathbf{F_b}(\dot{v}_b) \tag{4.34}$$

where $\mathbf{B} = \begin{bmatrix} 0 & 1 & 0 \\ -\omega_n^2 & -\left(2\xi\omega - \frac{\rho_{air}Ub_{struc}k_1}{2}\right) & -\chi \\ 0 & \frac{\chi}{C_p} & -\frac{1}{RC_p} \end{bmatrix}$; $\mathbf{G} = \begin{bmatrix} 0 \\ \frac{1}{2}\rho_{air}Ub_{struc}k_2\dot{v}_b \\ 0 \end{bmatrix}$; $\mathbf{C} = \begin{bmatrix} 0 \\ \frac{\rho_{air}b_{struc}}{2U}(k_4\dot{v}_bX_2^2 + k_5\dot{v}_b^2X_2 + k_6\dot{v}_b^3) \\ 0 \end{bmatrix}$; $\mathbf{N} = \begin{bmatrix} 0 \\ \frac{\rho_{air}b_{struc}}{2U}k_3X_2^3 \\ 0 \end{bmatrix}$;

$\mathbf{F_b} = \begin{bmatrix} 0 \\ k_7\ddot{v}_b \\ 0 \end{bmatrix}$

4.4.a Effects of the load resistance and wind speed on the global frequency and electromechanical damping

The effects of the electrical load resistance on the natural frequency and damping of the hybrid harvester, and consequently on the onset of galloping, are determined from a linear analysis of the coupled electromechanical problem. Inspecting the governing equations of motion (4.34), we note that the matrix **B** gives a clear idea about the effects of the wind speed and load resistance on the overall damping and frequency of the system.

There are there eigenvalues of matrix **B** λ_i, $i = 1, 2, 3$. The first two eigenvalues are similar to those of a pure galloping problem in the absence of the piezoelectricity effect. These two eigenvalues are complex conjugates ($\lambda_2 = \overline{\lambda_1}$). The real part of these eigenvalues represents the electromechanical damping element (the damping coefficient times the global frequency of the system) and the positive imaginary part corresponds to the global frequency of the coupled system. The third eigenvalue λ_3 is the result of the electromechanical coupling and is always real and negative [44, 45]. It is noted that the stability of the trivial solution depends only on the real part of the first two eigenvalues because λ_3 is always real and negative. The speed U_g for which the real part of the first two eigenvalues is zero corresponds to the onset of instability or galloping and self-excited oscillations takes place for higher values of the wind speeds.

Figure 4.2 shows the variation of global frequency and the coupling damping ratio as a function of load resistance When $U = 0m/s$. It follows from Figure 4.2(a) that when the load resistance is smaller than $10^4\Omega$ or larger than $5\times10^5\Omega$, the global frequency almost keeps constant. On the other hand, the global frequency increases from $40.7rad/s$ to $44.2rad/s$ as the load resistance is increased from $10^4\Omega$ to $5 \times 10^5\Omega$. When $R = 10^2\Omega$, we refer to this global frequency as the short global frequency. In contrast, when $R = 10^8\Omega$, we refer to this global frequency as the open global frequency. Turning to the coupled damping, Figure 4.2(b) shows that that the coupled damping ratio of the system is smaller in the range of load resistances between 10^2 and $10^3\Omega$ and between 10^6 and $10^8\Omega$. In the intermediate

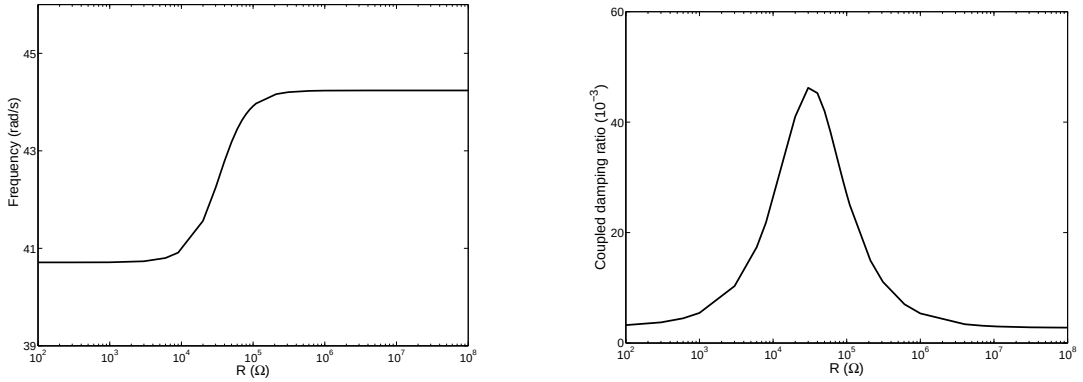

(a) (b)

Figure 4.2: (a) global frequency varied by load resistance When $U = 0m/s$, (b) electromechanical damping varied by load resistance When $U = 0m/s$

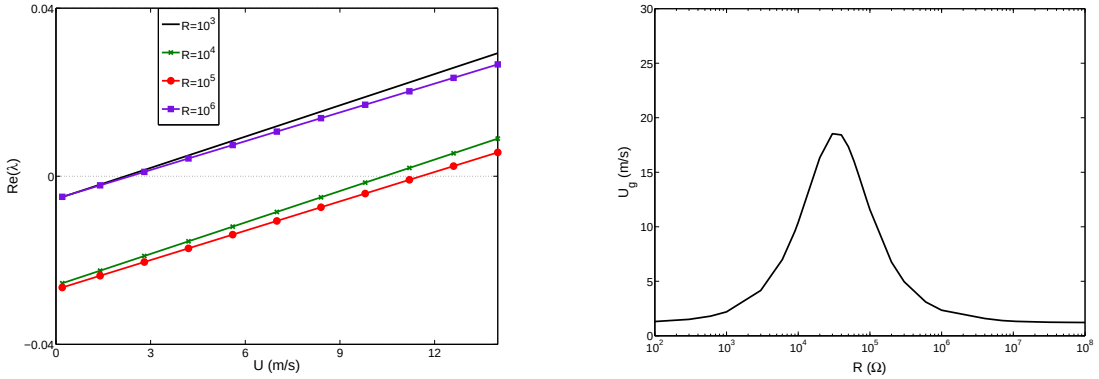

(a) (b)

Figure 4.3: (a) the real part of the first two eigenvalues varied by wind speed with different load resistances, (b) the onset galloping wind speed varied by load resistance

range of load resistances ($10^4\Omega < R < 10^5\Omega$), maximum values of the coupled damping are obtained. The coupled damping ratio reaches its maximum value for a load resistance value of $3 \times 10^4\Omega$.

To determine the effects of the load resistance on the onset of instability, we plot in figure 4.3(a) and (b) the variations of the the real part of the first two eigenvalues as a function of the wind speed and the variations of the onset speed of galloping as a function of the load resistance, respectively. It follows from Figure 4.3(a) that for a specific value of the wind speed, the real part of the the first two eigenvalues changes sign from negative to positive (onset of instability). It is also noted that the load resistance significantly affects the onset of instability. This is clearer in Figure 4.3(b) which shows that the onset speed

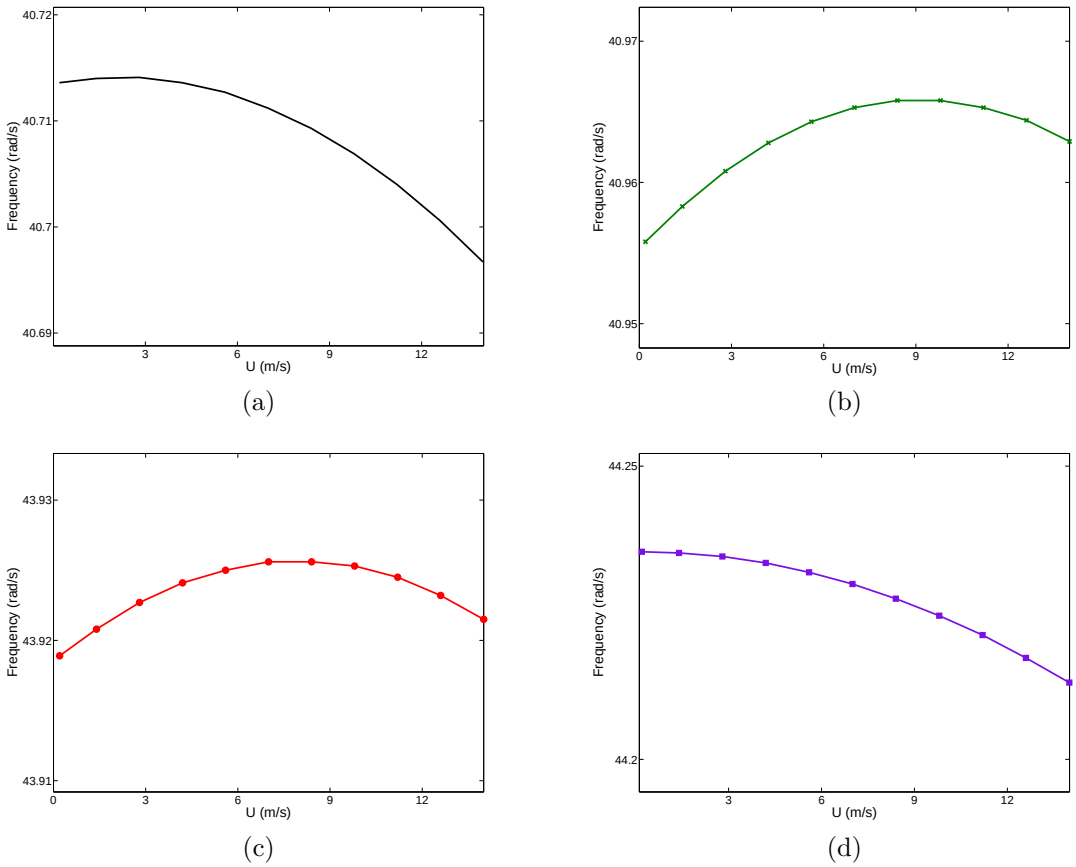

Figure 4.4: the global frequency varied by wind speed with different load resistances: (a) $R = 10^3\Omega$, (b) $R = 10^4\Omega$, (c) $R = 10^5\Omega$, (d) $R = 10^3\Omega$

of galloping strongly depends on the value of the load resistance. In the lower and higher ranges of the load resistances ($10^2\Omega < R < 5 \times 10^3\Omega$ and $5 \times 10^5\Omega < R < 10^8\Omega$), the effect of the load resistance on the onset speed of galloping is negligible. On the other hand, in the intermediate range of load resistances, the onset speed of galloping changes significantly when varying the load resistance. This is expected, because the global damping of the system is higher in this intermediate range of load resistance, as shown in figure 4.2(b).

The curves plotted in figure 4.4 show the variations of global frequencies as a function of wind speed for different load resistances. This analysis is helpful in determining the effects of varying the wind speed on the global frequency of the harvester. It follows from this figure that, for different load resistance values, the wind speed does not have much effect on the global frequency of the harvester. On the other hand, the variation of the global frequency as a function of the wind speed has a different tendency, depending on the associated electrical load resistance. In fact, When $R = 10^3\Omega$ and $R = 10^6\Omega$, the associated global frequencies decrease as wind speed is increased; However, when $R = 10^4\Omega$ and $R = 10^5\Omega$, there is a

specific value of the wind speed at which the associated global frequency is maximum.

4.5 Nonlinear analysis

4.5.a Analytical explanations and nonlinear phenomena

Before we perform nonlinear analysis of the governing equations of motion, we try to elaborate on a possible nonlinear phenomenon that can arise when there are hybrid (base and galloping) excitations. To simplify the analysis, we assume that the external forcing terms (equation 4.28) that contain $\dot{v}_b/U$ are relatively small compared to the pure galloping forcing term. This assumption allows us to neglect the coupled terms in equation (4.28). Due to the fact that the base excitation is a forced excitation and the galloping excitation is a self-excitation, the governing equations of motion of the harvester can be simplified and rewritten as the equation of motion of a self-sustaining system with harmonic excitation [92]. One example of such a system is the forced Rayleigh equation, which includes the self-excitation and the forced excitation and is written as

$$\ddot{u} + \omega_0^2 u = \varepsilon(u - \frac{1}{3}\dot{u}^3) + K\cos\Omega t \tag{4.35}$$

Where, ω_0 is the equal to global frequency of the system, Ω is the frequency of the base excitation, K is constant and ε is the small parameter (for the galloping case). According to Equation (4.32), it is noted that ε have the same sign as $\frac{\rho_{air} U b_{struc} k_1}{2} - 2\xi\omega$, which is positive when the wind speed is larger than the onset speed of galloping. Also, when $\ddot{v}_b$ is assumed to be $a\cos\Omega t$, K can be calculated as $k\frac{\varepsilon k_7 a}{\left|\frac{\rho_{air} U b_{struc} k_1}{2} - 2\xi\omega\right|}$. Here, k is the constant depending on the relationship between u and q.

Away from the possible resonances (primary, subharmonic of order 1/3, and superharmonic of order 3), the solution of equation (4.35) is given by [92]:

$$u = \left\{\frac{4\eta}{\omega_0^2 + \left[(4\eta/a_0^2) - \omega_0^2\right]\exp(-\varepsilon\eta t)}\right\}^{1/2} \cos(\omega_0 t + \beta) + \frac{K}{\Omega^2 - \omega_0^2}\cos\Omega t + O(\varepsilon) \tag{4.36}$$

Where, a_0 is the initial amplitude and $\eta = 1 - \frac{1}{2}\Omega^2 K^2(\omega_0^2 - \Omega^2)^{-2}$.

Inspecting equation (4.36), we note that the response of the harvester is composed of a homogeneous solution, which is the free-oscillation term due to galloping excitation, and a particular solution, which is a forced-oscillation term due to harmonic direct excitation. Based on this analysis. we conclude that the harvester mainly oscillates due to the presence of both excitations, with two harmonic frequencies, namely are ω_0 and Ω (not at resonance).

Thus, the response of the harvester is generally aperiodic, becoming periodic only when the excitation frequency matches the global frequency of the harvester.

Inspecting the free-oscillation term (homogeneous solution) in equation (4.36), we note that its amplitude depends on the value of $\eta = 1 - \frac{1}{2}\Omega^2 K^2(\omega_0^2 - \Omega^2)^{-2}$, which depends directly on the values of K and Ω. Therefore, the values of the forcing (acceleration) and frequency excitations significantly affect the value of η and hence the oscillations due to galloping excitation. When $\eta < 0$ (i.e. $K > \sqrt{2}\Omega^{-1}\left|\omega_0^2 - \Omega^2\right|$), the free-oscillation term, which is due to the galloping excitation, decays with time and only the forced-oscillation takes place (periodic motion). The phenomenon associated with the increase of the forcing excitation accompanies by a decay of the free-oscillations, which is due to galloping excitation, called quenching [92]. For small values of the forcing excitation K, then $\eta > 0$ and the steady-state response of the harvester contains both the global frequency (ω_0) and the excitation frequency (Ω). The free-oscillation term which is due to galloping excitation is expected to dominate when the excitation frequency is away from the global frequency. This process of unlocking between both excitations is called pulling-out. On the other hand, when the excitation frequency is almost equal to the global frequency of the harvester, the response of the harvester changes significantly and the free-oscillation term which is due to galloping is entrained or locked onto the forced term which is due to direct excitation. Consequently, a synchronization of the response at the excitation frequency takes place [92]. The frequency of external excitation when $K = \sqrt{2}\Omega^{-1}\left|\omega_0^2 - \Omega^2\right|$ is called pull-out frequency.

4.5.b Quenching phenomenon

We investigate whether the external force decreases the galloping effect when the external frequency comes near to the global frequency (quenching phenomena), as discovered from the simplified theoretical derivation in the section 4.5.a. The frequency response curves of the voltage when electrical load resistance, wind speed and amplitude of base acceleration are set equal to, respectively, $10^3\Omega$, $5m/s$ and $0.7g$ are plotted in figure 4.5. The plots show that the square root mean value of the voltage first decreases then increases as the base excitation approaches the global frequency. To prove the existence of quenching phenomenon, we plot the time history and power spectra of voltages when the external frequencies are $\Omega = \frac{3}{4}\omega_0$, $\frac{19}{20}\omega_0$, $0.954\omega_0$, $1.043\omega_0$, $\frac{23}{22}\omega_0$ and $\frac{3}{2}\omega_0$ in figure 4.6. When the external frequency is far away from the global frequency, such as $\Omega = \frac{3}{4}\omega_0$, the amplitude of voltage is mainly caused by the galloping effect. As the external frequency comes close to ω_0, the effect of the base excitation increases and the galloping effect decreases. For example, the amplitude of the voltage due to the base excitation is around ten times of galloping effect when $\Omega = \frac{19}{20}\omega_0$. As the external frequency increases a little further to $0.954\omega_0$, the galloping effect disappears. As such, the quenching phenomenon happens between $\Omega = \frac{19}{20}\omega_0$ and $0.954\omega_0$. Moreover, inspecting figure 4.5, we note that the quenching phenomenon appears when the square root

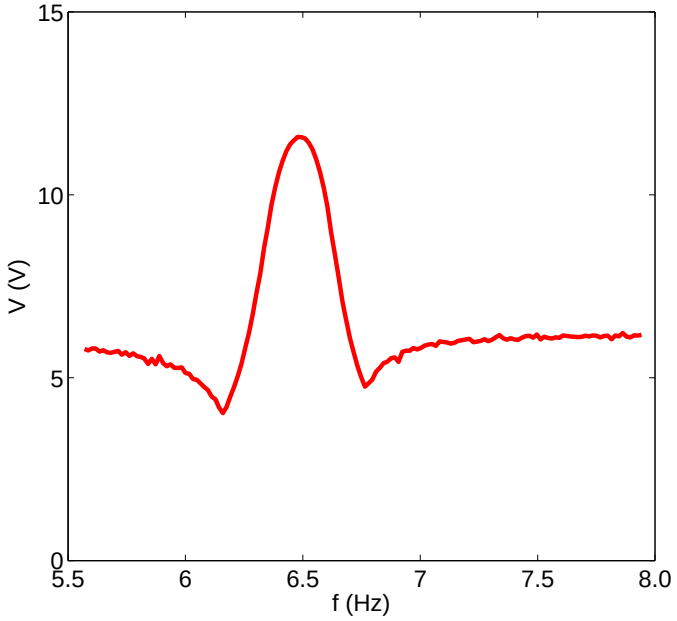

Figure 4.5: Frequency response curves for mean value of harvested voltage when electrical load resistance, wind speed and amplitude of base acceleration are set equal to $10^3\Omega$, $5m/s$ and $0.7g$, respectively.

mean value of the voltage arrives at the minimum value. As the frequency leaves away from the global frequency, the effect of galloping reappears when $\Omega = \frac{23}{22}\omega_0$. When the external frequency increases further, the galloping effect become dominant for the energy harvesting. Therefore, we can conclude that the base excitation will decrease the galloping effect and even make it disappear (quenching phenomenon) when the external frequency comes close to the global frequency.

4.5.c Effects of the load resistance, wind speed, and base acceleration on the harvester's performance

We first investigated the effects of the base excitations on the frequency-response curves of the harvester for different wind speeds and when the electrical load resistances are set equal to $R = 10^3\Omega$ and $R = 10^4\Omega$, see in figure 4.7 and 4.8, respectively. Inspecting the curves in figure 4.7, it is noted that the system becomes galloping except the wind speed is $0m/s$, This is expected for the reason that the onset wind speed of galloping excitation at that wind speed is smaller than $3m/s$ as shown in figure 4.3(b). Also, from comparison of different base excitations, we note that the base excitation does not affect the onset wind speed of galloping that can be explained by the fact that the matrix B does not contain

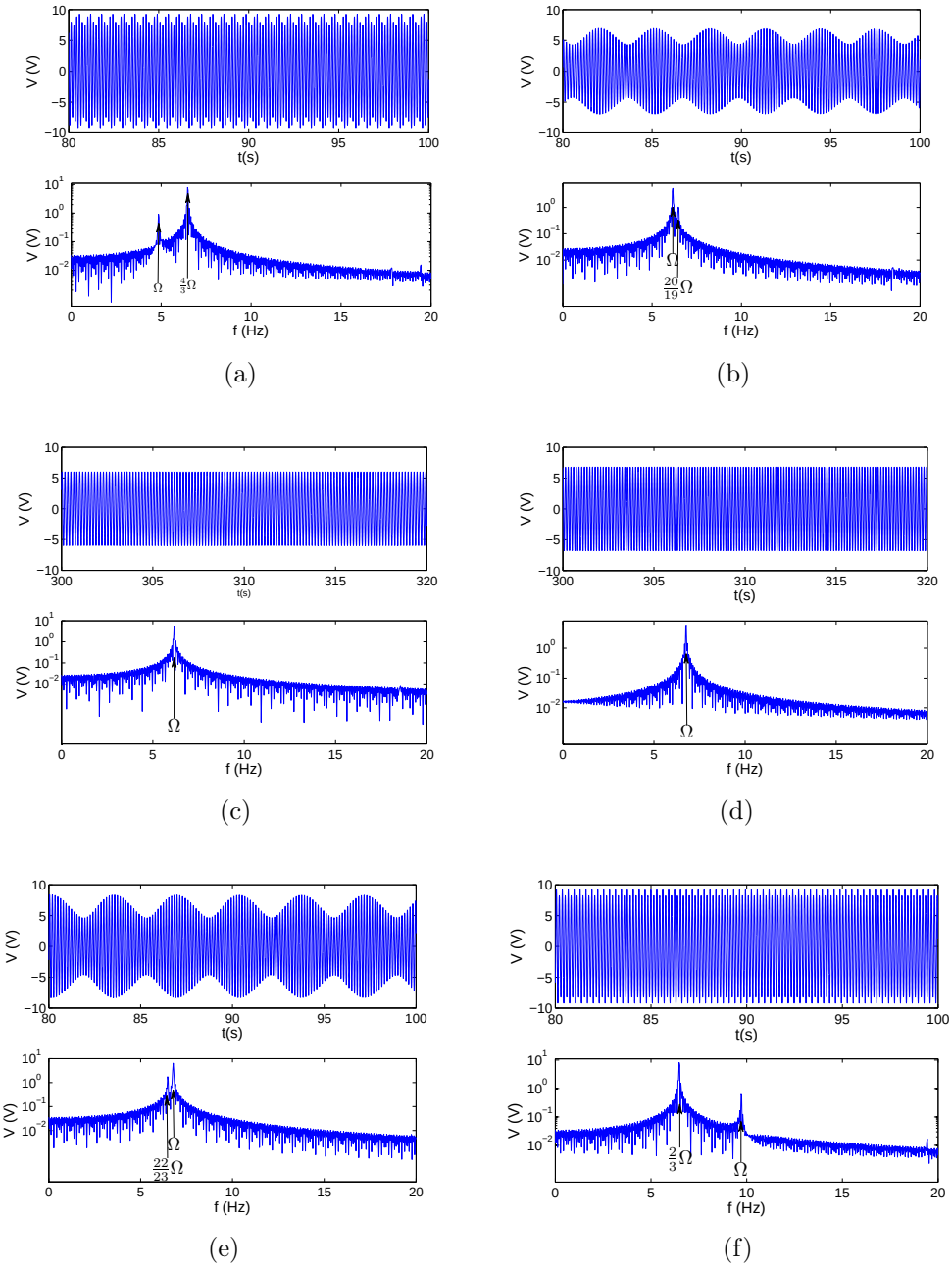

Figure 4.6: Time history and power spectra of the generated voltage for different excitation frequencies (Ω) when the load resistance, wind speed and amplitude of base acceleration are equal to $10^3\Omega$, $5m/s$ and $0.7g$, respectively: (a) $\Omega = \frac{3}{4}\omega_0$, (b) $\Omega = \frac{19}{20}\omega_0$, (c) $\Omega = 0.954\omega_0$, (d) $\Omega = 1.043\omega_0$, (e) $\Omega = \frac{23}{22}\omega_0$ and (f) $\Omega = \frac{3}{2}\omega_0$

elements depending on base excitation. Furthermore, we note that the galloping effect is

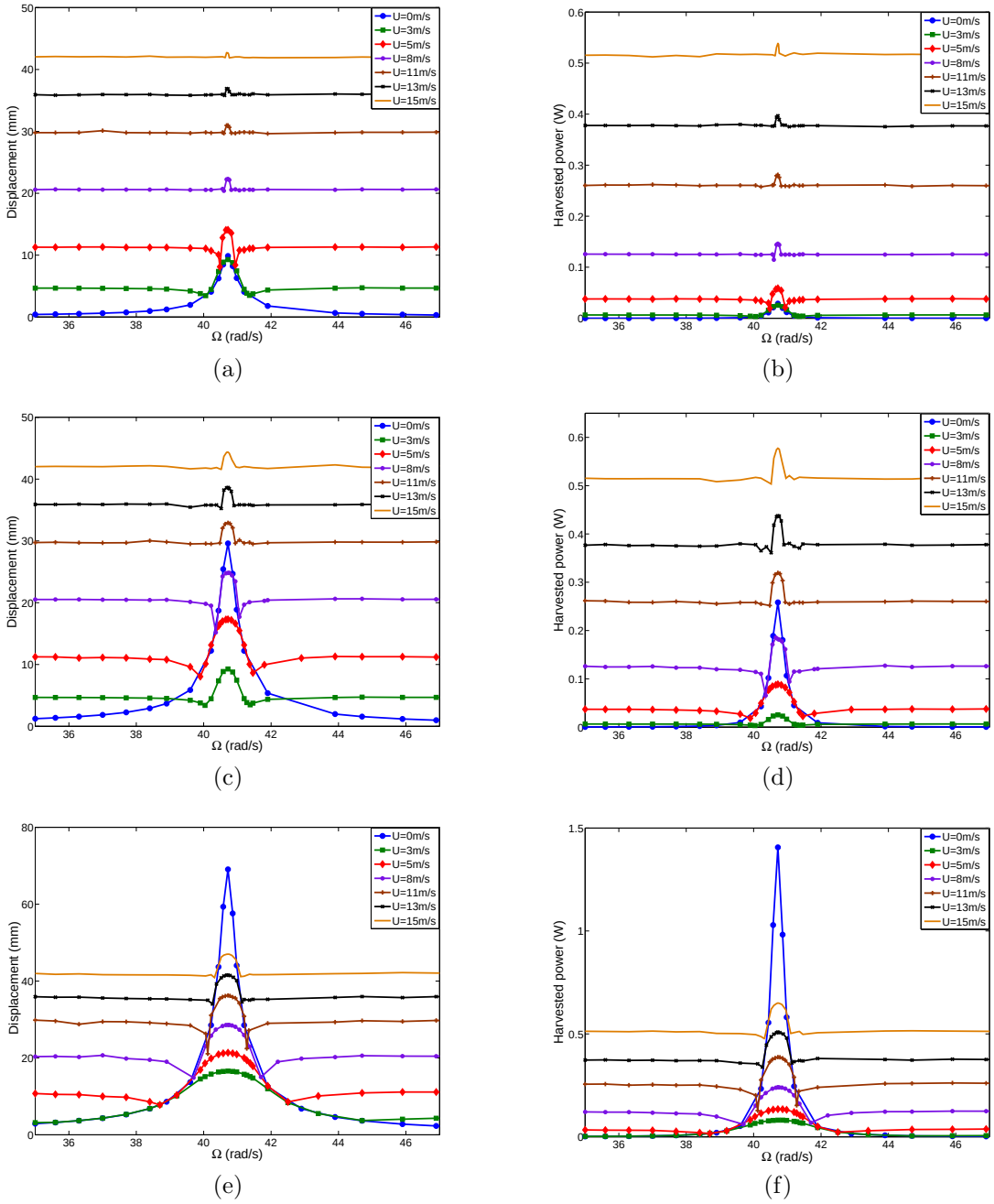

Figure 4.7: Frequency response curves for the tip displacement (a,c,e) and harvested power (b,d,f) when the load resistance is set equal to $10^3\Omega$ and for different base excitations and wind speeds. (a), (b) $a = 0.1g$, (c), (d) $a = 0.3g$ and (e), (f) $a = 0.7g$

more important as the wind speed is increased. This is clearer in the off-synchronization regions. In the synchronization or resonance region, the system can harvest energy from

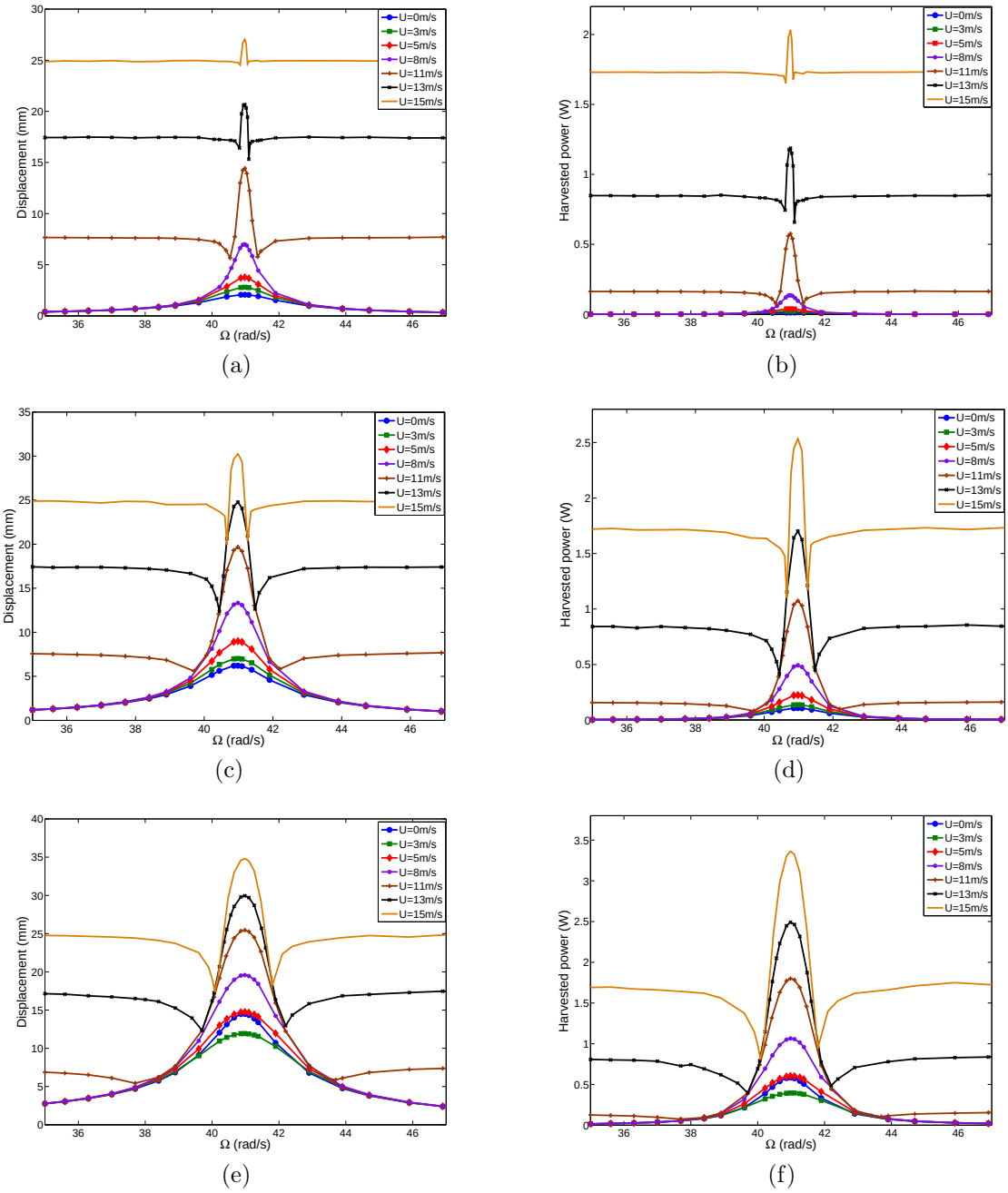

Figure 4.8: Frequency response curves for the tip displacement (a,c,e) and harvested power (b,d,f) when the load resistance is set equal to $10^4\Omega$ and for different base excitations and wind speeds. (a), (b) $a = 0.1g$, (c), (d) $a = 0.3g$ and (e), (f) $a = 0.7g$

both free- and forced-oscillation contributions. Inspecting figure 4.7(c) and 4.7(d), we find that the pulling-out frequency becomes nearer to the global frequency as the wind speed

increases. That can be explained by the facts that K decreases as wind speed U increases ($K = k\frac{\varepsilon k_7 a}{\left|\frac{\rho_{air} U b_{struc} k_1}{2} - 2\xi\omega\right|}$) and thus the difference between pull-out frequency and global frequency decreases ($K = \sqrt{2}\Omega^{-1}\left|\omega_0^2 - \Omega^2\right|$). In addition, the quenching phenomenon becomes more pronounced when the forcing excitation or base acceleration value increases. For example, comparing Figure 4.7(a), (c) with (e), it is noted that the difference between pull-out frequency and global frequency become larger as the base acceleration a is increased. That is because K increases as base acceleration a is increased ($K = k\frac{\varepsilon k_7 a}{\left|\frac{\rho_{air} U b_{struc} k_1}{2} - 2\xi\omega\right|}$). For the case when the load resistance is equal to $R = 10^4\Omega$, as shown in Figure 4.8. The tendency-response curves is changed for the cases when the wind speed is larger than $11m/s$. At smaller wind speed, the tendency of the frequency-response curves is similar to a base excitation case without galloping. At wind speeds values higher than $11m/s$, there is a galloping oscillation contribution which is clearer in the off-resonance regions. This result can be explained by the fact that onset speed of galloping is around $10m/s$ when the load resistance is set equal to $10^4\Omega$ shown in Figure 4.2. The result is same for different values of the base accelerations when the external frequency is away from the resonance. However, when the value of the base acceleration is increased, the range of the excitation frequency near resonance affected by the external force increases. Furthermore, at $a = 0.7g$, more power is generated at $U = 0m/s$ than at $U = 3m/s$. and is closer to the power levels generated at $U = 5m/s$. Furthermore, an increase in the value of base acceleration results in significant effects associated with quenching phenomenon.

The plotted curves in figure 4.9 show the frequency-response curves for tip displacement and harvested power for different load resistances and there distinct values of wind speed when the base acceleration is equal to $0.3g$. Inspecting these curves, we can note that the range of higher harvested power depends on the considered value of the load resistance. This is particularly clear when the wind speed is set equal to zero (without galloping effect). Furthermore, the plots show minimum values of the tip displacement are obtained when the load resistance is set equal to $10^4\Omega$ or $10^5\Omega$. This result is explained by the high values of the global damping shown in Figure 4.2(b). On the other hand, it is noted that these two values of the load resistance gives a wider range of excitation frequencies at which the system can harvest more energy. At $U = 5m/s$, the frequency-response curves when the load resistance is equal to $10^2\Omega$, $10^3\Omega$, $10^6\Omega$ and $10^7\Omega$ are effected by the galloping excitation. this is expected for the reason that the associated onset speed of galloping is smaller than $5m/s$ as shown in Figure 4.3(b). Inspecting figures 4.9(b) and (d), it is noted that the existence of the galloping effect ($U = 5m/s$) decreases the level of the harvested power in the resonance region when the load resistance is equal to $10^2\Omega$, $10^3\Omega$, $10^6\Omega$ and $10^7\Omega$. The highest levels of harvested power at resonance are observed for the base excitation cases (without galloping). The interesting result is that maximum levels of harvested power are accompanied by minimum displacement values when the load resistances is set equal to $10^4\Omega$ or $10^5\Omega$. At $U = 13m/s$, all frequency-response curves are affected by this wind speed

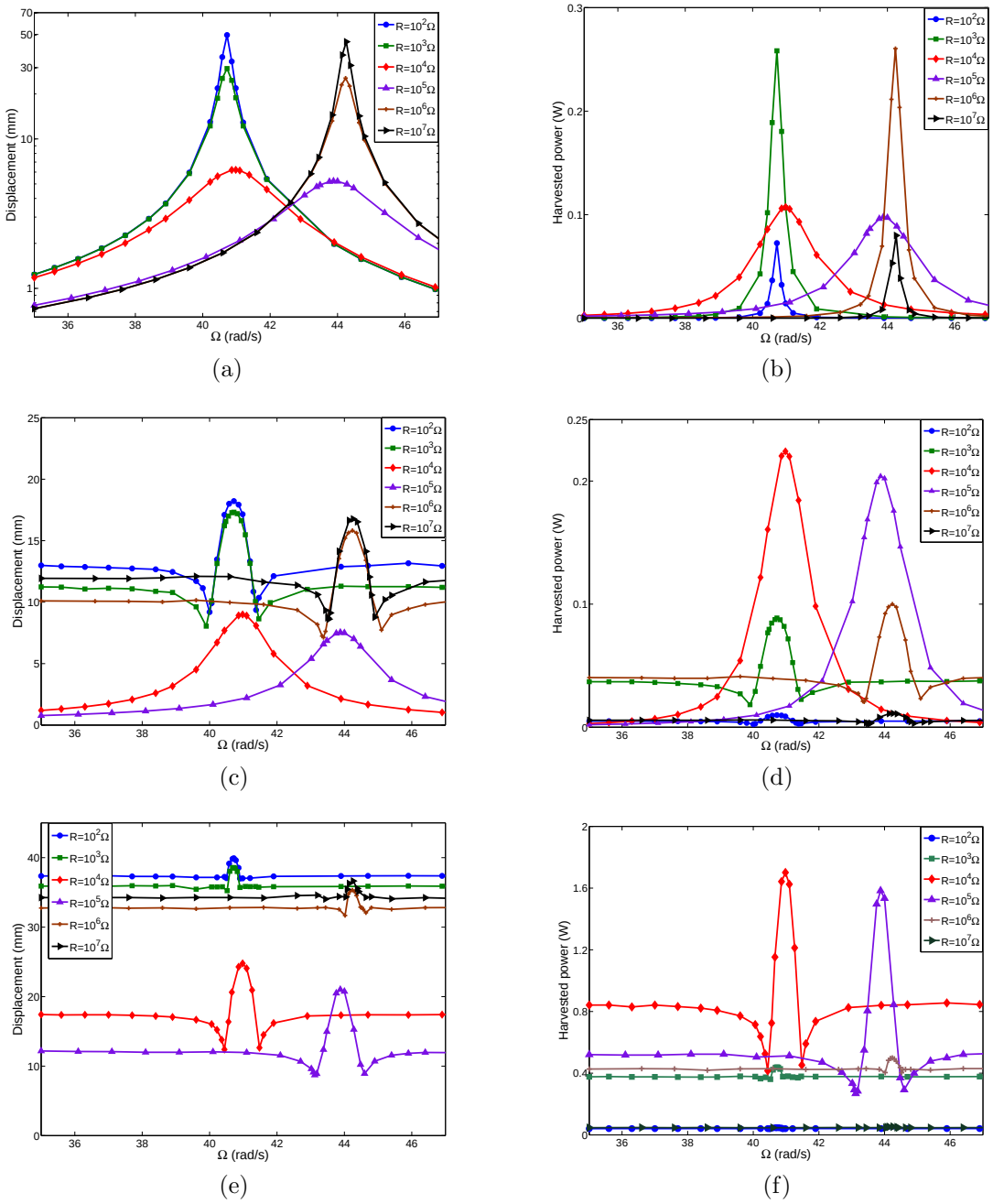

Figure 4.9: Frequency response curves for the tip displacement (a,c,e) and harvested power (b,d,f) when the base acceleration is set equal to $0.3g$ and for different load resistances and wind speeds. (a), (b) $U = 0m/s$, (c), (d) $U = 5m/s$ and (e), (f) $U = 13m/s$.

because the onset speed of galloping for all considered load resistances is smaller than $13m/s$, as shown in Figure 4.9(e) and (f). Furthermore, minimum values of the tip displacement are

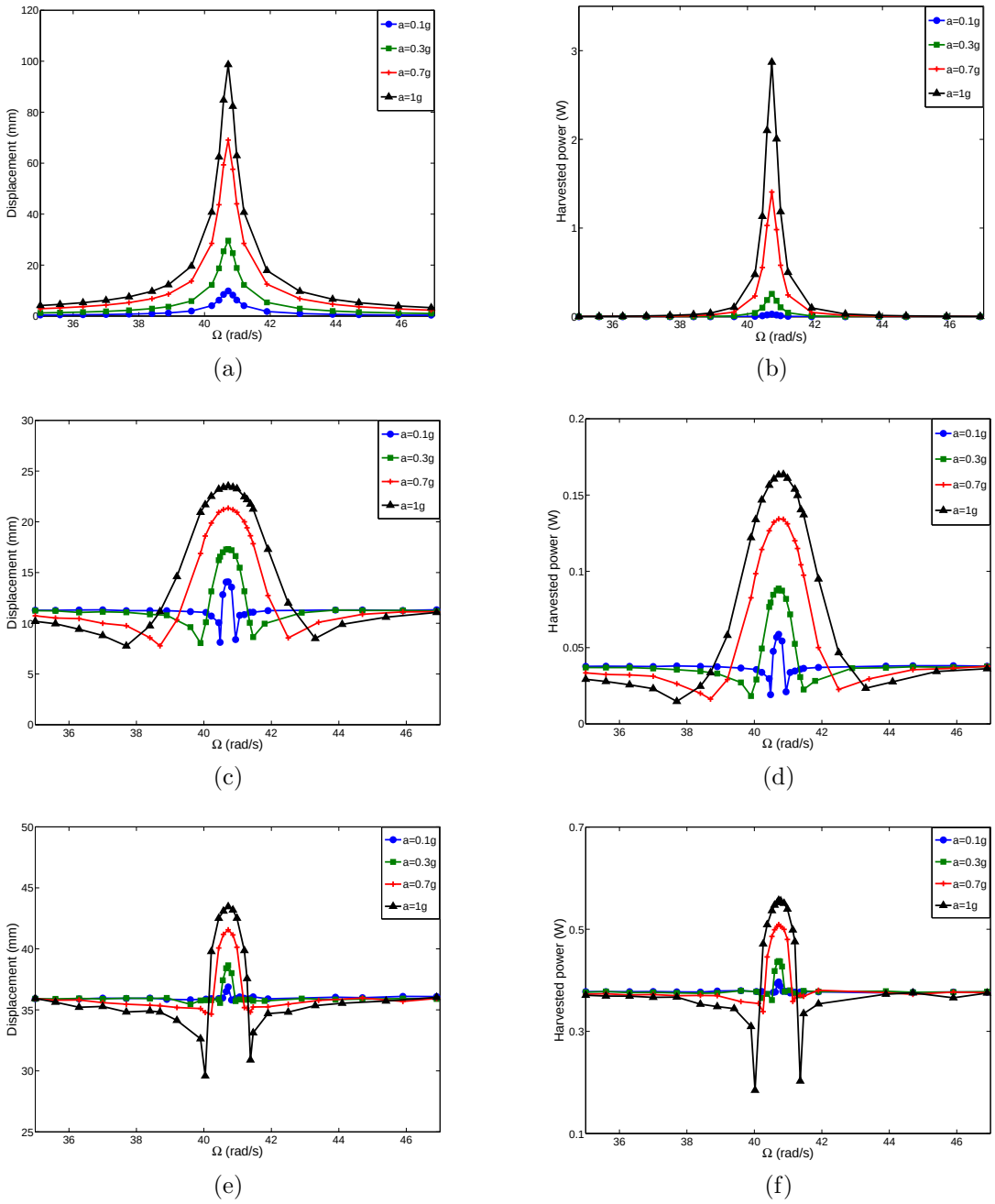

Figure 4.10: Frequency response curves for the tip displacement (a,c,e) and harvested power (b,d,f) when the load resistance is set equal to $10^3\Omega$ and for different base excitations and wind speeds. (a), (b) $U = 0m/s$, (c), (d) $U = 5m/s$ and (e), (f) $U = 13m/s$.

associated with maximum levels of harvested power when $10^4\Omega$ and $10^5\Omega$. It is also noted that the quenching phenomenon is more pronounced when $R = 10^4\Omega$ and $R = 10^5\Omega$. For

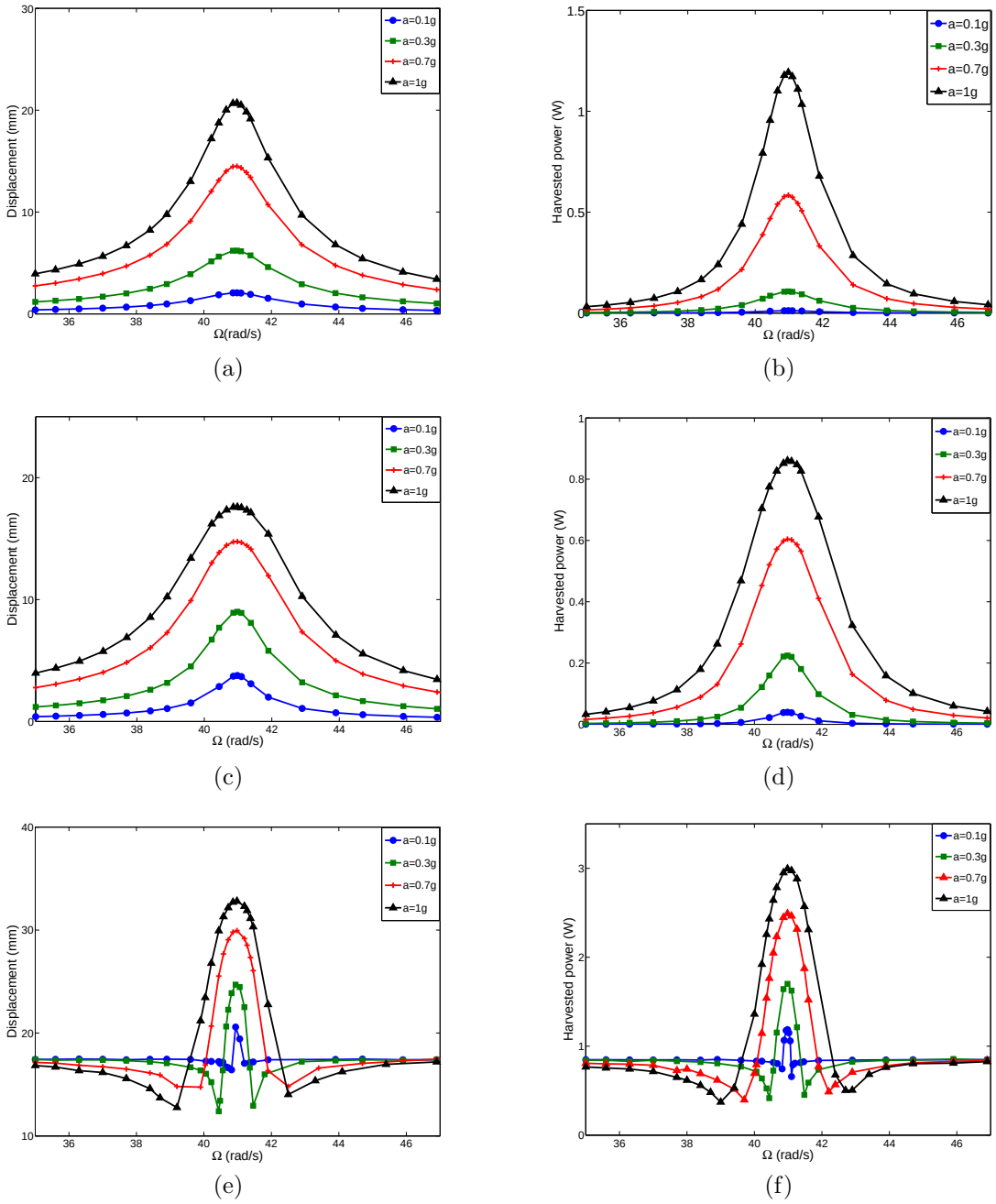

Figure 4.11: Frequency response curves for the tip displacement (a,c,e) and harvested power (b,d,f) when the load resistance is set equal to $10^4\Omega$ and for different base excitations and wind speeds. (a), (b) $U = 0m/s$, (c), (d) $U = 5m/s$ and (e), (f) $U = 13m/s$.

example, the differences between pull-out frequency and global frequency are much larger when $R = 10^4\Omega$ and $R = 10^5\Omega$ than that when $R = 10^2\Omega$ and $R = 10^7\Omega$. That is because

$\frac{\rho_{air} U b_{struc} k_1}{2} - 2\xi\omega$ is relative smaller due to the relative larger coupled damping ratios when $R = 10^4\Omega$ and $R = 10^5\Omega$ as shown in Figure 4.2(b). Thus, K is larger according to the expressing of K and then the differences between pull-out frequency and global frequency are much larger when $R = 10^4\Omega$ and $R = 10^5\Omega$.

The curves plotted in figures 4.10 and 4.11 show the frequency-response curves for the tip displacement and harvested power for different wind speeds and base excitations for the load resistances are $10^3\Omega$ and $10^4\Omega$, respectively. Inspecting these curves, we note that the tip displacement and harvested power increase as acceleration of the base excitation is increased. It follows from figure 4.10 that the harvester with $R = 10^3\Omega$ is affected by galloping for different base excitations when $U = 5m/s$ and $U = 13m/s$. In additional, At these wind speeds, the existence of the galloping effect decreases the level of the harvested power and displacement at the resonance region. On the other hand, it increases the level of the harvested power and displacement at the off-resonance region. It is also noted that the effect of the base excitation first decreases and then increases the level of the harvested power and displacement as the external frequency of the base excitation comes nearer to the system. Moreover, the differences between pull-out frequency and global frequency, show in Figure 4.10(c)-(f), increase as base accelerations is increased. Inspecting plotted curves in figure 4.11, we note that the galloping effect takes place only at $U = 13m/s$ when the load resistance is set equal to $10^4\Omega$. Furthermore, at $U = 5m/s$, the effect of wind speed decreases the level of displacement and harvested power when the external acceleration is set equal to $1g$. However, it increases the level of displacement and harvested power when the external acceleration is set equal to $0.1g$, $0.3g$ or $0.7g$. The quenching phenomenon is clearer when increasing the value of the forcing excitation when both the free- and forced-oscillations are present.

The short- and open-circuit configurations of the tip displacement and harvested power for different wind speed values, namely, $U = 0$, 5 and $13m/s$, have different responses, as shown in figure 4.12. These configuration are defined by setting the excitation frequency equal to the short- and open-circuit global frequencies, which are $40.7rad/s$ and $44.2rad/s$, respectively. For the short-circuit configuration, maximum values of the tip displacement are obtained in the low range of load resistance. At higher values of the load resistance, a significant decrease in the tip displacement values is observed. This is due to the fact that, when increasing the load resistance, the global frequency increases, as shown in Figure 4.2(a), and then the harvester is not at resonance for these load resistances. For the open-circuit configuration, an inverse tendency is obtained. Furthermore, there is a range of load resistances when minimum values of the tip displacement are accompanied by maximum levels of the harvested power for both the short- and open-circuit configuration. At $U = 5$ and $13m/s$, the tendencies of the short- and open-circuit configurations change significantly. We note that high values of the tip displacement are obtained in the low and high range of load resistances. The appearance of new branches in the short- and open-circuit configurations

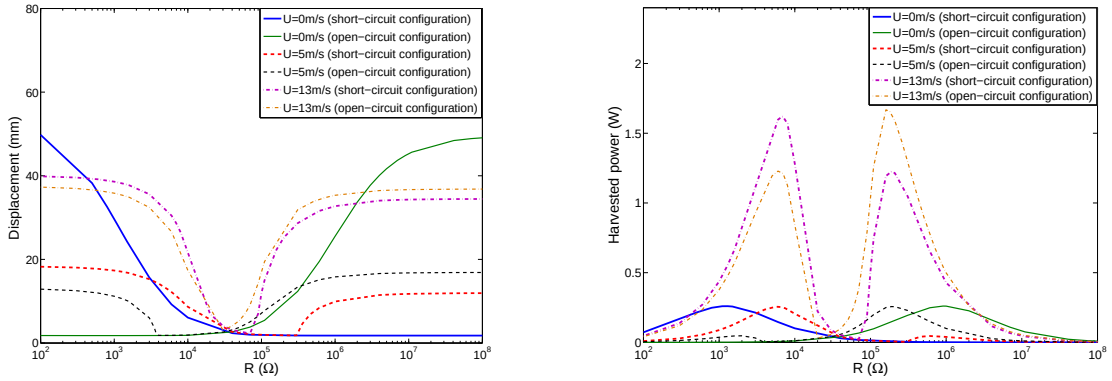

(a) (b)

Figure 4.12: response varied by load resistance in the short-circle (the frequency of the base excitation is equal to the global frequency when R is very small) and open-circle (the frequency of the base excitation is equal to the global frequency when R is very large) situations for different wind speeds when $a = 0.3g$: (a) displacement and (b) harvested power

for the tip displacement are due to the presence of the galloping oscillations. The associated range of the load resistances of these new branches is smaller when $U = 5m/s$ than that when $U = 13m/s$. Furthermore, in the intermediate range of load resistances, minimum values of the tip displacement are always obtained. This is due to the associated maximum global damping values in this range; hence, no galloping effect takes place. For the harvested power, it follows from figure 4.12(b) that new peaks of maximum levels of harvested power take place for both circuit configurations. The range of load resistances when the harvested power is maximum for both the short- and open-configurations is totally different than the range of load resistances when the tip displacement is maximized.

4.6 Conclusion

We have investigated the concept of harvesting energy from hybrid vibrations, namely, base and galloping of a bluff body with a triangular cross-section geometry. In order to convert the associated oscillations to usable electrical power, a piezoelectric transducer is attached to the transverse degree of freedom of the prismatic mass. A nonlinear distributed-parameter model that takes into consideration the galloping force and moment nonlinearities and the base excitation effect is derived based on extended Hamilton's principle. The galloping force and moment are modeled based on a quasi-steady approximation. The Galerkin procedure is introduced to discretize the governing equations of motion. The effects of the load resistance, wind speed on the overall damping, global frequency, and onset of instability were

investigated through a linear analysis of the coupled equations of motion. Then, a nonlinear analysis was performed to investigate the effects of the base acceleration, wind speed, and electrical load resistance on the performance of the harvester and the associated nonlinear phenomena that take place. The linear analysis shows that the load resistance has great effect on the electromechanical damping and global frequency. Moreover, during the nonlinear analysis of the effect of load resistance, wind speed and base acceleration on the harvester's performance, some interesting nonlinear phenomena, such as quenching and pull-out frequency, were investigated. The results also turned out as following: (1) the acceleration of the base vibration has no effect on the onset wind speed; (2)the interaction of galloping effect and base excitation have significant effect on the energy harvester's performance; (3) as the wind speed decreases, the acceleration increases or global damping increases, the difference between pull-out frequency and global frequency increases (the quenching phenomena of the system are more obvious). Furthermore, the existence of both types of excitations leads to the presence of new peaks in the maximum levels of harvested power of both short- and open-circuit configurations. The range of load resistances over which the harvested power is maximum for both the short- and open-circuit configurations is totally different from the range of load resistances over which tip displacement is maximized.

5

Energy Harvesting Through Autoparametric Resonance

We present a nonlinear distributed-parameter model for harvesting energy from an autoparametric vibration system. The system consists of a base structure subjected to an external force and a cantilever beam with a tip mass. The model is used to analyze the effects of the amplitude and frequency of the external force and load resistance on the nonlinear responses of the harvester. The analysis is then used to determine the optimum load resistance not only to control the motion of the base structure but also to harvest energy. Details of the proposed harvester's design and derivation of the governing equations are presented. A reduced-order model is derived using the exact mode shapes of the cantilever beam. The method of multiple scales is used to obtain an approximate analytical solution to the derived nonlinear set of differential equations. Solutions to different approximate orders are compared and validated. These solutions are used to analyze the stability and bifurcation of the system. Four kinds of generated motions are discussed. Approximate expressions of the global frequency and coupling damping ratio of the cantilever beam are derived and proved by the numerical simulation of the linearized governing equation. Nonlinear analysis is performed to determine effects of the external force and load resistance on the response of the harvester over a wide range of operating regimes.

5.1 Modeling of an autoparametric energy harvester

The energy harvesting system under investigation is based on the autoparametric vibration absorber which is similar to the one considered by Haxton and Barr [19]. This system consists of a base structure subjected to an external force $F(t)$ and a cantilever beam with a tip mass M_t, as shown in figure 5.1. The cantilever beam is composed of one steel and two piezoelectric layers. The two piezoelectric sheets are bonded to both sides of the steel layer and connected in parallel with opposite polarity to an electrical load resistance. The

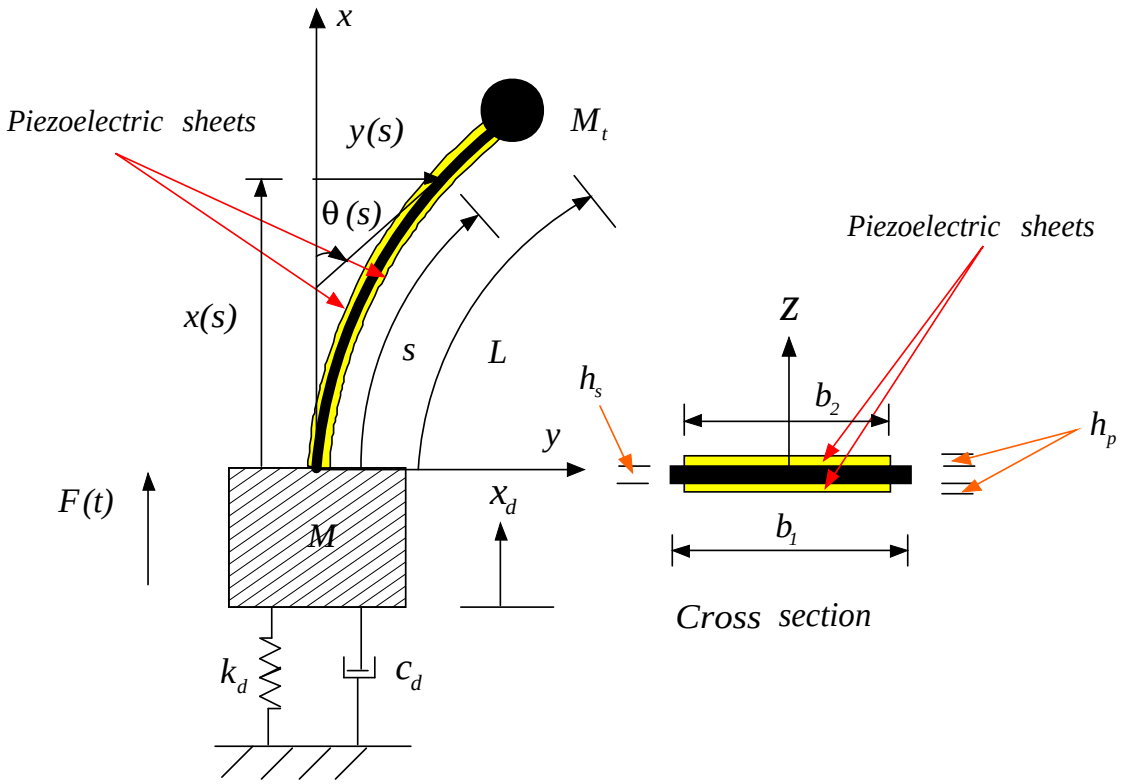

Figure 5.1: Schematic diagram of an autoparametric energy harvester

base structure M undergoes a vertical displacement x_d and has a stiffness k_d and damping coefficient c_d. One local coordinate $x - y$ is fixed on top of the base structure. The attached cantilever beam with the length L mainly moves in the horizontal direction $y(s)$ where s is the coordinate axis along the beam.

To derive the governing equation of the above system, we use the extended Hamilton's principle [78]:

$$\int_{t_1}^{t_2} (\delta T - \delta V + \delta W_{nc}) dt = 0 \tag{5.1}$$

where, T, V and W_{nc} are respectively the kinetic energy, potential energy and virtual work due to nonconservative forces. The kinetic energy T and potential energy V are expressed

Table 5.1: Physical and geometric properties of the energy harvester

E_s	Steel Young's Modulus (GN/m^2)	200
E_p	Piezoelectric material Young's Modulus (GN/m^2)	62
ρ_s	Steel density (kg/m^3)	7800
ρ_p	Piezoelectric material density (kg/m^3)	7800
L	Length of the beam (mm)	200
b_1	Width of the steel layer (mm)	38
b_2	Width of the piezoelectric layer (mm)	36.2
h_s	Steel layer thickness (mm)	0.7
h_p	Piezoelectric layer thickness (mm)	0.267
M_t	Tip mass (kg)	0.26
M	Mass of base structure (kg)	1
I_t	Rotational modulus of inertia of the tip body (m^3)	$4.33 * 10^{-5}$
d_{31}	Strain coefficient of piezoelectric layer (pC/N)	-320
ϵ_{33}^s	Permittivity component at constant strain (nF/m)	27.3

as [93]

$$
\begin{aligned}
&T = \tfrac{1}{2}M(\tfrac{\partial x_d(t)}{\partial t})^2 + \tfrac{1}{2}M_t[\tfrac{\partial x_d(t)}{\partial t} - \tfrac{d}{dt}(\int_0^L \tfrac{1}{2}(\tfrac{\partial y(\eta,t)}{\partial \eta})^2 d\eta)]^2 + \tfrac{1}{2}M_t(\tfrac{\partial y(L,t)}{\partial t})^2 + \tfrac{1}{2}I_t(\tfrac{\partial^2 y(L,t)}{\partial t \partial s})^2 \\
&+\tfrac{1}{2}\int_0^L\ m[\tfrac{\partial x_d(t)}{\partial t} - \tfrac{d}{dt}(\int_0^s \tfrac{1}{2}(\tfrac{\partial y(\eta,t)}{\partial \eta})^2 d\eta)]^2 ds\ + \tfrac{1}{2}\int_0^L m(\tfrac{\partial y(s,t)}{\partial t})^2 ds \\
&\text{and} \\
&V = \int_0^L \tfrac{1}{2}EI[(\tfrac{\partial^2 y(s,t)}{\partial s^2})^2 + (\tfrac{\partial^2 y(s,t)}{\partial s^2})^2(\tfrac{\partial y(s,t)}{\partial s})^2]ds + \int_0^L mg(x_d(t) - \tfrac{(L-s)}{2}(\tfrac{\partial y(s,t)}{\partial s})^2)ds \\
&+M_t g(x_d(t) - \int_0^L \tfrac{1}{2}(\tfrac{\partial y(s,t)}{\partial s})^2 ds) + Mgx_d(t) + \tfrac{1}{2}k_d x_d(t)^2
\end{aligned}
\tag{5.2}
$$

where M_t and M are respectively the tip mass and mass of the base structure, L is the length of the cantilever beam, I_t is the rotational inertia of the tip mass relative to tip of the cantilever beam, m is the mass of the beam per unit length and is given by: $m{=}b_1\rho_s h_s + 2b_2\rho_p h_p$ and EI is the stiffness of the cantilever beam and is given by: $EI{=}\ \frac{1}{12}b_1 E_s {h_s}^3 + \frac{2}{3}b_2 E_p[(h_p + \frac{h_s}{2})^3 - \frac{{h_s}^3}{8}]$. In the expressions of m and EI, ρ_s and ρ_p are the respective densities of the steel and piezoelectric layers, h_s and h_p are the respective thicknesses of these layers, b_1 and b_2 are the respective widths of multiple layers and E_s and E_p are the Young's Modulus of the steel and piezoelectric layers, respectively. The values of all these parameters, as used in this work, are shown in Table 5.1.

In this system, the nonconservative forces includes the damping force, external force and electric force. Thus, the virtual work due to nonconservative forces in Hamilton's equation (5.1) is written as

$$W_{nc} = W_{ele} + W_{damp} + W_{ext} \tag{5.3}$$

where W_{ele}, W_{damp} and W_{ext} represent the virtual work due to the electronic, damping and

external forces, respectively. The virtual work due to electric force W_{ele} is given by [42]

$$W_{ele} = \int_0^L -M_{ele}\frac{\partial^2 y(s,t)}{\partial s^2}ds \tag{5.4}$$

where M_{ele} is the moment due to the electric effect. For the case where the upper and lower layers are parallelly connected, it is expressed as

$$\begin{aligned} &M_{ele} = b_2[\textstyle\int_{-h_p-h_s/2}^{-h_s/2} -e_{31}(-\frac{V(t)}{h_p})zdz + \int_{h_s/2}^{h_p+h_s/2} e_{31}(-\frac{V(t)}{h_p})zdz](H(s)-H(s-L)) \\ &= \vartheta_p V(t)(H(s)-H(s-L)) \end{aligned} \tag{5.5}$$

where $V(t)$ is the voltage of the piezoelectric layer, $H(s)$ is the step function, $e_{31} = E_p d_{31}$ is the piezoelectric stress coefficient and ϑ_p is the piezoelectric coupling term which is given by $\vartheta_p = -b_2 e_{31}(h_p + h_s)$. Moreover, the virtual work due to the damping force W_{damp} and the external force W_{ext} are expressed as

$$\begin{aligned} &W_{damp} = \oint F_{d1}(t)dx_d + \textstyle\int_0^L \oint F_{d2}(s,t)dyds \\ &W_{ext} = F(t)x_d(t) \end{aligned} \tag{5.6}$$

where $F(t)$ is the external force acting on the base structure, as shown in figure 5.1, and is assumed to be of the form $F(t) = Fcos\Omega t$, F_{d1} is the damping force of the base structure and written as $F_{d1} = -c_d\frac{\partial x_d(t)}{\partial t}$ and F_{d2} is the damping force of the cantilever beam whose expression [58] is: $F_{d2} = -c_a\frac{\partial y(s,t)}{\partial t} - c_s I\frac{\partial^5 y(s,t)}{\partial s^4 \partial t}$. In these expressions of nonconservative forces, c_d is the damping coefficient of the base structure, c_s and c_a are respectively the viscous strain and air damping coefficients of the cantilevered beam and F and Ω are the amplitude and frequency of the external force, respectively.

Substituting the expressions for the kinetic energy T, potential energy V and virtual work W_{nc} due to nonconservative forces into extended Hamilton's equation (5.1), the governing equations of the electromechanical system are written as

$$\begin{aligned} &(M_t + M + \overline{M})\tfrac{\partial^2 x_d(t)}{\partial t^2} + c_d\tfrac{\partial x_d(t)}{\partial t} + k_d x_d(t) - M_t\textstyle\int_0^L \frac{d^2}{dt^2}[\frac{1}{2}(\frac{\partial y(s,t)}{\partial s})^2]ds - \int_0^L m\int_0^s \frac{d^2}{dt^2}[\frac{1}{2}(\frac{\partial y(\eta,t)}{\partial \eta})^2]d\eta ds \\ &+(M_t + M + \overline{M})g = F\cos(\Omega t) \\ &m\tfrac{\partial^2 y(s,t)}{\partial t^2} + EI[\tfrac{\partial^4 y(s,t)}{\partial s^4} + (\tfrac{\partial y(s,t)}{\partial s})^2\tfrac{\partial^4 y(s,t)}{\partial s^4} + 4\tfrac{\partial y(s,t)}{\partial s}\tfrac{\partial^2 y(s,t)}{\partial s^2}\tfrac{\partial^3 y(s,t)}{\partial s^3} + (\tfrac{\partial^2 y(s,t)}{\partial s^2})^3] \\ &+c_s I\tfrac{\partial^5 y(s,t)}{\partial s^4 \partial t} + c_a\tfrac{\partial y(s,t)}{\partial t} + [-mg - m\tfrac{\partial^2 x_d(t)}{\partial t^2} + m\textstyle\int_0^s \frac{d^2}{dt^2}[\frac{1}{2}(\frac{\partial y(\eta,t)}{\partial \eta})^2]d\eta - M_t\frac{\partial^2 x_d(t)}{\partial t^2}\delta(s-L) \\ &+M_t\textstyle\int_0^s \frac{d^2}{dt^2}[\frac{1}{2}(\frac{\partial y(\eta,t)}{\partial \eta})^2]d\eta\delta(s-L)]\frac{\partial y(s,t)}{\partial s} + N\frac{\partial^2 y(s,t)}{\partial s^2} + \vartheta_p V(t)\left(\frac{\partial\delta(s)}{\partial s} - \frac{\partial\delta(s-L)}{\partial s}\right) = 0 \end{aligned} \tag{5.7}$$

where $\overline{M}$ is the total mass of the multi-layered cantilever beam and calculated as $\overline{M} = \int_0^L m dx$, and N is representative axial force and given by $N = mg(L-s) + M_t g + M_t\frac{\partial^2 x_d(t)}{\partial t^2} + m\frac{\partial^2 x_d(t)}{\partial t^2}(L-s) - M_t\int_0^L \frac{d^2}{dt^2}[\frac{1}{2}(\frac{\partial y(\eta,t)}{\partial \eta})^2]d\eta - \int_s^L m\int_0^\xi \frac{d^2}{dt^2}[\frac{1}{2}(\frac{\partial y(\eta,t)}{\partial \eta})^2]d\eta d\xi$.

To relate the mechanical and electrical variables, we use the Gauss law [88] which is expressed as

$$\frac{d}{dt}\int_A \mathbf{D}.\mathbf{n}\; dA = \frac{d}{dt}\int_A D_2\; dA = \frac{V}{R} \tag{5.8}$$

where $\mathbf{D}$ is the electric displacement vector and $\mathbf{n}$ is the normal vector of the plane of the beam. The electric displacement component D_2 is given by the following relation [42]:

$$D_2(s,t) = e_{31}\varepsilon_{11}(s,t) + \epsilon_{33}^s E_2 \tag{5.9}$$

where ε_{11} is the axial strain component in the steel and piezoelectric layers and is given by $\varepsilon_{11}(s,y,t) = -z\frac{\partial^2 y(s,t)}{\partial s^2}$, ϵ_{33}^s is the permitting component at constant strain. Substituting Equation (5.9) into (5.8), we obtain the equation governing the strain-voltage relation:

$$-e_{31}(h_p + h_s)b_2\int_0^L \frac{\partial^3 y(s,t)}{\partial t \partial s^2} ds - \frac{2\epsilon_{33}^s b_2 L}{h_p}\frac{dV(t)}{dt} = \frac{V(t)}{R} \tag{5.10}$$

5.2 Representative reduced-order model

To characterize the linear and nonlinear responses of the energy harvester and investigate the effects of different parameters on its performance, we use distributed-parameter representation. To this end, we discretize the motions of the cantilever beam using the Galerkin Method and determine the exact mode shapes. We consider first the free vibrations of the cantilever beam, which leads to the eigenvalue problem. Therefore, we drop the damping, polarization and nonlinear coupling terms in the second expression in equation (5.7) and separate the horizontal displacement $y(s,t)$ into spatial and time variables as follows:

$$y(s,t) = \sum_{i=1}^{\infty} \phi_i(s) q_i(t) \tag{5.11}$$

where $q_i(t)$ and $\phi_i(s)$ are the modal coordinates and shapes of the cantilever beam attached by the tip mass, respectively. The modal shapes are expressed as [79]

$$\phi_i(s) = A_i \sin\beta_i s + B_i \cos\beta_i s + C_i \sinh\beta_i s + D_i \cosh\beta_i s \tag{5.12}$$

where A_i, B_i, C_i and D_i are coefficients to be determined from the boundary conditions. According to Ref [93], the linearized boundary conditions are written as

$$\begin{aligned} &y(0,t) = 0; \tfrac{\partial y(0,t)}{\partial s} = 0; \\ &EI\tfrac{\partial^3 y(L,t)}{\partial s^3} + M_t g\tfrac{\partial y(L,t)}{\partial s} - M_t\tfrac{\partial^2 y(L,t)}{\partial t^2} = 0; \\ &EI\tfrac{\partial^2 y(L,t)}{\partial s^2} + I_t\tfrac{\partial^3 y(L,t)}{\partial s \partial t^2} = 0 \end{aligned} \tag{5.13}$$

Substituting equation (5.11) into equation (5.13), we obtain the simplified boundary conditions

$$\begin{aligned} &\phi_i(0) = 0, \quad \phi_i'(0) = 0, \\ &EI\phi_i''(L) - \omega_i^2 I_t \phi_i'(L) = 0, \\ &EI\phi_i'''(L) + M_t g \phi_i'(L) + \omega_i^2 M_t \phi_i(L) = 0 \end{aligned} \tag{5.14}$$

where the $'$ is used to indicate the derivative with respect to s. Furthermore, based on the linearized dynamic equations and boundary conditions, the eigenfunctions are normalized by the following expression [93]:

$$\begin{aligned} &\int_0^L m\phi_p(s)\phi_r(s)ds + M_t\phi_p(L)\phi_r(L) + I_t{\phi_p}'(L){\phi_r}'(L) = \delta_{pr} \\ &\int_0^L EI{\phi_p}''(s){\phi_r}''(s)ds - \int_0^L M_t g{\phi_p}'(s){\phi_r}'(s)ds - \int_0^L mg(L-s){\phi_p}'(s){\phi_r}'(s)ds = \delta_{pr}\omega_r^2 \end{aligned} \tag{5.15}$$

where p and r are used to represent the vibration modes, ω_r is the rth natural frequency of the cantilever beam, and δ_{pr} is the Kronecker delta, defined as unity when p is equal to r and zero otherwise.

Substituting equation (5.11) into equations (5.7) and (5.10) and considering the first mode, the governing equations are reduced to

$$\begin{aligned} &\ddot{x}(t) + 2\xi_x\omega_x\dot{x}(t) + \omega_x^2 x(t) - \tfrac{\eta_1}{M+M_t+\overline{M}}\left(\dot{q}(t)^2 + q(t)\ddot{q}(t)\right) = F_0\cos\Omega t; \\ &\ddot{q}(t) + 2\xi_1\omega_1\dot{q}(t) + (\omega_1^2 - \eta_1\ddot{x}(t))q(t) + \eta_2 q(t)^3 + \eta_3 q(t)\left(\dot{q}(t)^2 + q(t)\ddot{q}(t)\right) + \theta_p V(t) = 0; \\ &\tfrac{V(t)}{R} + C_p\dot{V}(t) - \theta_p\dot{q}(t) = 0 \end{aligned} \tag{5.16}$$

where the dot is used to indicate the derivative with respect to time t, x is a new variable whose expression is $x = x_d + x_0$ where x_0 is the static vertical displacement of the system and is given by $\frac{(M+m+\overline{m})g}{k_d}$, ξ_x and ξ_1 are respectively the mechanical damping coefficients of base structure and cantilever beam, ω_x is the natural frequency of the base structure and is given by $\omega_x = \sqrt{\frac{k_d}{M_t+\overline{M}+M}}$, ω_1 is the first natural frequency of the beam which can be determined from equation (5.15), the coefficients θ_p and C_p are respectively the piezoelectric coupling term and capacitance of the harvester which are given by $\theta_p = \phi'(L)\vartheta_p$ and $C_p = \frac{2\varepsilon_{33}^s b_2 L}{h_p}$, F_0 is the nondimensionalized external force and is written by $F_0 = \frac{F}{M_t+\overline{M}+M}$ and η_1, η_2 and η_3 are the nondimensionalized coefficients whose expressions are $\eta_1 = M_t\int_0^L \phi'^2 ds + \int_0^L m\int_0^s \phi'^2 d\eta ds$, $\eta_2 = \int_0^L EI(\phi\phi'^2\phi^{IV} + 4\phi\phi'\phi''\phi''' + \phi\phi''^3)ds$ and $\eta_3 = M_t\Big(\int_0^L \phi'^2 ds\Big)^2 + \int_0^L m(\int_0^s \phi'^2 d\eta)^2 ds$.

5.3 Approximate solution

We use the method of mutiple sacles [80, 81] to determine an approximate solution of the governing equations. Particularly, we are interested in analytical solutions for the power as a function of the different parameters. Furthermore, the approximate solution can be used to assess the system's stability and bifurcation points and, as such, gives details on the limitations and operation range of this harvester. To simplify the representation of the physical system, we introduce new variables $u_1 = \frac{q}{\sqrt{M+M_t+\bar{M}}x_0}$, $u_2 = \frac{x}{x_0}$ and $u_3 = V$ and rewrite the governing equations as

$$\begin{aligned}
&\ddot{u}_1 + \omega_1^2 u_1 + 2\varepsilon\mu_1\dot{u}_1 - \varepsilon u_1\ddot{u}_2 + \varepsilon^2\delta_1 u_1^3 + \varepsilon^2\delta_2 u_1(\dot{u}_1^2 + u_1\ddot{u}_1) + \varepsilon\delta_3 u_3 = 0;\\
&\ddot{u}_2 + \omega_2^2 u_2 + 2\varepsilon\mu_2\dot{u}_2 - \varepsilon(\dot{u}_1^2 + u_1\ddot{u}_1) = F_0\cos\Omega t;\\
&R\delta_5\dot{u}_3 - R\delta_4\dot{u}_1 + u_3 = 0
\end{aligned} \tag{5.17}$$

where the new coefficients are given by: $\omega_2 = \omega_x$, $\varepsilon = \eta_1 x_0$, $\mu_1 = \frac{\xi_1\omega_1}{\varepsilon}$, $\mu_2 = \frac{\xi_x\omega_x}{\varepsilon}$, $\delta_1 = \frac{\eta_2(M+M_t+\bar{M})}{\eta_1^2}$, $\delta_2 = \frac{\eta_3(M+M_t+\bar{M})}{\eta_1^2}$, $\delta_3 = \frac{\theta_p}{\eta_1\sqrt{M+M_t+\bar{M}}x_0^2}$, $\delta_4 = \theta_p\sqrt{M+M_t+\bar{M}}x_0$ and $\delta_5 = C_p$. Next, we define new time variables as:

$$T_n = \varepsilon^n t, \quad n = 0, 1, 2 \tag{5.18}$$

where T_0 is a fast-time scale, and T_1 and T_2 are slow-time scales. Because the original independent time scale t has been replaced by the new independent time scales T_0, T_1 and T_2, the derivatives with respect to t are changed to:

$$\begin{aligned}
\tfrac{d}{dt} &= D_0 + \varepsilon D_1 + \varepsilon^2 D_1 + \vartheta(\varepsilon^3)\\
\tfrac{d^2}{dt^2} &= D_0^2 + 2\varepsilon D_0 D_1 + \varepsilon^2(D_1 + 2D_0 D_2) + \vartheta(\varepsilon^3)
\end{aligned} \tag{5.19}$$

where $D_i = \partial/\partial T_i$ and $\vartheta(\varepsilon^3)$ indicates order 3 of ε or higher. Following Nayfeh [80], we rewrite the solutions u_1, u_2 and u_3 as

$$u_j(t;\varepsilon) = u_{j0}(T_0, T_1, T_2) + \varepsilon u_{j1}(T_0, T_1, T_2) + \varepsilon^2 u_{j2}(T_0, T_1, T_2) + \vartheta(\varepsilon^3) \tag{5.20}$$

where u_{jk} are functions that depend on T_n and do not depend explicitly on ε, and $j = 1, 2, 3$ signify respectively the displacement of the beam, the displacement of the base structure and the generated voltage. To analyze the autoparametric vibration system, we assume the amplitude of the external force to be $F_0 = \varepsilon f$. Then, we substitute equations (5.18), (5.19) and (5.20) into nondimensional governing equation (5.17) and equate the terms with coefficients of equal ε powers to obtain the following set of equations

ε^0 order

$$\begin{aligned} &D_0^2 u_{10} + \omega_1^2 u_{10} = 0; \\ &D_0^2 u_{20} + \omega_2^2 u_{20} = 0; \\ &-R\delta_4 D_0 u_{10} + R\delta_5 D_0 u_{30} + u_{30} = 0 \end{aligned} \tag{5.21}$$

ε^1 order

$$\begin{aligned} &D_0^2 u_{11} + \omega_1^2 u_{11} = -2D_0 D_1 u_{10} - 2\mu_1 D_0 u_{10} + u_{10} D_0^2 u_{20} - \delta_3 u_{30}; \\ &D_0^2 u_{21} + \omega_2^2 u_{21} = (D_0 u_{10})^2 - 2D_0 D_1 u_{20} - 2\mu_2 D_0 u_{20} + u_{1,0} D_0^2 u_{10} + \tfrac{1}{2}\mathrm{e}^{-\mathrm{i}T_0\Omega} f + \tfrac{1}{2}\mathrm{e}^{\mathrm{i}T_0\Omega} f; \\ &-R\delta_4 D_0 u_{11} + R\delta_5 D_0 u_{31} + u_{31} = R\delta_4 D_1 u_{10} - R\delta_5 D_1 u_{30} \end{aligned} \tag{5.22}$$

ε^2 order

$$\begin{aligned} &D_0^2 u_{12} + \omega_1^2 u_{12} = -2D_0 D_1 u_{11} - D_1^2 u_{10} - 2D_0 D_2 u_{10} - 2\mu_1 D_0 u_{11} - 2\mu_1 D_1 u_{10} + u_{1,0} D_0^2 u_{21} \\ &+2u_{10} D_0 D_1 u_{20} - \delta_2 u_{1,0} (D_0 u_{10})^2 - \delta_2 u_{10}^2 D_0^2 u_{10} - \delta_1 u_{10}^3 + u_{11} D_0^2 u_{20} - \delta_3 u_{31}; \\ &D_0^2 u_{22} + \omega_2^2 u_{22} = 2D_0 u_{10} D_0 u_{11} + 2D_0 u_{10} D_1 u_{10} - 2D_0 D_1 u_{21} - D_1^2 u_{20} - 2D_0 D_2 u_{20} \\ &-2\mu_2 D_0 u_{21} - 2\mu_2 D_1 u_{20} + u_{10} D_0^2 u_{11} + 2u_{10} D_0 D_1 u_{10} + u_{11} D_0^2 u_{10}; \\ &-R\delta_4 D_0 u_{12} + R\delta_5 D_0 u_{32} + u_{32} = R\delta_4 D_1 u_{11} + R\delta_4 D_2 u_{10} - R\delta_5 D_1 u_{31} - R\delta_5 D_2 u_{30} \end{aligned} \tag{5.23}$$

The solutions of the first two expressions in equation (5.21) are of the form

$$u_{j0} = A_j(T_1, T_2) e^{\mathbf{i}\omega_j T_0} + cc \tag{5.24}$$

where $\mathbf{i} = \sqrt{-1}$, A_1 and A_2 are complex values of the displacements of cantilever beam and base structure depending on the slow time scales, respectively, cc stands for the complex conjugate, and $j = 1, 2$. Using equation (5.24), we can determine the solution of the third expression in equation (5.21) as

$$u_{30} = \frac{R\delta_4\omega_1}{-\mathrm{i} + R\delta_5\omega_1} A_1(\mathrm{T}_1,\mathrm{T}_2)\mathrm{e}^{\mathrm{i}\omega_1 T_0} + cc \tag{5.25}$$

To determine the values of A_1 and A_2, we express the nearness of Ω to ω_2 and of ω_1 to $\frac{1}{2}\omega_2$ by using the detuning parameters σ_1 and σ_2 as follows:

$$\begin{aligned} \Omega &= \omega_2 + \varepsilon\sigma_1 \\ \omega_1 &= \tfrac{1}{2}\omega_2 + \varepsilon\sigma_2 \end{aligned} \tag{5.26}$$

Using the above frequency relationship of ω_1, ω_2 and Ω and substituting equations (5.24) and (5.25) into the first two equations of (5.22), we determine the expressions of $D_1 A_1$ and $D_1 A_2$ from the secular terms. Moreover, u_{11} and u_{21} are determined by eliminating the secular

terms, which yields:

$$\begin{array}{l} u_{11} = \frac{\omega_2}{2\omega_1+\omega_2} A_1 A_2 e^{\mathrm{i}(\omega_1+\omega_2)T_0} + B_1(T_1,T_2)e^{\mathrm{i}\omega_1 T_0} + cc \\ u_{21} = B_2(T_1,T_2)e^{\mathrm{i}\omega_2 T_0} + cc \end{array} \tag{5.27}$$

where B_1 and B_2 are complex values of the displacements of the cantilever beam, u_{11}, and base structure, u_{21}, depending on the slow time scales, respectively. The solution of u_{31} is obtained by substituting equations (5.24), (5.25) and (5.27) into the third equation of (5.22). Using the solutions of u_{10}, u_{11}, u_{20}, u_{21}, u_{30} and u_{31} and detuning equation (5.26), we determine the expressions for D_2A_1 and D_2A_2 from the secular terms of the first two equations of (5.23). We write these expressions in the form of complex-valued modulation equations that are given by

$$\begin{array}{l} 2\mathrm{i}\omega_1\dot{A}_1 = 2\mathrm{i}\omega_1(\varepsilon D_1 A_1 + \varepsilon^2 D_2 A_1) \\ 2\mathrm{i}\omega_2\dot{A}_2 = 2\mathrm{i}\omega_2(\varepsilon D_1 A_2 + \varepsilon^2 D_2 A_2) \end{array} \tag{5.28}$$

where the dot indicates the derivative with respect to time t. To satisfy equations (5.28) deriving from a Lagrangian [93], we determine the expressions of B_1 and B_2 as

$$\begin{array}{l} B_1 = \frac{\mathbf{i}}{2\omega_1+\omega_2} D_1 A_1 \\ B_2 = \frac{8\omega_1^4 - 4\omega_1^3\omega_2 - 8\omega_1^2\omega_2^2 - 2\omega_1\omega_2^3 + \omega_2^4}{16\omega_1^4\omega_2 + 8\omega_1^3\omega_2^2} \mathbf{i} D_1 A_2 \end{array} \tag{5.29}$$

We then obtain complex-valued modulation equation as

$$\begin{array}{l} \dot{A}_1 = (m_{11} + \mathbf{i}m_{12})A_1 + (m_{21} + \mathbf{i}m_{22})A_2\overline{A_1}e^{-2\mathbf{i}\varepsilon\sigma_2 t} + (m_{31} + \mathbf{i}m_{32})A_1^2\overline{A_1} \\ +(m_{41} + \mathbf{i}m_{42})A_1A_2\overline{A_2} + (m_{51} + \mathbf{i}m_{52})f\overline{A_1}e^{\mathbf{i}\varepsilon(\sigma_1 - 2\sigma_2)t} \\ \dot{A}_2 = (n_{11} + \mathbf{i}n_{12})A_2 + (n_{21} + \mathbf{i}n_{22})fe^{\mathbf{i}\varepsilon\sigma_1 t} + (n_{31} + \mathbf{i}n_{32})A_1^2 e^{2\mathbf{i}\varepsilon\sigma_2 t} \\ +(n_{41} + \mathbf{i}n_{42})A_1A_2\overline{A_1} \end{array} \tag{5.30}$$

where the coefficients m_{jk} and n_{jk} are given by

$$m_{11} = \frac{\varepsilon\left(\varepsilon R^3\delta_3^2\delta_4^2\delta_5\left(-1+R^2\delta_5^2\omega_1^2\right) - 2\mu_1\left(1+R^2\delta_5^2\omega_1^2\right)^3 - R\delta_3\delta_4\left(1+R^2\delta_5^2\omega_1^2\right)\left(1+2R\varepsilon\delta_5\mu_1+R^2\delta_5^2\omega_1^2\right)\right)}{2\left(1+R^2\delta_5^2\omega_1^2\right)^3},$$

$$m_{12} = -\frac{\varepsilon\left(4\varepsilon\mu_1^2\left(1+R^2\delta_5^2\omega_1^2\right)^3 + R^2\varepsilon\delta_3^2\delta_4^2\left(1-6R^2\delta_5^2\omega_1^2+R^4\delta_5^4\omega_1^4\right) - 4R\delta_3\delta_4\left(R\delta_5\left(\omega_1+R^2\delta_5^2\omega_1^3\right)^2 + \varepsilon\mu_1\left(-1+R^4\delta_5^4\omega_1^4\right)\right)\right)}{8\omega_1\left(1+R^2\delta_5^2\omega_1^2\right)^3},$$

$$\begin{array}{l} m_{21} = \frac{1}{16\omega_1^4\left(1+R^2\delta_5^2\omega_1^2\right)\left(1+R^2\delta_5^2(\omega_1-\omega_2)^2\right)(2\omega_1+\omega_2)}\varepsilon^2\omega_2(-\mu_2\left(1+R^2\delta_5^2\omega_1^2\right)\left(1+R^2\delta_5^2(\omega_1-\omega_2)^2\right) \\ (24\omega_1^4 + 20\omega_1^3\omega_2 + 4\omega_1^2\omega_2^2 + 2\omega_1\omega_2^3 - \omega_2^4) - 4\omega_1^2\omega_2(4\mu_1\omega_1\left(1+R^2\delta_5^2\omega_1^2\right)\left(1+R^2\delta_5^2(\omega_1-\omega_2)^2\right), \\ +R\delta_3\delta_4\left(2R^2\delta_5^2\omega_1^3 - 2R^2\delta_5^2\omega_1^2\omega_2 - R^2\delta_5^2\omega_2^3 + \omega_1\left(2+R^2\delta_5^2\omega_2^2\right)\right))) \end{array}$$

$$\begin{array}{l} m_{22} = -\frac{1}{4\omega_1^2\left(1+R^2\delta_5^2\omega_1^2\right)\left(1+R^2\delta_5^2(\omega_1-\omega_2)^2\right)(2\omega_1+\omega_2)}\varepsilon\omega_2^2(-4R^4\delta_5^4\omega_1^6 + 4R^4\delta_5^4\omega_1^5\omega_2 - 2R^4\delta_5^3\omega_1^3\omega_2\left(2\varepsilon\delta_3\delta_4 + 3\delta_5\omega_2^2\right) \\ +\omega_2^2\left(1 - R^2\varepsilon\delta_3\delta_4\delta_5 + R^2\delta_5^2\omega_2^2\right) - 2\omega_1\omega_2\left(2 + R^2\varepsilon\delta_3\delta_4\delta_5 + 3R^2\delta_5^2\omega_2^2\right) + R^2\delta_5^2\omega_1^4\left(-8 + 2R^2\varepsilon\delta_3\delta_4\delta_5 + 5R^2\delta_5^2\omega_2^2\right) \\ +\omega_1^2\left(-4 + 6R^2\delta_5^2\omega_2^2 + R^4\delta_5^4\omega_2^4 + 2R^2\varepsilon\delta_3\delta_4\delta_5\left(1+R^2\delta_5^2\omega_2^2\right)\right)) \end{array}$$

$$m_{31} = 0,$$

$m_{32} = \frac{\varepsilon^2\left(-8(-3+4\delta_2)\omega_1^4-4(-5+4\delta_2)\omega_1^3\omega_2+4\omega_1^2\omega_2^2+2\omega_1\omega_2^3-\omega_2^4+24\delta_1\omega_1(2\omega_1+\omega_2)\right)}{16\omega_1^2(2\omega_1+\omega_2)}$,
$m_{41} = 0$,
$m_{42} = \frac{\varepsilon^2\omega_2^3\left(4\omega_1^2-2\omega_1\omega_2+\omega_2^2\right)}{8\omega_1^3(2\omega_1+\omega_2)}$,
$m_{51} = 0$,
$m_{52} = -\frac{\varepsilon^2\left(24\omega_1^4+20\omega_1^3\omega_2+4\omega_1^2\omega_2^2+2\omega_1\omega_2^3-\omega_2^4\right)}{64\omega_1^4(2\omega_1+\omega_2)}$,
$n_{11} = -\varepsilon\mu_2$,
$n_{12} = -\frac{\varepsilon^2\mu_2^2}{2\omega_2}$,
$n_{21} = \frac{\varepsilon^2\mu_2}{8\omega_2^2}$,
$n_{22} = \frac{\varepsilon\left(-16\omega_1^4+8\omega_1^3(\Omega-2\omega_2)+8\omega_1^2(\Omega-\omega_2)\omega_2+2\omega_1(\Omega-\omega_2)\omega_2^2+\omega_2^3(-\Omega+\omega_2)\right)}{32\omega_1^3\omega_2(2\omega_1+\omega_2)}$,
$n_{31} = -\frac{\varepsilon^2\left(-\left(R\delta_3\delta_4+2\mu_1\left(1+R^2\delta_5^2\omega_1^2\right)\right)(2\omega_1-\omega_2)\omega_2^3+4\mu_2\omega_1^3\left(1+R^2\delta_5^2\omega_1^2\right)(2\omega_1+\omega_2)\right)}{8\omega_1\left(1+R^2\delta_5^2\omega_1^2\right)\omega_2^2(2\omega_1+\omega_2)}$,
$n_{32} = \frac{\varepsilon\omega_2\left(4R^2\delta_5^2\omega_1^4+\left(4+\varepsilon R^2\delta_3\delta_4\delta_5\right)\omega_1\omega_2+4R^2\delta_5^2\omega_1^3\omega_2-\omega_2^2-\omega_1^2\left(-4+2\varepsilon R^2\delta_3\delta_4\delta_5+R^2\delta_5^2\omega_2^2\right)\right)}{8\omega_1\left(1+R^2\delta_5^2\omega_1^2\right)(2\omega_1+\omega_2)}$,
$n_{41} = 0$,
and
$n_{42} = \frac{\varepsilon^2\omega_2^2\left(4\omega_1^2-2\omega_1\omega_2+\omega_2^2\right)}{8\omega_1^2(2\omega_1+\omega_2)}$.
Next, we choose the polar form to express these two variables as:

$$A_j = \tfrac{1}{2}a_j(t)e^{\mathbf{i}\alpha_j(t)} \quad for \quad j = 1, 2 \tag{5.31}$$

In this expression, a_j and α_j are the amplitudes and phases of A_j. In fact, a_1 and a_2 are also the amplitudes of u_1 and u_2 shown in nondimenional governing equation (5.17), respectively. Substituting equation (5.31) into complex-valued modulation equation (5.30) and separating the real and imaginary parts, we obtain the following averaged equation:

$$\begin{aligned}
&\dot{a}_1 = m_{11}a_1 + \tfrac{1}{2}m_{21}a_1a_2\cos\gamma_1 + \tfrac{1}{2}m_{22}a_1a_2\sin\gamma_1 + \tfrac{1}{4}m_{31}a_1^3 + \tfrac{1}{4}m_{41}a_1a_2^2\\
&+m_{51}fa_1\cos(\gamma_1-\gamma_2) + m_{52}fa_1\sin(\gamma_1-\gamma_2)\\
&a_1\dot{\alpha}_1 = m_{12}a_1 - \tfrac{1}{2}m_{21}a_1a_2\sin\gamma_1 + \tfrac{1}{2}m_{22}a_1a_2\cos\gamma_1 + \tfrac{1}{4}m_{32}a_1^3 + \tfrac{1}{4}m_{42}a_1a_2^2\\
&-m_{51}fa_1\sin(\gamma_1-\gamma_2) + m_{52}fa_1\cos(\gamma_1-\gamma_2)\\
&\dot{a}_2 = n_{11}a_2 + 2n_{21}f\cos\gamma_2 - 2n_{22}f\sin\gamma_2 + \tfrac{1}{2}n_{31}a_1^2\cos\gamma_1\\
&-\tfrac{1}{2}n_{32}a_1^2\sin\gamma_1 + \tfrac{1}{4}n_{41}a_1^2a_2\\
&a_2\dot{\alpha}_2 = n_{12}a_2 + 2n_{21}f\sin\gamma_2 + 2n_{22}f\cos\gamma_2 + \tfrac{1}{2}n_{31}a_1^2\sin\gamma_1\\
&+\tfrac{1}{2}n_{32}a_1^2\cos\gamma_1 + \tfrac{1}{4}n_{42}a_1^2a_2
\end{aligned} \tag{5.32}$$

where $\gamma_1 = 2\alpha_1 - \alpha_2 + 2\varepsilon\sigma_2 t$ and $\gamma_2 = \varepsilon\sigma_1 t - \alpha_2$. The equilibrium solutions of equation (5.32) are obtained by setting $\dot{a}_1 = \dot{a}_2 = 0$ and $\dot{\gamma}_1 = \dot{\gamma}_2 = 0$. Based on the relationship between γ_i and α_i discussed above, $\dot{\alpha}_1$ and $\dot{\alpha}_2$ can be calculated as: $\dot{\alpha}_1 = \varepsilon(\frac{\sigma_1}{2} - \sigma_2)$ and $\dot{\alpha}_2 = \varepsilon\sigma_1$. The

fixed point of the autoparametric vibration system are determined from:

$$\begin{aligned}
&0 = m_{11}a_1 + \tfrac{1}{2}m_{21}a_1a_2\cos\gamma_1 + \tfrac{1}{2}m_{22}a_1a_2\sin\gamma_1 + \tfrac{1}{4}m_{31}a_1^3 + \tfrac{1}{4}m_{41}a_1a_2^2 \\
&+m_{51}fa_1\cos(\gamma_1-\gamma_2) + m_{52}fa_1\sin(\gamma_1-\gamma_2) \\
&\varepsilon(\tfrac{\sigma_1}{2}-\sigma_2)a_1 = m_{12}a_1 - \tfrac{1}{2}m_{21}a_1a_2\sin\gamma_1 + \tfrac{1}{2}m_{22}a_1a_2\cos\gamma_1 + \tfrac{1}{4}m_{32}a_1^3 + \tfrac{1}{4}m_{42}a_1a_2^2 \\
&-m_{51}fa_1\sin(\gamma_1-\gamma_2) + m_{52}fa_1\cos(\gamma_1-\gamma_2) \\
&0 = n_{11}a_2 + 2n_{21}f\cos\gamma_2 - 2n_{22}f\sin\gamma_2 + \tfrac{1}{2}n_{31}a_1^2\cos\gamma_1 \\
&-\tfrac{1}{2}n_{32}a_1^2\sin\gamma_1 + \tfrac{1}{4}n_{41}a_1^2a_2 \\
&\varepsilon\sigma_1a_2 = n_{12}a_2 + 2n_{21}f\sin\gamma_2 + 2n_{22}f\cos\gamma_2 + \tfrac{1}{2}n_{31}a_1^2\sin\gamma_1 \\
&+\tfrac{1}{2}n_{32}a_1^2\cos\gamma_1 + \tfrac{1}{4}n_{42}a_1^2a_2
\end{aligned} \tag{5.33}$$

5.4 Stability and bifurcation

Inspecting the first two equations in (5.33), we note that all terms contain the variable a_1. As such, $a_1 = 0$ yield the fixed-point equations that are identities [82, 83]. Subsequently, the polar form cannot be used to analyze the system's stability. To analyze the stability of the equilibrium points, we use the Cartesian form:

$$A_j = \tfrac{1}{2}(p_j(t) - \mathbf{i}q_j(t))e^{\mathbf{i}\theta_j(t)} \quad for \quad j = 1, 2 \tag{5.34}$$

In this expression, the variables p_j and q_j are functions of a_1, a_2, γ_1 and γ_2 which are determined from equations (5.26), (5.31), (5.34) and the definitions of γ_1 and γ_2 as [83]

$$\begin{aligned}
p_1 &= a_1\cos\tfrac{\gamma_2-\gamma_1}{2} \\
q_1 &= a_1\sin\tfrac{\gamma_2-\gamma_1}{2} \\
p_2 &= a_2\cos\gamma_2 \\
q_2 &= a_2\sin\gamma_2
\end{aligned} \tag{5.35}$$

Substituting equation (5.34) into the complex-valued modulation equation (5.30) and separating the real and imaginary parts, we obtain the Cartesian form of the modulation equa-

tions

$$\begin{aligned}
&\dot{p}_1 = \tfrac{1}{2}\epsilon(2\sigma_2 - \sigma_1)q_1 + m_{11}p_1 + m_{12}q_1 + \tfrac{1}{2}m_{21}(p_1p_2 + q_1q_2) + \tfrac{1}{2}m_{22}(p_1q_2 - p_2q_1) + \tfrac{1}{4}m_{31}(p_1^3 + p_1q_1^2)\\
&+\tfrac{1}{4}m_{32}(p_1^2q_1 + q_1^3) + \tfrac{1}{4}m_{41}(p_1p_2^2 + p_1q_2^2) + \tfrac{1}{4}m_{42}(p_2^2q_1 + q_1q_2^2) + m_{51}fp_1 - m_{52}fq_1\\
&\dot{q}_1 = -\tfrac{1}{2}\epsilon(2\sigma_2 - \sigma_1)q_1 + m_{11}q_1 - m_{12}p_1 + \tfrac{1}{2}m_{21}(p_1q_2 - p_2q_1) - \tfrac{1}{2}m_{22}(p_1p_2 + q_1q_2) + \tfrac{1}{4}m_{31}(p_1^2q_1 + q_1^3)\\
&-\tfrac{1}{4}m_{32}(p_1^3 + p_1q_1^2) + \tfrac{1}{4}m_{41}(p_2^2q_1 + q_1q_2^2) - \tfrac{1}{4}m_{42}(p_1p_2^2 + p_1q_2^2) - m_{51}fq_1 - n_{52}fp_1\\
&\textit{and}\\
&\dot{p}_2 = -\epsilon\sigma_1q_2 + n_{11}p_2 + n_{12}q_2 + 2n_{21}f + \tfrac{1}{2}n_{31}(p_1^2 - q_1^2) + n_{32}p_1q_1 + \tfrac{1}{4}n_{41}(p_1^2p_2 + p_2q_1^2)\\
&+\tfrac{1}{4}n_{42}(p_1^2q_2 + q_1^2q_2)\\
&\dot{q}_2 = \epsilon\sigma_1p_2 + n_{11}q_2 - n_{12}p_2 - 2n_{22}f + n_{31}p_1q_1 - \tfrac{1}{2}n_{32}(p_1^2 - q_1^2) + \tfrac{1}{4}n_{41}(p_1^2q_2 + q_1^2q_2)\\
&-\tfrac{1}{4}n_{42}(p_1^2p_2 + p_2q_1^2)
\end{aligned} \tag{5.36}$$

In this equation, we have made use of $2\theta_1 - \theta_2 + 2\varepsilon\sigma_2 t = 2n\pi$, $\varepsilon\sigma_1 t - \theta_2 = 2m\pi$, $\dot{\theta}_1 = \varepsilon\frac{\sigma_1 - 2\sigma_2}{2}$ and $\dot{\theta}_2 = \varepsilon\sigma_1$ [83], where, m and n are integers.

Inspecting equation (5.33), we differentiate two kinds of solutions: (1) $a_1 = 0$ and $a_2 \neq 0$ and (2) $a_1 \neq 0$ and $a_2 \neq 0$. The stability of these fixed points can be analyzed by the Jacobian matrix of the Cartesian form of the modulation equations (5.36). If the four eigenvalues λ_i have negative real parts, then the fixed point is stable. Otherwise, the equilibrium point will form a saddle point. Note that the Cartesian form of the equilibrium point (p_1, p_2, p_3, p_4) is needed to determine the Jacobian matrix of Cartesian form of the modulation equations (5.36), which can be obtained using Eq. (5.35). Four types of motions are identified. The first is $a_1 = 0$ and $a_2 \neq 0$. This solution corresponds to the case where the attached cantilever beam moves with the base structure (the base structure and the cantilever beam form a rigid body). The second is $a_1 \neq 0$ and $a_2 \neq 0$. In this case, the cantilever beam undergoes a horizontal motion in addition to that induced by the base structure. Because part of the energy has been transfered to the horizontal motion of the beam, the amplitude of vertical motion of the base structure is reduced. This solution is desired to control the vertical motion of the base structure. Simultaneously, we obtain a horizontal motion of the tip mass. This solution can also be used to obtain actuation in the horizontal direction from a vertical excitation. In a third type of motion, both fixed points are stable. Both masses undergo different motions depending on the initial conditions. The system exhibits interesting nonlinear phenomena, such as jumps and hysteresis. In the fourth type, none of the fixed points is stable and the system may undergo Hopf bifurcations and could become chaotic.

5.5 Linear analysis

By harvesting energy from any system, one is essentially adding damping. As such, it is important to perform a global analysis of the system whereby the effects of the load

resistance and energy harvesting on its performance are considered. First, we determine the effects of the electrical load resistance on the global frequency and damping ratio from a linear analysis of the coupled electromechanical problem. Introducing the following state variables

$$\mathbf{X} = \begin{bmatrix} X_1 \\ X_2 \\ X_3 \\ X_4 \\ X_5 \end{bmatrix} = \begin{bmatrix} x \\ \dot{x} \\ q \\ \dot{q} \\ V \end{bmatrix} \tag{5.37}$$

we rewrite the governing equations (5.16) as

$$\begin{aligned} \dot{X}_1 &= X_2 \\ \dot{X}_2 &= -\omega_x^2 X_1 - 2\xi_x\omega_x X_2 + \tfrac{\eta_1}{M+M_t+\overline{M}}(X_4^2 + X_3\dot{X}_4) + F_0 cos\Omega t \\ \dot{X}_3 &= X_4 \\ \dot{X}_4 &= -\omega_1^2 X_3 - 2\xi_1\omega_1 X_4 + \eta_1\dot{X}_2 X_3 - \eta_2 X_3^3 - \eta_3 X_3(X_4^2 + X_3\dot{X}_4) - \theta_p X_5 \\ \dot{X}_5 &= \tfrac{\theta_p}{C_p} X_4 - \tfrac{1}{RC_p} X_5 \end{aligned} \tag{5.38}$$

These governing equations have the form

$$\dot{\mathbf{X}} = \mathbf{B}(R)X + \mathbf{N}(X, \dot{X}) + \mathbf{F_b} \tag{5.39}$$

where $\mathbf{B}(R)$ is the linear matrix of the state variables, $\mathbf{N}(X, \dot{X})$ is the nonlinear matrix of the state variables and $\mathbf{F_b}$ is the matrix of the external forces. The detail expressions of these three matrices are as following:

$$\mathbf{B} = \begin{bmatrix} 0 & 1 & 0 & 0 & 0 \\ -\omega_x^2 & -2\xi_x\omega_x & 0 & 0 & 0 \\ 0 & 0 & 0 & 1 & 0 \\ 0 & 0 & -\omega_1^2 & -2\xi_1\omega_1 & -\theta_p \\ 0 & 0 & 0 & \frac{\theta_p}{C_p} & -\frac{1}{RC_p} \end{bmatrix}$$

$$\mathbf{N} = \begin{bmatrix} 0 \\ \frac{\eta_1}{M+M_t+\overline{M}}(X_4^2 + X_3\dot{X}_4) \\ 0 \\ \eta_1\dot{X}_2 X_3 - \eta_2 X_3^3 - \eta_3 X_3(X_4^2 + X_3\dot{X}_4) \\ 0 \end{bmatrix}$$

$$\mathbf{F_b} = \begin{bmatrix} 0 \\ F_0\cos\Omega t \\ 0 \\ 0 \\ 0 \end{bmatrix}$$

The linear matrix $\mathbf{B}$ shows the effects of the load resistance on the overall damping and

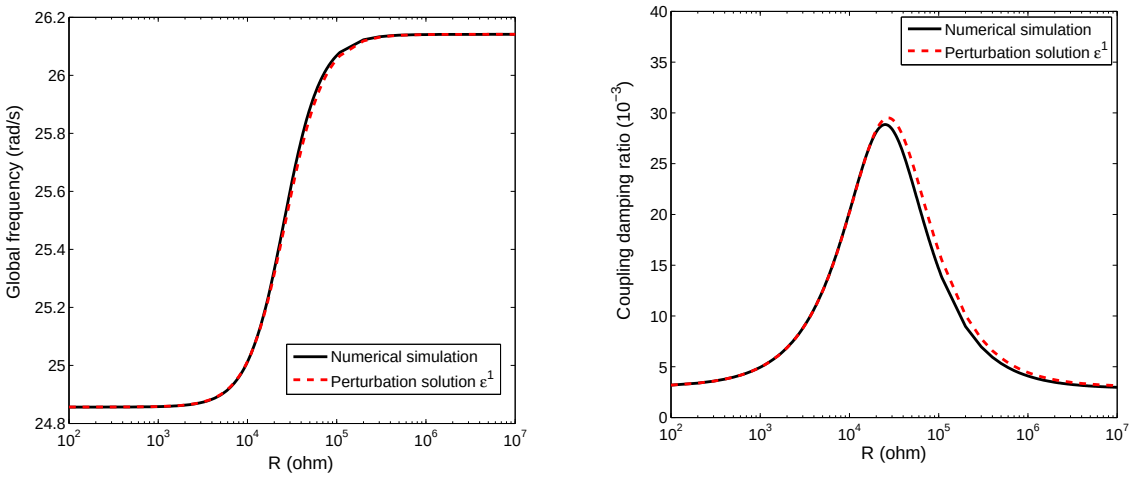

(a) (b)

Figure 5.2: Variation of the (a) global frequency and (b)coupling damping ratio of the cantilever beam as a function of the load resistance R

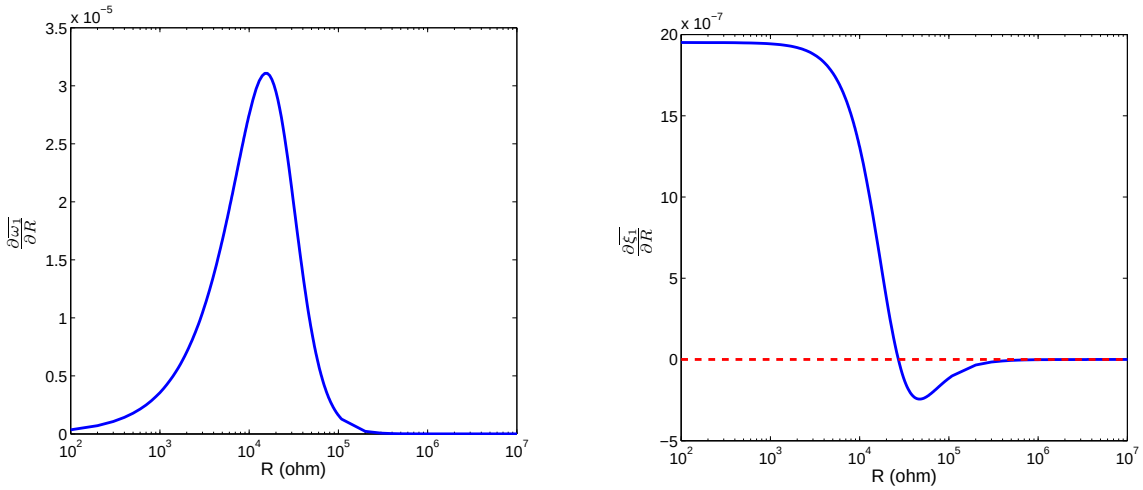

(a) (b)

Figure 5.3: Variation of the derivations of (a) global frequency and (b)coupling damping ratio of the cantilevered beam with respective to R as a function of the load resistance R

global frequency of the proposed energy harvester. This matrix has a set of five eigenvalues λ_i, $i = 1, 2, 3, 4, 5$. The first two eigenvalues correspond to the global frequency and damping coefficient of base structure which are similar to autoparametric vibration system without piezoelectric effects. They are independent of the load resistance and can be determined from the first two lines of linear matrix $\mathbf{B}$. The third and fourth eigenvalues are complex

conjugates ($\lambda_3 = \overline{\lambda_4}$). The real part and positive imaginary part of these two eigenvalues represent respectively the electromechanical damping coefficient and the global frequency of the cantilever beam, respectively. The fifth eigenvalue λ_5 corresponds to the electromechanical coupling and is always real and negative [58, 79].

To better understand the physical cause for the effect of the electronic load resistance and energy harvesting on the global frequency and damping ratio of the cantilever beam, we linearize the first equation of (5.17) as

$$\ddot{u}_1 + \omega_1^2 u_1 + 2\varepsilon\mu_1\dot{u}_1 + \varepsilon\delta_3 u_3 = 0 \tag{5.40}$$

Using equations (5.24) and (5.25) and assuming that $u_3 \approx u_{30}$ and $u_1 \approx u_{10}$, we obtain the relationship between u_3 and u_1 as

$$u_3 \approx \frac{R^2\delta_4\delta_5\omega_1^2}{1+(R\delta_5\omega_1)^2}u_1 + \frac{R\delta_4}{1+(R\delta_5\omega_1)^2}\dot{u}_1 \tag{5.41}$$

Substituting equation (5.41) into equation (5.40), we can determine the global frequency and damping ratio of the cantilever beam depending on electronic load resistance R as

$$\begin{aligned} \overline{\omega_1} &= \sqrt{1 + \frac{\varepsilon R^2\delta_3\delta_4\delta_5}{1+(R\delta_5\omega_1)^2}}\omega_1 \\ \overline{\xi_1} &= \xi_1 + \frac{\varepsilon R\delta_3\delta_4}{2\omega_1 + 2R^2\delta_5^2\omega_1^3} \end{aligned} \tag{5.42}$$

where $\overline{\omega_1}$ and $\overline{\xi_1}$ are the approximate global frequency and damping ratio of the cantilever beam, respectively.

Figure 5.2 shows the variation of the global frequency and the coupled damping ratio of the cantilever beam as a function of the load resistance. The plots show that the approximate global frequency and damping ratio derived by first-order perturbation solution match those obtained with the numerical results using the linear matrix $\mathbf{B}$. We also note that the global frequency increases monotonically from $24.86 rad/s$ to $26.14 rad/s$ as the load resistance R is increased from $10^3 ohm$ to $3 \times 10^5 ohm$. However, the global frequency of the cantilever beam is constant for $R < 10^3 ohm$ and $R > 3 \times 10^5 ohm$. That is because $\frac{\partial\overline{\omega_1}}{\partial R}$ is always larger than zero and the large value is mainly between $10^3 ohm$ and $10^5 ohm$, as shown in figure 5.3 (a). In a similar fashion, the global damping ratio is almost constant when $R < 10^3 ohm$ or $R > 10^6 ohm$. However, this ratio first increases then decreases as the load resistance R is increased from $10^3 ohm$ to $10^6 ohm$. For $R = 2.7 \times 10^4\Omega$, the coupling damping ratio is maximum with a value of 0.02884 which is about 10 times of the value of the mechanical damping ratio. The plot in figure 5.3 (b) demonstrates this result through the fact that $\frac{\partial\overline{\xi_1}}{\partial R} = 0$ when the electronic load resistance is around $2.7 \times 10^4\Omega$. The load resistance corresponding to the largest coupling damping ratio can also be calculated by the expression $R = \frac{1}{\delta_5\omega_1}$.

5.6 Numerical simulation

According to Yan et al. [93], the autoparametric vibration system without the piezoelectric sheets exhibits many interesting nonlinear phenomena including saturation, jumps, hysteresis and different kinds of bifurcations. These phenomena are observed over different ranges for the amplitude and frequency of the external force and the damping coefficient and frequency of the attached cantilever beam. Next, we consider the system's nonlinearities and assess the effects of amplitude and frequency of the external force and load resistance on the ability to harvest energy through autoparametric resonance.

5.6.a Effects of the amplitude of external force

We first analyze the effects of the amplitude of external force on the nonlinear response of the energy harvester. We consider different load resistances for three cases of frequencies of the external forcing and natural frequencies of the base structure. These are (1) $\omega_1 = 50 rad/s$ and $\Omega = 49 rad/s$, (2) $\omega_1 = 51 rad/s$ and $\Omega = 51 rad/s$ and (3) $\omega_1 = 52 rad/s$ and $\Omega = 53 rad/s$. All other parameters are fixed as shown in Table 5.1.

Figure 5.4 shows the variations of the root-mean-square (rms) values of the displacements of the base structure and tip mass and harvested voltage and power as functions of the external force amplitude. The plots show these variations for different values of load resistances and small and large initial displacements when the excitation frequency, Ω, is 49 rad/s and the natural frequency of the base structure is 50 rad/s. The solid lines correspond to the responses of the energy harvester for the case of small initial displacements. The dashed lines correspond to responses for the case of relatively large initial displacements. For all cases, we note a hysteresis whereby the horizontal motion of the tip mass and levels energy harvested are initiated with smaller external forces when the system is subjected to large initial conditions.

A comparison of the effects of the load resistance shows that the energy can be harvested at low amplitudes of the external forcing when $R = 10^3 ohm$. However, the level of harvested power is significantly larger when $R = 10^4 ohm$ and $10^5 ohm$ at the relatively higher forcing amplitudes. In the case of $R = 10^3 ohm$, the energy harvester, when activated by a large initial displacement, can generate energy at excitation amplitudes, F_0, that are as low as 0.1. This value changes to 0.25 for small initial displacements. Of particular interest is a comparison of the systems responses in terms of energy harvesting and control of the displacement of the base. The open circuit configuration (no energy harvesting) yields the smallest displacement over a broad range of excitation amplitudes except for the range between 1.2 and 1.3 where the base displacement is quite large. The case of $R = 10^3 ohm$ shows a significant control of the base displacement that matches that of the open circuit

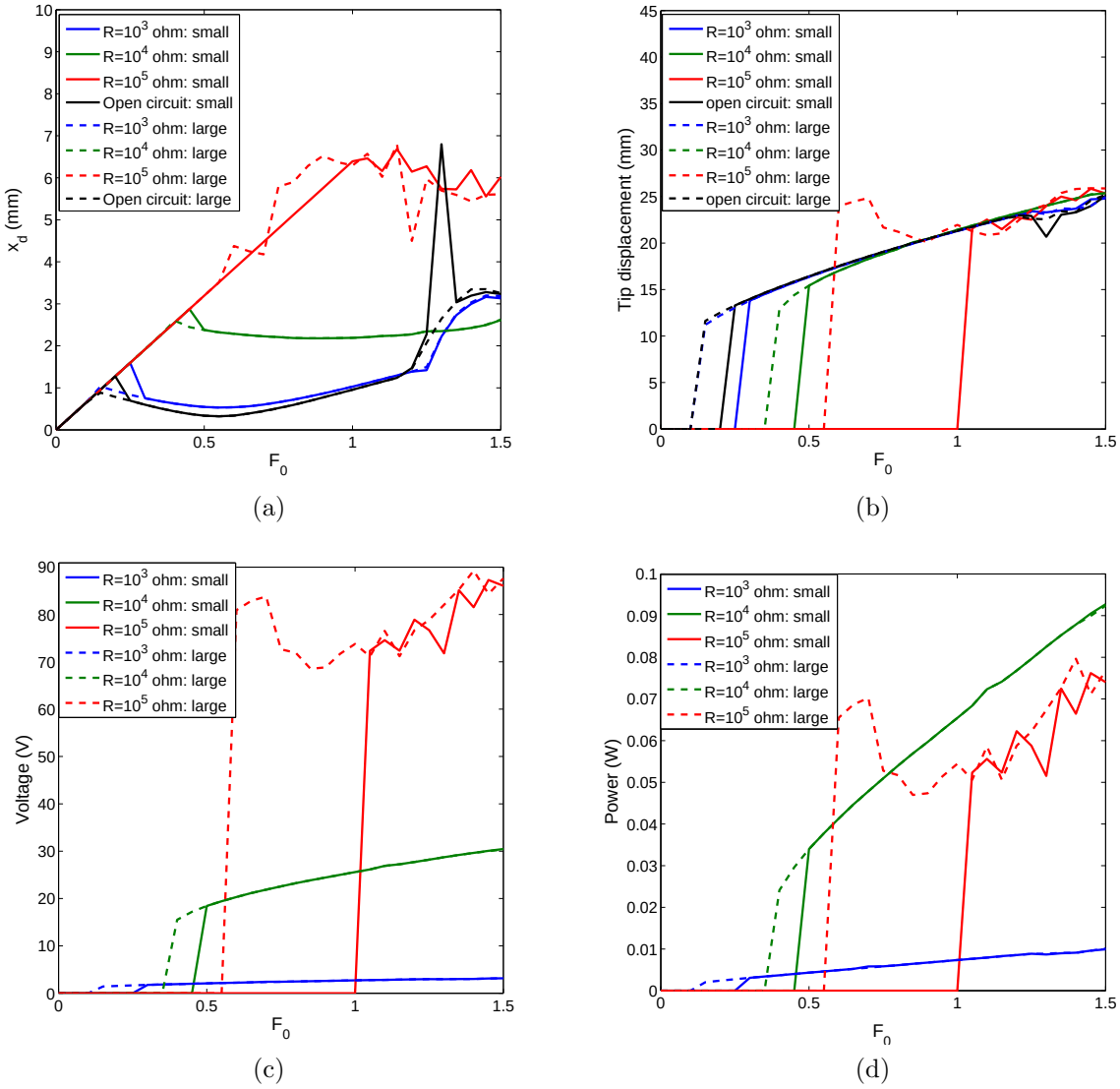

Figure 5.4: Variation of the root mean square (rms) values for (a) displacement of base structure, (b)displacement of tip mass, (c)harvested voltage and (d) harvested power as a function of the external force f with different load resistances and initial displacements when $\omega_1 = 50 rad/s$ and $\Omega = 49 rad/s$

configuration over the whole range and does not show the large response of the excitation amplitude between 1.2 and 1.3. This shows that the energy harvesting is actually helpful in the control of the displacement of the base structure over a broader range than that of the open circuit configuration. For the case of $R = 10^4 ohm$, the system yields the highest level of energy harvesting over a broad range of excitation amplitudes. However, the base displacement is much larger than that of the open circuit and $R = 10^3 ohm$ configurations.

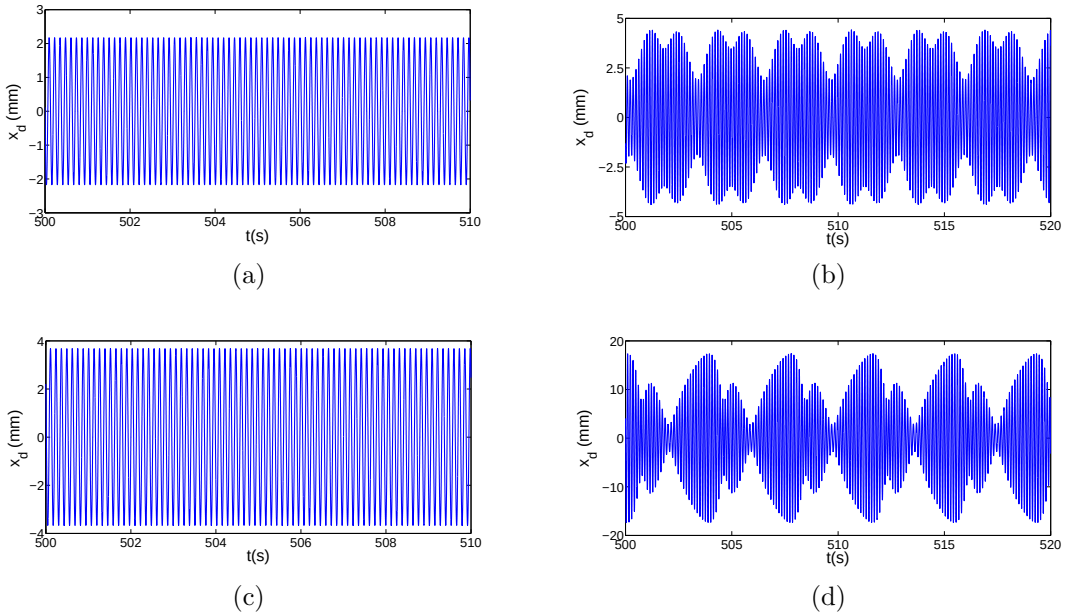

Figure 5.5: Time histories for displacement of base structure with the small initial displacement when $\omega_1 = 50 rad/s$ and $\Omega = 49 rad/s$: (a) f=1.2 and $R = 10^3 ohm$, (b) f=1.3 and $R = 10^3 ohm$, (c) f=1.3 and $R = 10^4 ohm$ and (d) f=1.3 and open circuit

These results show that the system can be configured depending on its purpose. Particularly, the load resistance can be varied to harvest a relatively high level of energy, to have a minimum base displacement over a broad range of excitation frequencies or to balance the level of harvested energy with the displacement of the base structure.

The system's nonlinearities also show different types of responses. Figure 5.5 shows time histories of the displacement of the base structure for different excitation amplitudes and load resistances. A comparison of the plots in figures 5.5 (a) and 5.5 (b) shows that the system's response changes from having one period to having multiple periods as the excitation amplitude is increased from $F_0 = 1.2$ to $F_0 = 1.3$ for the case of $R = 10^3 ohm$. This indicates the system undergoes bifurcations as the amplitude of the forcing changes. A comparison of the plots in figure 5.5 (b), 5.5 (c) and 5.5 (d) shows that the response changes in terms of its period content when the load resistance is varied or for the case of open circuit. Again, this indicates the system undergoes some bifurcations as the load resistance is changed.

Figure 5.6 shows the variations of the rms values of the displacements of the base structure and tip mass and harvested voltage and power as functions of the external forcing amplitude for the case of perfect resonance between the excitation and natural frequency of the base structure, i. e. $\Omega = \omega_1 = 51 rad/s$. The plots do not exhibit the hysteresis response observed in the case of $\Omega = 49 rad/s$ and $\omega_1 = 50 rad/s$. The initial displacements do not impact the

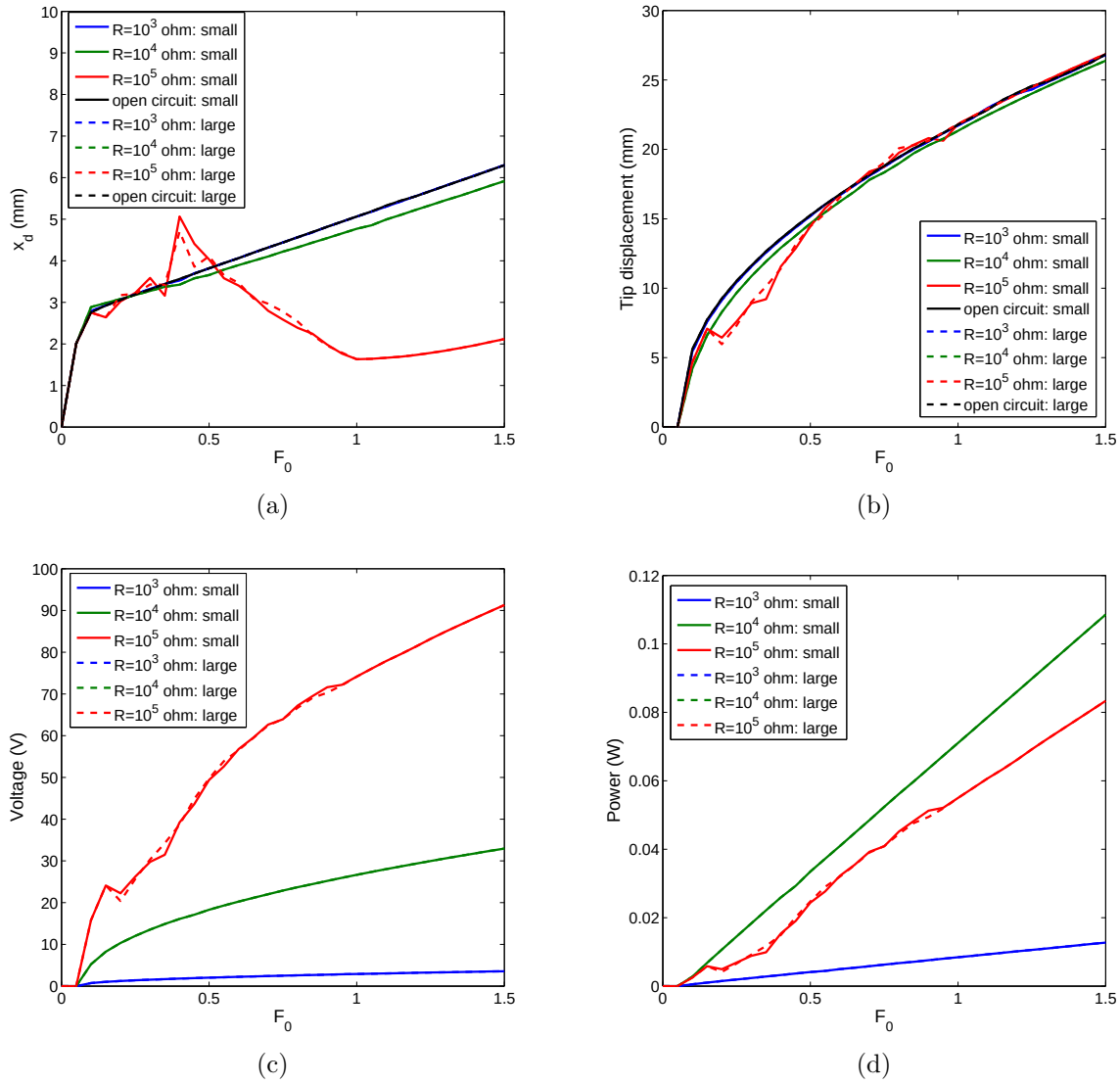

Figure 5.6: Variation of the root mean square (rms) values for (a) displacement of base structure, (b)displacement of tip mass, (c)harvested voltage and (d) harvested power as a function of the external force f with different load resistances when $\omega_1 = 51 rad/s$ and $\Omega = 51 rad/s$

response of the harvester or masses. The plots also show that the activation of the motion and energy harvesting takes place at very small values of forcing amplitudes. Still, the plots show that the harvested energy is larger for $R = 10^4 ohm$ than for $R = 10^3 ohm$ or $10^5 ohm$. Of interest is the fact that although the level of harvested power is larger in the case of $R = 10^4 ohm$, the displacement of the base is minimum for the case when $R = 10^5 ohm$ at high excitation amplitudes. In the range slightly below $f = 0.5$, this displacement is actually

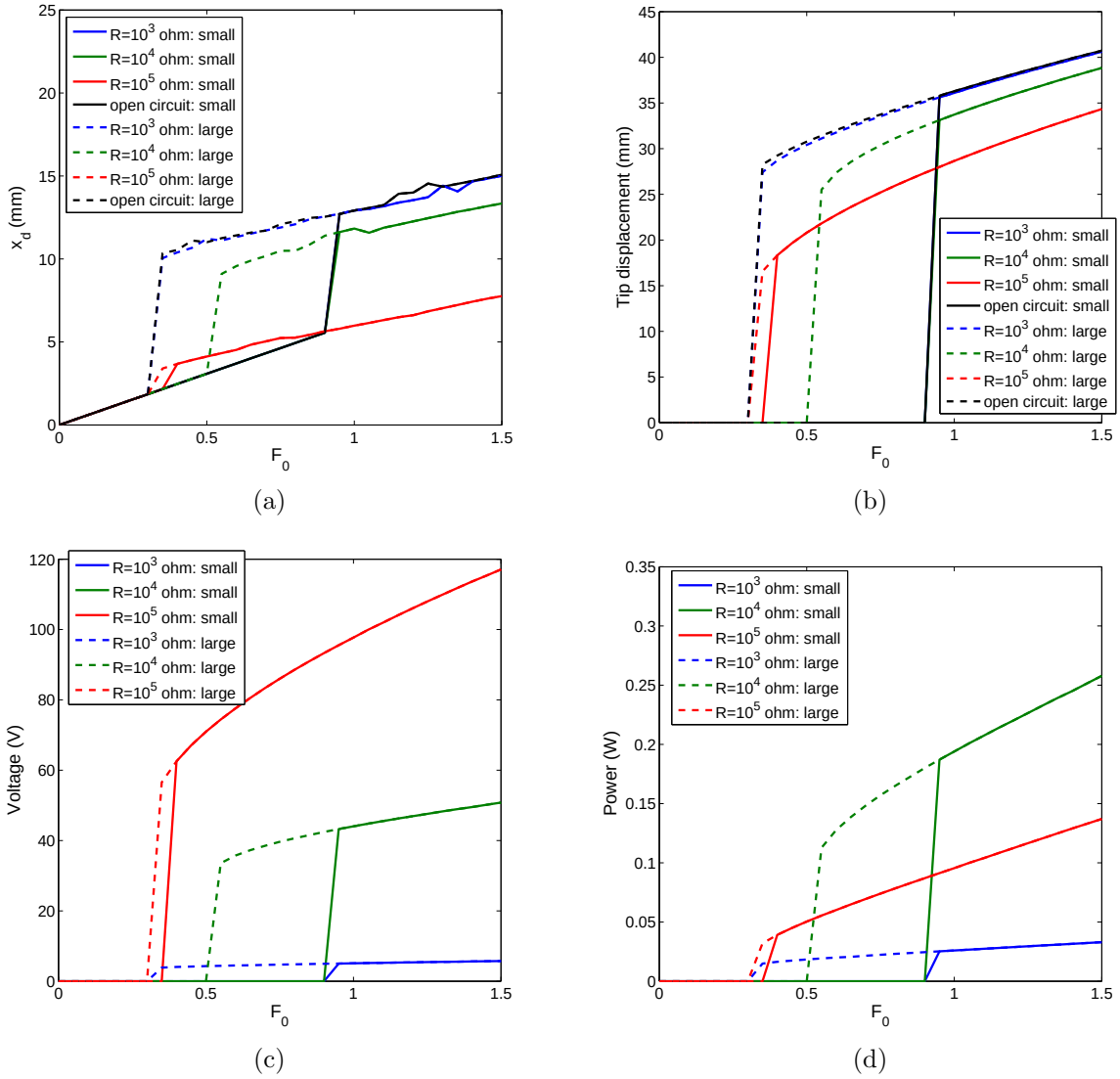

Figure 5.7: Variation of the root mean square (rms) values for (a) displacement of base structure, (b)displacement of tip mass, (c)harvested voltage and (d) harvested power as a function of the external force f with different load resistances when $\omega_1 = 52rad/s$ and $\Omega = 53rad/s$

larger than in the cases of $R = 10^3 ohm$ and $10^4 ohm$. These results show the importance of performing a global analysis of the coupled system.

Figure 5.7 shows the same variations as in figures 5.4 and 5.6 but for a different case of excitation and base natural frequency, namely the case of $\Omega = 53rad/s$ and $\omega_1 = 52rad/s$. The plots show a hysteresis similar to the one observed in figure 5.4; indicating that this hysteresis is associated with the detuning of the different frequencies. As for the effects

of the load resistance and displacement, we observe the same trends observed in the other conditions. To harvest the highest level of energy, it is better to choose a load resistance of $10^4 ohm$ than $10^3 ohm$ and $10^5 ohm$. This is expected because the highest coupled damping is near that value. The case of $R = 10^5 ohm$ leads to the lowest response amplitude of the base structure over a broad range of F_0. As such, if the system is to be used for control and energy harvesting, it may be better to use $R = 10^5 ohm$ than $R = 10^4 ohm$ because it provides a more effective control except for a small region in the case of perfect resonance. Both figures 5.6 and 5.7 show that smaller base and tip mass displacements are obtained when harvesting energy in comparison to the case of the open circuit. As such, it can be concluded that harvesting energy from this system can effectively help in the control of both base and tip mass motions.

5.6.b Effects of the external frequency

The above results have shown that the external frequency impacts the responses of the masses and level of harvested energy. Next, we examine frequency-response curves of the displacements of the base structure and tip mass, harvested voltage and harvested power.

The plots in figure 5.8 show the response of the energy harvester when $F_0 = 1$ and $\omega_1 = 50 rad/s$. Compared with the energy harvesting from direct base excitation [42], the autoparametric vibration system has a broader range over which energy can be harvested. This is especially true if the system is activated by the large initial displacements. For instance, energy can be harvested over the range of excitation frequency between $\Omega = 47.5 rad/s$ to $52.9 rad/s$ when $R = 10^5 ohm$. Moreover, the rms value of harvested energy remains large even if the excitation frequency is shifted from the natural frequency of the base structure (away from the resonance). The plots also show that higher power levels are harvested when $R = 10^4 ohm$ than when $R = 10^3 ohm$ or $10^5 ohm$. When control for the motion of the base structure is of interest, the small load resistance (i. e. $R = 10^3 ohm$) is a better choice when the external frequency is relatively small while the large load resistance, such as $R = 10^5 ohm$, is more suitable for the larger external frequency. This is due to the fact that the natural global frequency is a function of the load resistance which affects the efficiency of the energy transfer to the beam.

5.6.c Effects of the load resistance

We determine the effects of the load resistance on nonlinear responses of the energy harvester for different external forces and initial displacements. We consider three cases of excitations. These are: (1) $\omega_1 = 50 rad/s$ and $\Omega = 49 rad/s$, (2) $\omega_1 = 51 rad/s$ and $\Omega = 51 rad/s$ and (3) $\omega_1 = 52 rad/s$ and $\Omega = 53 rad/s$.

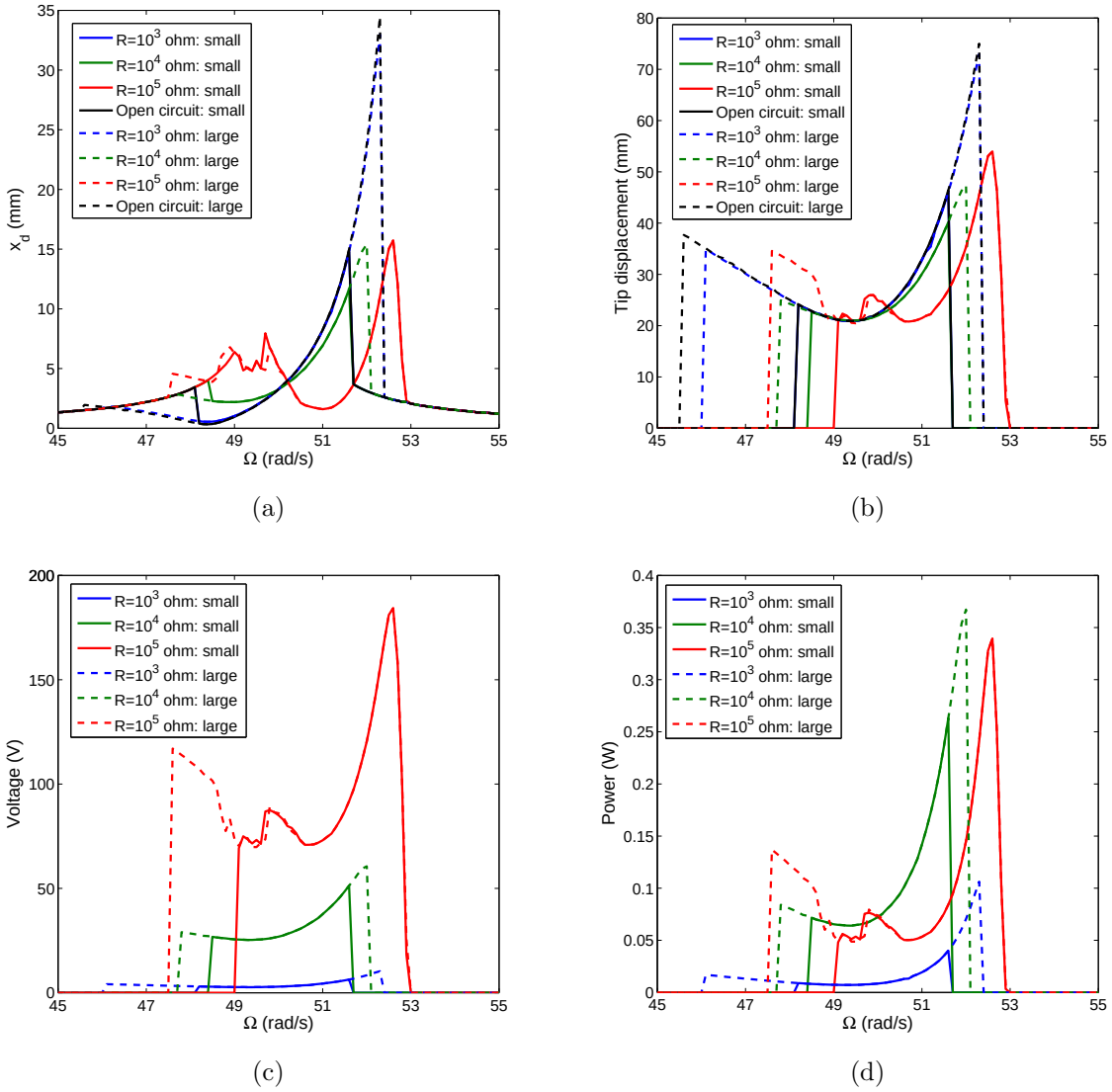

Figure 5.8: Frequency-response curves of the root mean square (rms) values for (a) displacement of base strucutre, (b)displacement of tip mass, (c)harvested voltage and (d) harvested power with different load resistances and different initial displacements when $F_0 = 1$ and $\omega_1 = 50 rad/s$

Figure 5.9 shows that variations of the displacements of the base structure and tip mass, harvested voltage and harvested power as the functions of the load resistance when $\omega_1 = 50 rad/s$ and $\Omega = 49 rad/s$. The external forces F_0 are chosen as 0.5, 1 and 1.5. When the external force is 0.5 with the small initial displacement, we note that there is no energy harvesting when $R \geq 2 \times 10^4 ohm$. This is because the motion of the cantilever beam is relatively easily activated when the ratio of frequencies between the cantilever beam and base

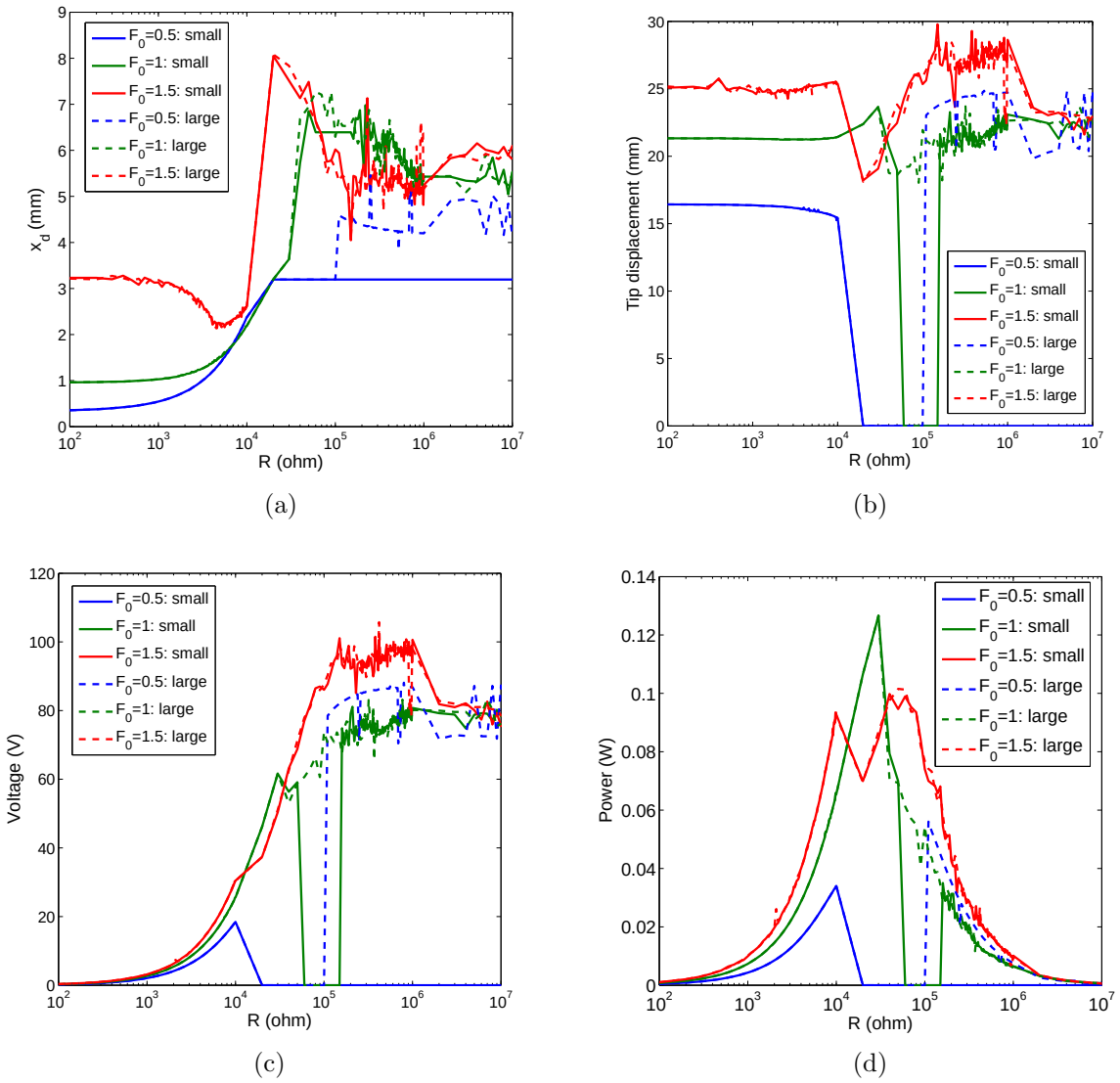

Figure 5.9: Variation of the root mean square (rms) values for (a) displacement of base strucutre, (b)displacement of tip mass, (c)harvested voltage and (d) harvested power as a function of the load resistance R with different external forces f and initial displacements when $\omega_1 = 50rad/s$ and $\Omega = 49rad/s$

structure is around 1/2 [93] and the global frequency of the cantilever beam corresponding to the low load resistance ($R \leq 2 \times 10^4 ohm$) is near 1/2 of natural frequency of the base structure, as shown in figure 5.2 (a). In this case, the small load resistance, such as $R = 10^3 ohm$, is good choice to control the motion of the base structure. However, large power can be harvested when the load resistance is large, such as $10^4 ohm$. Moreover, the autoparametric vibration system damping ratio of cantilever beam. As expected, the range of the load

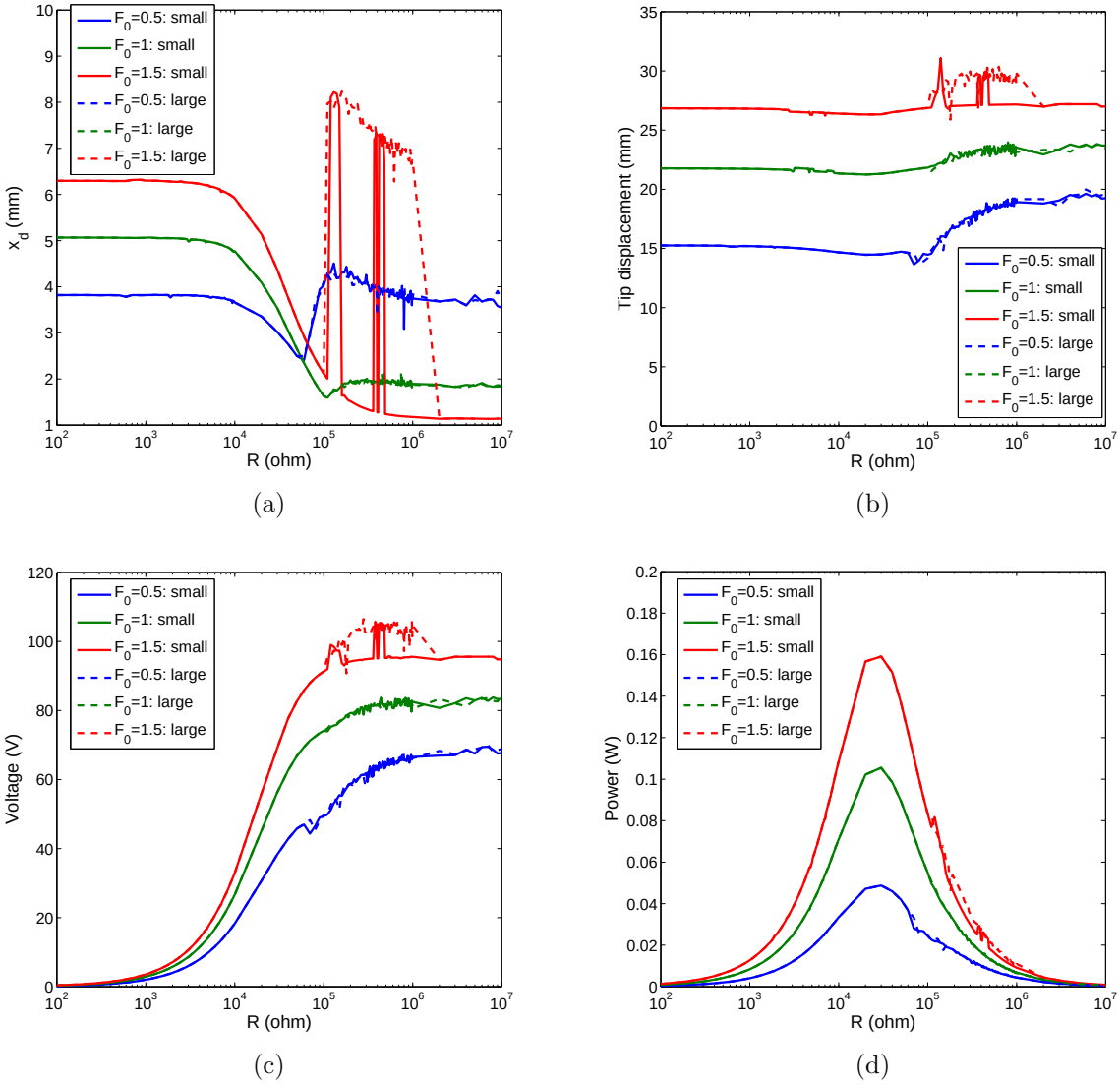

Figure 5.10: Variation of the root mean square (rms) values for (a) displacement of base strucutre, (b)displacement of tip mass, (c)harvested voltage and (d) harvested power as a function of the load resistance R with different external forces f and initial displacements when $\omega_1 = 51 rad/s$ and $\Omega = 51 rad/s$

resistance in which the system can harvest energy increases as the external force is increased because the onset external force to activate the horizontal motion of cantilever beam increases as the damping ratio of the cantilever beam is increased [93]. Considering the case of $F_0 = 1$, we note that the autoparametric vibration absorber with the small initial displacements can harvest energy when $R < 6 \times 10^4 ohm$ or $R > 2 \times 10^5 ohm$. If the system is activated by large initial displacements, electric power can be harvested with all load resistances. For the case

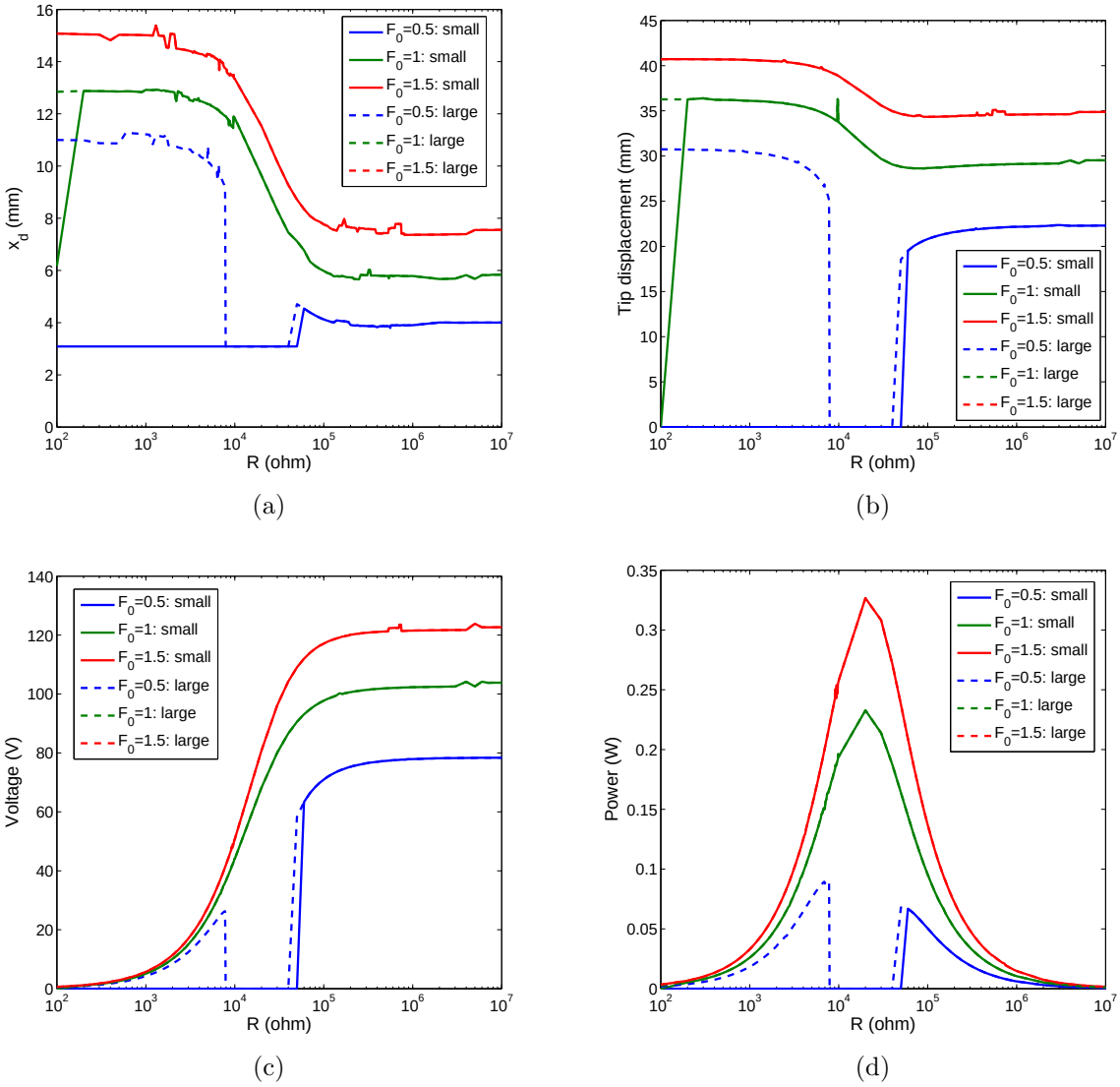

Figure 5.11: Variation of the root mean square (rms) values for (a) displacement of base strucutre, (b)displacement of tip mass, (c)harvested voltage and (d) harvested power as a function of the load resistance R with different external forces f and initial displacements when $\omega_1 = 52rad/s$ and $\Omega = 53rad/s$

of $F_0 = 1.5$, the system can harvester energy in all the range of load resistance with small initial displacements.

Figure 5.10 presents the effect of the load resistance on the nonlinear responses of the energy harvester when $\omega_1 = 51rad/s$ and $\Omega = 51rad/s$. It is noted that the system can harvest energy in all the range of the load resistance with the different external forces and initial displacements. The square root mean value of the displacement of the base structure first

decreases then increases as the load resistance is increased. However, the system becomes unstable when the load resistance is large. When the external force is small, such as $F_0 = 0.5$, the minimum displacement of the base structure and the maximum harvested power are obtained at the same load resistance (around $5 \times 10^4 ohm$). As the external force is increased to 1, the rms displacement of the base structure reaches the minimum value of $1.6mm$ with the load resistance $R = 1.1 \times 10^5 ohm$. This displacement is even smaller than the minimum value for the case of $F_0 = 0.5$. As the external force is increased further to 1.5, the smallest minimum displacement of the base structure are obtained compared with the above two cases. As such, the energy harvesting can better control the motion of the base structure especially when the external force become larger. However, the displacement of the tip mass is almost independent of the load resistance in all there cases when the system is stable. We also note that the large initial condition makes the system more unstable when $10^5 ohm < R < 10^6 ohm$.

The variations of the performances of the system as the function of the load resistance when $\omega_1 = 52 rad/s$ and $\Omega = 53 rad/s$ are shown in figure 5.11. We note that the motion of the system are stable with all the load resistances and external forces. In all external forces, the energy harvesting is useful to control both the motions of the base structure and tip mass with the large load resistance. This phenomenon is also useful in the design of an energy harvester with the condition that the natural frequency of the base structure is a little larger than the excitation frequency. Moreover, the load resistance around $5 \times 10^4 ohm$ is the optimum load resistance for both control of the base structure and energy harvesting when the external force is relatively large, such as $F_0 = 1$ and 1.5.

5.7 Approximate analysis

Based on the above discussion, we find that load resistance, external frequency and external force significantly impact the performance of the energy harvester. In this section, we want to determine the stability of the system. Before performing nonlinear analysis, we need to determine the expressions for the amplitudes for the base displacement, displacement of the tip mass and harvested power. Assuming $u_1 \approx u_{10}$, $u_2 \approx u_{20}$ and $u_3 \approx u_{30}$ and using definite expressions of u_1, u_2 and u_3 and equations (5.24) and (5.25), we obtain those amplitudes as

$$\begin{aligned} d_{bas} &= x_0 a_2 \\ d_{tip} &= \sqrt{M + M_t + \overline{M}} x_0 a_1 \phi(L) \\ P &= \frac{R\delta_4^2 \omega_1^2 a_1^2}{1 + (R\delta_5 \omega_1)^2} \end{aligned} \tag{5.43}$$

where d_{bas}, d_{tip} and P are the respective amplitudes of the base displacement, displacement of the tip mass and harvested power. Comparing the expressions of amplitude of harvested power and global coupling damping ratio (equation(5.42)), we find that the harvested power

is proportional to the net growth of global coupling damping ratio from mechanical damping ratio.

5.7.a Effect of the amplitude of external force

We first analyze the effects of the amplitude of external force on the nonlinear response of the energy harvester. We do so with different load resistances by considering three different cases of the external frequencies and natural frequencies of the base structure: (1) $\omega_1 = 51rad/s$ and $\Omega = 51rad/s$, (2) $\omega_1 = 51rad/s$ and $\Omega = 50rad/s$ and (3) $\omega_1 = 51rad/s$ and $\Omega = 52rad/s$. All other parameters are shown in table 5.1. The results are presented in figures 5.12, 5.13 and 5.14.

In the figure 5.12, we show the base displacement, displacement of the tip mass and harvested power as a function of the external force when the system is under resonance. The solid lines correspond to sinks (stable solutions) and the dashed lines indicate the saddles (unstable solutions). The nonlinear interaction between base structure and cantilever beam start at $F = 0N$ and the displacement of the base structure is much smaller than that without cantilever beam (the dashed line). This indicates that this system is very effective to both control the motion of the base structure and harvest electric power when the base structure is under resonance. Compared with the numerical simulation of governing equation (5.7), the perturbation method is relatively accurate to represent the system's responses. The plots show no differences for the base displacement and displacement of the tip mass between the case of $R = 10^3 ohm$ and open circuit (without energy harvesting) because the global frequency and damping ratio of the cantilever beam for these two cases are almost same, as shown in figure 5.2. When the electric load resistance is increased to $10^4 ohm$, the displacements of the base structure and tip mass do not change while the harvested power becomes ten times the value obtained for the case $R = 10^3 ohm$. This can be explained by the fact that harvested power is proportional to the net growth of global damping ratio from the mechanical damping, as discussed at the beginning in this section, and the net growth of coupling damping corresponding to $R = 10^4 ohm$ is increased to ten times of that of $R = 10^3 ohm$, as shown in figure 5.2 (b). When the load resistance is increased to $10^5 ohm$, the base displacement becomes much smaller but the system becomes unstable when the external force F is between $0.235N$ and $1.4N$. In this situation, the system with $R = 10^5 ohm$ is very effective to control base structure and harvest relatively high energy when the external force is large. However, $R = 10^5 ohm$ is not good to control motions of system when the external force is small. That is because the system undergoes a Hopf bifurcation and becomes chaotic in the unstable range of external force which enlarges the amplitude of base displacement much larger than that shown in dash line [93, 94]. When the load resistance is increased further to $10^6 ohm$, the unstable range becomes larger while the base displacement become smaller when the external force is large. However, the harvested

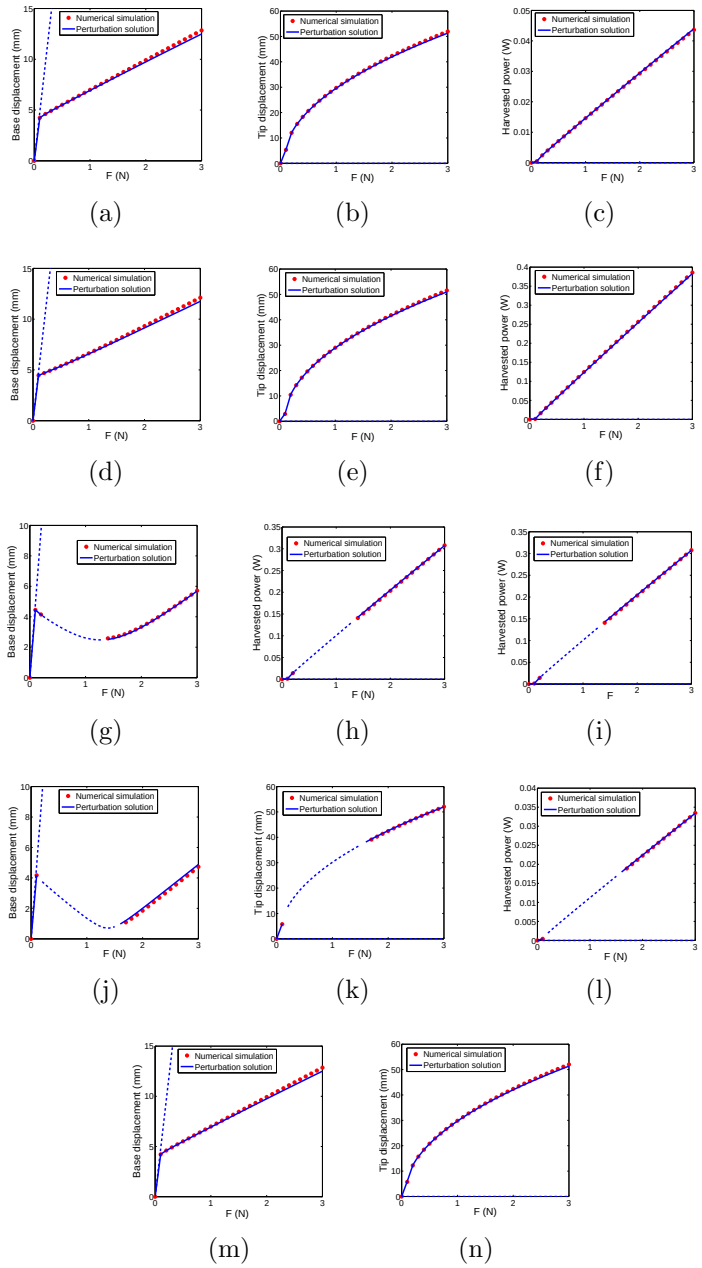

Figure 5.12: Variation of (a, d, g, j, m) displacement of base structure, (b, e, h, k, n) displacement of tip mass, and (c, f, i, l) harvested power as a function of the external force F with different load resistances when $\omega_1 = 51 rad/s$ and $\Omega = 51 rad/s$. The dashed lines are used to denote unstable solutions and the solid line are used to denote stable solution: (a, b, c) R=10^3 ohm, (d, e, f) R=10^4 ohm, (g, h, i) R=10^5 ohm, (j, k, l) R=10^6 ohm and (m, n) open circuit.

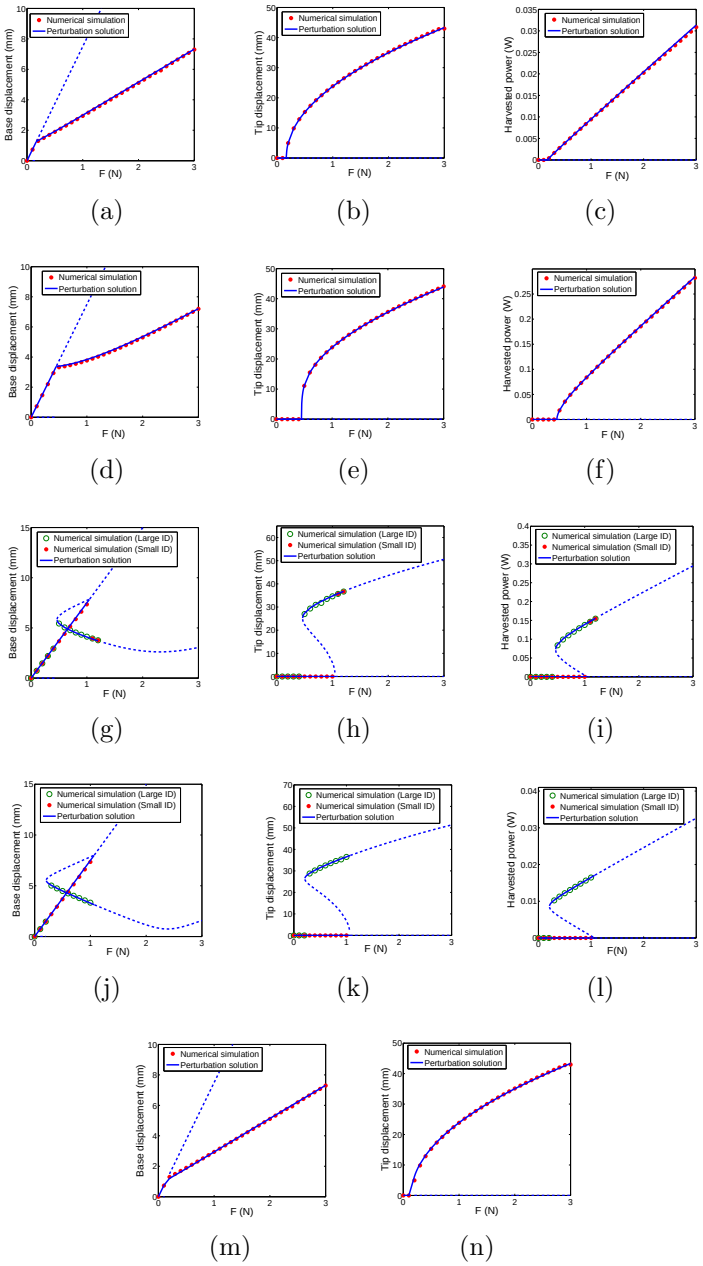

Figure 5.13: Variation of (a, d, g, j, m) displacement of base structure, (b, e, h, k, n) displacement of tip mass, and (c, f, i, l) harvested power as a function of the external force F with different load resistances when $\omega_1 = 51 rad/s$ and $\Omega = 50 rad/s$. The dashed lines are used to denote unstable solutions and the solid line are used to denote stable solution: (a, b, c) R=10^3 ohm, (d, e, f) R=10^4 ohm, (g, h, i) R=10^5 ohm, (j, k, l) R=10^6 ohm and (m, n) open circuit. ID denotes initial displacements.

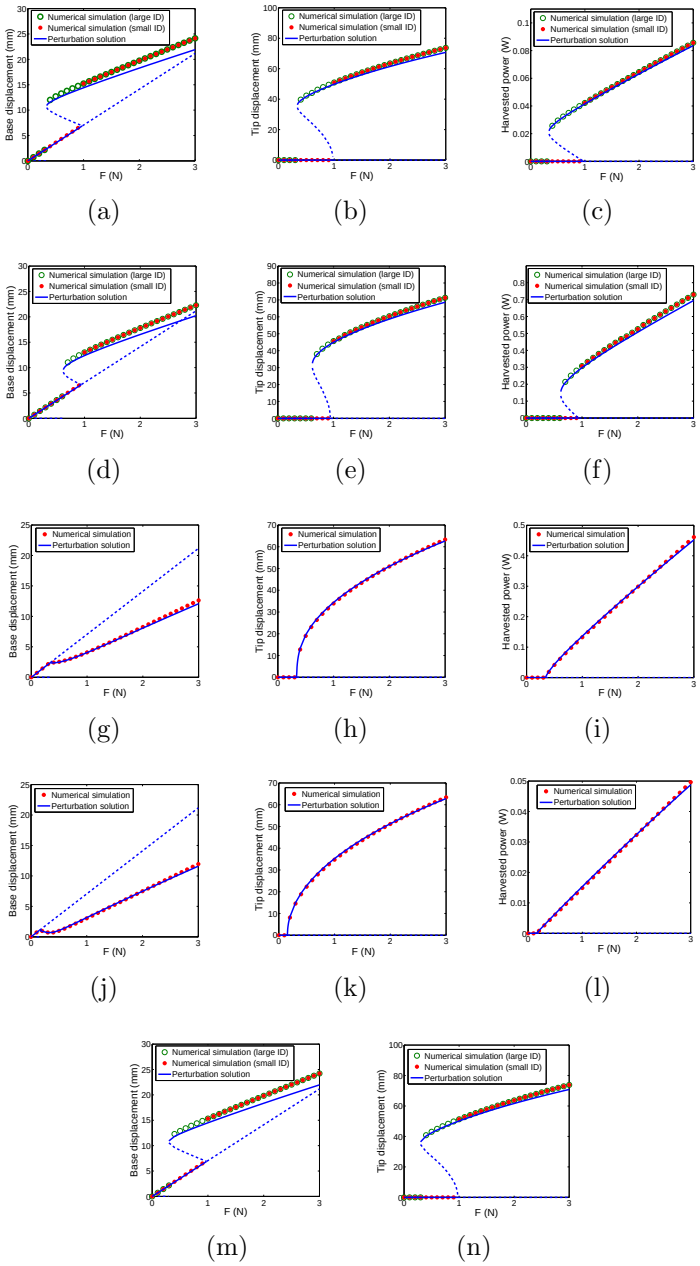

Figure 5.14: Variation of (a, d, g, j, m) displacement of base structure, (b, e, h, k, n) displacement of tip mass, and (c, f, i, l) harvested power as a function of the external force F with different load resistances when $\omega_1 = 51 rad/s$ and $\Omega = 52 rad/s$. The dashed lines are used to denote unstable solutions and the solid line are used to denote stable solution: (a, b, c) R=10^3 ohm, (d, e, f) R=10^4 ohm, (g, h, i) R=10^5 ohm, (j, k, l) R=10^6 ohm and (m, n) open circuit. ID denotes initial displacements.

power is much smaller than the case of $R = 10^5 ohm$ for the reason that the net damping ratio decreases as the load resistance is increased from $10^5 ohm$ to $10^6 ohm$.

As the external frequency is moved away from the natural frequency of the base structure, the responses of the system as a function of the external force are plotted in figures 5.13 ($\Omega = 50 rad/s$) and 5.14 ($\Omega = 52 rad/s$). Similar to the case of resonance, the displacements of the base structure and tip mass of $10^3 ohm$ are almost same as those of open circuit in both cases. Comparing the responses between $10^3 ohm$ and $10^4 ohm$ or between $10^5 ohm$ and $10^6 ohm$, we note that the increasing coupling damping ratio increases the harvested power but delays the onset of energy transfer. Moreover, the increased global frequency due to the effect of the electronic load resistance changes the form of bifurcations. That is, as the load resistance is increased, the supercritical bifurcation is shifted to a subcritical bifurcation when external frequency is $50 rad/s$ and the subcritical bifurcation is transformed into supercritical bifurcation when external frequency is $52 rad/s$. Therefore, the energy harvesting can be used to avoid subcritical responses. The plots in figure 5.13 also show that the amplitude of the base structure excited by large initial conditions decreases as the external force is increased when $F \leq 1.2N$ for the case of $R = 10^5 ohm$ and when $F \leq 1N$ for the case of $R = 10^6 ohm$. However, the system becomes unstable as the external force become larger. For the purpose of harvesting energy, it is better to choose the external load resistance as $10^5 ohm$ when the external force is small and $10^4 ohm$ when the external force is relatively large. When the external force is larger than the natural frequency ($\Omega = 52 rad/s$), the energy harvester with the large load resistance, such as, $10^5 ohm$, can both effectively control the motion of the base structure and harvest relatively high energy, as shown in figure 5.14. As discussed above, the external frequency has great effect on response of the system, which will be discussed in the next section.

5.7.b Effect of the external frequency

We analyze the effects of the excitation frequency on the nonlinear response of the energy harvester based on autoparametric vibration system with different load resistances when $\omega_1 = 51 rad/s$ and $F = 1.5N$, as shown in figure 5.15. All other parameters are presented in table 5.1. The plots show that this system can harvest relatively large electric power in broadband near resonance. However, compared with the results of numerical simulation, the harvested energy is highly dependent on initial displacements when the external force is smaller than the natural frequency of the base structure. When the electronic load resistance is increased, the unsteady motion of the system near resonance is increased. For the purpose of harvesting large electronic power near resonance, it is better to choose the load resistance corresponding to large damping ratio, such as $R = 10^4 ohm$ and $10^5 ohm$. For wide range of energy harvesting, the load resistance corresponding to small damping ratio is a better option.

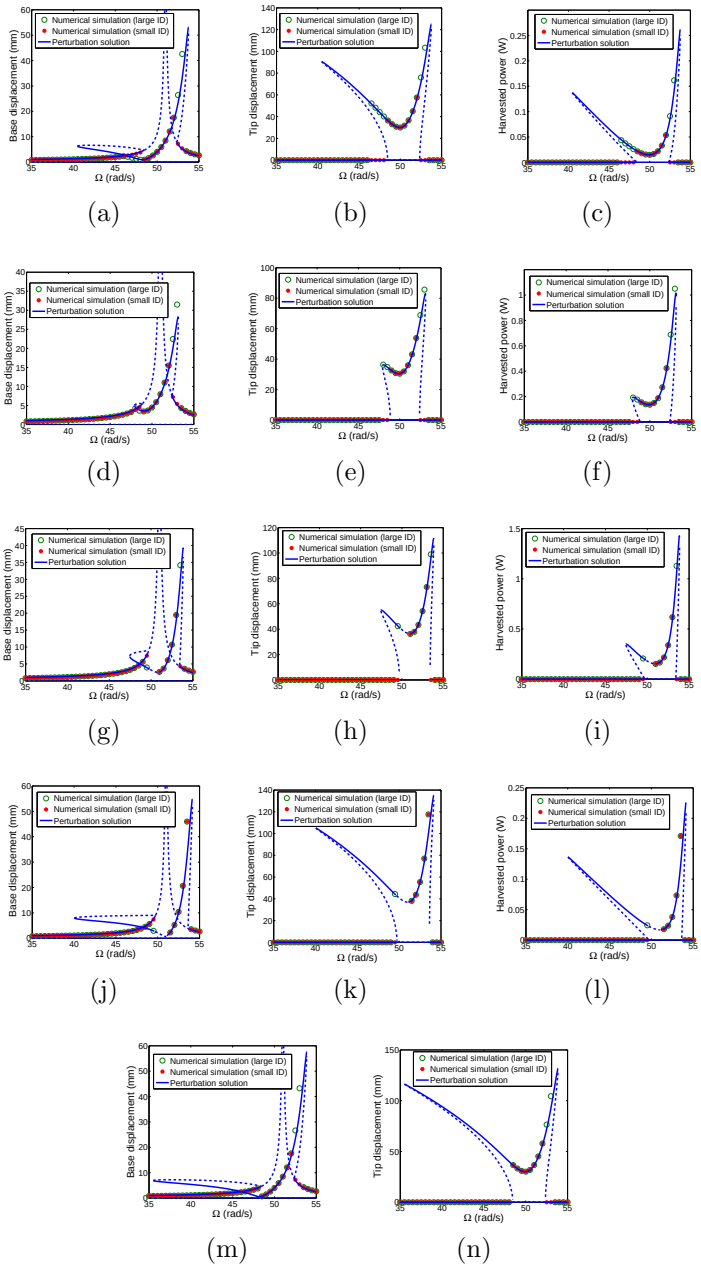

Figure 5.15: Variation of (a, d, g, j, m) displacement of base structure, (b, e, h, k, n) displacement of tip mass, and (c, f, i, l) harvested power as a function of the external frequency Ω with different load resistances when $\omega_1 = 51 rad/s$ and $F = 1.5N$. The dashed lines are used to denote unstable solutions and the solid line are used to denote stable solution: (a, b, c) R=10^3 ohm, (d, e, f) R=10^4 ohm, (g, h, i) R=10^5 ohm, (j, k, l) R=10^5 ohm and (m, n) open circuit. ID denotes initial displacements.

5.7.c Effect of the load resistance

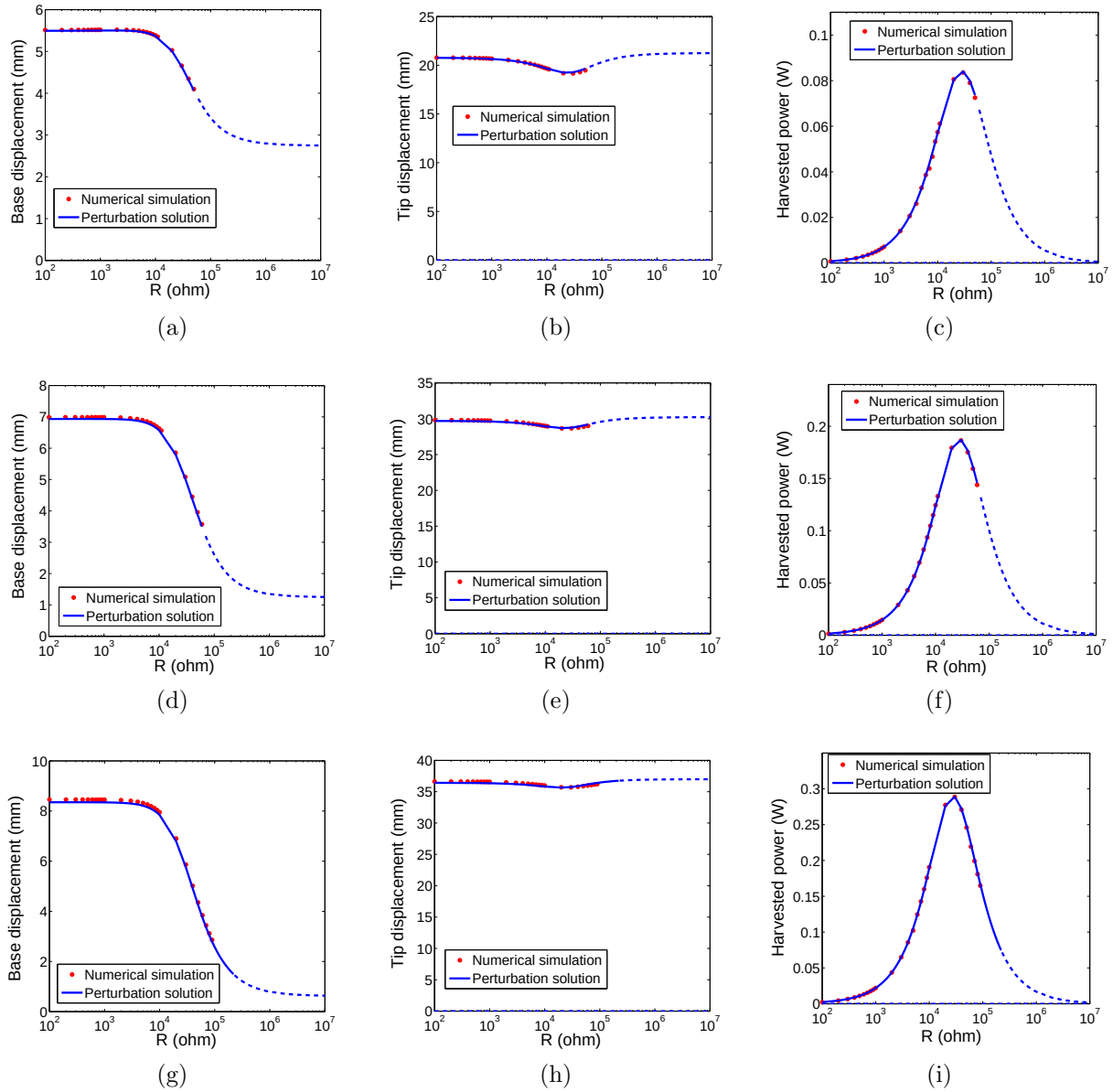

Figure 5.16: Variation of (a, d, g) displacement of base structure, (b, e, h) displacement of tip mass, and (c, f, i) harvested power as a function of the load resistance R with external force when $\omega_1 = 51 rad/s$ and $\Omega = 51 rad/s$. The dashed lines are used to denote unstable solutions and the solid line are used to denote stable solution: (a, b, c) F=0.5 N, (d, e, f) F=1 N and (g, h, i) F=1.5 N

As discussed in the above two sections, we note that load resistance has great effect on the nonlinear performances of the proposed energy harvester because both the global damping

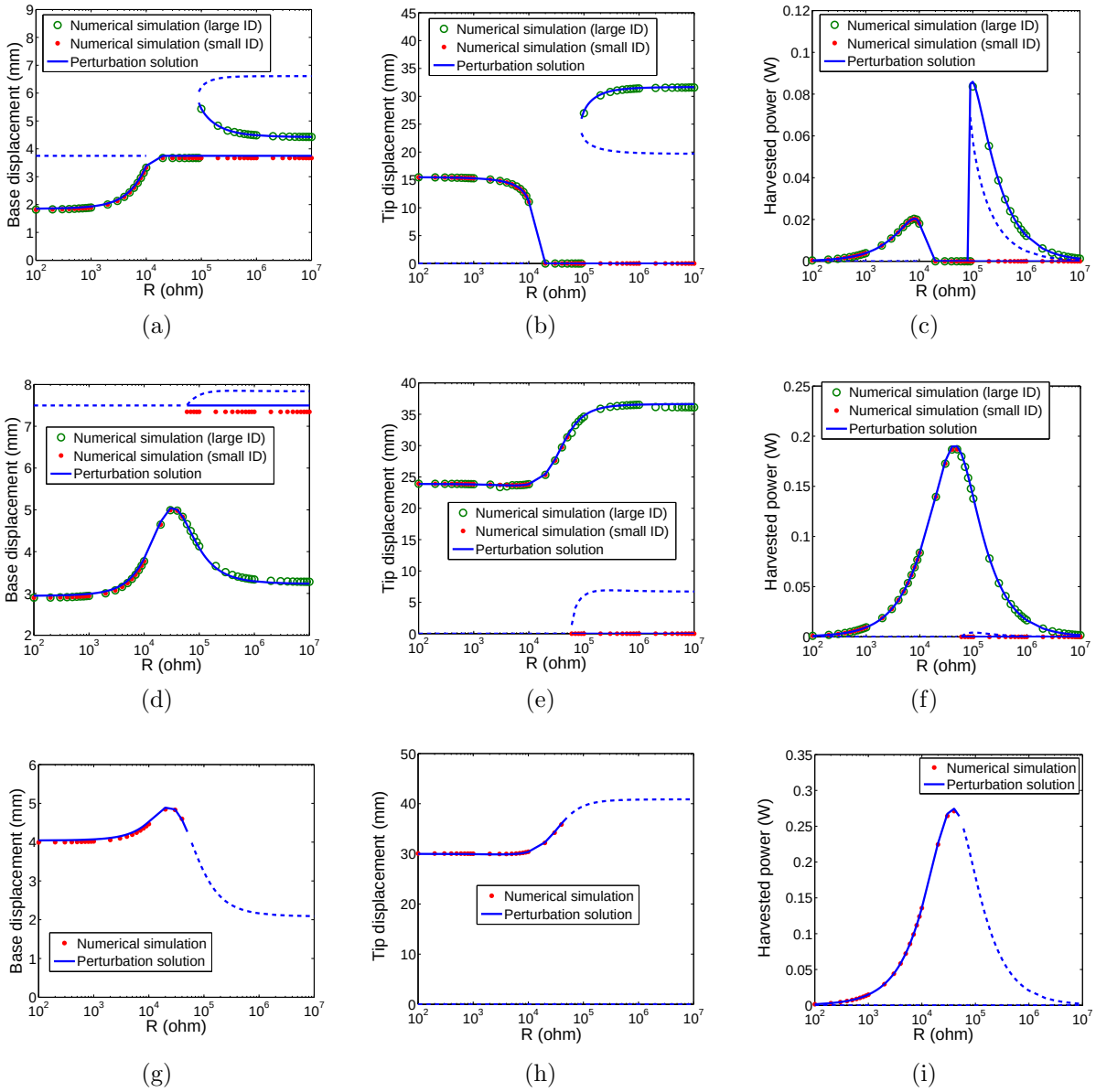

Figure 5.17: Variation of (a, d, g) displacement of base structure, (b, e, h) displacement of tip mass, and (c, f, i) harvested power as a function of the load resistance R with external force when $\omega_1 = 51 rad/s$ and $\Omega = 50 rad/s$. The dashed lines are used to denote unstable solutions and the solid line are used to denote stable solution: (a, b, c) F=0.5 N, (d, e, f) F=1 N and (g, h, i) F=1.5 N. ID denotes initial displacements.

ratio and frequency of the cantilever beam are strongly dependent on the electric load resistance, as shown in figure 5.2. Next, we analyze the effects of the load resistances on the nonlinear response of the energy harvester by varying load resistance with different external

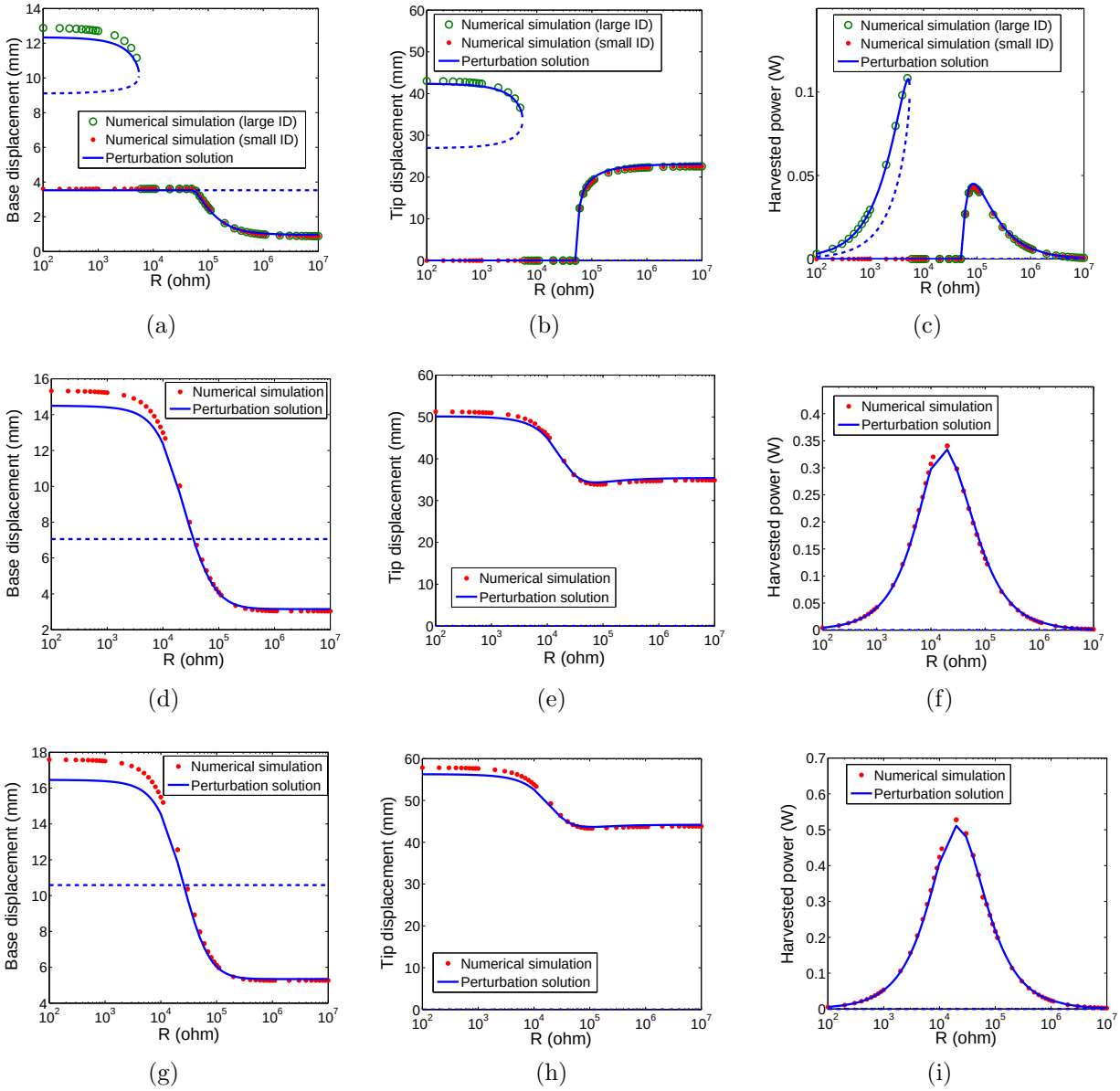

Figure 5.18: Variation of (a, d, g) displacement of base structure, (b, e, h) displacement of tip mass, and (c, f, i) harvested power as a function of the load resistance R with external force when $\omega_1 = 51rad/s$ and $\Omega = 52rad/s$. The dashed lines are used to denote unstable solutions and the solid line are used to denote stable solution: (a, b, c) F=0.5 N, (d, e, f) F=1 N and (g, h, i) F=1.5 N. ID denotes initial displacements.

forces, such as, $F = 0.5N$, $1N$ and $1.5N$, when $\omega_1 = 51rad/s$. The responses of the energy harvester with different external frequencies ($\Omega = 51rad/s$, $50rad/s$ and $52rad/s$) are plotted in figures 5.16, 5.17 and 5.18. All other parameters are shown in table 5.1.

The plots in figure 5.16 show that the electric power can be harvested with all load resistances when the system is under resonance. The system becomes unstable when the load resistance is increased in all there cases but the large external force decreases the unstable motion. In the stable range of load resistance, the displacement of the tip mass is almost kept constant while the base displacement decreases and harvested power first increases then decreases as the load resistance is increased. Therefore, there exists one optimum load resistance not only to harvest relatively large electronic power but also to control the motion of the base structure. One of interesting phenomena is that the smallest base displacement decreases as the external force is increased. In all, the system can be better controlled when the energy harvesting option is added to autoparametric vibration system.

When the external frequency is moved away from the natural frequency, the responses of the system as a function of the load resistance are plotted in figure 5.17 ($\Omega = 50 rad/s$) and figure 5.18 ($\Omega = 51 rad/s$). For the case of the external frequency smaller than the natural frequency of the base structure, the plots in figure 5.17 show that the base displacement is increased as the load resistance is increased when $F = 0.5N$. When the load resistance is around $9 \times 10^4 ohm$, one reversed saddle-note bifurcation appears. The system excited by the large initial displacements can harvested the largest power at the point of this bifurcation. The harvested power and base displacement decreases but the tip displacement of cantilever beam increases as the load resistance is increased after point saddle-note bifurcation. As the external force is increased to $1N$, the electric power can be harvested with all load resistance. Similarly, there appears one reversed saddle-note bifurcation when $6 \times 10^4 ohm$. Beyond the bifurcation point, the base displacement activated with large initial displacements is smaller than that of small initial condition (no energy harvesting) which is proved by the numerical simulation. Therefore, it is better to excite the system with large initial displacements when the load resistance is relatively large because we can not only obtain small base displacement but also harvest electric power. When the external force is increased to $1.5N$, the system become unstable when the load resistance is larger than $5 \times 10^4 ohm$. In the stable range, the large external force enables the base displacement more independent on the load resistance and thus the load resistance corresponding to large coupling damping ratio becomes the optimum load resistance for both purposes of control and energy harvesting. Figure 5.18 shows the response of the system when the external frequency is larger than the natural frequency of the base structure. For the case of $F = 0.5N$, the responses of the system are strongly dependent on the initial displacement when the load resistance is smaller than $5.5 \times 10^3 ohm$. Both displacements of the base structure and the tip mass decreases and the harvested power increases as the load resistance is increased until point of saddle-note bifurcation when the system is activated by large initial displacements. When the load resistance is increased further, the nonlinear interaction between the base displacement and cantilever beam disappear until $5 \times 10^4 ohm$ at which point a supercritical pitchfork bifurcation takes place. After that point, the base displacement decreases and harvested power first increases then decreases as the load resistance increases. When the external force

is increased to $1N$ and $1.5N$, we can harvest energy with all load resistance. In these two cases, both displacements of the base structure and tip mass decrease as the electric load is increased. Therefore, the added energy harvesting are very effective to control the motion of the system when the external frequency is larger than the natural frequency of the base structure.

5.8 Conclusion

We investigated the concept of an energy harvester based on autoparametric vibration absorber consisting of a base structure subjected to an external force and a cantilever beam with a tip mass. To convert vibrations of the base structure into electrical power, two piezoelectric sheets were bonded to both sides of cantilever beam and connected in parallel with opposite polarity with a load resistance. The coupled nonlinear distributed-parameter model is developed based on the extended Hamilton's principle to characterize the nonlinear interactions between the cantilever beam and base structure. Using the Galerkin approach, we discreted the motions of the cantilever beam and determined its exact mode shapes. Then, approximate analysis of the non-dimensional equation based on the method of multiple scales shows that there exists four types of motions. Approximate expressions of the global frequency and coupling damping ratio of the cantilever beam were derived based on the results form first order of method of multiple scales. The expressions indicate the global coupling damping and frequency are strongly dependent on the electrical load resistance which is proved by numerical results of linearized governing equation equation. Moreover, the expressions of amplitude of the base displacement, displacements of the tip mass and harvested power are presented to compare the responses of the system calculated from method of multiple scale with those from the numerical simulation of governing equations. The results show that method of multiple scale is relative accurate in determining the nonlinear responses of the system near resonance. Comparing the expressions of harvested power and the global damping ratio of cantilever beam, we also find that the harvested power is proportional to the net growth of the global damping and square of the displacement of the tip mass. Finally, the effects of different parameters, such as the amplitude and frequency of external force and electrical load resistance, on the nonlinear responses of the system are analyzed. The results show that: (1) the electrical load resistance shifts the forms of bifurcations near the resonances, (2) the motions of the system can be better controlled by adding energy harvesting to autoparametric vibration system and (3) there exists one optimum load resistance not only to effectively control the motion of the system but also to harvest largest power in some cases. Besides these, we find some forms of bifurcations, such as, saddle-node bifurcations, supercritical pitchfork bifurcations and Hopf bifurcations.

6 Conclusion and Future Work

6.1 Conclusion

In this dissertation, we performed nonlinear modeling and analysis of the unsteady aerodynamics, dynamics and fluid structure interactions.

6.1.a Unsteady aerodynamics

We developed a hybrid analytical-numerical approach to determine the lift coefficient associated with unsteady aerodynamics that involve high angles of attack. For this purpose, we revisited the classical Theodorsen's frequency response model and relaxed the major simplifying assumptions that led to limited region of applicability of Theodorsen's model such as (1) at wake, (2) small angle of attack, (3) small disturbances to the mean flow components, and (4) time-invariant free-stream. By relaxing these assumptions, we managed to develop a geometrically-exact potential flow model. In the developed model, the vortex kinematics were determined numerically. However, unlike the discrete vortex models, the circulation distribution and the associated aerodynamic loads were determined analytically after solving for the vortex kinematics.

The asymptotic steady behavior of the developed model was validated against two-dimensional experimental data and on the F-18 wing and the unsteady behavior of the developed model was validated against some experimental and computational results of canonical large-amplitude pitch maneuvers. The model also showed a good agreement with the experimental results in comparison to the classical unsteady theory without requiring high computational burden. The developed model was then used to determine the lift frequency response at various angles of attack. For small angles of attack, the obtained frequency response closely matches that of Theodorsen function. However, for high angles of attack (40°), both qualitative and

quantitative discrepancies are observed between the obtained frequency response and that of Theodorsen. In all, the developed model is efficient enough to be used in multi-disciplinary applications (e.g., dynamics and control) and also rich enough to cover some gaps that the classical theory of Theodorsen cannot cover.

6.1.b Autoparametric vibrations system and its application

The governing equations of autoparametric vibrations system were derived using the extended Hamilton's principle and non-dimensionalized. The method of multiple scales was used to solve for the equilibrium points and the Cartesian form of the modulation equations was then used to determine the stability and bifurcation of these equilibrium points. The effects of different parameters, such as the amplitude and frequency of external force, the damping coefficient and frequency of the attached cantilever beam and the tip mass, on the nonlinear responses of the system were analyzed. We find that the saturation phenomenon occurs as the external force is increased above a certain threshold and is very helpful to control the vibration of the base structure, particularly when the base structure undergoes resonance or near resonance and the frequency of the cantilevered beam is close to 1/2 of the natural frequency of the base structure. Moreover, there exists jumps and hysteresis for a specific range of parameters. Some interesting bifurcations, such as saddle-node, supercritical pitchfork, subcritical pitchfork, reversed saddle-node and reversed saddle-saddle bifurcations, are also observed. we also find that the tip mass has a considerable effect on the nonlinear response of the system, particularly when the damping ratio of the cantilever beam is small and the external force is large. Finally, time history, power spectra, phase portrait and Poincare section were used to analyze the system's responses. The results show that responses characterized by Hopf bifurcations and chaos.

We also investigated the concept of an energy harvester based on autoparametric vibration absorber consisting of a base structure subjected to the external force and a cantilever beam with a tip mass. To convert vibrations of the base structure into electrical power, two piezoelectric sheets were bonded to both sides of cantilever beam and connected in parallel with opposite polarity with a load resistance. The coupled nonlinear distributed-parameter model was developed based on the extended Hamilton's principle to characterize the nonlinear interaction between the cantilever beam and base structure. Using the Galerkin approach, we discretized the motions of the cantilever beam and determined its exact mode shapes. The approximate analysis of the non-dimensional equation based on the method of multiple scales showed that there exists four types of motions. Approximate expressions of the global frequency and coupled damping ratio of the cantilever beam were derived based on the results from the first order of method of multiple scales. The expressions indicate that the global coupling damping and frequency are strongly dependent of the electrical load resistance which was also proved by numerical results of linearized governing equation equation. More-

over, the expressions of amplitude of the base displacement, displacement of the tip mass and harvested power are presented to compare the responses of the system calculated from method of multiple scale with those from the numerical simulation of governing equations. The results show that the method of multiple scale is relatively accurate in presenting the nonlinear responses of the system near resonance. Comparing the expressions of harvested power and the global damping ratio of cantilever beam, we also find that the harvested power is proportional to the net growth of the global damping and square of the displacement of the tip mass. Finally, the effects of different parameters, such as the amplitude and frequency of external force and electrical load resistance, on the nonlinear responses of the system were analyzed. The results show that: (1) the electrical load resistance shifts the forms of bifurcations near the resonances, (2) the motions of the system can be better controlled by adding energy harvesting to autoparametric vibration system and (3) there exists one optimum load resistance not only to effectively control the motion of the system but also to harvest largest power in some cases. Besides these, we find some forms of bifurcations, such as, saddle-node bifurcations, supercritical pitchfork bifurcations and Hopf bifurcations.

6.1.c Energy harvesting from the galloping and base excitation

We have investigated the concept of harvesting energy from hybrid vibrations, namely, base and galloping of a bluff body with a triangular cross-section geometry. In order to convert the associated oscillations to usable electrical power, a piezoelectric transducer is attached to the transverse degree of freedom of the prismatic mass. A nonlinear distributed-parameter model that takes into consideration the galloping force and moment nonlinearities and the base excitation effect was derived based on extended Hamilton's principle. The galloping force and moment are modeled based on a quasi-steady approximation. The Galerkin procedure is introduced to discretize the governing equations of motion. The effects of the load resistance, wind speed on the overall damping, global frequency, and onset of instability were investigated through a linear analysis of the coupled equations of motion. Then, a nonlinear analysis was performed to investigate the effects of the base acceleration, wind speed, and electrical load resistance on the performance of the harvester and the associated nonlinear phenomena that take place. The linear analysis shows that the load resistance has great effect on the electromechanical damping and global frequency. Moreover, during the nonlinear analysis of the effect of load resistance, wind speed and base acceleration on the harvester's performance, some interesting nonlinear phenomena, such as quenching and pull-out frequency, were investigated. The results also turn out as following: (1) the acceleration of the base vibration has no effect on the onset wind speed; (2)the interaction of galloping effect and base excitation have significant effect on the energy harvester's performance; (3) as the wind speed decreases, the acceleration increases or global damping increases, the difference between pull-out frequency and global frequency increases (the quenching phenomena of the

system are more obvious). Furthermore, the existence of both types of excitations leads to the presence of new peaks in the maximum levels of harvested power of both short- and open-circuit configurations. The range of load resistances over which the harvested power is maximum for both the short- and open-circuit configurations is totally different from the range of load resistances over which tip displacement is maximized.

6.2 Future work

For unsteady aerodynamics, the assumption of potential flow does not capture specific physical aspects associated with large amplitude maneuvers. These include viscous friction, LE separation, and dynamic stall. One important extension is to study the appropriate conditions for switching between including and ignoring the LE suction. Another straightforward extension to the developed model is to allow for the emanation of a vortex sheet from the LE. The strength of the LE vorticity can be determined to satisfy the Kutta condition at the LE in the same way it is satisfied here at the TE. That is, the following two equations will be solved simultaneously to determine the strengths of the shed vorticity at both edges:

$$q'_{\theta N}(r = b/2, \theta = 0, t) + q'_{\theta TE}(r = b/2, \theta = 0, t) + q'_{\theta LE}(r = b/2, \theta = 0, t) = 0$$
$$q'_{\theta N}(r = b/2, \theta = \pi, t) + q'_{\theta TE}(r = b/2, \theta = \pi, t) + q'_{\theta LE}(r = b/2, \theta = \pi, t) = 0$$

where the subscripts N, TE, and LE refers to the non-circulatory, trailing edge wake, and leading edge wake contributions, respectively. This extension will be more suitable to capture the LE separation effects in comparison to the mere manipulation of the LE suction force inclusion.

Bibliography

[1] Berman, G. J. and Wang, Z. J., "Energy-minimizing kinematics in hovering insect flight," Journal of Fluid Mechanics., Vol. 582, 2007, 153-168.

[2] Andersen, A., Pesavento, U., and Wang, Z. J., "Analysis of Transitions Between Fluttering, Tumbling and Steady Descent of Falling Cards," Journal of Fluid Mechanics, Vol. 541, 2005, 91-104.

[3] Sane S. P. and Dickinson M. H.. "The aerodynamic effects of wing rotation and a revised quasi-steady model of flapping flight" The Journal of Experimental Biology Vol. 205, 2002, 10871096.

[4] Taha, H. E., Hajj, M. R. and Beran, P. S. "State-space representation of the unsteady aerodynamics of flapping flight". Aerospace Science and Technology, Vol. 34, 2014, 1-11

[5] Yan, Z., Taha, H. E. and Hajj, M. R. "Effects of Aerodynamic Modeling on The Optimal Wing Kinematics for Hovering MAVs". 10th AIAA Multidisciplinary Design Optimization Conference, 13-17 January 2014, National Harbor, Maryland

[6] Ellington C. P. "The Aerodynamics of Hovering Insect Flight. III. Kinematics " Philosophical Transactions of The Royal Society B. Vol. 305, 1984, 41-78

[7] Wagner, H. " Uber die entstehung des dynamischen auftriebs von tragflugeln". ZAMM 5, 1925.

[8] Theodorsen, T. "General theory of aerodynamic instability and the mechanism of flutter". Tech. Rep. 496. NACA, 1935.

[9] Von Karman, T. and Sears, W. R. " Airfoil theory for nonuniform motion". J. Aeronautical Sciences, Vol. 5 (10), 1938, 379-390.

[10] Peters, D. A. " Two-dimensional incompressible unsteady airfoil theory: an overview". J. Fluids and Structures Vol. 24, 2008, 295312.

[11] Reissner, E. " Effect of finite span on the air load distributions for oscillating wings, i- aerodynamic theory of oscillating wings of finite span". Tech. Rep. 1194. NACA T.N. 1947.

[12] Katz, J. and Plotkin, A. " Low Speed Aerodynamics", 2nd edn. Cambridge University Press, 2001.

[13] Ansari, S. A., Zbikowski, R. and Knowles, K. "Non-linear unsteady aerodynamic model for insect-like flapping wings in the hover. part1: Methodology and analysis". J. Aerospace Engineering, Vol. 220, 2006, 61-83.

[14] Ansari, S. A., Zbikowski, R. and Knowles, K. "Non-linear unsteady aerodynamic model for insect-like flapping wings in the hover. part2: Implementation and validation". J. of Aerospace Engineering, Vol. 220, 2006 169-186.

[15] Su, W. and Cesnik, C. E. S. "Nonlinear aeroelastic simulations of a flapping wing micro air vehicle using two unsteady aerodynamic formulations". 2010, 51st AIAA/ASME/ASCE/AHS/ASC Structures, Structural Dynamics, and Materials Conference.

[16] Brunton, S. L. and Rowley, C. W. Empirical state-space representations for theodorsens lift model. Journal of Fluids and Structures Vol. 38, 2013, 174-186.

[17] Ramesh, K., Gopalarathnam, A., Edwards, J. R., OL, M. V. and Granlund, K. " An unsteady airfoil theory applied to pitching motions validated against experiment and computation. Theoretical and Computational Fluid Dynamics, 2013, 1-22.

[18] Taha, H. E., Hajj, M. R. and Beran, P. S. "Unsteady nonlinear aerodynamics of hovering mavs/insects". AIAA-Paper, 2013, 2013-0504.

[19] Haxton, R. S. and Barr, A. D. S. 1972. "The Autoparametric Vibration Absorber", J. Manuf. Sci. Eng. 94(1), 119-125

[20] Cartmell, M. and Lawson, J. 1994. "Performance enhancement of an autoparametric vibration absorber by means of computer control", Journal of sound and vibration 177(2), 173-195.

[21] Hatwal, A., Mallik, A. K. and Ghosh, A.: Nonlinear vibrations of a harmonically excited autoparametric system. Journal of sound vibration 81(2), 1982, 153-164.

[22] Cuvalci, O. and Ertas, A.: Pendulum as vibration absorber for flexible structures: experiments and theory. J. Vib. Acoust. 118(4), 558-566 (1996).

[23] Dai, L. and Singha, M.C.: Periodic, quasiperiodic and chaotic behavior of a driven

Froude pendulum. International Journal of Non-Linear Mechanics. 33(6), 947-965 (1998).

[24] Vyas, A. and Bajaj, A. K. 2001. "Dynamics of autoparametric vibration absorbers using multiple pendulums", Journal of sound and vibration 241(1), 115-135.

[25] Vyas, A., Bajaj, A. K. and Raman, A.: Dynamics of structures with wideband autoparametric vibration absorbers: theory. Proc. R. Soc. Lond. A 2004 460, doi: 10.1098.

[26] Kecik, K. and Borowiec, M.: Dynamics of an Autoparametric Pendulum-Like System with a Nonlinear Semiactive Suspension. Mathematical Problems in Engineering (2011), doi:10.1155/2011/451047.

[27] Taguchi, D., Sakaguchi, R. and Sugiura, T.: Vibration Reduction of a High- T_c Superconducting Magnetic Levitation System With an Autoparametric Vibration Absorber. Applied Superconductivity, IEEE Transactions, 21(3), 1538-1542(2011).

[28] Muralt P., 2000, "Ferroelectric thin films for micro-sensors and actuators: a review", J. Micromech. Microeng. 10 13646

[29] Gurav S. P., Kasyap A., Sheplak M., Cattafesta L., Haftka R. T., Goosen J. F. L. and Van Keulen F. 2004, "Uncertainty-based design optimization of a micro piezoelectric composite energy reclamation device". 10th AIAA/ISSSMO Multidisciplinary Analysis and Optimization Conf. (Albany, NY)

[30] Zhou W., Liao W. H. and Li W. J. 2005 "Analysis design of a self-powered piezoelectric microaccelerometer Smart Structures and Materials" Conf.; Proc. SPIE 5763 23340

[31] Inman D. J. and Grisso B. L. 2006 "Towards autonomous sensing Smart Structures and Materials". Conf. SPIE, p 61740T

[32] Roundy S. and Wright P. K. 2005 "A piezoelectric vibration-based generator for wireless electronics". J. Smart Mater. Struct. 13 1131

[33] Capel I. D., Dorrell H. M., Spencer E. P. and Davis M. W., 2003, "The amelioration of the suffering associated with spinal cord injury with subperception transcranial electrical stimulation". Spinal Cord, 41, 10917.

[34] Priya S., Popa D. and Lewis F., 2006, "Energy efficient mobile wireless sensor networks". Proc. ASME Int. Mechanical Engineering Congr. Exposition (Chicago, IL)

[35] Magoteaux K. C., Sanders B. and Sodano A. H. 2008 "Investigation of energy harvesting small unmanned air vehicle Smart Materials and Structures: Active and Passive Smart Structures and Integrated Systems II" (Proceedings of the SPIE) vol 6928 (San Diego, CA).

[36] Arnold D. 2007, "Review of microscale magnetic power generation" IEEE Trans. Magn. 43 394051

[37] Mitcheson P., Miao P., Start B., Yeatman E., Holmes A. and Green T. 2004, "MEMS electrostatic micro-power generator for low frequency operation" Sensors Actuators A, 115, 5239.

[38] Anton S. R. and Sodano H. A. 2007, "A review of power harvesting using piezoelectric materials (20032006)" J. Smart Mater. Struct. 16 R1R21

[39] Sodano H., Park G. and Inman D. J. 2004 "A review of power harvesting from vibration using piezoelectric materials" Shock Vib. Dig. 36 197205

[40] Erturk A. and Inman D. J. 2009, "On mechanical modeling of cantilevered piezoelectric vibration energy harvesters" J. Intell. Mater. Struct. 19, 131125.

[41] Erturk A. and Inman D. J. 2008 "A distributed parameter electromechanical model for cantilevered piezoelectric energy harvesters" ASME J. Vib. Acoust. 130, 041002.

[42] Erturk, A. and Inman, D.J. 2009. "An experimentally validated biomorph cantilever model for piezoelectric energy harvesting from base excitations," Smart Materials and Structures, 18, 025009.

[43] Abdelkefi A, Nayfeh A H, Hajj M R and Najar F 2012 Energy harvesting from a multifrequency response of a tuned bendingtorsion system J. Smart Mater. Struct. 21 075029

[44] Abdelkefi, A., Nayfeh, A. H., Hajj, M. R., 2012, "Global Nonlinear Distributed-parameter Model of Parametrically Excited Piezoelectric Energy Harvesters," *Nonlinear Dynamics* 67, 1147-1160.

[45] Abdelkefi, A., Nayfeh, A. H. and Hajj, M. R. 2012. "Effects of Nonlinear Piezoelectric Coupling on Energy Harvesters under Direct Excitation," *Nonlinear Dynamics* 67, 1221-1232.

[46] Stanton, S.C., McGehee, C.C. and Mann, B.P. 2010. "Nonlinear Dynamics for Broadband Energy Harvesting: Investigation of a bistable piezoelectric inertial generator," *Physica. D*, 239, 640-653.

[47] Pobering, S. and Sechwesinger, N. 2004. "A Novel Hydropower Harvesting Device," *ICMENS'04, IEEE*, 480-485.

[48] Akaydin, H. D., Elvin, N. and Andrepoulos, Y. 2010. "Energy harvesting from highly unsteady fluid flows using piezoelectric materials," *Journal of Intelligent Material Systems and Structures*, 21, 1263–1278.

[49] De Marqui, C., Erturk, A. and Inman, D. J. 2010. "Piezoaeroelastic modeling and analysis of a generator wing with continuous and segmented electrodes," *Journal of Intelligent Materials Systems and Structures* 21, 983–993.

[50] Erturk, A., Vieira, W. G. R., De Marqui, C. and Inman, D. J. 2010. "On the energy harvesting potential of piezoaeroelastic systems," *Applied Physics Letters* 96, 184103.

[51] Bryant, M. and Garcia, E. 2009. "Energy harvesting: a key to wireless sensor nodes," *Proceeding SPIE* 7493, 74931W.

[52] Sirohi, J. and Mahadik, R. 2011. "Piezoelectric wind energy harvester for low-power sensors," *Journal of Intelligent Material Systems and Structures*, 22, 2215–2228.

[53] Abdelkefi, A., Nayfeh, A. H. and Hajj, M. R. 2011a. "Modeling and analysis of piezoaeroelastic energy harvesters," *Nonlinear Dynamics* 67, 925-939.

[54] Abdelkefi, A., Nayfeh, A. H. and Hajj, M. R. 2011b."Design of piezoaeroelastic energy harvesters ," *Nonlinear Dynamics* 68, 519-530.

[55] Abdelkefi, A., Nayfeh, A. H. and Hajj, M. R. 2011c."Enhancement of power harvesting from piezoaeroelastic systems ," *Nonlinear Dynamics* 68, 531-541.

[56] Abdelkefi, A., Hajj, M. R. and Nayfeh, A. H. 2012a. "Sensitivity analysis of piezoaeroelastic energy harvesters," *Journal of Intelligent Material Systems and Structures* 23, 1523–1531.

[57] Abdelkefi, A., Hajj, M. R. and Nayfeh, A. H. 2012c. "Power harvesting from transverse galloping of square cylinder," *Nonlinear Dynamics*, 70, 1377-1388.

[58] Abdelkefi A, Yan Z and Hajj M R 2013 Modeling and nonlinear analysis of piezoelectric energy harvesting from transverse galloping Smart Mater. Struct. 22 025016

[59] Abdelkefi A, Yan Z and Hajj M R 2013 "Temperature impact on performance of galloping-based piezoaeroelastic energy harvesters", Smart Mater. Struct. 22 055026

[60] Abdelkefi A, Yan Z and Hajj M R 2014 "Performance analysis of galloping-based piezoaeroelastic energy harvesters with different cross-section geometries", Journal of Intelligent Material Systems and Structures 25 (2), 246-256

[61] Eldredge, J. D., Wang, C. and Ol, M. V. A computational study of a canonical pitch-up, pitch-down wing maneuver. AIAA-Paper, 2009, 2009-3687.

[62] Bisplinghoff, R.L., Ashley, H. and Halfman, R.L. "Aeroelasticity" Dover Publications, Inc, Mineola, New York, 1996.

[63] Rauscher, M. "Introduction to Aeronautical Dynamics" John Wiley Sons, Inc, New York, 1953.

[64] Dowell, E. H., Curtiss, H. C., Scanlan, Jr. R. H. and Sisto, F. "A modern Course in Aeroelasticity", 1989.

[65] Brandon, J. M. " Dynamic stall effects and applications to high performance aircraft".

Tech. Rep. 776. AGARD, 1991.

[66] Schlichting, H. and Truckenbrodt, E. "Aerodynamics of the Airplane". McGraw-Hill, 1979.

[67] M.H. Dickinson, K.C. Gotz, Unsteady aerodynamic performance of model wings at low Reynoldsnumbers, J. Exp. Biol. 174(1) (1993) 4564.

[68] J.R. Usherwood, C.P. Ellington, The aerodynamics of revolving wings i. model hawkmoth wings, J. Exp. Biol. 205 (2002).

[69] E.C. Polhamus, A concept of the vortex lift of sharp-edge delta wings based on a leading-edge-suction analogy, Tech. Rep. NASA TN D-3767, Langely Research Center, Langely Station, Hampton, VA, 1966.

[70] Z. Wang, Vortex shedding and frequency selection in flapping flight, J. Fluid Mech. 410 (2000) 323341.

[71] Leishman, J. G. and Nguyen, k. Q. "State-space representation of unsteady airfoil behavior". AIAA Journal 28 (5), 1990, 836-844.

[72] Rufus Isaacs, Airfoil theory for flows of variable velocity, J. Aeronaut. Sci. 12(1) (1945) 113117.

[73] Greenberg, J. Mayo, Airfoil in Sinusoidal Motion in a Pulsating Stream, National Advisory Committee for Aeronautics, 1947.

[74] David A. Peters, Mong-che A. Hsieh, Almudena Torrero, A state-space airloads theory for flexible airfoils, J. Am. Helicopter Soc. 52(4) (2007) 329342.

[75] Kiran Ramesh, Ashok Gopalarathnam, Kenneth Granlund, MichaelV. Ol, JackR. Edwards, Discrete-vortex method with novel shedding criterion for unsteady aerofoil flows with intermittent leading-edge vortex shedding, J. Fluid Mech. (2014).

[76] Wallace J. Morris, Zvi Rusak, Stall onset on aerofoils at low to moderately high Reynoldsnumber flows, J. Fluid Mech. 733 (2013) 439472.

[77] I.E. Garrick, Propulsion of a flapping and oscillating airfoil, National Bureau of Standards, 1936.

[78] Meirovitch, L. . "Fundamentals of Vibration". McGraw Hill, 2001

[79] Yan Z., Abdelkefi A. and Hajj M. R., "Piezoelectric energy harvesting from hybrid vibrations", Smart Materials and Structures 23 (2), 2014, 025026.

[80] Nayfeh, A.H., "Perturbation methods", John Wiley and Sons, 1973.

[81] Nayfeh, A.H. and Chin, C., M., "Perturbation Methods With Mathematica ", ebook,

1999.

[82] Yan Z., Yan Z., Li Z. and Tan T., "Nonlinear galloping of internally resonant iced transmission lines considering eccentricity", Journal of Sound and Vibration 331 (15), 2012, 3599-3616.

[83] Nayfeh, A.H., "Nonlinear interactions: analytical, computational, and experimental methods", John Wiley and Sons, 2000.

[84] Yan Z. and Abdelkefi A., "Nonlinear characterization of concurrent energy harvesting from galloping and base excitations", Nonlinear Dynamics, 2014, 1-19.

[85] Nayfeh, A.H., Mook, D.T., Marshall, L.R., "Nonlinear coupling of pitch and roll modes in ship motion". J. Hydronaut. Vol. 7(4), 1973 145152 .

[86] Nayfeh, A.H. and Balachandran, B., "Applied nonlinear dynamics: analytical, computational, and experimental methods", Wiley-VCH Verlag Gmbh and Co. KGaA Weinheim, 2004.

[87] Abdelkefi A, Hajj M R and Nayfeh A H 2013 "Piezoelectric energy harvesting from transverse galloping of bluff bodies". Smart Mater. Struct. 22 015014

[88] IEEE. 1987. "Standard on Piezoelectricity".

[89] Naudascher, E. and Rockwell, D. 1994."Flow-induced vibrations, An engineering guide," *Dover Publications, New York*.

[90] Barrero-Gil, A., Alonso, G., and Sanz-Andres, A. 2010. "Energy harvesting from transverse galloping," *Journal of Sound and Vibration* 329, 2873–2883.

[91] Den Hartog, J. P. 1956. "Mechanical vibrations," *McGraw-Hill, New York*.

[92] Nayfeh, A.H., Mook, D.M. 1995. "Nonlinear Oscillation," *Wiley Classic Library Edition*

[93] Z. Yan, A. H. Nayfeh, H. E. Taha and M. R. Hajj. "Nonlinear characteristics of autoparametric vibration system" (Prepared to be submitted to Nonlinear Dynamics).

[94] Z. Yan and M. R. Hajj. "Energy Harvesting Through Autoparametric Resonance", Prepared to be submitted to Smart Materials and Structures.